INFORMATION TO USERS

This manuscript has been reproduced from the microfilm master. UMI films the text directly from the original or copy submitted. Thus, some thesis and dissertation copies are in typewriter face, while others may be from any type of computer printer.

The quality of this reproduction is dependent upon the quality of the copy submitted. Broken or indistinct print, colored or poor quality illustrations and photographs, print bleedthrough, substandard margins, and improper alignment can adversely affect reproduction.

In the unlikely event that the author did not send UMI a complete manuscript and there are missing pages, these will be noted. Also, if unauthorized copyright material had to be removed, a note will indicate the deletion.

Oversize materials (e.g., maps, drawings, charts) are reproduced by sectioning the original, beginning at the upper left-hand corner and continuing from left to right in equal sections with small overlaps. Each original is also photographed in one exposure and is included in reduced form at the back of the book.

Photographs included in the original manuscript have been reproduced xerographically in this copy. Higher quality 6" x 9" black and white photographic prints are available for any photographs or illustrations appearing in this copy for an additional charge. Contact UMI directly to order.

UMI

A Bell & Howell Information Company
300 North Zeeb Road, Ann Arbor MI 48106-1346 USA
313/761-4700 800/521-0600

Processing - Structure - Properties Relations in Titanium Carbide - Titanium Boride Composites Fabricated by Transient Plastic Phase Processing

A Thesis

Submitted to the Faculty

of

Drexel University

by

Dmitri Brodkin

in partial fulfillment of the

requirements for the degree

of

Doctor of Philosophy

June 1996

DREXEL UNIVERSITY

Thesis Approval Form
(For Masters and Doctoral Students)

This thesis, entitled Processing-Structure-properties Relations in Titanium Carbide-Titanium Boride Composites Fabricated by Transient Plastic Phase Processing and authored by Dmitri Brodkin, is hereby accepted and approved.

Signatures:

Chairman, Examining Committee:

Supervising Professor:

Committee Members:

Graduate Advisor:

Department Head:

Form T-1

DEDICATION

To my father.

Thank you.

ACKNOWLEDGMENTS

The author would like to express his sincere gratitude to his advisor Dr. M. Barsoum and co-advisors Dr. S. Kalidindi and Dr. A. Zavaliangos for their continuous guidance, support and understanding during the course of this work. The author also greatly appreciates their consideration of the author's personal matters. The author is also grateful to Dr. Shtessel whose advice and suggestions were very helpful. The author would like to thank Dr. W. Shih and Dr. C. Gasdaska for their time and interest in reviewing this thesis and participating on author's defense committee.

Special thanks are due to Mark Shiber for doing a great job in making the different fixtures necessary for this work and to David Van Rohr for his help with SEM. Also the author would like to express his true appreciation of Judy's Trachtman help and advice in all spheres of life not to mention her taking care of a lot of the paper work required for this degree.

Finally, thanks to all the graduate students in Material Engineering Department for making this work an enjoyable experience. Special thanks to Vicki Shtessel and Abdel Abusafesh for their sharing personal warmth, humor and support, and to Tamer El-Raghy for helping with experiments and bearing with the author's difficult character.

TABLE OF CONTENTS

Page

LIST OF TABLES.....x

LIST OF FIGURES.....xi

ABSTRACT.....xviii

1. INTRODUCTION.....1

2. BACKGROUND.....7

2.1 Toughening mechanisms in CMCs.....8

2.1.1 Fracture Mechanics Approaches.....9

2.1.2 Microcrack Toughening.....11

2.1.3 Ductile Phase Toughening.....13

2.1.4 Bridging Mechanisms.....14

2.1.5 Crack Deflection Toughening.....18

2.2 Fabrication of In Situ Reinforced CMCs and Self-Reinforced Ceramics.....20

2.2.1 Colloidal Methods.....21

2.2.2 Transient Viscous Sintering.....23

2.2.3 Reactive Infiltration Methods.....24

2.2.4 Directed Metal Oxidation.....27

2.2.5 Self-Reinforced Ceramics....30
2.2.6 SHS Methods....33
2.2.7 Reactive Hot-Processing....35
2.2.8 Transient Plastic Phase Processing....39
2.3 Titanium Carbide-Titanium Boride Material System....42
2.3.1 Ti-B-C Phase Equilibria....42
2.3.1.1 Ti-B-C Ternary Phase Diagram....42
2.3.1.2 Ti-B Binary Phase Diagram....43
2.3.1.3 Ti-C Binary Phase Diagram....44
2.3.2 Properties and Processing of TiB_2....44
2.3.3 Properties and Processing of Lower Borides....48
2.3.4 Properties and Processing of TiC....48
2.3.5 Development of TiC-TiB_2 composites....52
2.3.5.1 Structure and Chemistry of Interfaces....54
2.3.5.2 Toughness and Strength....55
2.3.5.3 Wear behavior....57
2.3.5.4 High Temperature Plasticity and Creep....59
2.3.5.5 Fabrication....59

3. EXPERIMENTAL PROCEDURE....61
3.1 Starting compositions....61
3.2 Starting Powders....62
3.3 Fabrication of composites....63
3.3.1 Mixing and Fabrication of Green Body....63
3.3.2 Hot-Pressing....64
3.3.3 Hot Isostatic Pressing (HIP-ing)....65

3.4 Interrupted Hot-Press Runs.....65

3.5 Determination of the 1600°C Isothermal Section of the Phase Diagram.....66

3.6 Characterization of the Produced Composites.....67

3.6.1 Density.....67

3.6.2 Microstructural Characterization.....67

3.6.3 Volume Fractions of Phases and Porosity.....68

3.6.4 X-ray Compositional Analysis and Lattice Parameters Measurement in TiC_x.....68

3.6.5 Determination of x in TiC_x.....69

3.7 Evaluation of Properties.....70

3.7.1 Hardness.....70

3.7.2 Elastic Modulus.....70

3.7.3 Flexural Strength.....70

3.7.4 Thermal Shock Resistance.....72

3.7.5 Fracture Toughness.....73

3.7.5.1 Indentation Fracture Method.....73

3.7.5.2 Chevron Notched Beam Method.....74

3.7.6 Oxidation Resistance.....78

4. RESULTS.....79

4.1 Final Compositions.....79

4.2 Produced Microstructures.....80

4.3 Microstructural Evolution.....81

4.4 Compositional Changes during Processing.....82

4.5 Densification Curves.....83

4.6 Mechanical properties....83
4.6.1 Fracture and Crack Morphology....84
4.6.2 Flexural strength....85
4.6.3 Chevron-Notched Beam Fracture Toughness....86
4.6.4 Abrasion wear....87
4.7 Thermal Shock....88
4.8 Oxidation kinetics....88

5. DISCUSSION....89
5.1 Isothermal Section of Ti-B-C Phase Diagram at 1600°C....89
5.1.1 Equilibrium Compositions....90
5.1.2 Non-Equilibrium Compositions....92
5.2 Transient Plastic Phase Processing....93
5.2.1 Dominant processing parameters....93
5.2.2 Processing envelope....94
5.3 Reaction Paths and Microstructural Evolution....95
5.3.1 Factors effecting reaction path....95
5.3.1.1 Effect of Impurities....95
5.3.1.2 Effect of the state of compaction....96
5.3.2 Platelet Composites....97
5.3.3 Equiaxed Composites....100

5.3.4 Morphology of the Ti_3B_4 Phase....100
5.4 Densification-Related Specifics of Microstructural Evolution....101
5.4.1. Commonality in Densification of Platelet and
Equiaxed Composites....101

5.4.2. Specifics of Densification in Platelet Composites.....102
5.4.3 Effect of Starting Powder Size in Platelet Composites.....103
5.4.4 Effect of deformation mode.....105
5.5 Structure - Properties Relations.....108
5.5.1 Effect of the third phase - Ti_3B_4.....108
5.5.2 Effect of platelet morphology.....109
5.5.3 Effect of microstructural homogeneity (for platelet composites).....111
5.5.4 Effect of grain size (for nonequilibrium equiaxed composites).....112
5.5.5 Effect of borides volume fraction (for nonequilibrium equiaxed composites).....113
5.5.6 Temperature Dependence.....114
5.5.6.1 Strength.....114
5.5.6.2 Fracture Toughness.....117
5.5.7 Thermal Shock Resistance.....118
5.6 Optimization of TPPP composites.....121
5.6.1 Platelet Composite with Refined Microstructure.....121
5.6.1.1 Oxidation Resistance.....121
5.6.1.2 Wear Resistance.....122
5.6.2 Stoichiometric TiC-based composites.....123

6. CONCLUSIONS.....126
6.1 Ti-B-C Phase Equilibria.....126
6.2 Transient Plastic Phase Processing.....126
6.3 Reaction Paths and Microstructural Evolution.....127
6.4 Structure-Properties Relations.....128
6.5 Microstructural optimization.....130

6.6. Effect of impurities.....131

7. FUTURE WORK.....132

REFERENCES.....133

TABLES.....145

FIGURES.....155

APPENDIX I Linearized Calibration Curve for C/Ti Ratio vs Lattice Parameter for TiC_x, x=0.5-0.7.....239

APPENDIX II Calculation of critical crack length for chevron notched beam tested in 4-point bending configuration.....240

VITA.....242

LIST OF TABLES

Table		Page
I	Toughened Ceramics	145
II	Properties of Monolithic TiC and TiB_2 Ceramics Compared to the Equimolar TiC/TiB_2 Composite [17,18]	146
III	Properties of Selected Cutting Tool Ceramics Compared to Titanium Borides-Titanium Carbide Composites	147
IV	Mechanical Properties of TiC, TiB_2, and TiC-TiB_2 Composites Fabricated by Various Processing Techniques	148
V	Characteristics and sources of starting powders	149
VI	Summary of X-ray diffraction results of the studied compositions. Runs 1-7 are listed in terms of increasing TiC_x content. The number of samples for each composition are shown in brackets	150
VII	Summary of Composites Produced in This Study for Property Evaluation	151
VIII	Summary of the room temperature mechanical properties for the composites tested in this study. Numbers in brackets indicate the number of samples used for each measurement	152
IX	Comparison of the Calculated And Measured Thermal Shock Resistance Characteristics for the Composites Studied in This Work and Comparable Materials	153
X	Wear Resistance of Optimized Platelet Composite Compared to Selected Engineering Ceramics (Data Obtained by ASTM G65 A Dry Sand Abrasion Wear Test)	154

LIST OF FIGURES

Figure		Page
1	Resistance-curve behavior characteristic of tough ceramics: K_R is the fracture resistance and Δa is the crack extension	155
2	Schematic diagram illustrating non-linear elemental response and the resulting stress-strain hysteresis associated with major toughening mechanisms in ceramics	156
3	Effects of damage (crack extension) on the strength of low-toughness and idealized high-toughness high-strength ceramics. The tearing modulus (T) is the slope of the resistance curve. Flaw-tolerant ceramics is associated with large tearing modulus but rarely with high strength	157
4	Increase in fracture toughness and simultaneous decrease in strength of self-reinforced silicon nitride with increase in diameter of the elongated grains [31]. Toughening is associated with crack bridging and pullout of the elongated matrix grains, however, the presence of these large grains and glassy grain boundary phase deteriorate the attendant strength	158
5	Schematic diagram illustrating three principal toughening mechanisms: (a) process-zone and bridging-zone mechanisms; (b) crack deflection and crack branching	159
6	Schematic of crack bridging by discontinuous reinforcing phases [31]: (a) Intact ligaments of discontinuous reinforcing phase impose a crack closure stress in the wake of the crack tip and enhance the fracture resistance of the brittle matrix; (b) Crack-opening displacement characterizing bridging zone is related to the tensile displacement in elastic bridging ligaments in the absence of interfacial friction. At the end of the bridging zone, the maximum crack opening is equivalent to the displacement in the ligament corresponding to its fracture stress	160
7	Schematic of microcrack toughening [29]: (a) formation of the residual stress-induced microcracks in or near second phase particles results in release of strain energy (modulus work) and residual microcrack opening (dilatational work); (b) the resulting stress-strain response	161
8	Schematic of ductile phase toughening. Ductile second-phase particles increase the attendant toughness by plastic dissipation in the process zone, as well as by crack bridging	162
9	Fracture energy and thermal expansion mismatch requirements for crack-front debonding [29]. Γ_i/Γ_f-ratio of fracture energy of the bridging ligament to that of the reinforcement-matrix interface, $(\alpha_f-\alpha_m)/\alpha_m$-relative thermal expansion mismatch between matrix and reinforcing phase	163

10 Schematic of twist of a crack around rod-like reinforcements of two aspect ratios (R) at constant volume fraction [34].....164

11 Schematic of Transient Viscous Sintering Process [10] for the formation of (top) single-phase mullite and (bottom) mullite/silicon carbide composite.....165

12 Schematic of isothermal CVI process for fabrication of carbon/carbon composites [53].....166

13 Schematic of forced CVI process (thermal/pressure gradient CVI) [56].....167

14 Schematic diagram of the DIMOX™ (direct metal oxidation) process for the fabrication of platelet-reinforced ZrB_2/ZrC/Zr composites [6].....168

15 Illustration of potential approach for fabrication of duplex Si_3N_4 matrix-Si_3N_4 whisker microstructures:
(a) SEM micrograph of α-silicon nitride whiskers (grown by VLS mechanism on a graphite substrate placed in the flow of SiO-enriched nitrogen) similar to those formed during reaction bonding of silicon powder compacts;
(b) schematic of the VLS mechanism for growth of Si_3N_4 whiskers.....169

16 Advantages of self-reinforced silicon nitride for applications as ceramic springs [72].....170

17 Densification maps used for comparison of dominant densification mechanisms during: (a) reactive hot-pressing of alumina zircon mixtures at 20 MPa [92]; (b) reactive sintering of the same [92]; (c,d) HIP consolidation of alumina at 100 MPa and 200 MPa, respectively, [170].....171

18 (a) Starting and final phases and the corresponding compositional changes during Transient Plastic Phase Processing (TPPP) in the hypothetical A-B-C ternary system; (b) Schematic of steps involved in TPPP.....172

19 Isometric view of the Ti-B-C phase diagram after Rudy [100].....173

20 1600°C isothermal section of the Ti-B-C phase diagram after Rudy [100].....174

21 TiB_2-$TiC_{0.92}$ pseudobinary phase diagram after Rudy [100].....175

22 Effects of dissolution of TiB_2 in TiC_x alloys [106] on their (a) microhardness, H_μ, and (b) lattice constant: (O) $TiC_{0.95}$; (Ψ) $TiC_{0.8}$; (Δ) $TiC_{0.68}$.....176

23 Ti-B binary phase diagram [101].....177

24 Ti-C binary phase diagram [100].....178

25 Dependence of the flexural strength on the average grain size of TiB_2 [28]. The arrow indicates the critical grain size, above which spontaneous cracking is considered to occur.....179

26 High temperature yield stress of TiB_2 compared to several structural ceramics (Data after ref. [114])....180

27 Dependence of the compression yield stress (σ_y) of TiB_2 on (a) reciprocal of absolute temperature (Arrhenius plots) for TiB_2 of different grain sizes; (b) reciprocal square root of mean grain size (Hall-Petch plots) at temperatures indicated (Data after ref. [114])....181

28 Dependence of the compression yield stress of TiC on (a) reciprocal square root of mean grain size (Hall-Petch plots) at various temperatures; (b) reciprocal of absolute temperature (Arrhenius plots) for TiC of different grain sizes produced by annealing (4 h, vacuum) at temperatures indicated, the corresponding grain sizes are 8μm (1700°C), 12μm (2000°C), 15μm (2300°C), 22μm (2600°C) (Data after ref. [134])....182

29 (a) Variation of four-point flexural strength of substoichiometric TiC_x with C/Ti atom ratio for temperatures indicated; (b) Yield stress of TiC_x as a function of temperature for C/Ti atom ratios indicated(Data after ref. [99])....183

30 Variation of properties of TiC-TiB_2 composites with mole% of TiB_2 (after De Mestral and Thevenot [17]): (a) three-point flexural strength and indentation fracture toughness; (b) electrical resistivity and coefficient of thermal expansion....184

31 Summary of the hardness of TiC-TiB_2 ceramics as a function of composition for (a) room temperature [17,18,106]; and (b) 600°C [18]. The presented data reveals both intrinsic compositional trends (Ordanyan et al.[106], Holleck et al.[18]) and compositional trends affected by processing-related factors (De Mestral and Thevenot [17]), most probably residual porosity....185

32 High-temperature bending creep behavior in TiC-TiB_2 system reported by Kats et al. [143]:
(a) Variation of steady-state creep rates with composition for σ_c=5 MPa and temperatures of 2300°C (3), 2200°C (4), 2100°C (5), compared with the results of Spivak et al. [23] at 2300°C (6);
(b) Effect of stress on creep rates for the following compositions and temperatures: (3) TiC-65%TiB_2 at 2150°C, (4) the same at 2300°C, (5) TiC-57%TiB_2 at 2100°C, (6) the same at 2280°C, (7) TiC-49%TiB_2 at 2315°C, compared with (1) ZrC-55% ZrB_2 at 1900°C and (2) ZrC-80% ZrB_2 at 2000°C....186

33 $TiC_{0.5}$ powder: (a) SEM micrograph; (b) particle size distribution....187

34 TiB_2 powder: (a) SEM micrograph; (b) particle size distribution....188

35 B_4C powder: (a) SEM micrograph; (b) particle size distribution....189

36 Ti-dehydride (4N) powder: (a) SEM micrograph of as-received powder; (b,c) particle size distributions of as-received (-325 mesh) and sieved (-500 mesh) powders, respectively....190

37 As-received Ti-hydride (4N) powder: (a) SEM micrograph; (b) particle size distribution.....191

38 Jet-milled Ti-hydride powder (~8 μm): (a) SEM micrograph; (b) particle size distribution.....192

39 Typical results of the least-squares fitting lattice parameters of TiC_x (determined from individual X-ray peaks) as a function of the $\cos^2\Theta/\sin\Theta$ for (a) run 2 with composition in Ti_3B_4-TiB_2-$TiC_{0.65}$ compatibility triangle (see Table VI); (b) run 3 with composition in TiB-Ti_3B_4-$TiC_{0.65}$ compatibility triangle and located in close proximity to Ti_3B_4-$TiC_{0.65}$ line; and (c) run 5 with composition in TiB-Ti_3B_4-$TiC_{0.65}$ compatibility triangle. The accurate lattice parameters are obtained by extrapolation of the shown linear functions onto $2\Theta=180°$.....193

40 Typical load-displacement curves obtained in four-point bending tests: (a) at room temperature; (b) at high temperatures.....194

41 Indentation fracture method for measuring fracture toughness: (a) Schematic diagram of median cracks, emanating from Vickers indentation in brittle material, illustrating the parameters used in calculation of fracture toughness; (b) SEM micrograph of typical indentation observed in this study (platelet composite)....195

42 Schematic of the loading configuration and specimen geometry used in the chevron-notched beam fracture toughness test.....196

43 Various types of load-displacement curves resulting from different crack initiation conditions in a chevron-notched beam fracture toughness test.....197

44 Backscattered SEM micrographs of the composites fabricated by TPPP. Phases: white - TiC_x; black - TiB_2, gray - Ti_3B_4.
(a) Starting composition of 4:1 Ti/B_4C with an average Ti particle size of 43 μm.
(b) Starting composition of 1:0.5:1 Ti/C/TiB_2 with an average Ti particle size of 20 μm.....198
(c) Starting composition of 1:1 $TiC_{0.5}$/TiB_2 (nonequilibrium) devoid of Ti_3B_4 in the final microstructure.
(d) Same as (c) with ~20 vol% of Ti_3B_4.....199

45 Evolution of microstructure in the processing of 4:1 Ti/B_4C starting composition:
(a) Optical micrograph of the 1000°C interrupted run specimen: the reaction layer is clearly visible at the periphery of the Ti particles;
(b) Optical micrograph of the 1200°C interrupted run specimen: the reaction has consumed all but the largest Ti particles;.....200
(c) Backscattered micrograph of the specimen quenched from 1450°C: shown is the development of platelet-like phase (TiB and/or Ti_3B_4);
(d) Backscattered micrograph of the 1600°C interrupted run specimen.....201

46 Summary of X-ray diffraction results from the interrupted hot-pressed runs and quenching experiments.....202

47 Evolution of phases during TPPP of 4:1 Ti/B_4C composition. (a) TiC_x (200) peak intensity and stoichiometry. (b) Other phases. All peak intensities are normalized by the intensities of (116) peak from the α-Al_2O_3 internal standard.....203

48 The DTA curve from the 1:1 $TiC_{0.5}/TiB_2$ powder mixture heated at 10°C/min to 1550°C under flow of argon. The observed weak exothermic peak centered around 1450°C is attributed to the sluggish reaction between the $TiC_{0.5}$ and TiB_2 components yielding the Ti_3B_4 phase.....204

49 X-ray diffraction patterns of 1:1 $TiC_{0.5}/TiB_2$ starting composition for (a) material obtained in a hot press run interrupted at 1400°C; (b) powder mixture heated to 1550°C and held at that temperature for 10 min in DTA; and (c) composite shown in Figure 44(d).....205

50 Densification of the platelet composite (4:1 Ti/B_4C starting composition):
(a) Ram displacement and temperature during typical hot-pressing run;
(b) Density and densification rate vs time for the same run.....206

51 Densification of the equiaxed composite (1:1 $TiC_{0.5}/TiB_2$ starting composition):
(a) Ram displacement and temperature during typical hot-pressing run;
(b) Density and densification rate vs time for the same run.....207

52 Fracture and crack morphology in the platelet composites:
(a) SEM micrograph of the fracture surface for the composite tested in 4-point bending at room temperature.....208
(b) SEM micrograph of the indentation crack propagating through $TiC_{0.65}$ regions with small Ti_3B_4 platelets;
(c) SEM micrograph of the indentation crack propagating through TiB_2 regions with large Ti_3B_4 platelets.....209

53 Fracture and crack morphology in the equilibrium equiaxed composites:
(a) SEM micrograph of the fracture surface for the composite tested in 4-point bending at room temperature;
(b) SEM micrograph of the crack emanating from Vickers indentation.....210

54 Fracture and crack morphology in the non-equilibrium equiaxed composites:
(a) SEM micrograph of the fracture surface for the composite tested in 4-point bending at room temperature;
(b) SEM micrograph of the crack emanating from Vickers indentation.....211

55 Variation of the flexural strength of the non-equilibrium equiaxed composites with the reciprocal of the square root of the average grain size in the composite.....212

56 Comparison of the flexural strength of the platelet composites (4:1 Ti/B_4C starting composition) fabricated using Ti powder of different particle sizes.....213

57 Variation of the flexural strength with temperature for the equilibrium platelet composite, the equilibrium equiaxed composite, and the non-equilibrium equiaxed composite.....214

58 Typical load-displacement curve obtained in a valid chevron-notched beam test carried out at room temperature.....215

59 Photomicrograph of the fracture surface showing the color contrast between the stable crack growth region and the fast fracture region in the chevron-notched beam tested at 500°C and displacement rate of 0.002 mm/min.....216

60 Variation of the fracture toughness with temperature for the refined equilibrium platelet composite and the equilibrium equiaxed composite.....217

61 Retained strengths of the refined platelet composite and the refined non-equilibrium composites quenched in water as a function of temperature drop.....218

62 Weight gain (normalized by surface area) during oxidation in air for the refined platelet composite at 900°-1000°C.....219

63 Isothermal section of the Ti-B-C phase diagram at 1600 °C. (a) as reported by Rudy [100] (here shown schematically, see Figure 20 for original version); (b) based on this work.....220

64 X-ray diffraction pattern of (a) specimen produced in run 1, in which the starting composition belongs to the TiB_2 - Ti_3B_4 - $TiC_{0.65}$ compatibility triangle, and (b) specimen, in which the starting composition belongs to the TiB - Ti_3B_4 - $TiC_{0.65}$ compatibility triangle, produced in run 5 and consequently annealed for 32 h in vacuum.....221

65 Backscattered SEM micrograph of the sample produced from the 1:0.5:1 Ti/C/TiB_2 starting composition (run 2) and consequently annealed for 32 h in vacuum. Phases: white - $TiC_{0.65}$, black - TiB_2, gray - Ti_3B_4.....222

66 Dominant processing parameters in TPP-processing of TiC_x-TiB_2-(Ti_3B_4) composites.....223

67 Hot-pressing diagrams for the platelet composition:
(a) The applied pressure required to achieve the certain level of porosity as a function of the starting Ti powder particle size;
(b) The final porosity in the produced composites as a function of the starting Ti powder particle size for the applied pressures indicated.....224

68 High-magnification backscattered micrograph of the non-equilibrium equiaxed composite with ~20 vol% of Ti_3B_4 phase showing the Ti_3B_4 phase surrounding multiple small TiC_x particles seemingly excluded from the reaction.....225

69 Dependence of the reaction path on the green density (state of compaction) of the 4:1 Ti/B_4C samples reacted by heating in vacuum (10^{-4} torr, 10°C/min) to 1200°C: (a) loose powder mixture; (b) pre-compacted specimen of 74% green density...226

70 Schematic of microstructural evolution in the "platelet" composites.....227

71 Proposed mechanism of the Ti_3B_4 phase formation in the equiaxed composites by displacement of C with B rather than mobility of Ti.....228

72 Effect of the starting Ti powder particle size on the final scale of microstructure of the platelet composites. Composites shown in the backscattered micrographs were produced using the following Ti powders: (a) 43 μm (dehydride 4N), (b) 20 μm (dehydride 4N, sieved), (c) 8 μm (hydride 4N, jet-milled), (d) 5 μm (MER-process, 98.5%).....229

73 Temperature and pressure schedules for the HIP and hot press runs which yielded platelet composites shown in Figures 74 (a) and 74 (b,c), respectively.....230

74 Microstructures of the platelet composites produced by (a) HIP-ing - backscattered micrograph; (b) Hot-pressing - backscattered micrograph of a transverse section;.....231
(c) Hot-pressing - backscattered micrograph of a longitudinal section; (d) optical micrograph of the sample from the hot-pressed run interrupted at 800°C (mag. x500).....232

75 Backscattered micrograph of the nearly laminate-type microstructure, comprised of alternating layers of TiB_2-Ti_3B_4 (black and gray) and $TiC_{0.65}$ (white) that was produced by occasional forging when the reaction product flew into the narrow gap between the die cavity and the pushing rod.....233

76 Effect of the starting Ti powder particle size on the morphological texture formation in the equilibrium equiaxed composites. Composites shown in the backscattered micrographs were produced using the following Ti powders: (a) 43 μm (dehydride 4N), (b) 20 μm (dehydride 4N, sieved).....234

77 Variation of the room and high temperature flexural strengths of the coarse-grained non-equilibrium equiaxed ($TiC_{0.5}$/TiB_2) composites, fabricated with different carbide/boride mole ratios, with the volume fraction of TiB_2.....235

78 Variation of the flexural strength with temperature for the two non-equilibrium equiaxed composites with the different impurity levels. Impurities (~0.2 wt.% Co) were introduced in the refined non-equilibrium equiaxed composite during ball-milling by WC-Co grinding media.....236

79 Variation of the flexural strength with temperature for the TiC_x/TiB_2 composites with the different stoichiometries of TiC_x and different volume fraction of borides as indicated.....237

80 Backscattered micrograph of the $TiC_{0.9}$-33.5 vol% TiB_2 composite.....238

ABSTRACT

PROCESSING - STRUCTURE - PROPERTIES RELATIONS IN TITANIUM CARBIDE - TITANIUM BORIDE COMPOSITES FABRICATED BY TRANSIENT PLASTIC PHASE PROCESSING

DMITRI BRODKIN

MICHEL BARSOUM

A systematic study of processing-structure-properties relations was carried out for a class of titanium carbide-titanium boride composites produced by Transient Plastic Phase Processing (TPPP), novel processing technique capable of in situ net-shape manufacturing fully dense refractory ceramic composites at relatively low homologous temperatures. These fully dense TiC_x-TiB_2-Ti_3B_4 composites were fabricated starting from Ti/B_4C, $TiC_{0.5}/TiB_2$, $Ti/C/TiB_2$ and $TiC_{0.5}/B_4C$ mixtures of different molar ratios with the resulting different morphologies of the final phases.

The starting composition was found to determine the final microstructure and properties. However, provided the starting composition and the temperature schedule were maintained the same, the mode of deformation (HIP-ing vs hot-pressing or forging) and particle size of the starting powder mixture were found to be the critical factors determining the nominal pressure required to achieve full density in the produced composites, and extent of homogeneity and morphological texture in their final microstructure. Plastic flow of $TiC_{0.5}$ combined with particle rearrangement and comminution of porous reaction product are believed to be the predominant mechanisms for the most part of densification process responsible for increase of relative density to ~95%.

Reaction paths and microstructural evolution in the two starting compositions with 4:4:1 ratio of Ti:B:C, namely: 4:1 Ti/B_4C and 1:1 $TiC_{0.5}/TiB_2$, were examined in detail. In the former, the Ti_3B_4 phase nucleated and grew as platelets, whereas it exhibited roughly equiaxed morphology in the latter. The presence of TiB as an intermediate phase in "platelet" composition appeared to determine the morphology of the Ti_3B_4 phase. Based on XRD and SEM results from interrupted runs, a model is proposed according to which the faster diffusion of C, relative to B, is instrumental in the microstructural evolution of the "platelet" composite. Consistent with the model is the observation that the reduction of the initial particle size of the Ti in the "platelet" composition resulted in a more homogenous microstructure. The microstructural evolution of the "equiaxed" composite is less complicated in that there are no intermediate phases. The resultant microstructure is believed to develop by a displacive reaction that only involves the diffusion of B and C.

The flexural strength in the temperature range 25°C-1400°C, plane strain fracture toughness in the temperature range 25°C-1000°C, room temperature hardness and microhardnesses of individual phases, thermal shock susceptibility, wear resistance, and oxidation resistance in the temperature range 750°C-1000°C were measured for a variety of fully dense titanium carbide-titanium boride composites with different microstructures. The Ti_3B_4 platelets are responsible for a 30% increase in fracture toughness when compared with the equiaxed composites. This toughening increment is largely attributed to the increased efficiency of crack deflection by Ti_3B_4 platelets compared to the equiaxed Ti_3B_4 grains. The K_{IC} value of ~6 MPa measured for the platelet composites is consistent with the fact that only crack deflection was observed in these composites and that there were very few indications of crack bridging and platelet pull-out. TiB_2 is the strength governing phase at ambient temperatures due to residual stresses induced by its thermal expansion anisotropy. At high temperatures, however, these residual stresses are relieved and the

presence of borides results in significant strengthening. TPPP composites exhibited adequate oxidation resistance up to 1000°C. Their relatively high thermal shock resistance and strength, and their competitive wear behavior combined with economic processing requirements make this class of materials an excellent candidates for cutting tools.

1. INTRODUCTION

Ceramic materials are primary candidates for numerous critical applications due to their extreme hardness, excellent wear resistance and chemical stability, along with high modulus and specific strength. Ceramic components could be used at temperatures or in environments beyond the reach of their metal or intermetallic counterparts. However, the inherent disadvantage of the monolithic (single phase) ceramics, their brittleness and hence tendency to catastrophic failure limits their applications as engineering material.

Within the last two decades, a number of approaches to improve fracture toughness of ceramics have been developed. These approaches have yielded high-performance ceramic materials with fracture toughness values as high as 10 to 20 MPa$\sqrt{m}$ (Table I). Among them, a term "ceramic-ceramic matrix composite" (CMC) is commonly applied to fiber or whisker reinforced ceramics as well as multiphase ceramics in which one of the phases serves as reinforcement. In the latter case this signifies the fact that different microstructural constituents interact with each other and the propagating crack providing additional crack energy dissipation mechanisms and thus increasing fracture toughness. Therefore, the distinction between multiphase ceramics and CMCs is in the synergy of combining different microstructural constituents that is achieved in composites and results in a multiphase ceramic material exhibiting better combination of mechanical properties compared to parent single phase ceramics. The search for this synergy is the major goal in the development of CMCs and other high-performance ceramic materials.

Novel concepts for fabrication of high-performance ceramic materials have also been developed in the recent years. Among them in situ methods have generated considerable interest. However, in situ methods often lose the competition to conventional techniques or techniques which are less innovative from a material point of view but can be used in conjunction with state-of-the-art manufacturing practices such as superplastic forming, 3-D printing etc. This in no way can be attributed to insufficient cost-efficiency or flexibility of in situ methods, but rather to the lack of understanding of in situ processes. In situ techniques, with only few exceptions, are not optimized to the extent, sufficient to make them attractive for end users, and, therefore, only few of them have found practical applications. Successful exceptions are the family of self-reinforced silicon nitrides [1-4] and Lanxide DIMOX™ platelet-reinforced composites [5-7]. Introduction and patenting of these materials in 1989-90, clearly showed that the optimization of these and other innovative techniques could be realized only through better understanding of processing-structure-properties relations which has not been achieved yet for many of them.

Recently, a novel processing technique called Transient Plastic Phase Processing (TPPP) was developed by Barsoum and co-workers [8, 9] for net shape processing certain classes of fully dense ceramic-ceramic composites. TPPP is a form of reactive hot-pressing that is generically related to such innovative approaches as Transient Viscous Sintering of Sacks et al. [10, 11] and solid state displacement reaction synthesis of Henager et al. [12-14]. This technique offers several advantages over other currently used techniques, which include lower processing temperatures, elimination of sintering aids, and feasibility of producing a variety of microstructures and compositions some of which are new and as yet unexplored in literature. TPPP has been successfully employed by Barsoum and co-workers [8, 15] to produce fully dense ceramic-ceramic composites in the Ti-B-C system, among others [16].

The initial work of Barsoum and Houng [8] has demonstrated the feasibility and some of the advantages of TPPP in the Ti-B-C system. In that study, two starting compositions, 3:1 Ti/B_4C and 4:1 Ti/B_4C (molar ratios), were investigated. It was observed that only the latter composition yielded a near fully dense composites. This was explained by the experimental observations that indicated the formation of intermediate compounds during the initial densification step in the 4:1 Ti/B_4C starting composition. These intermediate compounds were identified as $TiC_{0.5}$ and TiB_2. It was noted that since an intermediate "soft" $TiC_{0.5}$ did not form in the 3:1 Ti/B_4C starting composition, the produced composite had significant residual porosity. Some of the interesting features reported by Barsoum and Houng [8] included net shape capability and the development of Ti_3B_4 in platelet morphology.

Ti-B-C system appeared to be a rewarding object for both, in-depth study of processing-structure-properties relations and optimization of TPPP for the following reasons:

(i) Titanium carbide-titanium boride composites hold great promise for applications as high-temperature structural components in heat exchangers and engines, as wear-resistant elements in cutting tools and forming dies, as well as many other non-structural applications. It has been shown that multiphase composites containing these compounds exhibit strong synergistic effects resulting in remarkable overall mechanical properties [17-22].

(ii) In TiC-TiB_2 system TPPP has proven to be the only viable alternative to conventional processing techniques capable of producing fully dense, ultra-refractory TiC_x-TiB_2 or TiC_x-TiB_2-Ti_3B_4 composites at temperatures that are only about 0.62 of the eutectic temperature.

Indeed, the processing of these ultra-refractory composites into complex-shaped components with full densities requires extremely high temperatures and poses a serious technological challenge. For example, hot-pressing of TiB_2 and TiC at 2200°C and 10 MPa for 15 minutes yielded samples that were between 95% and 97% dense [23]. A number of techniques have been suggested in literature to overcome this problem. These include the aforementioned transient viscous sintering in mullite-matrix composites [10, 11] and reactive hot-pressing in Mo-Si-C and Ti-Si-C systems by employing displacement reactions [12-14]; addition of "tailored" sintering aids in TiB_2-TiC composites [24, 25]; self-propagating high-temperature synthesis assisted by a forced consolidation step such as high-pressure combustion sintering [26]; and directional reaction of molten Ti with B_4C preform [27]. Although these techniques have been partially successful in overcoming some of the problems in processing of the ultrarefractory composites, they still continue to suffer from at least one of the following limitations - high processing temperatures, significant residual porosity, or poor high temperature creep properties (largely due to the addition of sintering aids).

The composites produced in the Ti-B-C system by TPPP differ from the composites studied in the literature in many aspects. For example, the TPPP composites comprise significant amounts of Ti_3B_4 phase, unlike the composites studied in the literature, and the Ti_3B_4 phase appears with a platelet morphology in some cases. In addition, the TPPP composites contain significant amounts of substoichiometric TiC_x. The influence of these differences on the macroscopic mechanical properties of the titanium carbide-titanium boride composites has not yet been investigated. Furthermore, very little is known about high temperature mechanical properties of these composites as well as the TiC-TiB_2 composites studied in the literature.

The goals of the present study were (i) to elucidate general features of TPPP and its specifics in Ti-B-C system, specifically to examine the role of deformation mode and different transient plastic (Ti, $TiC_{0.5}$) and reaction phases (B_4C and TiB_2) in densification, (ii) to obtain a good understanding of the factors and reaction sequence responsible for the formation of the Ti_3B_4 in different morphologies; (iii) to evaluate the high temperature properties of the composites produced by TPPP in the Ti-B-C system, and (iv) to understand the effects of the various microstructural variables in this system such as the morphology of Ti_3B_4 phase, microstructural homogeneity, the volume fraction of borides, and the grain size on the attendant mechanical properties.

Specifically, fully dense composites were fabricated using the TPPP technique starting from Ti/B_4C, $TiC_{0.5}/TiB_2$, Ti/C/TiB_2 and $TiC_{0.5}/B_4C$ mixtures of different molar ratios with the resulting different morphologies of the final phases. The particle sizes of the starting powders were also varied to understand their effect on the homogeneity of the final microstructures. For the two selected starting compositions, namely, 4:1 Ti/B_4C and 1:1 $TiC_{0.5}/TiB_2$, the evolution of microstructure was documented through interrupted hot press runs using X-ray diffraction analysis, and optical and scanning electron microscopy. Note that these starting mixtures are equivalent in overall elemental composition and, hence, correspond to the same point on the Ti-B-C phase diagram, however, they yield Ti_3B_4 in different morphology. In an effort to understand the role of the various microstructural features and to optimize the microstructures for high temperature structural applications the flexural strength in the temperature range 25°C-1400°C, plane strain fracture toughness in the temperature range 25°C-1000°C, room temperature hardness and microhardnesses of individual phases, thermal shock susceptibility, wear resistance and oxidation resistance in the temperature range 750°C-1000°C were measured for a variety of fully dense compositions.

This dissertation is organized as follows. In Chapter 2 the review of toughening approaches and relevant in situ processing techniques are given, along with the detailed analysis of the available literature on the development of high-performance ceramics in the TiC-TiB_2 material system. The sample fabrication techniques, methods of analyses and the employed experimental procedures are detailed in Chapter 3. The obtained experimental results from the X-ray, microscopy, and mechanical tests are summarized in Chapter 4. Based on these experimental observations the processing-structure-properties relations for the fabricated composites are discussed in Chapter 5. Finally, Chapter 6 presents the important conclusions and Chapter 7 gives a list of suggestions for the future experimental work.

2. BACKGROUND

The growing demand for materials exhibiting exceptional hardness, durability and stability at very high temperatures has led to the increased interest in ultra-refractory CMCs based on carbides, borides, nitrides and silicides of transition metals. One of the material systems that has attracted significant attention is TiC-TiB_2 multiphase ceramics. Besides wide range of high temperature structural applications, other potential applications for this system include armor plates, cutting tools, dies, wear-resistant elements, tiles for first wall in nuclear fusion reactors, and, given its good electrical conductivity, cathodes in Hall-Heroult cells for the electrolytic production of aluminum and vaporizing elements for vacuum metal deposition installations.

Processing of ultra-refractory CMCs into complex shapes and full densities requires extremely high sintering temperatures and poses a veritable challenge. Additional difficulties are associated with incorporation of reinforcements, and their compatibility with matrices at high temperatures and aggressive environments [28]. These processing challenges have been circumvented in a variety of processing techniques, among which the processes of in situ formation of reinforcements constitute a new, but increasingly important field in fabrication of CMCs. Their advantages and disadvantages as applied to particular composite system are analyzed here in terms of their ability to attain fully dense composites, to control the final grain size, to tailor properties of a final product to specific applications, and to avoid sacrificing of final properties for ease of processability, e.g. addition of large amounts of sintering aids.

The following sections discuss in detail the mechanisms underlying the approaches to toughen ceramics in situ and relevant processing methods, and later a literature review of the current state of development of high-performance ceramics in the TiC-TiB_2 material system is given.

2.1 Toughening mechanisms in CMCs

The resistance of ceramics to the propagation of cracks can be strongly influenced by microstructure and by the use of various reinforcements. Among the known mechanisms that can contribute to fracture resistance are stress-induced transformation and microcracking; twinning, ductile phase toughening; crack pinning, crack deflection, crack bridging, and pullout by fiber/whisker reinforcements, dispersed particles, elastic-reinforcing phases and matrix grains. In most cases, toughening results in resistance curve (R-curve) behavior shown in Figure 1, wherein the fracture resistance increases with crack extension. It has been demonstrated [29] that the rising R-curve behavior is physically related to nonlinear processes in the wake of the propagating crack (e.g. plastic deformation zone, transformation zone, zone of bridging by intact fibers whiskers and grains, pullout zone etc.). These processes manifest in nonlinear stress-displacement characteristics. Furthermore, toughening can be explicitly related to stress-displacement hysteresis [29] (Figure 2) that results in the energy dissipated upon crack propagation.

Rising R-curve behavior is the underlying concept of flaw tolerant ceramics, (Figure 3) which emphasizes long crack behavior over short crack behavior, since the aforementioned toughening mechanisms are operative when the crack wake has been developed. Flaw tolerance is associated with high steady-state fracture toughness (crack

wake is fully developed) and graceful failure. The resulting material strength then depends on characrteristics of the resistance curve and the initial crack length, such that toughness and strength optimization usually involve different choices of microstructure (Figure 4). However, high strength and crack growth initiation resistance (short crack behavior) are required for many applications such as cutting tools. As a result, the concept of graceful failure nurtured by scientists has not been fully accepted by design engineers. Nevertheless, there are recent successful examples of high-performance ceramics that exhibits both high fracture toughness and strength, such as self-reinforced Si_3N_4, and in situ platelet reinforced CMCs fabricated by the DIMOX™ process.

These techniques are representative of alternative approaches that have been developed in the past decade to obtain the benefits of composite-type microstructures without the problems of incorporation and uniform distribution of a second phase. These approaches, based on forming reinforcements in situ, are becoming increasingly important in composite synthesis. Consequently, the emphasis of the following sections will be on the specific toughening mechanisms that are found to be operative in the in situ processed composites.

2.1.1 Fracture Mechanics Approaches

Introduction of fracture mechanics permitted to elucidate material and microstructural parameters governing toughening by various mechanisms. Evans [29] conveniently divides toughening mechanisms for ceramics into two categories: process zone formation and bridging. Both mechanisms involve energy dissipation in the crack wake. A third mechanism, crack deflection, elevates toughness by increasing the area of the fracture surface (Figure 5).

According to Evans, the process zone mechanisms exhibit toughening fundamentally governed by a critical stress for the onset of nonlinearity, σ^c, in elements near the crack and by the associated stress-free strain, ε^T. The resulting stress-strain hysteresis (due to nonlinear deformation) of those elements within a process zone then yields a steady-state toughness given by [29]

$$\Delta G_c \approx 2f\varepsilon^T\sigma^c h \tag{1}$$

where ΔG_c is the increase in the critical strain energy release rate of composite (above the matrix value) when the crack is long, f is the volume fraction of the toughening agent, and h is the width of the process zone in steady state. The term $\sigma^c\varepsilon^T$ approximates the strain energy density which is simply the area under the stress-strain curve in the case of uniaxial loading [30]. Thus the toughness is controlled by the width of the process zone, the concentration of the toughening agent, and the area under the stress-strain curve. Transformation, microcrack and twin toughening are mechanisms of this type.

The bridging category exhibits toughening governed by hysteresis along the crack surface, induced by intact material ligaments [29]

$$\Delta G_c = 2f\int_0^{u^*} t(u)\,du \tag{2}$$

where 2u is the crack opening, 2u* the opening at the edge of the bridging zone, t the tractions on the crack surfaces exerted by the intact ligaments (Figure 6 (a,b)), and f the area fraction of reinforcements along the crack plane. Ductile reinforcements, as well as whiskers, fibers, and large grains, toughen by means of bridging tractions.

It is also possible for a process-zone mechanism and a bridging mechanism to operate simultaneously, and thus generate a net toughness larger than that for the separate mechanisms [29, 31, 32]. In fact, the overall toughness can even be multiplicative [33].

It should be noted, that there are two equivalent methods for determining trends in toughness [29, 31, 30]: the one presented above is based on conservation integrals, G_c, and the other on stress intensity factors, K_c. Both approaches predict the same behavior, but have different utility when various aspects of toughening require elucidation. The former relates the energy dissipated upon crack propagation to the physical mechanisms of toughening, such as nonlinear deformation of second phase particles in a transformation zone [29], or work of crack closure forces exerted by intact ligaments in a bridging zone [29, 31]. In the latter the stress intensity difference (crack tip shielding, $\Delta K = K_{tip} - K_{global}$) associated with the specific toughening mechanism is characterized and related to microstructure [29, 34, 35].

2.1.2 Microcrack Toughening

A number of multiphase ceramic materials exhibit trends in toughness with particle size, temperature, etc. that are consistent with microcrack toughening mechanism. However, this mechanism has been validated only for Al_2O_3 toughened with monoclinic ZrO_2 [36] and for some TiB_2-toughened low thermal expansion matrices such as SiC [37] and B_4C [38]. The microcracking mechanism is relatively ineffective, as Table Evans-I indicates. Moreover, toughening by microcracks is normally accompanied by reduction of strength of the ceramic material [39].

Figure 7(a) schematically illustrates microcrack toughening mechanism [29]. Second-phase particles are often subject to residual stress due to thermal expansion mismatch or transformation. If the residual stress in the particle is tensile and the local stress in the matrix is compressive, the particle cracks. If the signs on the stresses are reversed, the matrix material cracks at the interface. In both cases there is a residual opening of the microcracks, which leads to an increase in volume of the sample. Figure 10(b) illustrates the stress-strain response of such a material. The material begins to crack at a critical stress, σ^c, and the stress-strain curve becomes nonlinear, due to a combination of compliance increase and dilatational strain, θ_T. If the material is unloaded prior to total failure, the relative contribution of dilatational effects (residual microcrack opening) and modulus effects (due to the release of strain energy) are readily apparent (see Figure 7(b)).

Accordingly, the crack shielding caused by microcracks can be separated into dilatational and modulus contributions. The former depends on process zone size and shape, whereas the latter depends only on the zone shape. As shown by Evans [29] the dilatational contribution has precisely the same form as given by Eq.1, but with $f\varepsilon^T$ replaced by θ_T. Following Hutchinson [35], who derived accurate analytical expressions for crack tip shielding by microcracking, both contributions are proportional to microcrack density, η. In general, the ΔK_c due to dilatational and modulus effects are similar in magnitude, however, they are not additive, and interaction terms are involved [29].

Anderson [30] used a simplified energy approach to derive the dependence of the modulus contribution (increase in compliance) on microcrack density. The formation of microcracks releases strain energy from the sample, which results in an increase in compliance. The change in strain energy density due to the microcrack formation is given by Anderson as

$$\Delta w = 2\eta\pi r^2\gamma_s \qquad (3)$$

where η - microcrack density, r is an average radius of penny-shaped microcracks activated by the passage of a macrocrack, γ_s is the fracture surface energy. For a macrocrack that produces a process zone of microcracks, the increment of toughening due to microcrack formation can be assessed by

$$\Delta G_c = 2h\Delta w = 4h\eta\pi r^2\gamma_s \quad (4)$$

where h is the width of the microcracking process zone in steady state.

The degree of microcrack toughening is temperature dependent [30]. Thermal mismatch and the resulting residual stresses tend to be lower at elevated temperatures, which implies less dilatational strain.

2.1.3 Ductile Phase Toughening

Ceramics with the incorporated ductile particles exhibit both bridging and process zone toughening as illustrated in Figure 8. Plastic deformation of the particles in the process zone contributes to toughness, as does the ductile rupture of the particles that intersect the crack path [29, 30]. Residual stresses in the particles can also add to the resulting toughness. The magnitude of the bridging and process zone toughening depends on the volume fraction and flow properties of the ductile phase. The process zone toughening also depends on the ductile particle size, with small particles giving the highest toughness [29].

Ductile phase toughening is a predominant mechanism in cemented carbides [29], and more recently has been observed in CMCs fabricated by the DIMOX™ process [5] due to the presence of residual Zr metal in the latter. It should be noted, that not only metal phase but also ceramic constituents above their ductile-to-brittle transition temperature can

induce ductile phase toughening, e.g. TiC (suggested as possibility in [8,17] and hinted by indirect experimental evidence in [21]) and $MoSi_2$ [12].

This toughening mechanism is temperature dependent, since the flow properties of the ductile phase vary with temperature. As a result, ductile phase toughening is ineffective for temperatures approaching the melting temperature of the ductile phase.

2.1.4 Bridging Mechanisms

Not only is crack-bridging a potent toughening mechanism for ceramics (see Table I Evans-I), it is also effective at high temperatures [40, 30]. Furthermore, toughening by crack-bridging mechanisms practically has no alternatives as the dominant toughening approach for high-temperature structural ceramics for applications that require load-bearing capability at temperatures above 1000°C.

A comprehensive analysis of bridging by discontinuous elastic reinforcements is given recently by Becher [31]. Becher considers toughening by the three broad classes of bridging ligaments, namely: whiskers, noncubic matrix grains, and platelet and rodlike reinforcements (matrix grains and second phases) formed in situ. His review shows inherent similarity of general principles as well as material and microstructural parameters governing the toughening response of these three major groups of discontinuous reinforcements. These principles are: weak interface (intergranular fracture), optimal thermal expansion and elastic moduli mismatch, and strong reinforcements. Consequently, the dominant parameters are: the relative ligament/matrix interface debond toughness (γ^l/γ^i); the thermal expansion misfit strain between the ligament and the matrix (ε^T) and the corresponding residual thermal expansion misfit stress (σ^r) imposed on the interface; the

friction coefficient at the debonded interface (μ); the fracture strength of bridging ligaments (σ^f); radius (r) or crossectional dimension (d) of the bridging ligament; volume fraction of bridging ligaments (V^l), elastic moduli of the ligament (E^l), matrix(E^m) and composite (E^c).

As widely acknowledged, e.g. [29, 31], the principle mechanisms that are complementing the crack-bridging toughening process (the work of crack closure tractions exerted by bridging ligaments) are debonding (generates new surface), crack deflection along debonded reinforcement-matrix interface (generates new surface and may cause local reduction of driving force), and pullout (induces frictional dissipation). It is shown [29, 31] that strong interfacial bonding and interfacial clamping stresses (when thermal expansion coefficient $\alpha_{matrix}>\alpha_{ligament}$) can preclude debonding and/or pullout, whereas debonding along reinforcement-matrix interface due to weak interface and/or optimal thermal expansion mismatch (see Figure 9) is important in achieving both crack bridging and subsequent pullout of reinforcing ligament. As pointed out by Becher, the formation of a debonded interface spreads the strain imposed on the bridging ligament over a longer gauge section generating a larger crack opening displacement per unit of stress supported by the ligament (Figure 6(b)). As a result, the bridging stress supported by the reinforcement increases more slowly with distance behind the crack tip, and longer bridging zone is developed behind the crack tip. The resultant increase in crack opening displacement with distance behind the crack tip significantly enhances the fracture resistance of the composite.

Again the simplified energy dissipation approach readily yields correct trends for crack-bridging contribution to the toughness. The additional energy consumed by the bridging zone is defined [29,31] as the product of the bridging stress, σ^f, and maximum crack opening displacement, 2u*:

$$\Delta G_c = 2f \int_0^{u^*} t(u)\, du \approx V^l \sigma^f u^* \qquad (5)$$

In the case of large matrix grains or rodlike self-reinforcements, the bridging stress supported by ligaments, is shown to be the product of frictional shear stress required to pull out each bridging grain, τ_{gb}, times the fraction of bridging grains, A^{gb}. As argued by Becher [31], 2u* can be approximated by the grain size, d, and the incremental increase in strain energy release rate due to grain bridging, ΔG_{gb}, is

$$\Delta G_{gb} = A^{gb} \tau_{gb}\, d/2 \qquad (6)$$

This model is consistent with experimental observations, where the measured fracture toughness of alumina is found to increase with increase in the square root of the grain size [29].

The results of more accurate derivations based on the same approach are given by Becher [31] in terms of

$$K^c_{Ic} = [E^c(G^m + \Delta G^{cb})]^{1/2} = (E^c G^c)^{1/2} \qquad (7)$$

$$K^m_{Ic} = (E^m G^m)^{1/2} \qquad (8)$$

where K^m_{Ic} is the fracture toughness of the matrix, K^c_{Ic} is the overall toughness of the composite, G_{cb} and G_m define energy change associated with the bridging process and with crack extension in the matrix, respectively.

Accordingly, the toughening increments resulting from crack bridging are initially evaluated in terms of ΔG (additional dissipated energy), which then being inserted in Eq. (8) yields the fracture toughness of composite. Becher considers two models of debonded interface: Mode II debonding (no interfacial friction) and frictional interface. The former gives toughening increment as

$$\Delta J^{db}=\frac{A^{el}(\sigma_f^l)^2}{2E^l}l_{db} \tag{9}$$

where A^{el} -the areal fraction of ligaments intercepting the crack plane (can be approximated by the volume fraction for aligned ligaments of high aspect ratio), $l_{db}=r(\gamma^l/\gamma^i)/6$ is the debonded length of the matrix-ligament interface. The latter, frictional model of bridging, yields the toughening increment as

$$\Delta J^{fb}=\frac{A^{fb}r(\sigma_f^l)^3}{6E^l\tau_i}=\frac{A^{fb}(\sigma_f^l)^2 l_{db}}{3E^l} \tag{10}$$

where A^{fb} -the areal fraction of ligaments intercepting the crack plane (can be approximated by volume fraction for aligned ligaments of high aspect ratio), $l_{db}=r\sigma^f/2\tau_i$ is the debonded length of the matrix-ligament interface, and $\tau_i=\mu\sigma^r$ is the interface frictional shear resistance.

Consequently the fracture toughness values for the debonding without friction and for frictional interface are given by, respectively:

$$K^c=\left[E^cJ^m+(\sigma_f^l)^2\frac{rV^{el}E^c\gamma^i}{12E^l\gamma^i}\right]^{1/2} \tag{11}$$

$$K^c=\left[E^cJ^m+(\sigma_f^l)^2\frac{rV^{fb}E^c}{6E^l}\frac{\sigma_f^l}{\tau_i}\right]^{1/2} \tag{12}$$

Based on the model of frictional interface, the pullout contribution is

$$\Delta J^{po}=A^{po}\tau_i\left(\frac{l_{po}}{r}\right)l_{po}=A^{po}\tau_i\, r\left(\frac{l_{po}}{r}\right)^2 \tag{13}$$

where A_{po} is the areal fraction of pullouts, and $l_{po}\sim r\sigma^f/2\tau_i$ is pullout length.

From Eqs. (9)-(13) follows that toughening effect of the discontinuous reinforcements is greater when: 1) the matrix and reinforcing phase have comparable elastic moduli; 2) the reinforcing phase has very high fracture strength; 3) the reinforcement content increases, and 4) reinforcement diameter (crossectional dimension) is large. These predictions are in excellent agreement with experimental fracture toughness results obtained

for a number of whisker-reinforced and self-reinforced ceramics [29, 31]. For instance, the measurements of fracture toughness of self-reinforced silicon nitrides have shown [31] that the toughening contribution from crack bridging increases with increase in volume content of elongated grains and is proportional to the square root of the diameter (crossectional dimension) of the elongated grains (Figure 4).

2.1.5 Crack Deflection Toughening

Crack deflection elevates toughness by increasing the area of the fracture surface [30] as illustrated in Figure 5. According to the more exact definition of Faber and Evans [34], deflection toughening arises whenever interaction between the crack front and the microstructure produces a non-planar crack, subject to a stress intensity lower than that experienced by the corresponding planar crack. The non-planar crack arises either from residual strains present in the material or from the existence of weak interfaces [34, 29, 31]. The former originates from elastic modulus and/or thermal expansion mismatch between the matrix and the second phase [41].

Faber and Evans [34] used fracture mechanics approach to predict fracture toughness increase due to crack deflection around second phase particles. Their analysis was based on a determination of the initial tilt and the maximum twist of the crack front between particles (Figure 10), which provided the basis for evaluation of the deflection-induced reduction of crack driving force. The model yielded the decrease of local stress intensity factor, ΔK, at the tip of a tilted and/or twisted crack as a function of deflection angle. The corresponding crack driving force, ΔG, was subsequently averaged in respect to deflection angle, which frequency distribution was related to morphology and volume fraction of a second phase. The toughness predictions were invariant with particle size. The

volume fraction of a second phase, the particle morphology and aspect ratio, and the distribution of interparticle spacing were found to determine the increase in toughness.

Three different morphologies of the second phase were considered by Faber and Evans, namely: spherical, disk-shaped and rod-shaped particles with different aspect ratios. The most effective morphology for deflecting propagating cracks was predicted to be the rod of high aspect ratio, which can account for four-fold increase in fracture toughness. Disk-shaped particles were shown to be less effective than rods of the same aspect ratio and the least effective in toughening were spheres. The toughening effect, regardless of morphology, was determined primarily by twist of the crack front between particles, rather than its initial tilt (see Figure 10).

Another important prediction of this model includes the appearance of asymptotic toughening limit for all three morphologies at volume fractions in excess of 0.2 (20 vol%). It is also noted that greater toughening by spherical particles is afforded when spheres are nearly contacting each other such that twist angles approach $\pi/2$. Finally, as demonstrated by Faber and Evans, the fracture surface area increase due to crack deflection process provides only a lower bound estimate of the corresponding toughening increment. The predicted magnitude of crack driving force diminution substantially exceeds the surface area lower bound. It was suggested that the excess energy may be dissipated by phonon release.

The trends predicted by this model were corroborated by the experimental study [42] on silicon nitrides comprised of rod-shaped grains of various aspect ratios (self-reinforced silicon nitrides), barium silicate glass ceramic containing spherulites, and lithium-alumino-silicate glass ceramics containing $Li_2Si_2O_5$ lath-shaped crystals, size of which was varied by heat treatment.

Presented above, are the mechanisms underlying the major toughening approaches employed to fabricate high-performance ceramics. The following section provides an understanding of how these approaches can be realized via in situ processing techniques.

2.2 Fabrication of In Situ Reinforced CMCs and Self-Reinforced Ceramics

In situ processing of CMCs is becoming an increasingly important concept in composite synthesis. A generic term "reactive processing" (of reinforcements, composite-like microstructures, CMCs) is sometimes used interchangeably with "in situ processing" to denote the same technique or approach. Processes of this kind have several key advantages:

(i) The reinforcing phases are produced in situ, which is a low cost processing route (no expensive or hazardous reinforcements to handle).

(ii) In situ processes are proved to yield unique materials with multifunctional combination of properties [43] and unique microstructures [12, 13, 8, 5, 44, 1] unattainable by other means.

(iii) The resultant mechanical properties are often superior to those of similar composites processed by conventional techniques. The origin of these superior properties lies in favorable phase interfaces and synergistic microstructural arrangements uniquely developed through in situ reactions. Desirable composite microstructures as given in [13] include: 1) dispersed-particulate phases, 2) whisker-and platelet-like reinforcing phases or elongated grains, and 3) three-dimensional interpenetrating phases.

(iv) Issues of microstructural control and cleanliness can be addressed using in situ approaches in ways that cannot be achieved with conventional techniques. For instance, in situ approaches often permit to obtain very fine microstructures starting from relatively coarse powders [15, 16, 12, 45]. This is of significant technological importance, since fine powders required to produce strong fine-grained ceramics via conventional routes are associated not only with higher cost but frequently with higher levels of impurities (gases adsorbed on the surface, contamination by grinding media etc.). Such impurities, as will be shown below using the example of the TiC-TiB_2 system, may have a detrimental effect on final properties of ceramics, especially high-temperature performance.

A detailed description of the most important in situ approaches for processing of CMCs is given in the following sections to characterize the current state of development of in situ techniques. Their specific advantages and disadvantages are discussed below in terms of their applicability to various material systems and their ability to attain fully dense composite, to control the final grain size, to tailor properties of a final product to specific applications, and to avoid sacrifice of final properties for processability such as addition of large amounts of sintering aids.

2.2.1 Colloidal Methods

Colloidal (sol-gel) approaches permit precise control over the chemical architecture and the scale of mixing of the sol-gel derived reactants [43]. This advantage is realized by the following means: 1) by controlling the rheology of powder slips through manipulation of the interparticle forces so that higher packing densities can be achieved, resulting in higher densities after sintering; and 2) by closely packing particles of two different compounds such that, on average, their nearest neighbors are of the opposite type [43]. For

instance, a novel method of making composites with any desired architecture, suggested by Iler [46], utilizes layer-by-layer deposition of positively and negatively charged colloidal particles. Iler's method may be conceptualized as colloidal lithography [43].

Control over the chemical architecture and the scale of mixing of the reactants is believed to be critical for a variety of reactive processing techniques [43, 13, 47]. For example, mullite ($3Al_2O_3 \cdot 2SiO_2$) and mullite-matrix composites can be prepared at lower sintering temperature by using precursor materials which react to form mullite matrix after densification has occured [48, 47]. If the Al- and Si-bearing species are mixed on the molecular level, then mullitization occurs at lower temperatures (~1000°C) and subsequent densification at low temperatures is very limited. In contrast, if the level of mixing is too coarse (i.e. micrometer scale), then high temperatures (≥1650°C) are required to accomplish both mullitization and densification. According to Sacks et al. [47] the lowest sintering temperatures are achieved when the scale of mixing is in the range of 5-50 nm, which can only be obtained by sol-gel process.

Although sintering temperatures are lowered by using sol-gel approaches, there are several difficulties associated with the method when processing bulk shapes. The large shrinkages and weight losses that occur during processing of gel monoliths can make it difficult to achieve the required dimensional tolerances on fabricated parts [10]. In addition, the advantage of sol-gel methods for lowering sintering temperatures is substantially diminished when mullite matrices containing second-phase reinforcements are processed. It has been shown [10] that compacts containing second phase inclusions have substantially lower densification rates compared with compacts prepared with matrix phase alone. In fact, in samples prepared with crystalline matrix materials, bulk densification may be completely arrested once the inclusion concentration exceeds a critical volume fraction [10].

2.2.2 Transient Viscous Sintering

Transient Viscous Sintering (TVS) of composite powders has been introduced recently by Sacks and co-workers [11, 10]. Figure 11 illustrates the TVS approach for the formation of mullite and mullite matrix composites. As schematically shown, powder compacts comprised of amorphous silica-coated particles are viscously sintered to near full density at relatively low temperatures (~1300°C). The primary densification mechanism operating at this stage is viscous flow of the amorphous silica coating. Subsequently, the temperature is increased (≥1500°C) so that the alumina cores react with the silica coating to form mullite matrix. To date TVS was used to fabricate mullite; mullite/zirconia/alumina, mullite/silicon carbide particulate, and mullite/silicon carbide whisker reinforced composites. TVS process is dependent upon the availability of composite particles in which a crystalline core is coated with amorphous silica. As has been described in [11], amorphous silica coatings of varying thicknesses can be precipitated on crystalline particles, such as Al_2O_3, ZrO_2, and SiC, by treating the suspension of corresponding powders with TEOS (tetraethyl orthosilicate) solution.

The advantages of TVS approach are given as [10]:

(i) Large weight losses and shrinkage during drying and sintering normally associated with sol-gel routes are avoided because of the use of 1) considerably larger particles, and 2) α-alumina instead of alumina precursors (e.g. aluminum hydroxide).

(ii) Densification by viscous sintering is completed at ~1300°C before the onset of mullitization at 1400°-1500°C. This is expected to be particularly beneficial for processing of mullite-matrix composites, since it has been shown [48] that once mullitization occurs, densification of samples containing second-phase reinforcements is arrested.

(iii) Fully densified compacts can be net shaped by some hot forming technique via viscous deformation at relatively low temperatures (1250°-1300°C) prior to reaction synthesis (mullitization).

(iv) Incorporation of reinforcing phases via TVS technique was shown not to impede densification. In fact, both densification and mullitization for mullite matrix composites were accomplished at temperatures similar to those for mullite matrix alone.

(v) The TVS process can be easily optimized. For example, it is expected that viscous sintering and mullitization temperatures can be varied by altering the size of the core particles and/or thickness of the amorphous coating.

Currently, the TVS process is limited to reactive sintering of mullite or mullite matrix composites. It remains to be established whether the TVS approach is specific to this system or extendible to other combination of materials.

2.2.3 Reactive Infiltration Methods

Reactive infiltration methods are suitable for production of advanced metal matrix composites (MMCs), intermetallic matrix composites (IMCs), CMCs, interpenetrating phase composites (IPCs) and reaction bonded SiC. These processes involve a thermodynamically driven reaction between a molten metal and ceramic preform to produce a new matrix and reinforcing phase. These reactions are often fast, and afford near net-shape capability.

A number of related techniques exploiting this concept has been introduced to date. For instance, Loehman and Ewsuk [49] at Sandia National Labs have developed a process for reactive infiltration of mullite with molten aluminum that results in composite comprised

of mutually interconnected Al-Si metal and Al_2O_3 ceramic phases. In the other version of this approach [50] porous Ni and Fe preforms containing large volume fractions of TiB_2 and $MoSi_2$ particles were fabricated via SHS from corresponding elemental powder blends. These preforms were subsequently infiltrated with a liquid Al alloy to form Ni or Fe aluminides. As a result, dense intermetallic matrix composites reinforced with fine TiB_2 and $MoSi_2$ particles were produced. The initial preform porosity was found to be a critical parameter, by varying which the different multiphase structures were obtained. Noteworthy, no significant coarsening of the fine in situ formed TiB_2 and $MoSi_2$ particles occured during the infiltration process was observed.

In a similar process [51], molten silicon is reacted with carbonaceous preform to yield SiC ceramics with some retained Si. In addition to relatively low processing temperatures, which are close to melting point of silicon (1410°C) this process is also extremely fast [52] due to rapid reaction kinetics that results from good wetting of carbon by liquid silicon and low Si-melt viscosities and is aided by a large exothermic heat of the reaction. Increased strength and improved fracture toughness have been achieved for SiC processed by this technique [52]. Its current disadvantage is the presence of un-reacted silicon, which inclusions act as failure initiation sites and lower application temperatures.

Another method of infiltrating a preform is chemical vapor infiltration (CVI), a process similar to CVD. This approach has been pioneered by the French company Societe Europeenne de Propulsion (SEP) as a method of making high-performance ceramic composite materials. Figure 12 shows a schematic of a process used by SEP to fabricate a number of critical components, such as SiC/SiC jet engine nozzle petals; SiC/SiC leading edges for re-entry; C/SiC for nose caps, rocket nozzles and protection shingles; and C/SiC integrally bladed turbine rotors [53].

One of the outstanding advantages of the CVI process is that it is possible to deposit a thin coating or multiple coatings on the preform prior to subsequent deposition of the matrix phase [43]. Both oxide and non-oxide coatings and matrices can be deposited. This permits creation of "tailored" interfaces with specific combination of properties, e.g. improved wetting behavior for processability, weak interfaces for toughening, or inert interfaces for high-temperature oxidation resistance [43]. Another important advantage is the use of a single, continuous deposition step to form complex shapes by manipulation of die design [54]. Although extensively used for fabrication of continuous fiber reinforced CMCs [54, 53], the technique is believed to be equally suited for the formation of particulate and interpenetrating phase composites [43].

Currently, this technique is a subject of considerable development efforts in a number of major materials laboratories [55, 56]. One of their objectives is elimination of the residual porosity inherent for the original CVI process because the reaction products tend to deposit more readily in the outer parts of the structure. Bessman and co-workers at Oak Ridge National Laboratory have successfully overcome this problem in a new technique, the "forced CVI" [56]. Figure 13 shows schematic of the forced flow-thermal gradient CVI process. This process is shown to form thicker sections with shorter densification times. Fabric preforms of Nicalon SiC, Al_2O_3 and Tyranno SiC have been densified with SiC on a laboratory scale [56].

The other recently developed process, closely related to CVI, is reactive vapor infiltration (RVI). In the RVI technique [57], successfully used to process monolithic and fiber reinforced $MoSi_2$, reinforcing fibers are embedded into molybdenum-based metal powders and compacted to hold shape. The compacts are then exposed to a vapor silicon source that converts the powder phase into $MoSi_2$ starting at the surface and proceeding inwards. In the processing temperature range of 1100°-1400°C the $MoSi_2$ phase growth

exhibited parabolic rate dependence that was attributed to a diffusion control of the reaction [57].

2.2.4 Directed Metal Oxidation

In another important variant of the infiltration method - the DIMOX™ (directed metal oxidation) process introduced by Lanxide Corporation - a liquid metal with appropriate dopants is reacted with a gaseous oxidant (e.g. oxygen or nitrogen) to form a continuous interconnected three-dimensional network of ceramic phase, with a minor amount of residual metal (~5-15 vol%). The metal content can be varied to tailor the mechanical, physical, and thermal properties of the product. Further, the ceramic body can also be grown through a filler bed composed of particulates, platelets or fibers. As an extension of this process, the oxidant may be a solid reactant, such as B_4C. A number of related processes, suited to fabrication of different materials, has been developed [52, 58, 59, 6]. These processes are somewhat similar to the approach of Halverson, Pyzik and Aksay for processing of B_4C cermets [60, 61].

In a variation of the DIMOX™ process illustrated in Figure 14, the Zr metal is placed on top of a bedding of B_4C particles. Upon subsequent heating to 1850-2000°C (above the melting point of Zr) in the atmosphere of argon, the molten Zr infiltrates into the bed of B_4C, reacting to form ZrB_2 platelets in a matrix of $ZrC_{0.6}$ according to reaction

$$(2.2+x)\ Zr + 0.6\ B_4C = 1.2\ ZrB_2 + \ ZrC_{0.6} + x\ Zr$$

The reaction is very fast with samples as thick as 10 cm being prepared in 2 hours. The reaction kinetics is parabolic with rate constant of $(2\text{-}4)\times10^{-2}$ cm^2/s [7]. The following mechanism of the reaction has been established [7]: initial exothermic reaction of molten Zr with B_4C leads to formation of boron-rich liquid, which is drawn into B_4C bed by capillary

forces. As additional boron and carbon are dissolved in the liquid, ZrB_2 and ZrC_x products precipitate out. Their grains grow by Ostwald ripening during the high-temperature processing so the microstructure becomes relatively uniform and homogeneous throughout the sample. Two alternative rate-limiting steps have been suggested: Zr diffusion through carbide/boride two-phase layer or capillary flow of molten Zr through a porous reaction layer.

Processing-structure-properties relations for this technique are well described in [5,6]. The resulting composites consist of equiaxed $ZrC_{0.6}$ grains, ZrB_2 platelets approximately 5-10 μm thick and 20-30 μm in lateral dimensions and residual Zr. The metal content can be varied from ~0.5 vol% to more than 30 vol% by altering the Zr/B_4C ratio. The residual Zr metal appears primarily at triple points in low metal composites, and as an interconnected phase in higher metal ones. It should be noted, that though bulk melting does not occur until above 2800°C [44], upon heating the first molten phase, a Zr-rich liquid, forms in these composites between 1615° and 1852°C [7]. The latter seriously limits application of Lanxide composites as refractory materials.

Property data for in situ platelet-reinforced $ZrC_{0.6}/ZrB_2/Zr$ composites (NX-3400™ series) is quite impressive, justifying the relatively high raw material and processing cost. For a composite containing 6 vol% Zr, the properties cited [44] include a flexural strength of 850 MPa, with very little scatter (a Weibull Modulus of 27), fracture toughness of 12 $MPa\sqrt{m}$, which can be increased to 23 $MPa\sqrt{m}$ at 30 vol% metal, Young's modulus of 390 GPa, hardness of 82 R_A and density of 6.2 g/cc. Strength retention at high temperature is reasonable, with a strength of 300 MPa at 1000°C cited [44]. These composites exhibit excellent thermal shock resistance ($\Delta T_c \approx 600$°C for 6 vol% Zr composite) demonstrated in a variety of field tests [44], including solid rocket motor, liquid rocket engine, and flame erosion tests. Recently, $ZrC/ZrB_2/Zr$ composite coatings on graphite substrates have been

fabricated by Lanxide technique [44], thereby combining the low density of the substrate with erosion, corrosion and thermal shock resistance of the platelet reinforced ceramics.

Similar processes have been reported in Ti/B_4C and Hf/B_4C systems [58, 27]. For instance, Lee et al. [27] studied the formation of fully dense TiB_2/TiC composites by the directional reaction of molten Ti with B_4C preform at 1600-1700°C under atmosphere of Ar. Reportedly, the reaction between pure molten Ti and B_4C preform could not progress due to reaction choking. However, when a few weight percent of Ni were added to Ti, the reaction progressed continuously and resulted in dense equiaxed-grained TiB_2/TiC composite with residual Ti-Ni metal phase. The reaction rate increased with increase of nickel content in molten Ti, which was attributed to the enhanced wetting behavior and the lowered viscosity of the Ti-Ni alloy compared to pure Ti. In contrast to DIMOX™ process, a gradient of grain sizes was observed in the reaction product. According to Lee et al., the processing temperature affected the microstructure of the reaction products rather than the reaction rate. Both the average grain size and the extent of grain size gradient in the product were found to increase with increase of the processing temperature.

The advantages of the DIMOX™ process , as presented by Jonson et al. [6], are near net shape capability, simple lay-up and processing, fast reaction times, easy control of microstructure. Process limitations are the required high temperature and vacuum or controlled atmosphere, use of relatively expensive mold materials necessary to hold liquid reactive metal at high temperatures. The resulting materials are primarily intended for use as rocket engine components (plates, nozzles, ducts), wear parts (shaft seals, valve components, nozzles) and biomaterials (joint replacements, prosthetic devices). Once again, the generic mark of the DIMOX™ process as well as most of the other infiltration techniques is practically unavoidable presence of the metal phase in the product, which may be detrimental for certain applications and beneficial for the others.

2.2.5 Self-Reinforced Ceramics

In the past decade innovative approaches have emerged to obtain the benefits of composite-type microstructures even in a monolithic ceramics. Considered in this section are the formation of whiskers in situ in sintered or reaction bonded Si_3N_4 (RBSN), and the fabrication of self-reinforced Si_3N_4, SiALON and SiC ceramics with in situ grown elongated or whisker-like grains. Both of these approaches have been employed successfully to produce monolithic ceramics with fracture toughness and strength superior to those of composites fabricated from physical mixtures of components.

Several research groups [62-64] have reported fabrication of in situ Si_3N_4-matrix composites reinforced with SiC whiskers. SiC whiskers form by the reaction of in situ generated CO gas with Si_3N_4 powder [40]. In the references cited, the carbon source is C powder which is mixed with Si_3N_4 and SiO_2 to form the starting material. The powder mixtures are subsequently hot-pressed to obtain dense composites. Whisker contents as high as 25 wt% have been realized by heat treatment for two hours at 1700°C [63]. Song and Liu [64] reported a flexural strength of 649 MPa and fracture toughness of 8.0 $MPa\sqrt{m}$ for a hot-pressed composite containing 15 vol% SiC whiskers, both impressively high and indicative of the considerable potential of this family of materials.

Another possible but as yet unexploited approach to the fabrication of Si_3N_4 composites is illustrated in Figure 15 (a). α-Si_3N_4 whiskers, such as the ones shown in the figure, are often observed in the nitridation of Si powder compacts to form reaction bonded Si_3N_4 (RBSN) [40]. The droplets at the tips of the whiskers suggest that they formed via the VLS (Vapor-Liquid-Solid) mechanism [40]. The VLS mechanism as applied to Si_3N_4

whisker growth is illustrated in Figure 15 (b). It was found [40], that the liquid droplet at the tip of the whisker contains low melting point iron silicide (Fe being a common contaminant in commercial Si powder), and the likely source of Si in the vapor phase is SiO gas. As illustrated in Figure 15 (b), the gaseous reactants dissolve in the liquid to precipitate Si_3N_4 at the solid-liquid interface, thus providing a means of growing the extremely elongated crystals in Figure 15(a) and, potentially, an in situ composite type of microstructure. The possibility of forming duplex Si_3N_4 microstructures (Si_3N_4 matrix-Si3N4 whiskers) was initially demonstrated by Messier and Wong in 1972 [65]. However, to date no evidence exists to show that such microstructures provide significant toughening, and whether or not these duplex structures can be exploited to fabricate tough composites is an open question.

Perhaps the most potent approach to the formation of composite-like Si_3N_4 ceramics is taking advantage of the propensity of Si_3N_4 to form high aspect ratio grains under certain conditions. The growth of high aspect ratio grains of β-Si_3N_4 from the liquid phase was reported in the early studies of the $\alpha \rightarrow \beta$ Si_3N_4 phase transformation [66]. The aspect ratio of such crystals depends upon the chemistry of the liquid from which they are grown [40]. Full advantage of this behavior has been taken by a number of processing techniques, e.g. [4, 67, 68, 1, 69]. In general, these approaches exploit the development of elongated (rod-like) β-Si_3N_4 grains through dissolution-reprecipitation mechanism during liquid phase sintering of α/β Si_3N_4 powder mixtures in the presence of certain sintering aids. The resulting material is comprised of β-Si_3N_4 having significant amount of rod-like grains in the microstructure. Seeding of the starting powder mixture with β-Si_3N_4 (2-25 wt%) is the effective way to control the final microstructure. As it was shown [70], the initial volume ratio of the α and β phases effects the resulting average aspect ratio of β-Si_3N_4, specifically large initial fraction of β-Si_3N_4 result in equiaxed grain morphologies, while large initial concentration of α-Si_3N_4 lead to highly anisotropic microstructures.

Indicative of the magnitude of the current research efforts in this area are 4 patents that were issued for processing of self-reinforced silicon nitride (U.S. Patents ## 5091347, 5098449, 5118645, 5120328) just during the year of 1992 alone. These patents authored by Pyzik and co-workers were assigned to Dow Chemical Co. In fact, Pyzik et al. announced the fabrication of self-reinforced Si_3N_4 with impressive properties [2-4] in 1990. Their pressure sintered composite-like Si_3N_4 exhibited flexural strength of 1200 MPa and fracture toughness of 10 MPa$\sqrt{m}$ (as compared to ~5 MPa$\sqrt{m}$ for state-of-the-art material without self-reinforcements [1]). In 1989 Allied Signal introduced a similar material (AS-700) prepared by gas pressure sintering [1]. Li and Yamanis [1] found pronounced R-curve behavior in the AS-700 silicon nitride, characterized by flexural strength of 550 MPa, fracture toughness of 10.6 MPa$\sqrt{m}$, and Weibull modulus of 18-27. Another similar material has been fabricated commercially by NGK Co., Japan [71]. The ultimate use of self-reinforced Si_3N_4 technology was demonstrated by NHK Spring Co, Japan, a manufacturer of silicon nitride coil and flat springs [72]. The advantages of Si_3N_4 springs are illustrated in Figure 16.

Analogous approaches were employed to produce self-reinforced SiALON [69] and SiC [73] ceramics. For example, "in situ toughened" SiC was fabricated recently [73] by hot-pressing. Again, the phase transformation, β (3C polytype) $\rightarrow$ α (4H polytype), induced by Al-B-C additive was believed to be instrumental in growth of platelike SiC grains. The use of Al-B-C sintering aid resulted in the presence of amorphous grain boundary phase. As reported [73], in situ toughened SiC exhibited a significant rising R-curve behavior with a steady state fracture toughness of 9.1 MPa$\sqrt{m}$, while retaining a flexural strength of 660 MPa.

As shown for self-reinforced Si_3N_4, these techniques permit significant flexibility and at the same time tight control of final microstructures. Grain size, aspect ratio, fraction of elongated grains and their orientation, and hence strength and toughness of the resulting composite-like ceramics can be optimized and tailored to specific applications. However, the presence of the grain boundary glassy (or amorphous) phase in these materials, inherent for the liquid-phase sintering process, deteriorates their strength and creep properties at high temperatures, e.g. above 1000°C for Si_3N_4 (see Figure 16), thus limiting their utility as high-temperature structural ceramics. This limitation can be alleviated in certain cases by use of more refractory additives, or, similarly to glass-ceramics approaches, by addition of dopants promoting crystallization of the grain-boundary glassy phase [67].

2.2.6 SHS Methods

In self-propagating high-temperature synthesis (SHS or SPS or combustion synthesis) highly exothermic reactions after being initiated locally become self-sustaining and the combustion wave formed upon ignition propagates through the reactant mixture. The advantages of the SHS process are elimination of external energy input and inexpensive facilities, along with its simplicity, flexibility, very short reaction times, products with fewer contaminants and as a result its cost effectiveness.

The SHS products, however, cannot be used directly as structural materials because they are generally quite porous (the porosity can be as high as 50 vol.%). The origin of a significant residual porosity is outgassing and volatilization of contaminants upon SHS reaction combined with high negative volume changes characteristic for SHS synthesis of refractory compounds [74]. For example, attempts to fabricate TiC-TiB_2 composites via SHS from elemental powders and Ti-B_4C yielded extremely porous sponge-like bodies

[75, 76]. One of the possible solutions was offered by Udwadia et al. [76], who used TiC-TiB_2 combustion product to produce composite powder which was consequently densified by hot-pressing and pressureless sintering. Two-phase composite powder produced via SHS exhibited significantly better densification behavior than the mixtures of conventionally produced TiC and TiB_2 powders of the same particle size densified under the same conditions [76]. The other way to overcome this inherent limitation of SHS is combining the SHS reaction with a densification step. Forced consolidation approach has been materialized as SHS/hot-pressing [77, 78], high-pressure combustion synthesis (SHS/HIP), and SHS/DC (dynamic compaction) and hot rolling-SHS [79].

The review of ceramic processing approaches using combustion synthesis under gas pressure (SHS/HIP) was presented by Miyamoto [80]. This method was successfully applied to produce 96% dense TiB_2-TiC composites with 0-30 wt.% of TiC [26]. The attendant density, Vickers microhardness and fracture toughness of the composites exceeded those of the TiB_2 compact.

In SHS/DC method initially developed at the US Army Ballistic Research Laboratory (BRL) the SHS-reacted , still hot body is consolidated to high density by the action of the pressure wave from the detonation of a high explosive [81, 82]. The experimental set up is described in the open literature by Wang et al. [82]. This method has been successfully tested for fabrication of refractory carbides and borides, such as HfC, TiC and TiB_2. For example, microhardness, elastic modulus and compressive strength of SHS/DC produced TiC (96.8%) and TiB_2 (99%) were found to be comparable to those for similar hot-pressed materials [82].

In the other version of SHS/DC a high-velocity forging machine has been utilized to densify hot SHS product while it is still in an easily deformable state [83, 84]. The highly

porous body is densified by a combination of fracture (communition), plastic deformation, and sintering. The principal advantages of the high-velocity forging step are that it is relatively safe, affords near-net shape capability, and lends itself to high-rate production runs with little or no down time between runs. This method has been applied to a number of material systems including TiC, TiB_2, Al_2O_3-TiB_2, TiB_2-SiC, TiC-Ni-Mo. A phenomenological constitutive model incorporating the Arrhenius type temperature dependence of the flow stress (E_A=366 kJ/mole) was developed by Hoke et al. [85] for consolidation of hot and porous SHS products. This model accurately describes the consolidation behavior of TiB_2-based materials subjected to compression at strain rate of ~0.1 sec^{-1} following their SHS synthesis.

2.2.7 Reactive Hot-Processing

Solid-state reactions can be carried out simultaneously with hot-pressing to produce fully dense ceramic-ceramic composites. The related methods have been introduced by Henager and co-workers [12, 14, 13], Cameron et al. [45], Telle and Petzow [86, 87] and Barsoum et al.[8, 9]. Other researchers [89, 90, 88, 91] have used a similar approach, termed reaction sintering, but with limited success in producing high quality structural ceramics. Among the important composite systems produced by reactive hot-pressing techniques are B_4C-TiB_2-SiC [86, 87]; alumina-matrix composites [45]; mullite-ZrO_2 [92, 93]; TiB_2-$TiC_{0.5}N_{0.5}$ [94]; TiC-TiB2 and TiC-TiB_2-Ti_3B_4 [8], ZrC-ZrB_2 [15]; Ti_3SiC_2-SiC-TiC [14, 95]; $TiSi_2$-SiC [14], $MoSi_2$-SiC [12], and (Ni-Al) intermetallics-Al_2O_3 interpenetrating-phase composites [13].

Control of the morphology of the product phases is a critical aspect of these methods, yet the least understood [13, 96]. Achievement of synergistic microstructural

arrangements, which can overperform conventionally produced composites is a challenging task. For instance, Cameron et al. [45] compared reaction vs conventionally hot-pressed α-alumina-matrix composites with TiB_2, TiC, B_4C and SiC particulate reinforcements. Analyzed parameters were density, hardness, flexural strength, elastic modulus and electrical resistivity. The same compositions and similar microstructures were fabricated under the same processing conditions by hot-pressing of the physical mixtures of the final constituents and by reactive hot-pressing starting from low-cost reactants such as powders of TiO_2, SiO_2, B_2O_3, Al, and C. As reported, reactive hot-pressing consistently produced finer grain sizes for the reinforcing phases and often higher values of strength for resulting composites. Cameron et al. concluded that the advantages realized with reaction hot-pressing are likely to be related to specific reactions and specific precursors rather than generic differences between two processing techniques employed.

A number of studies addressed the other crucial aspect of reactive hot-pressing, namely interaction between reaction and densification. As shown by Rupo et al. [92,93] and Bowen et al. [97] this problem can be treated relatively easily for phase transformations through solution-diffusion-reprecipitation mechanism or reactions between compounds, in which reaction is not competing with densification i.e. no significant internal porosity (associated with negative volume changes upon reaction [74]) is generated. Using the example of reaction hot-pressing and sintering of zircon-alumina mixtures, Rupo et al. demonstrated how deconvolution of diffusive (e.g. particle reshaping) and non-diffusive contributions (e.g. particle rearrangement or plastic deformation) to densification can be accomplished. Their approach was based on the use of the reaction rate to identify the diffusive contribution, the remaining contributions then being determined by the difference from the observed total densification rate.

Rupo et al. identified three stages in reactive hot-pressing using the plot of the reaction rate vs densification rate. In the first stage, the densification was much more rapid than can be attained by diffusion alone and was attributed to particle rearrangement. The second stage was dominated by diffusional mechanisms. At this stage the relative densification rate closely followed the theoretical line, calculated on the assumption that the density changed only due to the diffusional transport of atoms participated in reaction. In the third stage, the relative rate of densification decreased while the reaction continued in the completely densified regions of the sample, such as grain cores. Maps of the dominant mechanisms during hot-pressing in temperature-density coordinates were established (see Figure 17). Particle rearrangement was found to be the dominant mechanism at relative densities up to 72%, above which grain boundary diffusion prevailed to approximately 90% density.

In regard to fabrication of microstructures important for composite strength and toughness, one of the most productive reactive hot-pressing techniques to date is displacement reaction synthesis developed by Henager and co-workers at Pacific Northwest Laboratory, Richland, WA. According to definition of Henager [14], displacement-reaction processing combines two phases that are not in equilibrium to achieve a composite of thermodynamically stable product phases via diffusional phase transformations (reactions). Using blended powder compacts and hot-pressing, displacement reactions that exhibit morphological instabilities generally lead to dispersed-phase microstructures because the interdiffusion and growth fronts occur randomly in three dimensions [12]. Whisker-like reinforcing phases can be produced by displacement reaction processing through controlling the dimentionality of interdiffusion during the reaction. Systems exhibiting stable layered growth can be used to produce interpenetrating-phase composites (IPCs) with improved mechanical properties [13]. As mentioned, this

technique has been successfully applied in Mo-Si-C [12], Ti-Si-C [14] and Ni-Al-O [13] systems.

Henager and co-workers have adopted an interesting phenomenological approach whereby reactant materials were combined by means of diffusion couples to screen a number of promising reactions efficiently. This approach was proved to be useful [13] for relaying simplified diffusion models in a sense of van Loo [96] and Rapp [98] to complex multicomponent systems. In addition, comparison of the product morphologies obtained in diffusion couple with the ones produced by hot-pressing of blended powder mixtures yielded some general understanding of how diffusion couple data could be extrapolated onto reactions between powders with the added dimension of applied pressure. For example, a diffusion couple processed at 1200°C for 16 hr produced SiC platelets in $MoSi_2$ matrix which were nominally 1 μm wide and 10 μm long and were aligned in the direction of diffusion. Whereas, hot-pressing (2 hr at 1350°C then 1 hr at 1700°C, 27.5 MPa) of relatively coarse (d<45 μm) MoC_2/Si powder mixture yielded fine-grained $MoSi_2$ (~1-2 μm) matrix with uniformly distributed equiaxed SiC reinforcements of ~ 1 μm in diameter.

Properties of fully dense $MoSi_2$-SiC in situ composite were shown to compare favorably with those of SiC whisker-reinforced $MoSi_2$. The 26% increase in toughness of the in situ composite compared to unreinforced $MoSi_2$ was attributed to crack deflection and crack wake bridging observed in the former. Simplicity and the demonstrated versatility of the method are among its clear advantages. Its disadvantage is unsatisfactory understanding of how to control size and morphology of in situ formed reinforcements within the same reaction system.

2.2.8 Transient Plastic Phase Processing

Another innovative form of reactive hot-pressing, introduced recently by Barsoum and co-workers [8, 9, 15], is Transient Plastic Phase Processing (TPPP), capable of producing fully dense, ultra-refractory composites at temperatures that are considerably lower than the melting temperatures of the constituents.

According to the initial concept of Barsoum et al. [8], TPPP starts with a mixture of powders of a transient plastic phase (TPP), defined as a compound with a wide range of stoichiometry and a yield point that is a strong function of that stoichiometry, and a reactant phase (RP). The RP will react with the TPP according to:

"soft" transient plastic matrix + reactant phase → hard matrix + reinforcement phase {1}

in such a way as to shift the stoichiometry of the TPP towards its harder and more refractory composition. The basic steps involved in TPPP are: (i) plastic forming at a relatively low temperature in a soft condition resulting in densification of the powder mixture with no change in the composition of the constituents, followed by (ii) reaction synthesis at a higher temperature in which the RP reacts with the TPP according to reaction {1}. These basic steps are schematically illustrated in Figure 18 using a compositional map of a hypothetical ternary system A-B-C. The starting constituents are AC_x and AB_2, which represent the TPP and the RP, respectively. In this case, the A-rich compositions of the AC_x are assumed to have lower yield strengths than the C-rich compositions along the binary AC composition axis of the ternary diagram. TiC_x is an excellent example of a TPP phase: its compressive yield strength at 1200 °C [99] drops from ≈ 430 MPa to less than 60 MPa as x decreases from 0.93 to 0.66. TiB_2, B_4C, SiC or Si_4Ti_5, among others, can be suitable RP for TiC_x.

The two phases in powder form are mixed and either hot pressed, extruded, or forged. The ductility of AC_x prior to the reaction (i.e. A-rich) ensures that the compact will achieve full density with the required net or near-net shape. Following this initial densification step, the temperature of the compact is raised to promote the type of reaction indicated in (1). With specific reference to Figure 18(a), the reaction can be expressed as

$$(1\text{-}x)\,AB_2 + AC_x \Rightarrow 2\,(1\text{-}x)\,AB + x\,AC \qquad \{2\}$$

where AB is a new, in-situ formed, reinforcing phase and AC is the refractory matrix phase in the resulting ceramic-ceramic composite. As the reaction in equation {2} proceeds, the stoichiometry of the TPP shifts towards the C-rich side of the binary line, AC, and the TPP becomes more refractory. In other words, the reaction depletes the TPP of the element A that renders it soft. At the end of TPPP, the material is a ceramic-ceramic composite.

Several conditions must be met for successful processing using TPPP. Reaction {1} must be slow enough to permit additional densification and removal of the porosity developed in the course of the reaction. This condition is met if the TPP is relatively soft at higher temperatures, and reaction rates are slow. Furthermore, to achieve full density, the volume changes during reaction must be small. Since the reactions of interest are usually exothermic, the overall volume change upon the reaction is expected to be negative [74], giving rise to internal porosity in the product. If the amount of the generated internal porosity is small, however, it can be eliminated by moderate pressures and/or a high temperature anneal. The shrinkage associated with reaction synthesis when the RP is in elemental form is characteristically high; thus RP phases in the form of compounds are preferred.

The ability to fabricate and shape refractory materials at temperatures well below the melting point of their constituents is of significant technological importance. The initial plastic forming step can be designed to result in a near net-shaped preform with closed

porosity at lower temperatures, which can lead to cost effective mass production of fully dense parts and components by subjecting such preforms to hot isostatic pressing *without* a can. In addition, TPPP has the potential to produce composites with superior properties when compared to other existing processing techniques because of the unique microstructures that are possible and the elimination of sintering aids which usually result in a loss in high-temperature properties (most notably the creep resistance).

In addition, a new, and as yet, unexplored class of ultra-high temperature material systems can be developed with new microstructures and compositions that could potentially exhibit superior mechanical, electrical, and magnetic properties. Other potential advantages of TPPP include: producing graded metal-ceramic composites, near net shape manufacturing, and avoiding health hazards associated with ceramic reinforcements such as whiskers.

The initial work of Barsoum and Houng [8] has demonstrated the feasibility and some of the advantages of TPPP in the Ti-B-C system. In that study, two starting compositions, 3:1 Ti/B_4C and 4:1 Ti/B_4C (molar ratios), were investigated. It was observed that only the latter composition produced a near fully dense composite, comprising 43% $TiC_{0.6}$, 32% TiB_2, and 25% Ti_3B_4. This was explained by the experimental observations that indicated the formation of intermediate compounds during the initial densification step in the 4:1 Ti/B_4C starting composition. These intermediate compounds were identified as $TiC_{0.5}$ and TiB_2 which served as the TPP and RP, respectively. It was noted that since an intermediate "soft" $TiC_{0.5}$ did not form in the 3:1 Ti/B_4C starting composition, the produced composite had significant residual porosity. Some of the interesting features reported by Barsoum and Houng included net shape capability and the development of Ti_3B_4 in platelet morphology.

2.3 Titanium Carbide-Titanium Boride Material System

The development of high-performance ceramics in the TiC-TiB_2 material system is discussed in the following sections. First, the current understanding of Ti-B-C phase equilibria will be reviewed. The latter is required for intelligent processing and understanding of high-temperature behavior of materials in this system. Subsequently, properties and processing of individual compounds, TiC, TiB_2, and lower borides, will be presented; and finally the current advances in development of TiC-TiB_2 composites will be examined.

2.3.1 Ti-B-C Phase Equilibria

2.3.1.1 Ti-B-C Ternary Phase Diagram

One of the most commonly accepted versions of the Ti-B-C ternary phase diagram was published by Rudy [100] in the late sixties. The isometric view and 1600°C isothermal crossection of the Rudy's diagram are shown in Figure 19 and Figure 20, respectively. Rudy listed TiB_2 and TiB as the only phases present along the Ti-B tie line. It is now well established, however, that Ti_3B_4 is also an equilibrium phase in this system [8, 75, 101-105]. Attempts to revise the ternary diagram were made by McCauley et al. [75] (1982) and Barsoum et al. [8] (1993). In the latter study it was reported that the end member of the TiB_2 - TiC_x - Ti_3B_4 compatibility triangle was $TiC_{0.6}$.

Since a significant amount of work in the Ti-B-C system has been focused on TiC-TiB_2 composites, the TiC_{1-x}-TiB_2 pseudobinary section of Ti-B-C phase diagram deserves particular attention. This is a pseudobinary system of the eutectic type with low intersolubilities of the components (see Figure 21). Rudy reported TiC-TiB_2 eutectic at 57=±2 mole% $TiC_{0.92}$ and 2620±15°C. Ordan'yan et al. [106] reported a eutectic at 43.6 mole% $TiC_{0.95}$ and 56.4 mole% TiB_2, T_{eut}=2520°±40°C. It was established [106] that, with deviation from the stoichiometric composition, the solubility of TiB_2 at the eutectic temperatures of 2520°, 2450° and 2390°C, respectively, for the $TiC_{0.95}$-TiB_2, $TiC_{0.8}$-TiB_2, and $TiC_{0.68}$-TiB_2 sections increases from 3-4 wt% (corresponding to ~6 at% of B) for $TiC_{0.95}$ to 7-8 wt% (~12 at% B) for $TiC_{0.68}$. The lattice constants of the carbide phases grow from 0.4328 nm (0% B) to 0.4332 nm (6 at% B) in $TiC_{0.95}$, and from 0.4320 nm (0% B) to 0.4323 nm (12 at% B) in $TiC_{0.68}$ (see Figure 22(b)).

2.3.1.2 Ti-B Binary Phase Diagram

One of the latest versions of Ti-B binary phase diagram [101] is shown in Figure 23. It accounts for Ti_3B_4 as an equilibrium phase in the Ti-B system and thus contains three intermediate phases: TiB and Ti_3B_4, both of which melt incongruently by peritectic decomposition at 2200° and 2180°C, respectively; and TiB_2, which melts congruently at about 3225°C. It was found that TiB and TiB_2 posses a discernible homogeneity range, whereas Ti_3B_4 is a line compound.

2.3.1.3 Ti-C Binary Phase Diagram

The Ti-C binary phase diagram is shown in Figure 24. The Ti-C system contains only one intermediate phase, TiC, which melts congruently at about 3077°C and has a very large homogeneity range from 32 at% ($TiC_{0.47}$) to 49 at% C ($TiC_{0.96}$) at 1875°C, at its widest section, and from 38 at% ($TiC_{\sim 0.6}$) to 49 at% C ($TiC_{0.96}$) at room temperature. The variation of lattice parameter of TiC_x with stoichiometry was reported by a number of authors [100, 106, 107, 99] and showed reasonable agreement, especially in the range of x=0.5-0.7. This data is summarized in Appendix II.

2.3.2 Properties and Processing of TiB_2

TiB_2 is representative of refractory ceramics with very high melting points (3225°C), high stiffness (500 GPa) and high hardness (~20-30 GPa). The other attractive properties include good wear resistance [108], excellent resistance to chemical attack and oxidation resistance, high metallic thermal and electrical conductivities [109] (see Table II). The fracture toughness of 5-7 MPa$\sqrt{m}$ is also encouraging. Noteworthy, the oxidation resistance of refractory diborides decreases in the order of HfB_2>ZrB_2>TiB_2>TaB_2>NbB_2, and for a given diboride it decreases as the boron concentration increases [110]. Young's modulus and thermal expansion behavior of TiB_2, being the lightest (4.52 g/cc) and the hardest (>20 GPa) in this homologous row, are very similar to ZrB_2 (6.10 g/cc and ~20 GPa) and HfB_2 (11.19 g/cc and <20 GPa) [110].

One of the important properties of TiB_2 is a strong anisotropy of its thermal expansion coefficients of about 40% up to 1000°C [109], which may be detrimental to coarse single-phase ceramics (spontaneous microcracking) and beneficial for generating

crack deflection in composite materials (residual stresses). The presence of inhomogeneous microstrain caused by thermal expansion mismatch between individual grains, even in fine-grained diboride, was experimentally verified by observing the broadening of the X-ray diffraction lines [21]. By the same reason, TiB_2 with grain size coarser than certain critical value tends to spontaneous microcracking resulting in loss of stiffness and strength [28, 111, 112]. The relationship between grain size and flexural strength [113] (Figure 25) reveals a characteristic particle size of ~5 μm, which is considered to correspond to the critical diameter for spontaneous microcracking. Based on microscopic observations, Ferber et al. [111] have suggested that the critical grain size may be larger than 7 μm. Microcracking phenomenon in anisotropic materials [112] also reveals itself in expansion-contraction hysteresis observed in dilatometric studies due to healing of microcracks on heating and their reopening on cooling. In their dilatometric tests in the range of 25°-1000°C, Ferber et al. [111] found no significant hysteresis for fine <7 μm and coarse >40 μm TiB_2 and concluded that maximum hysteresis should occur at intermediate grain sizes.

High temperature deformation of TiB_2 in vacuum was studied by Ramberg and Williams [114]. With the exception of high-purity fine-grained SiC, the yield stress of TiB_2 is greater than any other ceramics for which such data is available (Figure 26). Plastic deformation was detected only above 1700°C. The compressive yield stress data fit an Arrhenius function with an apparent activation energy of 0.8 eV (77 kJ/mole) (see Figure 27 (a)). Dislocation glide over the Peierls barrier was believed to be the deformation mechanism, the other competing mechanisms being ruled out based on the measured activation energy value. Ramberg and Williams proposed a modified creep equation for thermally activated plastic yielding with effective activation energy of 3.2 eV (308 kJ/mole). They concluded that five or more independent slip systems can operate in TiB_2 at high temperatures and stresses. The dependence of the yield stress on the grain size obeyed the Hall-Petch relation which was established at various temperatures in the range of 1750°-

2000°C (see Figure 27(b)). The extraordinary resistance of TiB_2 to plastic deformation at high temperatures can be further increased by precipitation hardening (e.g. by doping with C). As shown by Ramberg and Williams, a TiB_2 single crystal containing TiC precipitates (coherent, residing on prismatic planes of TiB_2) exhibited yield stress at 2000°C that was approximately four times the stress predicted by the Hall-Petch expression for a pure TiB_2 single crystal.

TiB_2 has been fabricated by a variety of techniques including pressureless sintering [115, 116]; hot-pressing [116] and HIP-ing [117]; SHS/HIP [118] and SHS/DC [81, 82, 84, 85]; physical and chemical vapor deposition techniques (coatings and thin films) [119]. However, the majority of data as well as the most fully characterized properties have been reported for hot-pressed samples. Representative values for flexural strength and hardness are 580 MPa and 18 GPa, respectively, as obtained by Mroz [116] for nearly fully dense fine-grained TiB_2 hot-pressed at 1900°C (21 MPa, 1hr in argon). Flexural strength of 700 MPa and hardness of 25 GPa are reported for TiB_2 commercially produced via glass encapsulated HIP by ABB Cerama [117]. Though reasonably high, these values are inferior compared to the ones obtained by Watanabe et al. [113]: 1000 MPa and 22 GPa, respectively, for TiB_2-5 wt% W_2B_5-1 wt% CoB material of 3 μm average grain size. In addition, the latter was hot-pressed at relatively "mild" conditions (1700°C, 20 MPa, 0.5 hr in vacuum) due to CoB-W_2B_5 sintering aid.

Without sintering aids, pressureless sintering of TiB_2 requires utilization of ultrafine powders and temperatures in excess of 2100°C [115, 116]. Because of their low melting points and the suitable wetting behavior, the borides of Fe, Ni and Co can be used as additives for liquid phase sintering of TiB_2 [25, 28]. The observed densification mechanism is dissolution and reprecipitation which generates an accelerated grain growth. Grain size refinement below the critical diameter for spontaneous microcracking is achieved

by the addition of transition metal borides [113] such as MB_2 (M=Ta,V,Nb,Cr,Mo,Mn) and W_2B_5 which form $(Ti,M)B_2$ solid solutions layers on the TiB_2 particles. An even more efficient retardation of the rapid grain growth is obtained by transition metal carbide additives such as TiC or WC which partially dissolve in the liquid phase when combined with Ni binder. It is important that metal phase disappears during reprecipitation: in the first stage of reprecipitation, a $(Ti,W)B_2$ solid solution forms, then ternary phases WCoB or W_2NiB_2 grow from the melt, and finally the residual liquid phase solidifies as Ni_3B or (Ti,W)C solid solution [120]. These composites are pressureless sinterable at temperatures of 1600°-1700°C, yielding grain sizes of 0.8-1.5 μm.

TiB_2 has been considered as prospective material for cathodes in Hall-Heroult cells [121-126]. Despite the relatively high contact angle of molten Al on TiB_2 (Θ=60° at 1200°C [119]) penetration by molten Al degrades mechanical properties of TiB_2 cathode. Microchemistry of intergranular phases was found to be a controlling parameter in this process [125]. Segregation of impurities such as Fe and Si at grain boundaries increase wettability of TiB_2 with liquid Al (interfacial energy ratio $\gamma_{sl}/\gamma_{ss} \rightarrow 0.5$ and $\Theta \rightarrow 0°$). Better understanding of degradation mechanisms and improved (cleaner) processing are required if boride cathodes are to be used in Hall-Heroult reduction cells.

TiB_2 is currently used as an armor material, crucibles for handling liquid metals, electrodes, parts for flow meters and pumps, slurry nozzles, and evaporation boats for coating capacitor films with Al at 1400°C-1500°C. Because of its chemical compatibility to B_4C, SiC, TiC and WC, TiB_2 may also be used as an additive for the improvement of these important ceramic materials. However, the use of TiB_2, even fully densified, particularly for structural or wear applications is limited by the variability of its mechanical properties, its sensitivity to subcritical crack growth and tendency to spontaneous

microcracking. TiB_2 is a subject of intensive efforts to improve its strength, Weibull modulus and toughness.

2.3.3 Properties and Processing of Lower Borides

Little is known about the individual properties of lower Ti borides, Ti_3B_4 and TiB, beyond basic crystal and thermochemical data [119, 127]. They both have orthorhombic crystal structure and the same theoretical density of 4.56 g/cc. Their melting points are close as well, 2190°C and 2200°C, respectively. Reportedly [119], TiB exhibits hardness of 22.7 GPa and resistivity of $40x10^{-8}$ Ωm. TiB and Ti_3B_4 are often cited as side products of SHS synthesis in Ti-B-C system [75, 102]. A few available processing studies are focused on fabrication of TiB-Ti-matrix composites. For example, Ranganath et al. [128] studied combustion assisted synthesis of Ti-TiB-TiC composite via the casting route. In this work TiB-TiC reinforcements were produced in situ and thermodynamics and kinetics of the underlying reactions as well as some properties of the resulting composites were characterized.

2.3.4 Properties and Processing of TiC

In recent years, titanium carbide has found a wide range of potential applications, including composite materials such as Al-TiC, SiC-TiC, Al_2O_3-TiC, and TiB_2-TiC, field emission sources, and single crystal substrates for heteroepitaxial growth of SiC thin films. TiC is a covalently-bonded ceramics that crystallizes in the rock salt structure and possesses a combination of attractive properties (Table II). The compound exhibits a wide range of

substoichiometry (i.e. TiC_x, $x \approx 0.6\text{-}0.98$), a high melting temperature (3100°C), and a relatively low ductile-to-brittle transition temperature (DBTT) of ~800-900°C. Below the DBTT, the material is hard and resistant to slip, cleaving on {100} planes. At the transition temperature range, the slip system undergoes a gradual change from {110}⟨110⟩, the slip system normally exhibited by rock salt structures, to {111} ⟨110⟩, the slip system characteristic for fcc structures. The brittle-ductile transition is usually attributed to this change in slip system [129-131].

Several investigations have been focused on deformation behavior of single crystal TiC [129-132]. The compound is often regarded as carbon-stabilized fcc titanium because of the fcc-type slip systems and the fact that the relatively small carbon atoms occupy octahedral interstitial sites in fcc titanium sublattice. Perhaps the most interesting of the recent findings was reported by Chien et al. [133], who had found a new deformation mode induced during high speed abrasive machining of TiC single crystals. The deformation mode involves a stress-induced martensitic phase transformation to a previously unreported isomorph of TiC. The new phase was designated 8H, to reflect the height of the unit cell (8 Ti-C atom planes), and the hexagonal symmetry (H). Though the observed martensitic transformation in TiC appears to be peculiar to dynamic deformation at high loading rates, however, under certain types of loading, it might be possible to produce similar transformations in the vicinity of crack tip or other stress concentrations. Because the transformation involves a volume contraction, it is unlikely to contribute to an enhancement of fracture toughness. The authors speculate, however, that if the β (8H) phase could be stabilized, there might be conditions where the reverse transformation ($\beta \rightarrow \alpha$) could be exploited to inhibit crack propagation and enhance fracture toughness.

The mechanical properties and high temperature deformation behavior (room temperature -1600°C) of polycrystalline TiC were studied by Das et al. [134]. Flexural

strength of 540 MPa for the as-hot-pressed samples was almost fully retained up to 900°C. The DBTT in compression was determined to be ≈800°C and was found to decrease with increase in grain size. The yield-point behavior was observed for fine-grained TiC and was found to depend on grain size and test temperature. The yield stress as a function of grain size obeyed Hall-Petch relation (Figure 28(a)) and demonstrated strong Arrhenius type dependence on the temperature of deformation as shown in Figure 28(b). A plot of log yield stress vs 1/T showed a change in slope above 1500°C, which indicates that two rate controlling mechanisms are in operation during the deformation at different test temperatures. The determined activation energy value of 3.2-3.6 eV (308-347 kJ/mole) at 1050°-1500°C suggested that the rate controlling mechanism during deformation in this temperature range is cross slip.

The marked decrease in DBTT to as low as 600°C was reported by Miracle et al. [99] for substoichiometric $TiC_{0.93}$ and $TiC_{0.83}$. This was explained by weakening of Ti-Ti covalent bonds due to the partial removal of carbon (stabilizing and strengthening these bonds) from the TiC lattice. In this work a detailed characterization of polycrystalline substoichiometric TiC_x was made for x from 0.66 to 0.93. Hardness, strength and yield stress dropped with decreasing C/Ti atom ratio. The effect of substoichiometry on strength and yield stress was more pronounced at higher temperatures (Figure 29(a,b)). Miracle et al. observed a transition from primarily transgranular fracture at lower temperatures to predominantly intergranular fracture at higher temperatures. Interestingly enough, Das et al. [134] observed a higher fraction of intergranular fracture in the range from room temperature to 1575°C in stoichiometric TiC. On the contrary, Katz et al. [135] reported the fracture mode in stoichiometric TiC at room temperature as predominantly transgranular cleavage. For all stoichiometries the fraction of transgranular fracture is greater at lower than at high temperature which is to be expected in TiC which cleaves easily along the {100} cube plane below DBTT.

The sharp drop in strength observed above certain temperature both for stoichiometric [134] and substoichiometric [99] TiC was associated with premature intergranular fracture that was attributed to a segregation of impurities such as Fe, Co and Si at the grain boundaries. The exact temperature at which this sharp loss of strength occurs was shown by Katz et al. [135] to depend on the composition of the low-melting-point impurity film at the grain boundary. It is a general observation corroborated by a number of studies, that the segregation of impurities (Fe, Co, Cr, Si, P, and sometimes Cu) at the grain boundaries is characteristic for TiC and results in the impurity film of a few monolayers thickness (~2 nm) which is believed to deteriorate the overall mechanical behavior of polycrystalline TiC [99, 134, 135, 19] and TiC-based composites [19, 126], especially at elevated temperatures, and to effect the predominant fracture mode (transgranular vs intergranular).

In contrast, doping of single crystal TiC with B mitigates the loss of strength at high temperatures, providing a ten-fold increase at 1600°C [136]. Williams [136, 137] showed that the presence of B leads to the formation of precipitates (suggested to be TiB_2) and concluded that the increased strength of the alloyed TiC is due to the precipitation hardening. Venables [138] established that these precipitates are partially coherent precipitate platelets of TiB_2 ~10 Å in thickness and nucleate heterogeneously on the extrinsic three-fold dislocation nodes, such as precipitate density and hence the hardness may be controlled simply by varying the number of dislocation nodes present in the material before or during doping, e.g. by twist deformation.

These TiB_2 precipitate platelets, residing on the {111} glide planes of TiC lattice, inhibit dislocation movement and substantially increase the critical resolved shear stress, especially at high temperatures. As a result, addition of ~1% of B to TiC powder

substantially raises the temperature required for its consolidation by hot-pressing [136]. Likewise, the pronounced increase in hardness is expected for polycrystalline TiC alloyed with B. This was confirmed by Ordan'yan et al. [106], who found that hardness of the TiC_x significantly increased with the dissolution of B (see Figure 22). It should be noted that the effect of B on hardness increases with the decrease of x in TiC_x. The opposite trend was found for lattice constant (see Figure 22). Thus according to Ordan'yan et al. [106], the dissolved B has the weakest effect on lattice constant, and the strongest effect on hardness for $TiC_{0.68}$ compared to TiC_x with higher x. The authors speculated that this may be an indication of formation of covalent B-C bonds, resulting in a compression of the lattice [106].

A fully dense TiC is routinely produced by hot-pressing [99, 116, 134, 135] at 1600°-1700°C (70-55 MPa). Significant efforts have been directed towards processing of TiC-based materials via SHS. The pressure assisted modifications of SHS such as high-pressure combustion sintering or SHS/DC yielded nearly fully dense compacts. For example, Yamada et al. [139] employed SHS from elemental powders under pressure of 3 GPa to obtain 96.5% dense TiC. Kecskes et al. [81] and Wang et al. [82] utilized SHS/DC to produce 93-98% dense compacts with hardness and elastic modulus comparable to hot-pressed material. LaSalvia et al. [83] showed that TiC could be densified in excess of 96% of the theoretical density by dynamically compacting the SHS product using a high velocity forging machine.

2.3.5 Development of $TiC-TiB_2$ composites

In retrospect, the concept of $TiC-TiB_2$ composite was developed from two opposite directions. Originally, precipitation hardening by TiB_2 was proposed as a way to alleviate

the loss of strength at high temperatures, characteristic for TiC [136, 138]. At the same time TiB_2 was a subject of intensive efforts to improve its structural reliability. TiC was envisioned as a prospective toughening second phase for TiB_2 [21, 126, 140], since TiC possesses five independent slip systems above DBTT which allow the material to deform plastically at high temperatures in a manner similar to fcc metals. Recently, it has been shown that multiphase TiC-TiB_2 composites exhibit strong synergistic effects resulting in remarkable overall mechanical properties [17-22, 141] and improved densification behavior [18, 23, 142, 143] in regard to the parent single phase ceramics.

The evolution of flexural strength, fracture toughness, critical flaw size, hardness, coefficient of thermal expansion and electrical resistivity over the complete range of compositions for TiC-TiB_2-SiC system were reported by De Mestral et al. [17] They observed a pronounced improvement of properties in two-phase (TiC-TiB_2, SiC-TiB_2, and SiC-TiC) composites as compared to single phase materials. Nonlinear and favorably deviating from the rule of mixture (synergistic) dependence of strength and fracture toughness on composition for TiC-TiB_2 composites is shown in Figure 30(a) (data after ref. [17]). In accord with De Mestral et al., Holleck et al. found considerable increase in wear resistance and fracture toughness of TiC-TiB_2 composite compared to monolithic TiC and TiB_2 (see Table II [18]). In addition, they reported improved sintering behavior of the TiC-TiB_2 mixture and noted that the phase boundaries between the TiC and TiB_2 grains in the resulting composite are frequently flat or only slightly curved. TEM analysis showed that grains were partially oriented, so that the crystal surfaces matched between TiC and TiB_2 yielding coherent phase boundaries.

2.3.5.1 Structure and Chemistry of Interfaces

Epitaxial relationships in TiC-TiB_2 system were analyzed in a number of studies [138, 144, 20, 145]. The arrangement and interatomic distances of the Ti atoms on several dense packed crystal planes of TiC (NaCl type) and TiB_2 (AlB_2 type) structures appeared to be very similar (e.g. {111} planes of TiC and basal plane of TiB_2) leading to simple epitaxial relationships such as:

Interfacial plane $\| (111)_{TiC} \| (0001)_{TiB2}$; and direction $[110]_{TiC} \| [1210]_{TiB2}$

The latter was reported for TiB_2 platelet precipitates in TiC [138] and directionally solidified carbide-diboride eutectics [144]. Four different coherence relations were found by Holleck et al. [20] at the phase boundaries of the sintered TiC-TiB_2 composite. It has been shown that coherent phase boundaries in this system are responsible for the improved sintering behavior [142], significant reduction in hardness characteristic for near-eutectic compositions [146] (see Figure 31), and high temperature superplasticity exhibited by such materials [143]. In particular, sintering is drastically activated by the presence of coherent phase interfaces which constitute effective vacancy sinks, ensuring "dissolution" of pores and development of more perfect internal volumes of grains for both phases [142]. This was confirmed by the results of an investigation into the thermal conductivity of TiC-TiB_2 composites [147].

It is widely accepted that microchemistry of phase interfaces is one of the critical parameters controlling behavior of CMCs, especially at high temperatures. Unfortunately, only very few studies are available in the literature on the microchemistry of TiC-TiB_2 interfaces. Among them the most comprehensive is recent work of Nold et al. [19]. In their previous studies [18, 20] they related superior combination of properties in TiC-TiB_2 composites to the contribution of the favorable phase boundaries. In the latter study [19] the observed synergistic effects were attributed to the presence of TiB_xC_y phase on the

grain boundaries. High-resolution scanning Auger electron spectroscopy combined with UHV ($<10^{-9}$ mbar) in-situ fracture stage was employed in this study to examine TiC-TiB_2 composites and compare them to monolithic TiC and TiB_2 fabricated from the same powders. Oxygen-rich TiB_xO_z phase was identified in hot-pressed TiB_2 as round particles of about 1 μm size uniformly distributed at the triple points of the diboride grains. The TiB_xC_y phase, that had never been previously reported in the literature, was observed as a layer surrounding the TiC and TiB_2 grains, both on fresh fracture surfaces and polished crossections. TiB_xC_y layer was considerably thicker than a few monolayers (sometimes as thick as ~200 nm) and covered significant fraction of phase boundaries. Neither stoichiometry, nor crystal structure of the TiB_xC_y phase was reported. The conclusion that this was indeed new phase and not solid solution was based on low intersolubilities found in pseudobinary TiC-TiB_2 system [100, 106]. In the same study [19], the formation of this TiB_xC_y phase was confirmed in TiC-TiB_2 diffusion couple and the mechanism was identified by which TiB_xO_z phase (found in TiB_2) can be reduced by carbon to the TiB_xC_y phase. Zdaniewski [126] also found an appreciable amount of grain boundary phases in TiB_2(83wt%)-TiC(17wt%) composite and concluded that it was an intergranular TiC_x of variable stoichiometry with metallic substitutions (W, Zr, Al, Si). It should be noted, however, that EDX electron microprobe employed by him for compositional analysis was inadequate tool to rule out the presence of boron in the intergranular phases.

2.3.5.2 Toughness and Strength

It is clear from above that TiC-TiB_2 composites have been considered as having "strong" interfaces between constituent phases. The fracture mode reported by most studies is predominantly transgranular or mixed transgranular-intergranular with the relative fraction of intergranular fracture being dependent on the purity of starting powders, final

grain size distribution and grain morphology. It should be noted that no toughening mechanisms, recognized for certain TiB_2-containing CMCs [28], have been identified in the conventionally produced TiC-TiB_2 composites. Whereas addition of TiB_2 to low-expansion matrices such as SiC or B_4C was shown to improve fracture resistance through mechanisms of crack deflection, grain bridging and microcracking [28]. The absence of these mechanisms in TiC-TiB_2 composites may be attributed to the fact that TiC and TiB_2 have close coefficients of thermal expansion (7.7-8x$10^{-6}K^{-1}$ and 7.4-7.8x$10^{-6}K^{-1}$, respectively) and since most of the results have been reported for composites with fine-grained (< 5μm) equiaxed microstructures, the possible toughening contribution of thermal expansion anisotropy of the TiB_2 phase is expected to be negligible.

Toughening by a ductile phase is believed to be operative in TiC-TiB_2 composites at temperatures above DBTT of TiC constituent [[17, 8, 126], 21] as well as in TiC-TiB_2 cermets [24]. However, in the former it has been only suggested as a possibility [17, 8, 126] or hinted by indirect experimental evidence [21] and has never been an object of rigorous study, e.g. by combined fractography and fracture toughness measurements at elevated temperatures. In the latter, toughening effects of metal binder (sintering aid), was shown to depend on its chemistry, which controls the binder's wetting behavior and the formation of embrittling boundary phases such as Ni_3B [24]. For TiC-TiB_2 composites sintered with (Ni+X) binder, where X is an undisclosed transition metal, the fracture mode was reported [24] as predominantly transgranular for 2.5 wt% (Ni+X); and as ductile tearing, characteristic for cermets, for 5 wt% (Ni+X). Corresponding values of fracture toughness were 7.1 MPa$\sqrt{m}$ and 8.4 MPa$\sqrt{m}$, respectively. Besides a specific case of TiC-TiB_2 cermets [24], grain size refinement has been suggested [28] as a major strengthening approach in TiC-TiB_2 system to date. However, there are indications in the literature that introduction of the third phase [17, 148, 8] and attainment of layered [18, 140] or aligned

(i.e. lamellar eutectics) [144] microstructures may improve fracture toughness and strength of $TiC-TiB_2$-based composites.

2.3.5.3 Wear behavior

The origin of synergy in the wear behavior of $TiC-TiB_2$ composites deserves particular attention. In extensive study by Wu et al. [108] the wear behavior of TiC, TiB_2, AlN, Si_3N_4, SIALON, Al_2O_3, SIALON-BN composite, and Al_2O_3-matrix composites with SiC, TiC and TiB_2 reinforcements was characterized by diamond pin-on-disk technique (POD). TiC and TiB_2 exhibited wear resistance superior to Al_2O_3 of comparable grain sizes. Al_2O_3-TiC and Al_2O_3-TiB_2 particulate composites showed 50-100-fold greater wear resistance than that of either constituent. Among all the evaluated materials the least wear was found in Al_2O_3-47 vol% TiC and Al_2O_3-64 vol% TiB_2. According to Wu et al. the friction wear rate for ceramics scales with a square root of grain size - the dependence well recognized for cemented carbides [149]. Recently, Lahrez [141] has established that TiC/TiB_2 PVD coating of tungsten carbide cutting inserts clearly improved their wear behavior tested in machining of gray cast iron. The coating of 5 μm thickness was composed of two phase TiC/TiB_2 layers (1:1 molar ratio) with a crystallite size of 100 nm. The superior wear behavior of the coating was shown to be directly related to its hot hardness and the constitution of interfaces between TiC and TiB_2 phases. Previously, Evans et al. [150] have shown that abrasive wear resistance of ceramics scales with fracture toughness, reciprocal of Young's modulus and hardness. The results of Wu et al. and Lahrez demonstrate that strength ($\sim$ (grain size)$^{-1/2}$) and hot hardness are also critical for application-specific wear behavior of ceramics. The comparison with commercial ceramic cutting tool materials [151] (see Table III) shows that $TiC-TiB_2$ composites have favorable combination of the properties controlling wear resistance.

Some light on the mechanisms of wear in this system was shed by Tkachenko et al. [21], who studied friction and wear behavior of eutectic TiC-TiB_2 composites in the range of 25°C-1400°C (friction against like and unlike, HfC-HfB_2, surfaces). The minimal coefficient of friction and minimal wear rate were observed around 800°C, simultaneous with the ductile-to-brittle transition in the studied material. (Note that DBTT for the TiC constituent is ~ 800°C [134].) The separate effects induced by dispersion of crystallites and distortion of the crystal lattice were derived from broadening of X-ray peaks. The study revealed predominant distortion of the TiB_2 crystal lattice in the process of wear. A minimum in the lattice distortion of diboride phase vs friction temperature was observed at 800°C, within the ductile-to-brittle transition range for the carbide phase. The TiC constituent exhibited a low level of lattice distortions which completely disappeared above 800°C. Both TiC and especially TiB_2 constituents underwent intense fractionation. However, for TiC the opposite process, crystallite growth, took over above 1000°C. The decrease in the rate of wear with the increase of temperature was attributed to plasticity in the TiC-TiB_2 composites at higher temperatures. Above 800°C the marked softening of the surface layer was detected, accompanied by the increase in the deformed layer thickness. The increase in wear at temperatures above 800°C was related to the predominant role of adhesion processes and was not observed for the friction of unlike surfaces. Tkachenko et al. concluded that the principal phase taking up the loads was TiB_2. In agreement with Holleck et al. [20], they found wear behavior of eutectic composites to be far superior compared to monolithic phases.

2.3.5.4 High Temperature Plasticity and Creep

High temperature creep of TiC-TiB_2 composites at 1700°-2400°C was studied by Spivak et al. [23] in bending and later by Kats et al. [143] in compression. Similar behavior was observed in both studies. However, Kats et al. obtained significantly lower creep rates than Spivak et al. and attributed it to contamination with WC (from grinding media), which had dissolved in the carbide phase. Among the most interesting findings were nonlinear variation of steady state creep rate with composition shown in Figure 32 and superplastic behavior mentioned earlier in relation to existence of semicoherent phase boundaries in these composites. Maximal total strain without rupture of more than 30% as well as maximal steady-state creep rate were attained for near eutectic compositions (1:1 TiC/TiB_2) with the most well developed phase boundary networks. Even after such severe reductions the grains were undeformed, however, a large degree of intergranular damage[1] was observed, consequently grain boundary sliding was identified as the predominant mechanism [143]. In addition, based on high apparent activation energy of 335-460 kJ/mole and stress exponent, n=1.5, Kats et al. concluded that a certain contribution to the total strain comes from threshold mechanisms ($n \geq 1.5$), rate-limited by diffusion of metal atoms in the boundary zones of grains [153].

2.3.5.5 Fabrication

To date all the techniques used for fabrication of monolithic TiC and TiB_2 have been applied to TiC-TiB_2 composites. These include pressureless sintering [18, 142, [tkach&ordan,] 76]; hot-pressing and HIP-ing [19, 17, 148, 76]; SHS [75, 76, 154];

[1] A high degree of damage found on grain boundaries may not be intrinsic for the TiC-TiB_2 system and can be attributed to combination of microstructural (grain size 2-4 μm, porosity 2-3%) and strain rate conditions which may not be optimal for superplasticity, and also to segregation of impurities at grain boundaries, i.e. due to 0.12-0.36 wt% of Co transferred from WC-6%Co grinding media.

plasma spray deposition, and physical and chemical vapor deposition techniques for coatings [141, 18] and thin films [140]. It has been realized that the processing of ultra-refractory TiC-TiB_2 composites into complex-shaped components with full densities requires extremely high temperatures and poses a serious technological challenge. Some of the novel techniques described in Section 2.2 have been implemented in TiC-TiB_2 system to overcome this problem. Among them are SHS/hot-pressing [78] and SHS/HIP [26], directional reaction of molten Ti with B_4C preform [27], addition of "tailored" sintering aids [24], and reactive hot-pressing (TPPP). Although these techniques have been successful in overcoming some of the existing processing problems, most of them continue to suffer from at least one of the following limitations - inability to control grain size and other microstructural parameters, significant residual porosity, or poor high temperature creep properties (largely due to the addition of sintering aids). Other innovative approaches, such as directional solidification of carbide-diboride eutectics by floating zone technique [144], have yielded unique microstructures, however, they are too sophisticated to be practical. In TiC-TiB_2 system TPPP has proven to be the only viable alternative to conventional processing techniques, capable of producing fully dense, ultra-refractory TiC-TiB_2 or TiC_x-TiB_2-Ti_3B_4 composites at temperatures that are only about 0.62 of the eutectic temperature. The other advantages of TPPP in this system reported in the previous studies [8] included net shape capability and formation of Ti_3B_4 platelet reinforcements in situ. Table IV summarizes processing details and properties of monolithic TiC and TiB_2 ceramics, and TiC-TiB_2 composites fabricated by various techniques reported in the literature.

3. EXPERIMENTAL PROCEDURE

The initial stage of the experimental work was to delineate more accurately the 1600°C isothermal section of the Ti-B-C phase diagram, that is required for intelligent processing of CMCs in this system. The second stage was to study the reaction paths and microstructural evolution mechanisms leading to formation of varying final phase morphologies starting from different initial powder mixtures. The third stage of this experimental study was to determine room and high temperature mechanical properties of the fabricated composites and to relate them to microstructure. In addition, the optimization of microstructure was attempted and the mechanical properties, wear and oxidation resistance of the resultant composite were evaluated. In the following sections the starting materials are characterized, then the processing technique is detailed, and finally the characterization and testing methods are described.

3.1 Starting compositions

The starting compositions employed for evaluation of properties were 4:1 Ti/B_4C, 1:0.5:1 $Ti/C/TiB_2$, 1:1 $TiC_{0.5}/TiB_2$. Note that these compositions have identical elemental composition and, hence, correspond to the same point on the Ti-B-C phase diagram. Two different types of microstructure were observed in the produced composites. The 4:1 Ti/B_4C starting composition yielded one of the final phases in platelet morphology and this type of microstructure is referred to below as "***platelet***". Microstructures produced from

the 1:0.5:1 Ti/0.5C/TiB_2 and 1:1 $TiC_{0.5}$/TiB_2 starting compositions, respectively, comprise roughly equiaxed grains and are referred to below as "***equiaxed***".

3.2 Starting Powders

The powders employed in this study are listed in Table V. The particle size distributions of these powders were obtained using Horiba laser scattering particle size analyzer (Model LA-910).

In order to elucidate the effects of shape, size and purity of the starting Ti powders on the final microstructure, three different Ti powders were employed. An angular dehydride high purity (99.99%) titanium powder with a 43 ± 21 μm (median ± standard deviation) particle size was used in most of the runs. In some hot press runs the particle size of this powder was reduced to 20±9 μm by sieving it through a -500 mesh screen. In addition, an angular hydride (4 at% H) high purity (99.99% metal basis) titanium powder with a 33 ± 21 μm particle size was employed. Prior to mixing the size of hydride powder was reduced to 6-8 μm by jet-milling in TROST Air Mill (Garlock Inc., Newton, PA) with argon stream at operating pressure of 0.35 MPa. For comparison, a spherical titanium powder of lesser purity (98.5%) with a particle size of 5 ± 2 μm was also used.

The $TiC_{0.5}$ powder was produced by an SHS reaction from high purity elemental powders. The sintered body synthesized by SHS was dry ground under argon with tungsten carbide grinding media. The obtained powder was sieved to -325 mesh yielding a particle size of 13±4 μm. The stoichiometry of $TiC_{0.5}$ was verified by lattice parameter measurement and comparison with calibration curves (see Section 3.6.5).

The other powders employed, B_4C and TiB_2, had particle sizes of 6± 2 μm and 10± 5 μm, respectively. The SEM micrographs and particle size distributions of $TiC_{0.5}$, TiB_2, B_4C, and Ti powders are shown in Figures 33(a,b) through 38(a,b), respectively.

3.3 Fabrication of composites

3.3.1 Mixing and Fabrication of Green Body

The starting mixtures were V-blended under argon for 12 hours, and subsequently cold compacted at 400 MPa into 69x12x(5 - 10) mm bars. The resulting green densities were about 74% (2.84 g/cm^3) of the theoretical for 4:1 Ti/B_4C, ~72% (3.1 g/cm^3) for 1:0.5:1 Ti/C/TiB_2, and ~67% (3 g/cm^3) for 1:1 $TiC_{0.5}$/TiB_2 compacts. In order to reduce particle size some of the 1:1 $TiC_{0.5}$/TiB_2 mixtures were wet ball-milled in 2-propanol for 12-24 hours using tungsten carbide grinding media and vacuum dried prior to compaction. These wet ball-milled powder mixtures had average particle size of 8 μm and 5 μm after 12 h and 24 h of grinding, respectively. The wear of grinding media (WC-10 wt% Co balls) and the concomitant contamination of powder mixture was found to be 0.2-0.3 wt% per hour of milling for the volume ratio of powder charge/WC-balls/2-propanol of 1:1:1 employed in this work.

It should be noted, that, initially, wet ball-milling with corundum grinding media for 24 hrs in 2-propanol was used according to the procedure described in [8]. Since no specific advantages in regard to homogeneity of final microstructure and resulting properties was found compared to V-blending, the latter was preferred. However, V-blending necessitated the use of dry powders, which were kept in vacuum at 50°C for 12

hours prior to mixing. The presence of moisture in V-blended powders appeared to cause macroagglomeration which was eliminated by additional rolling of dry powder mixture in the sealed polyethylene container with a few heavy WC-carbide balls for 1-2 hours.

3.3.2 Hot-Pressing

The green bars were placed in a graphite die and vacuum hot-pressed at various pressures in the range of 40-80 MPa. The pressure was applied before initiation of the heating schedule and held constant until it was completed. Afterwards the sample was naturally cooled to ambient temperature with simultaneous reduction of pressure. The vacuum during hot-pressing was kept at less than 10^{-3} Pa (10^{-4}-10^{-5} torr).

Typically, for the Ti/B_4C mixture, a two-stage heating sequence was used. The first stage consisted of heating at 10°C/min to 800°C and soaking at that temperature for 4 hours. The second stage involved continued heating at the same rate to 1600°C and soaking at that temperature for 4 hours to promote further densification and complete the reaction synthesis. For the $TiC_{0.5}/TiB_2$ mixture, on the other hand, the densification and reaction steps were combined in a one step heating sequence comprising of heating at 10°C/min to 1600°C and soaking at that temperature for 4 hours. The same sequence was used for 1:0.5:1 Ti/C/TiB_2 starting mixtures, since it was believed that Ti reacted with C to form $TiC_{0.5}$ at earlier stages of the heating ramp and subsequent progress of reaction and densification was somewhat similar to $TiC_{0.5}/TiB_2$ starting mixture.

The vacuum hot press (Centorr Vacuum Industries) was instrumented with a data acquisition system such that load and ram position were continuously recorded during each run. The raw data was corrected for compliance and thermal expansion of the die and load

train using the data collected in runs carried out with the same die, load train and pressure-temperature schedule but without a specimen in the die (top and bottom punches were pressed upon each other).

3.3.3 Hot Isostatic Pressing (HIP-ing)

The green body was sealed in a boro-silicate glass (pyrex) tube under vacuum. The glass encapsulated body was inserted in the chamber of the HIP and hot isostatically pressed (HIP-ed) by subjecting it to hydrostatic pressure of argon and high temperature. The typical temperature cycle comprised two segments. Initially the sample was heated at 10°C/min to 850°C (above softening point of pyrex) and held at this temperature for 1 hr, while argon in the chamber was pressurized to 40-45 MPa. Then heating was continued at 10°C/min to 1600°C and this temperature was maintained for 4 hrs. The pressure of the argon at constant volume was increasing with temperature according to universal gas law and reached 60-70 MPa at 1600°C. After completion of the heating cycle the chamber with a sample was allowed to cool naturally. Then the sample was removed from the HIP and soaked in concentrated HF for few hours to remove the glass.

3.4 Interrupted Hot-Press Runs

In order to study the reaction sequence and the evolution of microstructure for the 4:1 Ti/B_4C starting composition, hot press runs were interrupted at 800°C (after the 4-hour soak), 1200°C, and 1600°C (before soaking). In addition, samples fabricated at 800°C for 4 hours (which yielded density of 3.17 g/cc (83%), were cut in smaller pieces, and heated to different temperatures (1200°C, 1300°C, 1400°C, 1450°C, 1500°C, 1600°C) under argon

at 10°C/min. After reaching the predetermined temperature, the samples were held at that temperature for 5 min and then quenched on a massive aluminum plate under intense flow of argon. The oxide layer on the quenched samples was removed, and the samples were analyzed using X-ray diffraction and scanning electron microscopy to document the evolution of phase composition and morphology.

To verify that the quenched samples reproduce faithfully the microstructural evolution in the absence of pressure, the samples quenched from 1200°C and 1600°C were compared with the corresponding ones produced in the hot press runs interrupted at 1200°C and 1600°C, and no significant difference was found in phase composition and morphology.

3.5 Determination of the 1600°C Isothermal Section of the Phase Diagram

Powder mixtures of different molar ratios of Ti/B_4C, Ti/C/TiB_2 and $TiC_{0.5}$/TiB_2 (see Table VI) were vacuum hot pressed at 1600°C for 4 hr and a pressure of 40 MPa. To ensure that equilibrium was achieved the hot pressed samples were further annealed in the vacuum hot press for additional 16 and 32 hours. Runs 4-7 were not hot pressed, but simply pressureless sintered in the vacuum hot press for 4 hours and subsequently annealed for additional 16 hours.

The compositions were chosen such as to determine the exact position of the Ti_3B_4-TiC_x line [75] or field [8] separating TiB_2-TiC_x-Ti_3B_4 and Ti_3B_4-TiC_x-TiB compatibility triangles. Final phase compositions and stoichiometry of the TiC_x constituent were determined as described in Sections 3.6.3-3.6.5. The number of separate samples for each composition is shown in brackets in Table VI.

3.6 Characterization of the Produced Composites

3.6.1 Density

The bulk density of the hot-pressed samples were measured by Archimedes method (water immersion technique). The theoretical densities were calculated using the volume fractions of phases obtained from image analysis and/or from a mass-balance based on TiC_x stoichiometry derived from its lattice parameter (similarly to example calculation in Section 3.6.5). The densities of TiC, $TiC_{0.65}$, TiB_2 and Ti_3B_4 were taken to be 4.9, 4.6, 4.5 and 4.6 g/cm^3, respectively. The corresponding molar volumes are 12.23, 12.11, 15.38, and 40.64 cm^3/mole, respectively. Both calculations yielded close values for the theoretical density. However, the ratio of measured density to theoretical density (in % th. density) appeared not to be a reliable measure of residual porosity for nearly fully dense composites. In the latter, the measured densities were often equal or exceeded slightly the calculated theoretical values, while residual porosity of 1-2 vol% was clearly observed microstructurally. Thus, direct porosity measurements were undertaken as described below.

3.6.2 Microstructural Characterization

The microstructural observations were carried out in SEM (Amray 1830) on polished cross-sections as well as on fracture surfaces. The SEM was equipped with WDS (wavelength-dispersive spectrometry) and EDS (energy-dispersive spectrometry) microprobes which allow to determine grain composition in situ. For instance, boron

mapping was performed to determine the distribution of the dissolved boron in TiC_x areas. Since the constituent phases were clearly resolved in backscattered electron images of examined microstructures (based on their atomic number contrast), no etching was found to be necessary.

3.6.3 Volume Fractions of Phases and Porosity

The volume fractions of TiB_2, TiC_x, and Ti_3B_4 phases were determined by image analysis of the backscattered SEM micrographs of the densified and annealed composites. For image analysis, the SEM images were input into a computer through a videocamera (MTTI series 68, Dage-MTTI, Michigan City, IN) and analyzed by Image Analyst 7.2 software (Automatic Inc.). The reported values were an average of six micrographs at a magnification of 500X. The accuracy in volume fractions measurements for the individual phases was estimated to be ±3-5 vol%.

The porosity was measured by image analysis of carefully polished cross-sections. The image at magnification of 500X-1000X (depending on pores size) was taken directly from the optical microscope (Olympus PMG-3) to the videocamera and analyzed as described above. The accuracy in porosity measurements for nearly fully dense composites was estimated to be ±0.5 vol%.

3.6.4 X-ray Compositional Analysis and Lattice Parameters Measurement in TiC_x

Siemens D500 diffractometer was employed for X-ray analysis. Phase composition of the fabricated composites and precise lattice parameters of their TiC_x constituent were

determined from X-ray diffraction patterns of the powdered samples using Cu$K\alpha$ radiation.

The lattice parameters of TiC_x were measured by least squares fit and extrapolation to $2\theta = 180°$ of the $\cos^2\theta/\sin\theta$ function as described in [155]. In all cases the least-squares fit yielded correlation coefficients greater than 0.9. The typical least-squares fitted results are shown in Figure 39(a,b,c). The attained accuracy in lattice parameters determination was ±0.0001 nm, that is quite reasonable, given the technique employed [155].

Semiquantitative compositional analysis was carried out with α-Al_2O_3 (50% wt.) admixed to the powdered samples as an internal standard. The relative intensities of the strong diffraction lines of Ti (100), TiC (200), TiB (102), TiB_2 (101), and Ti_3B_4 (031) were normalized by that of (116) α-Al_2O_3 line. This analysis performed on the interrupted runs samples provided a semiquantitative measure of compositional changes during hot-pressing.

3.6.5 Determination of x in TiC_x

The stoichiometry of TiC_x was calculated from the calibration curve given in Appendix II, summarizing the results reported in the literature [99, 100, 106, 107]. In addition, the TiC_x stoichiometry was independently calculated by converting the volume fractions measured from image analysis of the final microstructures to mole fractions and choosing the value of x to satisfy the equation of the corresponding reaction. For example, for 30.5 vol% TiB_2, 34.9 vol% TiC_x, and 34.6 vol% Ti_3B_4 the corresponding reaction equation would be

$$4\,Ti + B_4C = 0.46\,Ti_3B_4 + 1.08\,TiB_2 + 1.54\,TiC_x$$

Consequently, to balance this equation x=0.65 is required.

3.7 Evaluation of Properties

3.7.1 Hardness

Hardness measurements were performed at room temperature using a Vickers diamond indentor with a test load of 10 kg. When necessary, microhardness of individual grains and/or phase fields was measured with Vickers Microhardness Tester and loads ranging from 25 g to 100 g. The values reported here are averaged from at least 15 individual measurements.

3.7.2 Elastic Modulus

The Young's modulus of the fabricated composites was measured by resonance frequency technique using Grindosonic Mk5 "Industrial" equipment (J.W. Lemmens Inc., St. Louis MO).

3.7.3 Flexural Strength

The flexural strength of the produced composites was determined by four-point bending according to procedure outlined in ASTM C1161 and ASTM C1211. Specimens were diamond-tool machined by Chand Kare Technical Ceramics, Worcester, MA with

dimensions conforming to ASTM C1161 type A (25mm x 2mm x 1.5mm). The surfaces of the bending specimens were finished by 320 grit diamond wheel according to MIL-STD-1942A Standard (11/8/90). The edges were beveled to minimize edge effects. The tests were performed in a semiarticulating SiC fixture with outer span of 20 mm and inner span of 10 mm on a servo-hydraulic MTS testing machine with load resolution of 5N at a strain rate of 10^{-4} s^{-1}. The load-displacement curves were digitally recorded using DOS-based personal computer equipped with Labtech Notebook data-acquisition software.

For testing at elevated temperatures the furnace surrounding the fixture with the sample was brought to the test temperature at heating rate of 30°C/min, 15 min were allowed for thermal equilibration and test duration was 1-2 min depending on the temperature. Since the studied materials are sensitive to oxidation at the temperatures above 500°C the high temperature 1000°-1400°C four-point bending tests were performed in the atmosphere of argon on the samples protected with BN coating. Specimens tested in air at 1000°C following the same heating sequence but without oxidation protection showed a reduction in strength of the order of 40%.

Fracture strength, S, was calculated from the standard formula for the strength of a beam in four-point-1/4 point bending given in ASTM C1161

$$S=3PL/(4bd^2) \qquad (14)$$

where P - breakload (see Figure 40(a), L=20 mm - outer span, b=2 mm - specimen width, d=1.5 mm - specimen thickness. For specimens which exhibited plastic deformation (during high temperature tests) P was taken as the load at the onset of nonlinearity in the load-displacement curve (see Figure 40(b) - curve at 1200°C). In bending tests performed at 1400°C this point could not be easily determined because of sinusoidal signal of ±(3-5) N in amplitude observed to be superimposed on the load-displacement curves (see Figure 40(b) - curve at 1400°C) as a result of interference from the electromagnetic field induced

by the overloaded heating system. The corresponding fracture strength, S, was again taken to be equal to the yield stress which in these cases was calculated from the well-known equation for fully yielded bend beam

$$S=P_{max}L/(2bd^2) \quad (15)$$

where P_{max} - maximum load on the load-displacement curve. It should be noted that this equation is derived in the assumption that the absolute value of stress through the whole crossection of the yielded specimen is the same and equal to the yield stress. Therefore, for this equation to be valid the maximum load should occur before fracture or load-displacement curve should exhibit plateau prior to fracture. These conditions were met in all of the tests at 1400°C.

3.7.4 Thermal Shock Resistance

The susceptibility to thermal shock was evaluated by quenching standard bend specimens (25mm x 2mm x 1.5mm) from successively higher temperatures into water of room temperature. The samples were inserted into the hot furnace and held at temperature for approximately 10 min. The retained four-point bend strength was measured as described above and plotted vs ΔT (°C) of quenching. From this plot ΔT_c, critical temperature change, was obtained as the temperature at which the drastic loss of strength occurred.

3.7.5 Fracture Toughness

3.7.5.1 Indentation Fracture Method

The estimates of fracture toughness at ambient temperature were obtained by measuring the lengths of the median cracks emanating from the Vickers indentation (load of 98 N). The total length of the two cracks emanating from five indentations were averaged and used to calculate K_{1c} for each composite using the equation given by Evans and Charles [156]:

$$K_{1c} = \{0.15k(C/a)^{-3/2}H\sqrt{a}\}/\Phi = 0.15(C/a)^{-3/2}H\sqrt{a} \quad (16)$$

where H is the Vickers hardness, k=2.6-3.2 - correction factor, Φ=3 - constraint factor, a - one half of the average diagonal length of the pyramidal indentation, and C - one half of the average total crack length as shown in Figure 41(a,b). When Young's modulus was known the similar but more accurate expression [156] was used

$$K_{1c} = Z(\Phi E/H)^{0.4}(C/a)^{-3/2}H\sqrt{a}=0.044(E/H)^{0.4}(C/a)^{-3/2}H\sqrt{a} \quad (17)$$

where Z=0.0285 is an empirical constant. According to Evans and Charles Eq.16 gives an estimate of fracture toughness within an accuracy of 30% and Eq.17 estimates fracture toughness within an accuracy of 10%. Although indentation fracture (IF) technique provided a simple and direct way of evaluating the fracture toughness of the produced composites, the results gained by this method were used only as a comparative guide in assessment of the relative trends in toughness of different microstructures.

3.7.5.2 Chevron Notched Beam Method

In order to obtain more quantitative measure of the plain strain fracture toughness (K_{Ic}) of the produced composites and extend measurements to elevated temperatures, a chevron notched beam method was employed. This method has gained wide acceptance in recent years for fracture toughness testing of brittle materials [157-159] and recently was successfully applied to TiB_2 ceramics [160]. Despite certain difficulties, chevron notched beam method (CVNB) provides several distinctive advantages, namely: 1) the specimen can be easily tested at elevated temperatures; 2) no fatigue precracking is required since a sharp natural crack can be produced at the early stage of loading; 3) K_{Ic} is calculated from the maximum load (P_{max}) alone without measuring the crack length. Features 2) and 3) are related to the special chevron notch geometry and are subject to specific limitations and assumptions which are outlined below.

The loading configuration and specimen geometry are shown in Figure 42. After crack initiation at chevron apex, the width of the crack front, b, continuously increases from zero to a full specimen width. Consequently, an increased load is required to continue the crack extension, resulting in a stable crack growth. Finally, unstable fracture occurs when crack length reaches a certain critical value. It was shown, e.g. [157, 161], that for the case where the crack propagates at a constant stress intensity factor K_{Ic} (flat crack-growth resistance curve), the load maximum occurs for a given specimen geometry at the fixed relative crack length, α_m, independent of the material. Then fracture toughness is given by

$$K_{Ic}=P_{max}Y^*_{min}/B\sqrt{W} \qquad (18)$$

where $Y^*_{min}=Y^*(\alpha_m)$ and Y^* is a dimensionless compliance function that passes through a minimum Y^*_{min} at a maximum load P_{max}.; B - specimen width and W - specimen height.

The compliance function can be derived from either the Munz et. al. [157] straight-through crack assumption (STCA) or the Bluhm [162] slice model. The Y^*_{min} value is obtained by curve fitting [161] as

$$Y^*_{min} = (3.08 + 5.00\alpha_o + 8.33\alpha_o^2)\left[\frac{S1 - S2}{W}\right]\left[1 + \left[0.007\left(\frac{S1 \cdot S2}{W^2}\right)^{\frac{1}{2}}\right]\right]\left[\frac{\alpha_1 - \alpha_o}{1 - \alpha_o}\right] \qquad (19)$$

where a_0 and a_1 are dimensionless parameters related to geometry of a chevron notch, S_1 is outer and S_2 is inner span of four-point bending fixture.

To apply Eq.18 with validity, stable crack growth must precede the final unstable crack growth. This condition appears on the load displacement curve as a nonlinear region between the initial elastic region and final fracture. An overload greater than P_{max} triggers immediate fast fracture based on the initial crack length, a_o, and results in an exclusive elastic region prior to fracture. This result is unacceptable for valid K_{Ic} determination. A small overload $\leq P_{max}$ for crack initiation is expected to result in "pop-in" (sudden crack extension) followed by stable crack extension. This behavior still gives a valid K_{Ic} result. These three conditions are shown schematically in Figure 43 (types I to III) and are consistent with experimental results reported in the literature [158, 159] However, the crack initiation at lower loads in chevron notched specimens is not guaranteed either because of improper specimen geometry or because of intrinsic material properties [159]. Precracking of the chevron-notched beam $\leq a_m$ will produce a load displacement curve of type IV, which exhibits a truncated stable-crack-growth region following the higher-compliance elastic region characteristic of the precrack length. This situation allows valid K_{Ic} determination.

Difficulties associated with initiation of a stable crack can be alleviated by a number of approaches such as a modified chevron-notched bend bar [158], in which Knoop

indentation was used to introduce a sharp starter crack at the chevron tip. Another technique was introduced recently by Sung and Nicholson [159], who conducted in-test precracking of a chevron-notched beam by applying the appropriate stress intensity level to induce subcritical crack growth. Subcritical crack growth can be induced by moisture in the air, high temperatures and corrosive environments. This subcritical precracking is facilitated by sufficiently low displacement rate. After subcritical crack growth manifests in deviation of load-displacement curve from linearity, the displacement rate was increased quickly to the predetermined level for fast fracture. In other techniques starter cracks were produced by thermal shock [157] and short exposure to etchant [this study].

The procedure used in this study for valid K_{Ic} testing of chevron notched beam is detailed below.

(i) Chevron Notched Specimen:

Chevron notched beams were diamond-tool machined by Chand Kare Technical Ceramics, Worcester, MA, to the following dimensions: B=3.81 mm, W=5.08 mm, $\alpha_0=a_0/W=0.2$, $\alpha_1=a_1/W=1.0$ and the slot width t=200 μm. The value of Y^*_{min} for tested configuration, given by Eq.19 [161], was calculated to be 8.86. The corresponding critical crack length $a_m=0.4W$ was obtained using STCA assumption (see Appendix III). Thus the amount of crack extension (a_m-a_o) at Y^*_{min} is 102 μm.

It should be noted that the chevron notch can be machined in two different orientations in relation to compaction axis. In the first orientation the tip of a chevron notch is parallel to the direction of the load applied during hot-pressing. In the second orientation the tip of a chevron notch is normal to that direction. When the first orientation is tested the crack propagates through the thickness of a hot-pressed billet, whereas for the second one the crack propagates through the width of a hot-pressed billet. The first orientation is

considered to yield the higher strength and thus was consistently used in the present study since its purpose was to study different microstructures rather than different textures.

Since some of the tests were performed at the temperatures above DBTT of the TiC_x constituent (600°-900°C [99, 134]) care was taken to ensure that the specimen dimensions satisfy plain-strain condition (small scale yielding criterion 30). This requirement is given in ASTM E 1304-89 as $B \geq 1.25 (K_{Ic}/\sigma_y)^2$ for chevron-notched short bar and short rod specimen. The specimen employed in the present study readily satisfied this criterion at least up to 1000°C as $B > (W-a_m) > a_m > a_o > 2.5(K_{Ic}/\sigma_y)^2$, where K_{Ic} and σ_y were taken to be $<8MPa\sqrt{m}$ and >400 MPa, respectively. Here, yield stress was considered to be higher than fracture strength since no plastic deformation was observed in bending at 1000°C.

(ii) Testing:

The specimens were tested in four-point bending fixture (S_1=20mm, S_2=10mm) described in Section 3.7.3 with displacement rates ranging from 0.01 mm/min to 0.06 mm/min. Load-displacement curves were digitally recorded using sampling rate of 5-10 points/s. The corresponding fracture toughness was then calculated using Eq.18.

Because of the non-ideal geometry of the chevron notch, i.e. excessively wide slot and blunt apex of the notch, precracking was found to be necessary for valid K_{Ic} testing. Three different techniques were employed to induce starter cracks in the specimen: preloading of the specimen to 50-75% of the expected maximum load at 600°C for 30 min, thermal shock by quenching into water from 250°-300°C (temperature range close to ΔT_c condition), and etching of chevron notch by a mixture of $H_2O/HNO_3/HF$ in volume proportion of 5:5:2 for 1 min. All three precracking techniques increased the fraction of valid tests to 50%. However, the thermal shock precracking was found to be more effective

for "equiaxed" microstructures, whereas precracking by chemical etching was more effective for "platelet" microstructures.

3.7.6 Oxidation Resistance

To characterize the oxidation kinetics the time dependence of the weight changes of small cubes annealed in air were measured at 750°, 900° and 1000°C. Parabolic rate constants, K_w ($kg^2m^{-4}s^{-1}$), were determined from the plot of the weight gain, normalized by the area of the oxidized surface, vs $(time)^{1/2}$.

4. RESULTS

The experimental results reported in the following sections describe final compositions and microstructures; microstructural evolution, the corresponding compositional changes and dynamics of densification during the processing; and, finally, the properties of the resultant composites.

4.1 Final Compositions

The final compositions are summarized in Table VI. For reasons that are addressed later, only the compositions in which the high purity (99.99%) Ti was used as a reactant achieved equilibrium (Runs 1-7). The corresponding composites will be termed below as "***equilibrium***". The composites corresponding to non-equilibrium compositions (Runs 8-11) will be termed below as "***non-equilibrium***". The experimental results presented in the following sections mainly deal with the three starting compositions, 4:1 Ti/B_4C, 1:0.5:1 $Ti/C/TiB_2$ and 1:1 $TiC_{0.5}/TiB_2$, of which only the first one yields Ti_3B_4 in platelet form while the latter two have invariably yield equiaxed final phase morphologies. Based both on the attainment of equilibrium and final phase morphology, the resultant composites are termed in the following sections as "***platelet***", "***equilibrium equiaxed***" and "***non-equilibrium equiaxed***", respectively.

4.2 Produced Microstructures

The final microstructures for the three starting compositions, 4:1 Ti/B_4C, 1:0.5:1 $Ti/C/TiB_2$ and 1:1 $TiC_{0.5}/TiB_2$, are compared in Figures 44(a)-(c), respectively. Three phases can be identified in these backscattered SEM micrographs: TiB_2, TiC_x and Ti_3B_4, with the brightest phase being TiC_x, and the darkest being TiB_2. The 4:1 Ti/B_4C and 1:0.5:1 $Ti/C/TiB_2$ starting compositions yielded $TiC_{0.65}$ which is the equilibrium phase in the TiB_2 - $TiC_{0.65}$ - Ti_3B_4 compatibility triangle (see Section 5.1). The volume fractions of Ti_3B_4, TiB_2 and $TiC_{0.65}$ phases determined by image analysis are 33%:30%:37% and 36%:30%:34%, respectively. The equilibrium composition calculated from the ternary diagram for this system, revised in this study (Section 5.1), is 34.6%:30.5%:34.9%. The 1:1 $TiC_{0.5}/TiB_2$ starting compositions yield composites comprising TiC_x (x=0.5-0.6) and TiB_2 in equal amounts and some fraction (0% - 20 vol%) of Ti_3B_4, and have not reached equilibrium due to reasons addressed in Section 5.1.1. Shown in Figure 44(c) is a micrograph of the nonequilibrium composite almost completely devoid of Ti_3B_4 phase. These composites were stable in a sense that no significant changes in their phase composition and microstructure were observed even after extended anneals.

In the micrograph of the platelet composite (Figure 44(a)) three distinct features are discernible; bright platelet-free $TiC_{0.65}$ fields, dark TiB_2 fields, and $TiC_{0.65}$ regions with "bushes" of small Ti_3B_4 platelets surrounding the TiB_2 fields in which occasionally large Ti_3B_4 platelets can also be found. The $TiC_{0.65}$ and TiB_2 fields are polycrystalline with 6 μm and 1 μm average grain sizes, respectively. Another important observation is that the "small" Ti_3B_4 platelets surround the TiB_2 fields in a layer of more or less uniform thickness of approximately 15-20 μm.

The microstructure of the equiaxed composites (Figure 44(b)) is surprisingly devoid of platelets; the Ti_3B_4 phase appears with roughly an equiaxed morphology. It should be noted, that the Ti_3B_4 grains in the equiaxed composites are actually quite irregular (see Figure 44(b)). The term "equiaxed" is used here loosely to describe this morphology in contrast to the "platelet" one. The final grain sizes in the equiaxed composites are comparable to the particle size of the starting powders. The phase boundaries between the Ti_3B_4 and TiC_x grains, and especially between the Ti_3B_4 and TiB_2 grains are frequently flat. Often small TiC_x grains are enclosed in Ti_3B_4 grains as if the reaction front avoided certain localities in TiC_x.

4.3 Microstructural Evolution

Figures 45(a)-(d) document the evolution of the microstructure for the 4:1 Ti/B_4C starting composition. At 1000°C the intermediate reaction products are observed as a layer of 2-3 μm thickness advancing into the original Ti grains (Figure 45(a)). By 1200°C (Figure 45(b)) the thickness of the reaction layer has reached 15-20 μm, while all but the largest of Ti grains have been consumed. At 1450° C, some features that resemble platelets are observed (Figure 45(c)). The gray color of the platelet-like phase in the backscattered SEM micrograph at 1450°C indicates that it is either TiB or Ti_3B_4. Small Ti_3B_4 platelets are clearly seen in the micrographs at 1600°C (Figure 45(d)); they are fully developed only after the four hour soak at 1600° C, however. At the end of the soak we also observe a few isolated large Ti_3B_4 platelets growing in TiB_2 fields (Figure 44(a)).

4.4 Compositional Changes during Processing

The X-ray diffraction (XRD) patterns of the samples obtained in the interrupted hot press runs and quenching experiments are presented in Figure 46. Summarized in Figures 47(a,b) are the results of a semiquantitative compositional analysis documenting the progress of reaction for the 4:1 Ti/B_4C starting composition. In Figure 47(a), the normalized intensity (see Section 3.6.4) of the TiC_x (200) peaks are plotted versus processing temperature. Also depicted in Figure 47(a) is the evolution of C/Ti ratio in TiC_x as determined from lattice parameter measurements. The normalized intensities of the other phases are plotted in Figure 47(b). The first reaction products resolvable by XRD are $TiC_{0.5}$ and TiB in the temperature range of 800-900°C. (It is important to note, that the exact temperature at which the reaction starts could not be determined from the interrupted runs.) Peak intensities for both TiB and TiC_x continue to increase up to 1300°C, accompanied by simultaneous consumption of the remaining unreacted titanium. At 1300°C the TiC_x peak intensity reaches a plateau (Figure 47(a)), while the intensity of the TiB peak was observed to decrease above 1300°C. By the end of the 4 hour soak at 1600°C, the TiB peaks disappear completely. At 1450°C a sufficient amount of the Ti_3B_4 phase develops to be detected by XRD. The TiB_2 content increases continuously during the temperature ramp to 1600°C. During the isothermal soak at 1600°C, a slight decrease of TiB_2 content is observed with a concomitant slight increase in the Ti_3B_4 content. As the reaction progresses the stoichiometry of the TiC_x increases from 0.5 to 0.65 (see Figure 47(a)).

For 1:1 $TiC_{0.5}/TiB_2$ starting composition DTA (see Figure 48) showed the onset of the sluggish reaction yielding Ti_3B_4, TiB_2, and TiC_x in the temperature range 1450°-1500°C . An interrupted hot press run at 1400°C confirmed the absence of Ti_3B_4 phase at this temperature. XRD analysis of the powders reacted in DTA indicated that the amount of

Ti_3B_4 gradually increases above 1450°C and approaches a plateau during the 1600°C soak (see Figure 49 (a,b,c)).

4.5 Densification Curves

Temperature and ram displacement (corrected for compliance and thermal expansion as described in Section 3.3.2) are plotted vs time for typical hot-press runs in Figures 50(a) and 51(a) for 4:1 Ti/B_4C and 1:1 $TiC_{0.5}/TiB_2$ starting compositions, respectively. The corresponding densities and densification rates are shown in Figures 50(b) and 51(b) as functions of time. Densification of both compositions exhibits a maximum rate at about 1200°C and gradually comes to a completion during the 1600°C soak, when the last few percents of porosity (~5%) were eliminated. The reasons for this similarity and certain differences apparent from Figures 50 and 51 will be discussed later in Section 5.4.3.

4.6 Mechanical properties

The fully dense composites fabricated by TPPP in this study for the evaluation of properties are characterized in Table VII (Note that in contrast to Table V, characterizing the powders used in this study through their volume-based particle size distributions, particle sizes of the starting powders in Table VII are given as area-based mean±S.D. to compare them with final grain sizes of the resulting composites). The mechanical properties (elastic modulus, Vickers hardness, flexural strength and fracture toughness) at room temperature of the studied composites are summarized in Table VIII. Also given in Table VIII are the

critical flaw sizes calculated from the corresponding fracture toughness and flexural strength using the Griffith relationship.

4.6.1 Fracture and Crack Morphology

Fracture surfaces of the studied composites from the flexural tests are shown in Figures 52(a)-54(a). Interaction of cracks (from Vickers indentations) with the corresponding microstructural features is shown in Figures 52(b,c), 53(b), 54 (b). As revealed in these figures, mixed intergranular-transgranular mode of fracture was observed for all three types of microstructures addressed in this work: "equiaxed nonequilibrium" (two-phased), "equiaxed equilibrium", and "platelet". The extent of intergranular fracture was observed to increase from relatively small fraction in "equiaxed-nonequilibrium" composites to much more noticeable fraction in "equiaxed-equilibrium" composites and significant fraction in "platelet" composites. In accord with these observations, interaction of cracks with microstructural features appeared to be much more pronounced for equilibrium, three-phased, microstructures. Furthermore, crack deflection was observed only in equilibrium, three-phased, microstructures. Crack deflection at phase boundaries was found to be more extensive in the platelet composites and occasionally we have observed crack bridging by the Ti_3B_4 platelets and platelet pull-out. Fracture and corresponding crack morphology were distinctly inhomogeneous for the "platelet" microstructure in that crack propagation characteristics through the $TiC_{0.65}$ fields (Figure 52(b)) and the TiB_2 fields (Figures 52(c)) were observed to be quite different from each other.

4.6.2 Flexural strength

The variation of the room and high temperature flexural strength of the fully dense TiC_x-TiB_2-(Ti_3B_4) composites with composition, the grain size and morphology of the constituent phases, and finally, starting powders particle size (and the resulting microstructural homogeneity) is determined in this study by four-point bending. The typical load-displacement curves obtained in these tests are shown in Figure 40(a) and (b) for room and high temperature, respectively.

The effect of the final grain size or starting powders particle size on the flexural strength of the "non-equilibrium equiaxed" and the "platelet" composites is shown in Figure 55 and Figure 56, respectively.

The flexural strengths of the equilibrium platelet composite, the equilibrium equiaxed composite, and the nonequilibrium equiaxed composite (whose microstructures were shown in Figures 43(a) - 43(c), respectively) were measured in the temperature range 25°C-1400°C and are plotted in Figure 57. The flexural strengths of all these composites were found to be insensitive to temperature up to 1000°C. At 1200°C, the tested composites showed a significant reduction in strength. Furthermore, an examination of the samples after the test revealed that the initially straight bend beams have been imparted with a permanent curvature that can be easily seen with the naked eye. This trend continued to 1400°C for all of these composites. In addition to permanent curvature, multiple cracks parallel to fracture plane were found to originate on the tensile surface of the tested specimens. It should be noted that the severity of these tensile cracks (their number, length and width) were substantially higher for coarse-grained equiaxed composites than for fine-grained equiaxed composites.

4.6.3 Chevron-Notched Beam Fracture Toughness

The typical load-deflection curve for chevron notched beam is shown in Figure 58. The length of nonlinear region between the initial elastic region and final fracture in terms of the beam deflection is of the order of few microns. The corresponding length of the stable crack extension was directly measured on the fracture surface of the chevron-notched beam tested at 500°C (at displacement rate of 0.002 mm/min) as a length of the yellow-orange tip (see Figure 59) clearly distinct from the rest of the fracture surface, which is bluish-colored (less oxidized). The length of this tip is 115 μm which is in good agreement with calculated value of 102 μm (see Appendix III). The origin of the color contrast - which allowed the direct measurement of crack extension prior to fast fracture - is in interference of incident light in thin oxide layers of the varying thickness, the phenomenon widely used in metallography. In our case, the oxide layer formed during stable crack propagation (~12 min) was much thicker compared to the layer covering the fast fracture area (the heating was aborted immediately after fracture).

The measured values of K_{IC} for the three studied compositions (the refined equilibrium platelet composite, the equilibrium equiaxed composite, and the nonequilibrium equiaxed composite) are shown in Figure 60 as a function of the temperature. These measurements were limited to 1000°C, since the measurements of flexure strength shown in Figure 57 indicate that these composites are structurally useful only up to about 1000°C. The refined platelet composite was used in these measurements since this composite had much more homogeneous microstructure, and as a result, significantly higher flexural strength and less scatter in the measurements of fracture toughness at room temperature than the coarser platelet composite (see Table VIII). The behavior depicted in Figure 60 bears the following distinct features: First, fracture toughness initially decreases with

temperature, passes through minimum around 500°-750°C and then increases at higher temperature reaching the values above the room temperature ones. Second, equilibrium (three-phased) microstructures consistently have higher fracture toughness than the nonequilibrium (two-phased) one. Finally, "platelet" composites exhibit higher fracture toughness in the studied temperature range.

4.6.4 Abrasion wear

In order to characterize the wear behavior of the platelet composite with the optimized microstructure the abrasive erosion test was performed by Falex Corporation, Aurora, Illinois, according to ASTM G65-Procedure A. In this test the sample 2x0.9x0.25 in^3 was subjected to abrasion by dry sand delivered between the sample and the rotating rubber wheel, against which the sample was pressed. The results of the test were reported in the following format:

TEST LOAD, lbf	30 (133N)
WHEEL SPEED, rpm	200
WHEEL DIAMETER, mm	225.9
DURATION, cycles	6000
SAND FLOW, g/min	343.8
STANDARD	Tool steel D2 (60 HRC)
SAMPLE VOLUME LOSS, mm^3	11.1
STANDARD's VOLUME LOSS, mm^3	39

4.7 Thermal Shock

Figure 61 summarizes the thermal shock susceptibility of the refined platelet composite as well as two of the refined non-equilibrium equiaxed composites produced with different final grain sizes. The critical temperature change (ΔT_c) was measured to be 330°C for the refined platelet composite, and about 350°C and 450°C for the refined non-equilibrium equiaxed composites with grain sizes of 4 and 2 μm, respectively.

4.8 Oxidation kinetics

Oxidation of the equilibrium composites (refined platelet composite was employed in these tests) was negligible at 750°C (weight gain was not detected after 16 hr annealing in air at 750°C and was only 0.5% after 64 hrs at this temperature) and was found to obey parabolic law at 900°-1000°C. Parabolic oxidation curves for the equilibrium "platelet" composite tested air at 900°-1000°C are shown in Figure 62. Corresponding parabolic rate constants, K_w ($kg^2m^{-4}s^{-1}$), are $1.8x10^{-7}$ and $5.2x10^{-7}$, from which the apparent activation energy for oxidation was calculated to be 130 kJ/mole.

5. DISCUSSION

Two morphologically different microstructures were produced and studied in this work, ***platelet*** and ***equiaxed***. Based on the suggested revision of Ti-B-C phase diagram, the attainment of equilibrium in different starting compositions is addressed first. Then the dominant processing parameters, reaction paths and microstructural evolution leading to corresponding phase morphologies are discussed in detail. The subsequent sections highlight effects of various microstructural parameters, characterizing these phase morphologies, on mechanical properties of the produced composites. Finally, the examples of application of the acquired knowledge of processing-structure-properties relations in Ti-B-C material system are presented.

5.1 Isothermal Section of Ti-B-C Phase Diagram at 1600°C

Based on the experimental results summarized in Table VIII, the isothermal section of the Ti-B-C phase diagram at 1600 °C for compositions in and adjacent to the TiB_2 - TiC_x - Ti_3B_4 compatibility triangle was revised to reflect the fact that Ti_3B_4 is an equilibrium phase in this system. The revised version is presented in Figure 63(b). For reasons that are addressed below, only the samples in which the high purity (99.99%) Ti had been used as a reactant achieved equilibrium and were considered in the suggested version of the Ti-B-C phase diagram. The following discussion is thus focused on these compositions first. The non-equilibrium cases are dealt with separately.

5.1.1 Equilibrium Compositions

The equilibrium results (Runs 1 - 7 in Table VIII) are mapped on the revised isothermal section in Figure 63(b). Runs 1 and 2, had identical compositions and yielded almost identical X-ray diffraction patterns (Figure 64(a)) from which three phases were identified namely: TiB_2, $TiC_{0.65}$ and Ti_3B_4. The extended anneals did not affect the stoichiometry of the TiC_x which was determined to be 0.65 ± 0.02, corresponding to a lattice parameter of 0.4319 nm with a standard deviation of ±0.0001 nm. Such accuracy is quite reasonable, given the technique employed [155]. It is important to note that a total of 12 samples comprising $TiC_{0.65}$ with compositions on both sides of the Ti_3B_4-$TiC_{0.65}$ line were used to determine the lattice parameter and its standard deviation. This determination of x is in excellent agreement with that of Miracle and Lipsitt [99], who measured a lattice parameter of 0.4399 for a stoichiometry of 0.66.

Given this value of x, we can write the following overall reaction:

$$4\,Ti + B_4C \Rightarrow 0.46\,Ti_3B_4 + 1.08\,TiB_2 + 1.54\,TiC_{0.65} \qquad \{3\}$$

Assuming the densities of TiB_2, $TiC_{0.65}$ and Ti_3B_4 to be 4.5, 4.6 and 4.6 gm/cm^3 respectively, the volume fractions of the three phases are calculated to be 0.305, 0.349 and 0.346, respectively. This is in excellent agreement with the volume fractions of TiB_2, TiC_x and Ti_3B_4 determined from image analysis of the densified and annealed composite (Figure 65), namely: 0.30, 0.34 and 0.36, with an uncertainty of ±0.05 respectively. This independently confirms the accuracy of the 0.65 value for the TiC_x stoichiometry determined from X-ray diffraction. This is important because in determining the TiC_x stoichiometry it was implicitly assumed that the boron and oxygen contents in the TiC_x

were low enough so as not affect the lattice parameter of the latter.* Given that the B content in TiC_x was measured by wavelength-dispersive X-ray spectrometry in the SEM to be 1.5 at% and the total oxygen content was measured to be less than 1 at%, we believe this is a good assumption. It is worth noting that the volume fractions are quite sensitive to the value of x chosen. For example, for x = 0.6, the volume fractions of TiB_2, TiC_x and Ti_3B_4 would be 0.38, 0.37 and 0.25, respectively, whereas for x = 0.67, the volume fractions would be 0.28, 0.34, and 0.38, respectively.

Thus, considering both the lattice parameter and image analysis results, we estimate the value of x in TiC_x that is in equilibrium with TiB_2 and Ti_3B_4 to be 0.65±0.02.

Runs 3-5 yielded four phases after hot pressing or pressureless sintering. However, upon extended annealing the TiB_2 phase slowly but invariably disappeared and only three phases remained, $TiC_{0.65}$, TiB and Ti_3B_4 (Figure 64(b)), in accordance with the proposed phase diagram. Runs 6 and 7 only yielded two phases namely TiB and TiC_x, with $x < 0.65$ again in accordance with the proposed diagram.

In order to ascertain that the stoichiometries and phase assemblages detected at room temperatures were indeed indicative of the phases present at 1600 °C and did not change during slow cooling in the hot press we compared the X-ray diffraction patterns of the as-hot-pressed samples with the patterns of the samples that were annealed and quenched from 1600°C. No significant changes were observed. This is not too surprising given that TiB_2 and Ti_3B_4 are line compounds and that at 0.65 the stoichiometry of the TiC_x is far enough removed from the edges of the TiC_x phase field so as to preclude its dissociation upon cooling. More general conclusion follows from consideration of

* The boron content in TiC was determined by WDX, using TiB_2 as an internal standard. The total oxygen content in the sample was determined by chemical analysis of three samples (LECO) by NSL Analytic Services Inc., Cleveland, OH.

isometric view of the Ti-B-C phase diagram presented in Figure 19 (after Rudy [100) and Ti-B binary diagram in Figure 23, which lists Ti_3B_4 as an equilibrium phase in this system. It is apparent from combination of Figures 19 and 23 that the revised area of the diagram within the boundaries outlined in Figure 63(b) will not undergo any specific changes on cooling from 1600°C to ambient temperature. Therefore, the suggested revision is equally applicable for all isothermal sections at temperatures lower than 1600°C.

It is obvious from Figure 63, that in the area of interest, the only difference between Rudy's diagram and the one proposed here is the presence of the Ti_3B_4 phase and the line joining that phase to the $TiC_{0.65}$ composition. In the next section we speculate as to why this discrepancy exists.

5.1.2 Non-Equilibrium Compositions

Runs 8 and 9, were carried out, respectively, with a Ti of lesser purity than runs 1-7 and with a $TiC_{0.5}$ that was made via an SHS process also starting from impure Ti. Based on the proposed diagram, these two compositions, that were identical to each other and to runs 1 and 2 in terms of elemental composition, should have had a TiC_x stoichiometry of 0.65. However, in all cases , the stoichiometry of TiC_x was less than 0.65 and tended to vary from run to run. This was taken as unambiguous indication that runs 8 and 9 did not achieve equilibrium. Furthermore, the volume fraction of the Ti_3B_4 phase, as estimated from X-ray diffraction and image analysis was always less than that obtained in runs 1 and 2. For example, the volume fractions of TiB_2, TiC_x and Ti_3B_4 in run 9, with $x = 0.6$, calculated from lattice parameter were respectively 0.42, 0.38 and 0.20. Run 8 represents an extreme case, where no Ti_3B_4 whatsoever was detected even after extended anneals.

The same trends of less Ti_3B_4 content and/or lower values of x were also observed in runs 10 and 11.

Given that runs 1 and 8 were identical except for the purity of the Ti powder (99.99% vs 98.5%, respectively), it is reasonable to assume that the impurities somehow prevented the nucleation and/or growth of Ti_3B_4. The exact nature of these impurities and their role is unclear at this time but preliminary evidence suggests that it may be non-metallic electro-negative impurities such as O, N and Cl. Indeed, Ti powders obtained via chlorine process (99.9% pure) and MER process (98.5% pure with 0.8% O) yielded nonequilibrium final compositions, whereas hydride-dehydride powders (99.99% pure) and Plasma Arc Rotating Electrode processed (under Ar) powder (99+% pure) were found to be sufficiently pure not to effect the attainment of equilibrium. Furthermore, presintering the Ti/B_4C mixtures in a low vacuum at 800 °C tended to reduce the amount of Ti_3B_4. A correlation was also found between the time of presintering and the Ti_3B_4 content. These results could very well explain why Ti_3B_4 was not detected and reported by Rudy [100] despite the fact that its existence had been reported earlier [104, 105].

5.2 Transient Plastic Phase Processing

5.2.1 Dominant processing parameters

Dominant processing parameters and their effects on the microstructure of the produced composites and the attendant properties are summarized in block-diagram shown in Figure 66. Among them, the starting compositions and particle size of the starting powder mixtures were found to determine the final microstructure and properties and thus

will be discussed in the following sections in detail. This discussion implies that the other parameters, pressure-temperature schedules and the initial state of compaction (green density), were chosen such as to assure the attainment of fully dense composites, as explained in the next section. The effect of triaxiality (deformation mode) will be addressed in Sections 5.4.4.

5.2.2 Processing envelope

Temperature and pressure cycles were chosen to ensure the attainment of fully dense composites with compositions close to equilibrium. For this purpose, pressures >40 MPa for coarse starting powders and >60 MPa for fine starting powders were found to be sufficient. These conditions are given by the isoporosity lines in the hot-pressing diagram shown in Figure 67. Heating rates of 10°C/min and lower proved to be optimal to permit densification simultaneous with the reaction. Isothermal segment duration of ≥4 hr at 1600°C was chosen such as the diffusion distance of C at this temperature was of the order of the length scale of the final microstructure and, therefore, this time was believed to be sufficient for attainment of equilibrium composition. The first (optional) low temperature isothermal segment at 800-900°C employed for the 4:1 Ti/B_4C starting composition was found to be important for net shape forming and for removal of residual hydrogen if Ti hydride (4 at% H) was employed.

5.3 Reaction Paths and Microstructural Evolution

5.3.1 Factors effecting reaction path

Among the factors affecting the path of TPPP reactions (see Figure 66) the starting composition is clearly the determining one. The reaction paths for the 4:1 Ti/B_4C starting composition, resulting in the platelet composite, and for the 1:1 $TiC_{0.5}/TiB_2$ starting composition, resulting in the equiaxed composite, are considered separately in Sections 5.3.2 and 5.3.3, respectively. The other factors that were found to be important in this study, the presence of impurities in starting powders and state of compaction (relative density) of the reacting body, are examined below.

5.3.1.1 Effect of Impurities

Impurities can affect the progress of reaction and resulting phase assemblages in two ways. First kinetically, when impurities inhibit or catalyze the reactions of interest. It is well established that minor impurities can strongly influence the nucleation and growth of various phases [96]. The absence of Ti_3B_4 phase in nonequilibrium composites (run 8 in Table VIII) is attributed to such effects. The second possible effect is thermodynamical in nature, when impurities stabilize the non-equilibrium phase assemblages. However, no conclusive evidence of this effect was found in the present study. It should be noted that impurities may effect the studied reactions and the equilibrium only locally if the impurity is not homogeneously distributed in the starting powder mixture, and if it is relatively immobile in a time frame of processing such as sufficiently slowly diffusing species with $D<10^{-14}$ m^2/s at 1600°C. This conclusion is corroborated by the frequent observations of

small TiC_x particles (≤1 μm) found inside Ti_3B_4 grains (as in Figure 68) as if the reaction front "mysteriously" avoided certain locations in TiC_x and proceed normally in the others.

5.3.1.2 Effect of the state of compaction

As found, the state of compaction (relative density) controls the reaction mode (rate-limiting step and the resultant reaction rates) by imposing certain threshold relative density below which the Ti-B_4C system reacts in SHS mode. This effect is illustrated in Figure 69 that shows two samples of the same initial composition 4:1 Ti / B_4C at different compaction states (one was prepared as a loose powder mixture and the other was cold compacted to a green density of 74%) which were reacted in vacuum by heating at 10°C/min to a temperature of 1200°C. Their final shape and phase compositions were distinctly different. The reaction product derived from loose powder (Figure 69(a)) showed signs of an explosive reaction (perhaps of SHS type). This contrast in morphology of the reaction products and their composition is believed to be attributed to the different reaction heat release characteristics in the two samples caused by the differences in the thickness of the diffusion layer separating reactants and the effective heat conductivity of the starting powder mixtures. Both parameters depend strongly on the relative density of the powder mixture [163]. The diffusion layer limiting the reaction rate is more developed in the precompacted powder mixture than in the loose one due to the extensive contacts between Ti and B_4C giving the larger crossection of the diffusion flux. In contrast, the heat conductivity of the loose powder mixture is lower than that of the precompacted sample [164,165]. Consequently, it is expected, that the net heat release = (heat release due to reaction) - (heat loss due to thermal conductivity) in the loose powder is much more intensive than in the precompacted sample and can exceed certain threshold value causing the reaction to propagate in SHS mode.

Noteworthy, this phenomenon is equally applicable to any exothermic system and has been well described in SHS-related studies [163, 166]. Its immediate implication in this work and similar investigations is that to study the reaction sequence, Differential Thermal Analysis (DTA) should be performed not on powders but on compacted samples with densities comparable to those obtained during the processing. Alternatively and more accurately, processing should be interrupted at various stages to study the evolution of composition and microstructure. This approach is employed here.

5.3.2 Platelet Composites

Barsoum and Houng [8] postulated that for the 4:1 Ti/B_4C starting composition, the reaction between Ti and B_4C yields $TiC_{0.5}$ and TiB_2, which in turn reacts to form the final phases according to:

$$2\,TiC_{0.5}\,(TPP) + 2\,TiB_2\,(RP) \Rightarrow 0.333\,Ti_3B_4 + 1.667\,TiC_{0.6} + 1.333\,TiB_2 \qquad \{4\}$$

This reaction sequence was proposed on the basis of DTA on loose powders. Although DTA on powders has been routinely employed in similar cases for reaction studies, it is misleading for exothermic Ti/B_4C mixtures, because the reaction path and the final composition depend on the state of compaction (i.e. the relative density) as described in the previous section. In particular, the geometry of the diffusion layer and the effective heat conductivity are significantly different in the hot press samples (which were densified in the first step of TPPP, before onset of the reaction) when compared to the loose powders commonly used in DTA. The results reported in this study, clearly indicate that the reaction sequence is more intricate than suggested by reaction {4} in that TiB is yet another intermediate phase.

The model for the microstructural evolution of the 4:1 Ti/B_4C composition proposed here is shown schematically in Figure 70. The major assumption of the model is that the evolution of microstructure is governed by the diffusion of C and B into Ti. The diffusivity of C is significantly greater than that of B in accordance with the literature data [167, 168]. For example at 1200 °C, the diffusivity of C in Ti is about 3 orders of magnitude higher than that of B in Ti [167, 168]. It should be pointed out that a detailed analysis of diffusion in this complex system is not practical because of the need to determine a large number of diffusion constants in the various phases, and their temperature and concentration dependencies.

During the initial stages, carbon diffuses rapidly from the B_4C areas into Ti, forming $TiC_{0.5}$ and leaving behind areas of high B activity. This is supported strongly by our XRD results that indicate that $TiC_{0.5}$ is one of the first intermediate phases identified and that the volume fraction of $TiC_{0.5}$ phase remains relatively constant after the initial reaction period (800°-1200°C).

The B atoms will also dissolve and diffuse into the $TiC_{0.5}$. Once the activity of B exceeds the solubility limit, the following displacive reaction occurs:

$$TiC_{0.5} + [B] \Rightarrow TiB + 0.5\,[C] \qquad \{5\}$$

Given the sluggish diffusivity of B (compared to C), however, TiB forms only in the vicinity (within 15-20μm) of the original B_4C fields as observed microstructurally and confirmed by WDX mapping of boron in the 1200°C-interrupted-run sample. Unreacted Ti and $TiC_{0.5}$ provide effective sinks for the rejected C according to

$$0.5[C] + Ti \Rightarrow TiC_{0.5} \qquad \{6\}$$

$$x\,[C] + TiC_{0.5} \Rightarrow TiC_{0.5+x} \qquad \{7\}$$

This reaction scheme is consistent with the observation that TiB is one of the major constituents of the reaction product at lower temperatures. At temperatures above 1300 °C, B further reacts with the TiB phase to form TiB_2 according to

$$[B] + TiB \Rightarrow TiB_2 \quad \{8\}$$

In the temperature range 1450°-1600°C, the nucleation and growth of the "small" Ti_3B_4 platelets occurs by further diffusion and reaction of B with TiB according to:

$$3\,TiB + [B] \Rightarrow Ti_3B_4 \text{ ("small" platelets)} \quad \{9\}$$

Both reactions {8} and {9} explain the increase in relative amount of TiB_2 and Ti_3B_4 at the expense of TiB observed in Figure 47(b). Neither of these reactions affects the TiC_x content as observed (Figure 47(a)). It is worth noting, however, that the stoichiometry of the TiC_x remains fixed at 0.5 as long as there is unreacted Ti, i.e. up to 1300 °C (Figure 47(a)). This also proves indirectly that the diffusivity of C in Ti is rapid enough to keep the concentration of C uniform and fixed at that of the Ti/TiC_x equilibrium, i.e. $x = 0.5$. It is only when the last traces of Ti are consumed that the content of C in the TiC_x increases to its final equilibrium value of 0.65 (see Section 5.1.1).

Finally, as the system approaches equilibrium during the 1600°C soak, TiB reacts with TiB_2 to form the "large" platelets, according to:

$$2TiB + TiB_2 \Rightarrow Ti_3B_4 \text{ ("large" platelets)} \quad \{10\}$$

which explains the slight decrease in the TiB_2 and complete disappearance of the TiB phase content during the 1600 °C soak (Figure 47(b)).

Based on these results we can trace the reaction path in this system to be $Ti\text{-}TiC_{0.5}\text{-}TiB\text{-}Ti_3B_4\text{-}TiB_2\text{-}B_4C$. This reaction sequence is in accord with the results of Mogilevsky et al. [169], who determined the reaction path in the same system from $Ti\text{-}B_4C$ diffusion

couples to be Ti-$TiC_{0.5}$-TiB-TiB_2-B_4C (1000°-1200°C). Mogilevsky et al. also observed that the thin inner layer of the coating on B_4C was carbide free and contained only borides, whereas the thicker outer layer was a mixture of TiC_x and TiB, which is again consistent with our results.

5.3.3 Equiaxed Composites

The microstructural evolution in the "equiaxed" composites is less complicated and is believed to occur by the formation of Ti_3B_4 at the interface between the TiB_2 and $TiC_{0.5}$ by the following displacive reaction:

$$2\,TiC_{0.5} + 0.92\,TiB_2 \Rightarrow 0.46\,Ti_3B_4 + 1.54\,TiC_{0.65} \qquad \{11\}$$

The proposed mechanism for this reaction that invokes transport of B and C rather than mobility of Ti is shown schematically in Figure 71. It is believed that the B atoms diffuse from the TiB_2 into the $TiC_{0.5}$, forming Ti_3B_4 and displacing the C atoms, which in turn increases the C/Ti ratio to its equilibrium value of 0.65. For reasons that are not entirely clear, but speculated upon below, the Ti_3B_4 phase in this case does not nucleate and grow as plates but rather is roughly equiaxed.

5.3.4 Morphology of the Ti_3B_4 Phase

The arguments presented above lead us to believe that TiB is a necessary precursor for the formation of the Ti_3B_4 platelets. The complete absence of intermediate TiB phase and Ti_3B_4 platelets in final microstructure when starting with 1:1 $TiC_{0.5}/TiB_2$ composition is consistent with this hypothesis. Furthermore, we note that TiB and Ti_3B_4 have the same

orthorhombic crystal structure and their shortest lattice parameters (b_{TiB} = 0.305 nm, and c_{Ti3B4} = 0.304 nm) are almost identical. XRD results show that the intensities of both TiB and Ti_3B_4 peaks do not quite match the standard relative intensities, and actually point to distinct (020) and (002) preferred orientations, respectively. These orientations correspond to the direction of the matching lattice parameter, the shortest one for both phases. Such a preferred orientation in the direction of the shortest lattice parameter is often observed during the diffusion growth of compounds [96], and has already been reported for TiB [169].

5.4 Densification-Related Specifics of Microstructural Evolution

5.4.1. Commonality in Densification of Platelet and Equiaxed Composites

Densification of platelet and equiaxed compositions exhibits at least one feature in common in that maximum densification rate is observed at about 1200°C for both compositions (compare Figures 50 and 51) and is attributed to the role of $TiC_{0.5}$, one of the major constituents for both compositions at this temperature range (see Figure 47 for platelet composition). At this low homologous temperature (~$0.55T_m$ for $TiC_{0.5}$, $0.39T_m$ for TiC, and $0.37T_m$ for TiB_2) contribution of diffusion-driven creep and sintering can be practically neglected, especially considering the relatively high attendant strain rates of ~$2x10^{-4}$ s^{-1}, more characteristic for deformation-driven densification [170] (see Figure 17(c,d)). The reverse dependence of applied pressure necessary to attain full density on the starting powder particle size shown in Figure 67 is another indication of deformation-driven densification mechanism in these composites. Finally, note that $TiC_{0.5}$ is expected to be very "soft" at 1200°C. This estimate is based on the results of Miracle and Lipsitt [99],

who reported the significant decrease in yield stress with the decrease of x in TiC_x and measured yield stress of ~60 MPa for $TiC_{0.66}$ at 1200°C (curve fit of their data with power function and extrapolation on x=0.5 gives yield stress of ~14 MPa for $TiC_{0.5}$ at 1200°C). Accordingly, the common trend observed in densification of the two different compositions is attributed to plastic flow of substoichiometric $TiC_{0.5}$, therefore, substantiating the previously suggested role of $TiC_{0.5}$ as transient plastic phase.

5.4.2. Specifics of Densification in Platelet Composites

In densification of platelet composites, however, in addition to plastic flow of Ti and subsequently TiC_x, the other important mechanism should be considered, namely, continued contribution of particle rearrangement "compensating" for the large and inhomogeneous negative volume changes of ~14% which accompany the reaction between Ti and B_4C. This mechanism is believed to be operative at least until B_4C is completely consumed by the reaction (at about 1400°-1500°C) and is suggested by the model of microstructural evolution presented in Figure 70 which implies that internal porosity generated by the reaction is predominantly localized within B_4C fields (or more accurately B_xC since its stoichiometry may change in the course of the reaction from $x \leq 4$ to $x \approx 10$ because of higher diffusion rate of C than B). According to this model, discussed in Section 5.3.2 and 5.4.2, B and C are escaping from B_4C, invariably leaving pores behind by virtue of volume conservation. As the reaction progresses, residual porosity should be seen in the original B_4C locations. Indeed, the concentration of porosity in these areas are clearly observed in the samples from the interrupted runs (Figures 45(b) and (d)). However, upon completion of the reaction nearly pore-free TiB_2 fields were found in the original locations of B_4C (compare Figures 44(a) and 45(a)). Since the diffusion of Ti is sluggish, in order to produce fully dense body, the conversion of initially B_4C fields into TiB_2 fields should be necessarily aided by rearrangement of newly formed TiB_2 grains to

replace pores left by decomposition of B_4C. The resulting densification process could be, therefore, visualized as crashing of a porous "cake" formed upon reaction by combination of comminution and plastic yielding, wherein reaction layers of TiB_2 are impressed into the space initially occupied by B_4C.

Plastic flow and particle rearrangement are believed to be the predominant mechanisms for the most part of densification process responsible for increase of relative density to ~95%. The remaining porosity, however, is completely eliminated during high temperature step, when diffusion-driven sintering mechanisms have taken over.

5.4.3 Effect of Starting Powder Size in Platelet Composites

The striking feature of the microstructure of the platelet composite shown in Figure 44(a) is the extent of non-homogeneity and a morphological texture of the microstructure. This is attributable to the difference in particle sizes between the Ti and B_4C. In most of the experiments coarse Ti powders (~43 μm) and fine B_4C powders (~6 μm) were used. When starting from such mixtures, the small nondeformable B_4C particles tend to fill the interstitial sites between the larger Ti particles (see Figure 45(a)) effectively forming agglomerates of the size of the interstitials. During compaction the shape of the interstitials changes and their dimension normal to the compaction axis increases. The fine B_4C particles conform to the changing shape of the interstitials resulting in the observed morphological texture. Given the relative sluggishness of the diffusion of B, it is not surprising that the boron containing phases (TiB, TiB_2, Ti_3B_4) are localized around the original B_4C fields.

Based on this model it is clear that starting with smaller Ti should result in a more homogenous microstructure. This is confirmed by the micrographs shown in Figure 72(a-d). Reducing the average Ti particle size to 20 μm resulted in a more homogeneous microstructure (compare Figures 72(a) and (b)). Starting with an even finer (~8 μm) hydride Ti powder resulted in further and distinct improvement in the scale of microstructural homogeneity (compare Figures 72(a) and (c)). Shown in Figure 72(d) is the composite fabricated from 5 μm spherical Ti powder which is devoid of Ti_3B_4 phase, and only comprises $TiC_{0.5}$ and TiB_2 in roughly equal amounts. The absence of Ti_3B_4 in this composite was attributed to the low purity of the spherical Ti powder (see Section 5.1.2).

Note that composites produced from fine Ti powders (see Figure 72(c) and (d)) exhibit nearly "interpenetrating phase" microstructures, where black TiB_2 fields and gray Ti_3B_4 fields seem to be topologically interconnected with each other in an almost continuous network similarly to interpenetrating phase composites reviewed recently by Clarke [43]. Though the extent and implications of the observed "marginal interconnectivity" are not specifically studied in this work, however, it is reasonable to expect the potential for increase in creep resistance of TiC_x-TiB_2 and $TiC_{0.65}$-TiB_2-Ti_3B_4 composites through interlocking of TiB_2 fields (or TiB_2-Ti_3B_4) resistant to plastic deformation even at very high temperatures [114]. This argument is supported by indications in the literature that interpenetrating networks of ductile phase (TiC_x above DBTT in our case) and stiff phase (TiB_2 in our case) enhance structural reliability and creep resistance of ceramics [5, 13, 43].

5.4.4 Effect of deformation mode

Since the densification process associated with the employed processing technique is believed to be predominantly deformation-driven with relatively high attendant strain rates (~10^{-4} s^{-1}) and strains along the compaction axis (0.4-0.5), the mode of deformation (triaxiality), is expected to affect strongly the densification and microstructure development. Of particular interest is to deconvolute the effects of shear and isostatic pressure on the development of microstructure in the platelet composites, in which processes of agglomeration and morphological texture formation were found to occur during reactive hot-pressing. A value of triaxiality, X, ($X=P/\Sigma$, where P-hydrostatic pressure and Σ-equivalent stress) will be used below to describe quantitatively the relative contributions of shear and isostatic pressure components. For example, X=0 for pure shear, X=1/3 for compression, and $X=\infty$ for isostatic pressure (HIP-ing). Triaxiality of uniaxial compaction (hot-pressing) is in the range of 1-3.

Qualitative understanding of the relative effects of shear and hydrostatic components of deformation was obtained by comparing the microstructures of the hot-pressed composite and the composite HIP-ed at approximately the same nominal pressure. To assure the objective comparison green bars were cold-pressed from the same starting powder mixture (4:1 Ti (43 μm)/B_4C) and subsequently processed by HIP-ing ($X=\infty$) and hot-pressing (X=1-3) using the similar temperature-pressure schedules shown in Figure 73. The resulting microstructures are shown in Figure 74 (a) for HIP-ed sample and in Figure 74(b) for the transverse and 74(c) longitudinal cross-sections of the hot pressed sample. In order to provide comparison with the low-triaxiality conditions ($X\leq0.33$) the microstructure was obtained (see Figure 75) for the material that had flown in the gap between the die cavity and the pushing rod.

Apparent from comparison of the micrographs in Figures 74 (a) and 74(b,c) is noticeably higher porosity in the HIP-ed sample. In addition, the microstructure of the hot-pressed sample exhibits higher scale of inhomogeneity, specifically size and separation of TiB_2 fields as well as size of platelet-free $TiC_{0.65}$ fields seem to be higher in the hot-pressed sample (both in the transverse and longitudinal cross-sections) than in the HIP-ed one. Partially the observed effect can be attributed to the changes in aspect ratios of these microstructural inhomogeneities in the plane normal to the compaction axis due to formation of the morphological texture by the mechanism described in Section 5.4.2, however, the proposed mechanism (for the development of morphological texture) can hardly explain all the aforementioned microstructural differences. For example, this mechanism implies the reasonable correspondence in the scale of microstructures observed at earlier and later stages of processing. Shown in Figure 74 (d) is the micrograph of the sample obtained in the hot-pressed run interrupted at 800°C (before the onset of reaction). Comparison of this micrograph with the ones presented in Figures 74 (a) and (b,c) shows that the microstructure of the HIP-ed (Figures 74(a)) sample conforms well to the scale of microstructure found in the run interrupted before the onset of reaction, whereas hot-pressed sample (Figures 74(b,c)) yields seemingly higher scale of microstructural inhomogeneity in the final microstructure (both in the transverse and longitudinal cross-sections) than the one observed prior to reaction. These effects are even more pronounced in micrograph shown in Figure 75 where nearly laminate-type microstructure, comprised of alternating layers of TiB_2-Ti_3B_4 and $TiC_{0.65}$, was produced in conditions analogous to forging ($X \leq 0.33$) resulting from a flow of the reaction product into a narrow cavity.

Based on these observations the effect of shear is believed to be two-fold: first, shear facilitates densification driven by plastic flow and particle rearrangement; second, combined with the reaction synthesis, shear promotes morphological texture formation, and "coarsening" of microstructural inhomogeneities. In contrast, isostatic pressure (HIP-ing),

though, less effective in the process of densification coupled with particle rearrangement, does not cause additional agglomeration and the resulting "coarsening" of microstructural inhomogeneities seen in hot pressed samples. The observed phenomena are not well described in the literature. Furthermore, the dominating view is that hydrostatic pressure is the component of deformation primarily responsible for pore closure. However, this argument does not account for important contribution of particle rearrangement, which is argued here to be facilitated by shear rather than by hydrostatic pressure. It is combination of particle rearrangement and plastic flow that is believed to cause the de-homogenizing effect of shear observed in this study.

This phenomenon is believed to be attributable to the combined effects of plastic flow and particle rearrangement occurring simultaneously with the reaction synthesis. Interaction of these processes results in (i) a redistribution of particles of the constituent phases in the reacting compact, and (ii) the consequent change in shape of the reacting phases and associated changes in dimensionality of diffusion processes affecting the mass-transport rates and the resulting spatial distribution of activities of different components. Contributions of the deformation and the shear-driven particle rearrangement changing the shape of the reacting phases and so shape of the corresponding diffusion interfaces, and the resultant effect of the changed shape of these interfaces on mass-transport rates of the reacting species (known in the literature as a diffusion dimensionality effect [96, 171]) are believed to provide a reasonable explanation for the most part of the aforementioned microstructural observations. In addition, the concurrent reaction can amplify the observed topological effect of shear on the final microstructure by responding non-linearly to the argued trends in the redistribution of activities. The term "responding non-linearly" is used here to describe the non-linear effects (instabilities) in multicomponent diffusion-controlled reactions not very well understood but described in the literature [96, 171].

It is clear from the arguments presented here that, besides values of strains and strain rates (accurately described by corresponding tensors) and flow and diffusion properties of the participating phases, the governing parameter is the initial particle size. This argument of grain size dependent flow is confirmed as well for the equilibrium equiaxed composites. Compared in Figures 76(a) and 76(b) are the microstructures of the two equilibrium equiaxed composites produced from the Ti/0.5C/TiB2 (molar ratios) starting mixtures with different sizes of Ti powder, 43 μm Ti and 20 μm, respectively. Apparent from this comparison, that the inhomogeneity in distribution of TiB_2 grains was clearly removed when finer Ti powder was used.

However, the suggested explanations of this interesting phenomenon are highly speculative at this point. The experiments designed to exact and understand this effect will be listed in Chapter 7 (Future Work).

5.5 Structure - Properties Relations

5.5.1 Effect of the third phase - Ti_3B_4

As apparent from Table VIII and Figure 60 equilibrium (three-phased) microstructures exhibit higher fracture toughness than the nonequilibrium (two-phased) one. These results are consistent with fracture and crack morphology observations presented in Figures 52-54. Much more pronounced interaction of cracks with microstructural features found in equilibrium (three-phased) microstructures (compare Figures 52(b) and 53(b) with Figure 54(b)) indicates that the presence of Ti_3B_4 phase promotes crack deflection and branching which is believed to be attributed to thermal

expansion mismatch and associated residual microstresses which cause the crack to circumvent local, highly stressed regions [34, 172]. Despite the similar thermal expansion coefficients of TiC and TiB_2 (see Table II), the thermal expansion mismatch stresses can exist in nonequilibrium (two-phased) composites around the large TiB_2 grains due to their thermal expansion anisotropy (see Table II). Yet, since the volume fraction of these large grains (>>5μm) is relatively low, their potential effect on toughness is expected to be negligible, whereas their negative effect on strength has been clearly demonstrated in this work and will be discussed later.

5.5.2 Effect of platelet morphology

A comparison of the properties measured for the equiaxed and platelet composites (equilibrium compositions) indicates the platelet composite has a higher flexure strength (630 MPa for platelet composite vs. 515 MPa for equiaxed composite) and a higher K_{IC} (5.3 MPa$\sqrt{m}$ for the platelet composite vs. 4.4 MPa$\sqrt{m}$ for the equiaxed composite) This result leads us to believe that the platelet morphology of the Ti_3B_4 phase is beneficial to these properties. Although, the fracture surfaces in both the equiaxed and platelet composites (Figures 52(a) and 53(a)) exhibit a mixed intergranular-transgranular fracture mode, the fracture surface of the platelet composite is, however, more roughened in the $TiC_{0.65}$ regions which contain bushes of "small" Ti_3B_4 platelets. In addition, though crack deflection at phase boundaries can be seen in both composites, it is more extensive in the platelet composites and occasionally crack bridging by the Ti_3B_4 platelets and platelet pull-out are observed.

These noticeable effects of platelet morphology on the attendant fracture characteristics are reduced by inhomogeneity of the "platelet" microstructure and the corresponding inhomogeneity of fracture and crack morphology in these composites.

In the "platelet" composites, crack propagation characteristics through the TiB_2 fields and $TiC_{0.65}$ fields are observed to be quite different from each other (compare Figures 52(b) and 52(c)) The cracks in $TiC_{0.65}$ fields exhibit much more tortuosity and branching, with both equiaxed $TiC_{0.65}$ grains[2] and Ti_3B_4 platelets contributing to crack deflection. Furthermore, some of the relatively thicker platelets (thickness ≥ 1 μm) among the "small" Ti_3B_4 platelets in the $TiC_{0.65}$ fields seem to contribute to platelet crack bridging and/or pullout. However, since the number of these sufficiently thick platelets is relatively low in the produced platelet composite, we have not observed a drastic improvement in the fracture toughness of the platelet composite by crack bridging and pull-out when compared to the equiaxed composite. The observed increases, reported in Table VIII, between the platelet and equiaxed composites are therefore largely attributed to enhanced efficiency of crack deflection by Ti_3B_4 platelets compared to the equiaxed Ti_3B_4 grains. The observed differences in the crack propagation characteristics in the TiB_2 fields and the $TiC_{0.65}$ fields of the platelet composite (Figures 52(b) and 52(c)) are attributed to the differences in the magnitude of residual stresses in these regions caused by mismatches in thermal expansion coefficients and elastic moduli, and to differences in the strengths of the interfaces between these phases and Ti_3B_4 platelets.

It should be noted that a maximum fracture toughness of about 10 MPa$\sqrt{m}$ has been reported in literature for in-situ reinforced ceramics toughened by crack deflection and

---

[2]These grains are most probably $TiC_{0.65}$, however, based on their sometimes greyish contrast in backscattered micrographs (apparently due to higher concentration of low-Z element such as C or B) and the results of WDX mapping, it appears that some of them contain boron as well. The possibility that these grains are not TiC_x but rather TiB_xC_y phase similar to one reported by Holleck et al. [6] is not ruled out at this time.

bridging, e.g. the platelet reinforced ZrB_2/ZrC/Zr composites produced by the DIMOX™ process [5] and the self-reinforced silicon nitrides [1]. Therefore, this value may be considered as an intrinsic limitation of this toughening mechanism in platelet reinforced ceramic-ceramic composites. The maximum fracture toughness value reported in the present study for the platelet composite is about 6 MPa$\sqrt{m}$. This value is consistent with the fact that only crack deflection was observed in the composites studied here and that there were very few indications of crack bridging and platelet pull-out.

5.5.3 Effect of microstructural homogeneity (for platelet composites)

The distribution of the phases and their grain sizes are also expected to strongly influence the mechanical properties. As described earlier, it is possible to control the grain sizes and improve microstructural homogeneity of the produced composites by using finer starting powders. The platelet composite shown in Figure 72(a) was produced using a coarse high purity Ti powder (~43 μm) with a fine B_4C powder (~6 μm) and exhibits significant inhomogeneities in the distribution of the different phases in the microstructure. As described earlier in Section 5.4.2, a finer Ti powder (average particle size ~8 μm) obtained by jet-milling was used to produce a "refined" platelet composite (see Figure 72(c)). A comparison of the flexural strengths and fracture toughnesses of the refined platelet composite with those for the "coarser" platelet composite is provided in Table VIII. It is observed that the flexural strength of the refined platelet composite increased to 800 MPa (from 630 MPa), while the fracture toughness decreased slightly to 5.3 MPa$\sqrt{m}$ (from 5.8 MPa$\sqrt{m}$.) It should also be noted that the scatter in the measurements decreased significantly for the refined microstructure.

Comparison of Figures 72(a) and 72(c) reveals three important differences between the microstructures of the refined and coarse platelet composites: (i) There is a significant reduction in the length scale of the TiB_2 fields in the refined platelet composite. (ii) The refined microstructure is devoid of the platelet-free $TiC_{0.65}$ fields. (iii) The thicknesses and lengths of the Ti_3B_4 platelets seem to be slightly lower in the refined platelet composite. In the "coarser" platelet composite the average length scale of microstructural inhomogeneities in the direction normal to the tensile surface (e.g. the length scale of the textured TiB_2 fields) is roughly in the range of 20-70 μm. This length scale agrees reasonably with the calculated critical flaw size (27 μm for surface crack and 54 μm for volume crack; see Table VIII). While a similar comparison between the critical flaw size and the length scale of TiB_2 fields was not possible for the refined platelet composite (because the TiB_2 fields are not as distinctly shaped), we believe that the increased homogeneity of the microstructure has resulted in a reduced critical flaw size, which in turn yielded higher flexural strength for this composite. The small decrease in the fracture toughness for the refined platelet composite is believed to be a result of the reduction in thickness and length of the Ti_3B_4 platelets, which tend to lower the ability of this platelets to deflect cracks and induce crack bridging or platelet pull-out toughening.

5.5.4 Effect of grain size (for nonequilibrium equiaxed composites)

In order to study the effect of the final grain size on the attendant flexural strengths, the fully dense "refined" non-equilibrium equiaxed composites were produced, containing $TiC_{0.5}$ and TiB_2 with roughly equal grain sizes in both phases (the micrograph of the original coarse $TiC_{0.5}/TiB_2$ composite is shown in Figure 44(c)). The refinement of the microstructure was accomplished by wet ball-milling of the starting powder mixture using WC-10%Co grinding media. The measured room temperature flexure strengths of the

produced non-equilibrium equiaxed composites were plotted against the reciprocal of the square root of the average grain size in these composites (the two phases in these composites had essentially equal grain sizes), and are shown in Figure 55. This figure indicates a good correlation for the flexure strength against (grain size)$^{-0.5}$, which seems to suggest that the critical flaw size in the non-equilibrium equiaxed composites scales with the average grain size (see also Table VIII). This dependence can be specifically attributed to the effect of coarse boride particles as critical flaw sites and requires further exploration.

5.5.5 Effect of borides volume fraction (for nonequilibrium equiaxed composites)

To examine the effect of the borides' volume fraction on the flexural strength at room temperature, fully dense composites were fabricated, comprising 20 and 30 vol% of borides (predominantly TiB_2) and TiC_x, x=0.56-0.57). The grain sizes in these composites (an average grain size of the TiB_2 phase was 7 μm, with the largest grains being of about 20 μm in diameter) were roughly the same as the grain size in the original coarse non-equilibrium equiaxed composite with microstructure shown in Figure 44(c)). This is due to the fact that the same starting powders with the same particle sizes, but different molar ratios of $TiC_{0.5}/TiB_2$, were employed. The room temperature flexural strengths of the resulting composites are plotted against the corresponding volume fraction of borides in Figure 77. This figure reveals that the flexural strength of titanium carbide-titanium boride composites decreases proportionally to the volume fraction of the borides. From the observed trends in Figures 55 and 77, we argue that the critical flaws in these composites originate on the largest TiB_2 grains and thereby dominate their flexural strengths. This argument is supported by the known tendency of coarse-grained TiB_2 ceramics to exhibit spontaneous microcracking due to thermal expansion anisotropy of TiB_2 (~40% difference between CTEs along **a** and **c** crystal axis [119]).

5.5.6 Temperature Dependence

5.5.6.1 Strength

The major factors that are expected to determine the high temperature properties as well as oxidation resistance of the produced composites is the presence of the boron-containing phases (TiB_2 and Ti_3B_4) in their microstructure and the stoichiometry of titanium carbide constituent. The effects of these factors on the flexural strength at high temperatures are considered in this section.

Effect of boron

The presence of the boron-containing phases (TiB_2 and Ti_3B_4) in the studied composites was found to exert a strong beneficial effect on their high temperature properties. Note that the composites tested in our study had significant amounts (34-44 vol%) of TiC_x (x ranging from 0.5 to 0.65). Miracle and Lipsitt [99] have reported yield strengths of about 250 MPa for $TiC_{0.66}$ at 1000°C, which is substantially lower than the flexure strengths measured in our study at this temperature (see Figure 57). Furthermore, it has been reported [99, 134] that substoichiometric TiC_x undergoes a ductile to brittle transition at about 600°-800°C. We attribute the absence of softening in the strengths of the composites studied here to the strengthening effect of the borides. The exact mechanism of this strengthening effect is not presently apparent. We, however, believe that the strengthening effect is due to a solid solution of ~1.5 at% of boron in TiC_x (determined by

WDX with TiB_2 standard). This conclusion is consistent with the results reported in the literature [106, 136, 138] and was substantiated in the present study by microhardness measurements of individual phases. The microhardness of the $TiC_{0.65}$ phase in the equilibrium composites was measured to be 20-24 GPa (100 g load), which is noticeably higher than a values of 13-18 GPa (loads of 100-1000g) estimated by extrapolation of the data available in the literature for microhardness of monolithic TiC_x [81, 99, 106] onto x=0.65. Similarly, the microhardness of the $TiC_{0.5}$ phase in the non-equilibrium composites, determined to be 15-16 GPa (100 g load), is noticeably higher than microhardness of monolithic $TiC_{0.5}$ measured to be 11±2 GPa (300 g load) for fully dense material fabricated in this study by hot-pressing of Ti-0.5C powder. Note that the latter value is in agreement with the extrapolated values of 10-13 GPa for the loads in the range of 100-1000g.

To examine the effect of the borides on the high temperature properties, the variation of flexural strength with temperature was determined for the composite comprised of 80 vol% of $TiC_{0.57}$ (the rest being titanium borides) described earlier. The flexure strength of this composite was measured to be about 520 MPa at room temperature and 500°C, but dropped to 320 MPa at 1000°C. These results once again indicate that the borides play a significant role in the high temperature properties of the composites studied here by extending their softening temperature after which the plasticity of the carbide phase dominates the mechanical properties.

Plotted against temperature in Figure 78 is the high temperature flexural strength of the refined non-equilibrium equiaxed composite with the room temperature flexural strength shown in Figure 55 to be 700 MPa. A significant drop in strength was observed in this composite at 1000°C compared to the room temperature value, quite unlike the composites shown in Figure 57, and specifically, surprisingly different from the composite designated

as non-equilibrium equiaxed in this figure (and also added to Figure 78 for contrast) produced from the same powders, however, simply mixed by V-blending. It was found that in the process of reducing the particle sizes in the starting powder by ball-milling, about 0.2 wt.% of Co was introduced into the mixture due to wear of WC-Co grinding media containing 10 wt.% Co. We believe that the introduction of this impurity results in a grain boundary film, and the softening of this grain boundary film at high temperatures is responsible for the drop in strength at 1000°C seen in Figure 78. The deteriorating effect of a grain-boundary impurity films on high temperature strength of polycrystalline TiC is well documented in the literature [99, 134, 135].

Effect of stoichiometry

To elucidate the effect of stoichiometry on the high temperature properties the 67 vol% $TiC_{0.9}$-33 vol% TiB_2 composite was produced using the TPPP technique (see Section 5.6.2). Based on the previously reported mechanical properties of substoichiometric titanium carbide [99], the higher the C/Ti ratio (x) in the TiC_x constituent, the better high temperature performance may be anticipated. Therefore, non-equilibrium equiaxed composites comprised of $TiC_{0.5}$ (44 vol%) and TiB_2 (56 vol%) were expected to have inferior high temperature properties relative to $TiC_{0.9}$-composite. The variations of flexural strength with temperature for both composites are compared in Figure 79. For comparison the flexural strengths of $TiC_{0.57}$-composite (20 vol% borides) are also shown in this plot. This comparison seems to suggest that the favorable effect of borides on strength at high temperatures is matching the effect of higher stoichiometry of the TiC_x constituent. Specifically, high volume fraction of TiB_2 (or the resulting solid solution of boron in $TiC_{0.5}$) appears to extend the softening temperature in the fabricated composites as effectively as the higher stoichiometry of $TiC_{0.9}$.

5.5.6.2 Fracture Toughness

The fracture toughness of both the equilibrium equiaxed and the refined equilibrium platelet composites in Figure 60 is found to first decrease with temperature up to about 500°-750°C and then increase with temperature reaching at 1000°C values slightly above the room temperature ones. As shown below, the observed trends in fracture toughness as a function of the temperature seems to corroborate the arguments of thermal expansion mismatch driven crack deflection and strengthening effect of borides at high temperatures presented in Sections 5.5.1 and 5.5.6.1, respectively.

As discussed earlier, crack deflection is the main toughening mechanism at ambient temperature in the composites studied here. The crack deflection mechanism in multi-phased composites is largely influenced by the residual stresses introduced during processing due to the differences in thermal expansion coefficients of the different phases [31, 172]. These residual stresses are lowered at elevated temperatures, and consequently the contribution from crack deflection to toughness of the composite is also lowered. The decrease in residual stresses with temperature has been previously reported for SiC-whisker-reinforced alumina [31]. At very high temperatures, the toughness of the composites studied here is expected to increase due to plasticity of the $TiC_{0.65}$ constituent above its brittle to ductile transition temperature. These opposing trends of fracture toughness at low and high temperatures explain the observed trends in Figure 60.

Both the small extent of the observed increase in the fracture toughness of the studied composites at 1000°C and the fact that the bending tests at the same temperature have not shown any plasticity indicate that at this temperature the studied composites can

exhibit only microplasticity. The fact that the considered temperature is significantly higher than the reported value of ~700°C for DBTT of $TiC_{0.66}$ [99] and yet no indications of macroplasticity has been observed once again attest to the strengthening effect of borides extending the softening temperature after which the plasticity of the carbide phase dominates the mechanical properties.

5.5.7 Thermal Shock Resistance

The critical temperature change (ΔT_c) was measured to be 330°C for the refined platelet composite, and about 350°C and 450°C for the refined non-equilibrium equiaxed composites with grain sizes of 4 and 2 μm, respectively. Clearly, the obtained ΔT_c values depend on the size of the specimen tested. The simple thermoelastic analysis [173] gives this dependence as

$$\Delta T_c=(\sigma_t(1-\nu)/E\alpha)*F(k/rh)=(\sigma_t/\sigma_{fl})*[\sigma_{fl}(1-\nu)/E\alpha)]*F(k/rh) \quad (20)$$

where σ_t - tensile strength, σ_{fl} - flexural strength, n - Poisson's ratio, α - thermal expansion coefficient, E - elastic modulus, F - function of (k/rh), k - thermal conductivity of the specimen, r - half-thickness of the sample, h - heat transfer coefficient of a quenching media. For sufficiently large samples ΔT_c is better approximated by thermoelastic parameter $R=\sigma_{fl}(1-\nu)/E\alpha$, the values of which, computed for the tested composites, are given in Table IX.

Two interesting effects were observed in thermal shock susceptibility of non-equilibrium equiaxed composites: (i) grain size dependence of ΔT_c (composites with finer grain size and, hence, higher strength were found to exhibit higher values of ΔT_c); and (ii)

consistent increase of ~9% in strength of 2μm-grain non-equilibrium equiaxed composite attained for specimens quenched from temperatures in the range of about 400°-450°C. The correlation of ΔT_c with the strength was previously reported [174, 175] and was attributed to the corresponding reduction in critical flaw size. However, according to Eq.20, for the same material the percentage increase in strength should be equal to the resulting percentage increase in ΔT_c, provided the other relevant material properties and sample sizes are maintained the same. Whereas, comparison of thermal shock susceptibility of 4μm-grain and 2μm-grain composites shows that ~28% increase in ΔT_c far exceeds 13% increase in room temperature strength measured for these composites.

This seeming discrepancy could be cleared if we consider why composites quenched from the temperatures above 400°C but below 450°C consistently exhibit higher strength compared to the strength of the same material, not subjected to heating and consequent quenching. The higher strength (870 MPa) exhibited by the heat-treated specimens is believed to be related to microstructural flaw corresponding to grain size, whereas the room temperature strength (790 MPa) measured in regular specimens may be attributable to surface flaw related primarily to surface finish. Our arguments in support of "surface healing" effect in thermal shock tests of 2μm-grain composite are the following: A critical flaw size of ~9 μm for this composite (see Table VIII) is significantly higher than its average grain size and close to the roughness of a surface finish of the tested specimens (6 μm). Thus, it is reasonable to assume that the exhibited strength is indeed limited by the surface flaw. Then the observed consistent increase of about 9% in strength attained for specimens annealed for 10-12 min and consequently quenched from temperatures of 400°-450°C may be attributed to the change in the surface condition induced by this heat-treatment. This beneficial surface modification is most probably related to the thin oxide layer forming on the surface during heating and quenching. Indeed, a goldish tint manifesting the formation of thin oxide film was observed in the specimens quenched from

the temperatures above 400°C. This layer may very well blunt the surface flaws, removing the surface limitation of strength. Apparently in agreement with this speculation, is the fact that the resulting strength of the heat-treated specimens (870 MPa) conforms better than strength of regular specimens to linear strength-(grain size)$^{-0.5}$ dependence plotted in Figure 55.

Since, as we believe, this heat treatment shifts the control of the strength from surface finish related flaw to microstructural flaw thus exposing the intrinsic material behavior, we would expect that the resulting strength conforms better to strength-ΔT_c relation expected from Eq.20. Indeed, the increase in strength of 24% observed in heat-treated specimens of 2μm-grain composite compared to 4μm-grain composite is in excellent agreement with the measured percentage difference in ΔT_c of ~28%. Equivalently, based on the computed thermal shock parameter R for the equiaxed composite of the same strength as quenched specimens, $\Delta T_c = R*F$ is calculated to be 440°C (F is taken to be 2.05), which is well in the range determined for 2μm-grain composite.

One of the conclusions of the aforementioned findings is that coating of $TiC_{0.5}/TiB_2$ composites is required to improve their strength and oxidation resistance for certain applications such as cutting tool inserts. A possible coating is titanium nitride one which is widely used for similar purposes and can be possibly produced by annealing of $TiC_{0.5}/TiB_2$ composites in a nitrogen atmosphere.

Finally, the data available in the literature shows that the thermal shock resistance of the composites studied in this work compares favorably to similar materials. For example, 20% TiB_2-55%TiC-25%SiC (molar%) composite has been reported to exhibit ΔT_c of 300°C (R=286°C, specimen size is 3x4x18mm^3) [148], while it is about 280°C for the ZrO_2-Al_2O_3 composites (R≈230°C, specimen size is 2x4x15mm^3) [174]. Furthermore,

thermal shock resistance of the composites studied here is superior to Al_2O_3-30vol%TiC composite (R=102°C, $\Delta T_c \approx 150°$-200°C) [176] used in cutting tools.

5.6 Optimization of TPPP composites

5.6.1 Platelet Composite with Refined Microstructure

Properties of the platelet composite with the refined microstructure shown in Figure 72(c) are summarized in Table III. The susceptibility of this material to thermal shock and oxidation is characterized in Figures 61 and 62, respectively.

One of the potential applications of TiC_x-TiB_2-Ti_3B_4 composites fabricated by TPPP is believed to be cutting tool inserts. Wayne and Buljan [176] showed that high-speed machining ceramic tools experience temperatures at the cutting edge as high as 800°C and thermal gradients of 150°C along the length of 5 mm from the cutting edge. It is clear from the from the previous discussion and Figures 57, 61 that platelet composites could withstand these severe conditions without noticeable degradation of strength. The other properties important for abrasive and structural applications are discussed below.

5.6.1.1 Oxidation Resistance

As reported in Section 4.7 oxidation of this material was found to obey parabolic law at 900°-1000°C (see Figure 62) with rate constants, K_w ($kg^2m^{-4}s^{-1}$), of 1.8×10^{-7} and 5.2×10^{-7}, respectively, and apparent activation energy for oxidation of 130 kJ/mole. The

favorable parabolic rate dependence of the oxidation process was attributed to diffusion control imposed by the dense TiO_2-B_2O_3 oxide layer formed on the surface of the samples. This layer effectively retards the oxidation of the weak link - substoichiometric TiC_x, present in the studied composites. The oxidation resistance of TiC_x is known to decrease significantly with decreasing x, and at low stoichiometries, the oxidation resistance of TiC_x is approximately one hundred times lower than the oxidation resistance of TiB_2 at 1000°C [127]. As a result of the formation of the dense TiO_2-B_2O_3 oxide layer, the oxidation resistance of the studied $TiC_{0.65}$-TiB_2-Ti_3B_4 composites is only slightly lower than the monolithic fully dense TiB_2 [119] and an order of magnitude lower compared to Al_2O_3-30vol%TiC composites [177] with $K_w=(2\text{-}6)\times10^{-8}$ $kg^2m^{-4}s^{-1}$ at 900°-1100°C and corresponding activation energy of 190 kJ/mole.

5.6.1.2 Wear Resistance

A criterion for comparing the wear resistance of different ceramics was provided by Evans and Marshall [150] through the abrasive wear factor (AWF), which can be computed from the fracture toughness (K_{IC}), Young's modulus (E), and hardness (H) as

$$AWF=K_{IC}^{0.5}E^{-0.8}H^{1.43} \quad (21)$$

The higher the AWF, the higher is the expected resistance of the ceramic to abrasive wear. Good correlation of predictions based on the wear factor with the results of flycut milling and turning tests conducted on various cast irons were reported [151]. The wear factor of the refined platelet composite is 1.26, which favorably compares to commercial Al_2O_3-TiC and SiALON cutting-tool materials having wear factors of 1.22 and 1.21 [151], respectively.

The wear behavior of the refined "platelet" composite was characterized by ASTM G65 - Procedure A abrasive erosion test (see Section 4.6.4) and summarized in Table X along with the reported data on some of the ceramics being used in abrasive applications. These results show that wear rates observed for the refined "platelet" composite are comparable to Sialon and coarse-grained WC-Co cutting tool materials. Significantly higher wear rates in the tested composite compared to the best grades of cemented carbides and Al_2O_3-TiC cutting tool ceramics may be attributed to specifics of wear modes encountered in this test. Thus, application oriented tests are required to compare accurately the wear behavior of TPPP composites to other cutting tool ceramic materials. An example of such application oriented test was given by Holleck et al. [20], who reported superior wear behavior of eutectic TiC-TiB_2 composite in the process of turning steel.

5.6.2 Stoichiometric TiC-based composites

Starting from $TiC_{0.5}$ (Transient Plastic Phase) and B_4C (Reaction Phase) 95% dense composite comprised of 66.5 vol.% of $TiC_{0.9}$ and 33.5 vol.% of TiB_2 was hot-pressed at pressure of 40 MPa for 4 hr at 1600°C according to reaction

$$7\,TiC_{0.5} + B_4C \Rightarrow 5\,TiC_{0.9} + 2\,TiB_2 \qquad \{12\text{-a}\}$$

The resultant microstructure, shown in Figure 80, is similar to that of the nonequilibrium $TiC_{0.5}$-TiB_2 composite shown in Figure 72(d). Likewise, in $TiC_{0.93}$-TiB_2 composite TiB_2 fields have a tendency to be topologically interconnected in a network throughout microstructure. The amoebae-like shape of polycrystalline TiB_2 fields, characteristic of composites fabricated using B_4C powders finer than the particles of the

other reactant, is in full agreement with the microstructural evolution models presented above.

The higher volume fraction of TiB_2 phase required for better interconnectivity can be obtained by increasing $B_4C/TiC_{0.5}$ ratio in the starting powder mixture according to

$$6\,TiC_{0.5} + B_4C \Rightarrow 4\,TiC_{1-x} + 2\,TiB_2 + 4x\,C \qquad \{12\text{-b}\}$$

where $1\text{-}x \approx 0.95$ (see Figure 24). In the resulting TiC-TiB_2 composite the volume fraction of TiB_2 phase will be close to 39 vol%. In addition, TiC-TiB_2 composites containing controlled amounts of free carbon could be produced by this approach, which is another interesting possibility, since it has been shown that in TiC-TiB_2-C system combined advantages of both ceramics and graphite can be realized [22]. Such materials hold great promise for fabrication of low atomic number (low-Z) ultrarefractory composites with the enhanced thermal shock resistance and toughness [22]. Moreover, by further increasing $B_4C/TiC_{0.5}$ ratio TiB_2-B_4C-C composites can be produced. Similar composites studied by Sigl and Kleebe [38] exhibited encouraging fracture toughness of 6 MPa$\sqrt{m}$ (SEPB) attributed to microcrack toughening.

Preliminary measurements of mechanical properties of $TiC_{0.9}$-TiB_2 composite indicated that both its hardness (22±4 GPa) and flexural strength (400±30 MPa) are comparable to fully-dense coarse-grained 44%$TiC_{0.5}$-56%TiB_2 (non-equilibrium equiaxed) composite (see Table VIII) despite the significant porosity found in the $TiC_{0.9}$-composite (95% dense). The variation of flexural strength with temperature for this material is shown in Figure 79 and also found to be similar to coarse-grained 44%$TiC_{0.5}$-56%TiB_2 (non-equilibrium equiaxed) composite. As discussed earlier, the observed lack of improvement in high-temperature behavior for the composite comprised of 67% $TiC_{0.9}$-33%TiB_2 in comparison with the 44%$TiC_{0.5}$-56%TiB_2 one is speculated to be attributed to the effect of

TiB_2 (or the resulting solid solution of boron in $TiC_{0.5}$) in the latter matching the effect of a higher stoichiometry in the former. Assumed in this argument is that a porosity of 5 vol% in the $TiC_{0.9}$-composite does not significantly effect the high temperature properties of this composite, especially above DBTT of $TiC_{0.9}$.

6. CONCLUSIONS

6.1 Ti-B-C Phase Equilibria

Ti_3B_4 is an equilibrium phase in the Ti-B-C system at 1600 °C and at lower temperatures. The end member of the TiB_2 - TiC_x - Ti_3B_4 compatibility triangle is $TiC_{0.65}$, with an uncertainty in x of ±0.02. The nucleation and growth of Ti_3B_4 appear to be quite sensitive to impurity levels. Equilibrium is only achieved in this study when high purity titanium is used and the sintering is carried out under reducing or inert conditions.

6.2 Transient Plastic Phase Processing

It has been demonstrated that TPPP is capable of producing fully dense, ultra-refractory deflection-toughened TiC_x-TiB_2-Ti_3B_4 composites at temperatures that are considerably lower than the melting temperatures of the constituents. The attainment of the full density was related to the role of one of the intermediate phase in this reactive processing, $TiC_{0.5}$, as a transient plastic phase. The densification during TPP-processing of the studied composites appeared to be a deformation-driven process. Plastic flow and particle rearrangement by comminution are believed to be the predominant mechanisms for the most part of the densification process responsible for increase of relative density to ~95%.

Dominant processing parameters were established. Among them, the starting composition was found to determine the final microstructure and properties. However, provided the starting composition and the temperature schedule were maintained the same, the mode of deformation (triaxiality) and particle size of the starting powder mixture were found to be the critical factors determining the nominal pressure required to achieve full density in the produced composites, and extent of homogeneity and morphological texture in their final microstructure. These effects can be summarized as follows: the higher is the triaxiality and the lower the grain size of Ti powder the more homogeneous and less textured is the final microstructure, however, higher pressures are required for complete densification. In contrast, lower triaxiality (larger shear component in the deformation) and larger grain sizes of Ti favor the inhomogeneity and morphological texture formation in the final microstructure, and yet, lower pressures are required for densification.

6.3 Reaction Paths and Microstructural Evolution

Reaction paths and microstructural evolution in the two starting compositions with 4:4:1 ratio of Ti:B:C, namely: 4:1 Ti/B_4C and 1:1 $TiC_{0.5}/TiB_2$, were examined in detail. In the former, the Ti_3B_4 grains nucleated and grew as platelets, whereas they were equiaxed grains in the latter. The presence of TiB as an intermediate phase in "platelet" composition appeared to determine the morphology of the Ti_3B_4 phase. Based on XRD and SEM results from interrupted runs, a model is proposed according to which the faster diffusion of C, relative to B, is instrumental in the microstructural evolution of the "platelet" composite. Consistent with the model is the observation that the reduction of the initial particle size of the Ti in the "platelet" composition resulted in a more homogenous microstructure. The microstructural evolution of the "equiaxed" composite is less complicated in that there are

no intermediate phases. The resultant microstructure is believed to develop by a displacive reaction that only involves the diffusion of B and C.

6.4 Structure-Properties Relations

The flexural strength in the temperature range 25°C-1400°C, plane strain fracture toughness in the temperature range 25°C-1000°C, room temperature hardness and microhardnesses of individual phases, thermal shock susceptibility, and oxidation resistance in the temperature range 750°C-1000°C were measured for fully dense titanium carbide-titanium boride composites produced from 4:1 Ti/B_4C, 1:0.5:1 $Ti/0.5C/TiB_2$ and different molar ratios of $TiC_{0.5}/TiB_2$. Often equilibrium was not achieved in the latter composition which, as a result, sometimes was almost completely devoid of the Ti_3B_4 phase. Strength, fracture toughness and crack propagation characteristics of these Ti_3B_4-free non-equilibrium composites were compared to those of equilibrium ones.

Ambient Temperature

Non-equilibrium composites exhibited predominantly trans-granular fracture and no favorable crack propagation characteristics were observed for this type of equiaxed microstructure. A good correlation for their flexure strength with $(\text{grain size})^{-0.5}$ was found. In addition, the flexural strength of these composites was measured to decrease proportionally to the volume fraction of the borides. Consequently, it was argued that the critical flaws in these composites originate on the largest TiB_2 grains which thereby dominate their flexural strengths.

Crack deflection was found to be the main toughening mechanism at ambient temperature in the equilibrium composites containing ~35% Ti_3B_4 phase in platelet or equiaxed morphology. Superior fracture toughness and 4-point flexure strength of the platelet composites were largely attributed to enhanced efficiency of crack deflection by Ti_3B_4 platelets compared to the equiaxed Ti_3B_4 grains. The K_{IC} value of ~6 MPa measured for the platelet composites is consistent with the fact that only crack deflection was observed in these composites and that there were very few indications of crack bridging and platelet pull-out.

Elevated Temperatures

The flexural strengths of the studied composites (with exception of 5:1 $TiC_{0.5}/TiB_2$ composition and the refined 1:1 $TiC_{0.5}/TiB_2$ composites contaminated with ≥0.2 wt.% of Co) were found to be insensitive to temperature up to 1000°C. Boron-containing phases (TiB_2 and Ti_3B_4) in these composites were found to exert a strong beneficial effect on their high temperature properties by extending their softening temperature after which the plasticity of the carbide phase dominates the mechanical properties. This effect was argued to be attributed to the effect of solid solution of boron in TiC_x which is corroborated by the increased microhardness of this phase.

The fracture toughness of the equilibrium composites was found to first decrease with temperature up to about 500°-750°C and then increase with temperature, consistent with the removal of the residual stresses (related to thermal expansion mismatch) and associated deflection-toughening increment at higher temperatures and onset of ductile phase toughening at even higher temperatures. Specifically, the observed small increase in fracture toughnesses of the equilibrium composites at 1000°C compared to the room

temperature values was attributed to the effect of microplasticity related to ductile-to-brittle transition in $TiC_{0.65}$ constituent.

Susceptibility to Thermal Shock and Oxidation

The critical temperature change (ΔT_c) was measured to be 330°C for the refined platelet composite, and about 350°C and 450°C for the refined non-equilibrium equiaxed composites with grain sizes of 4 and 2 μm, respectively. The simple thermoelastic analysis based on the equilibrium equation $\{\Delta T_c=(\sigma(1-\nu)/E\alpha)*F(k/rh)\}$ proved to be useful in relating the obtained ΔT_c values to the values reported in the literature for other ceramic materials, however, tested using different specimen sizes.

Oxidation of the refined platelet composite was found to obey a parabolic law kinetics at 900°-1000°C with rate constants, K_w ($kg^2m^{-4}s^{-1}$), of $1.8x10^{-7}$ and $5.2x10^{-7}$, respectively, and apparent activation energy for oxidation of 130 kJ/mole.

6.5 Microstructural optimization

Refinement of the platelet composite by using the finer Ti powder have led to more homogeneous microstructures with higher strength (800-830 MPa) and practically the same value of fracture toughness (5.3 MPa$\sqrt{m}$) as those for "coarse" platelet composite (630 MPa and 5.8 MPa$\sqrt{m}$). One of the potential applications of the optimized TiC_x-TiB_2-Ti_3B_4 composites is expected to be cutting tool inserts. Resistance of these composites to thermal shock, high-temperature oxidation in air and abrasive wear compares favorably to similar cutting tool ceramics. Specifically, the wear rates observed for the refined "platelet" composite are comparable to Sialon and coarse-grained WC-Co cutting tool materials. The oxidation resistance of the optimized "platelet" composite is slightly lower than monolithic

fully dense TiB_2 and an order of magnitude lower compared to Al_2O_3-30vol%TiC cutting tool composite, however, it is superior to the monolithic TiC and much superior to the monolithic substoichiometric TiC_x.

6.6. Effect of impurities

Cleaner processing is required to obtain better properties in TiC_x-TiB_2-Ti_3B_4 composites. Impurities in the starting powders were found to affect the final microstructure and the attendant properties in two ways: (i) Non-metallic electro-negative impurities such as O, N and Cl are suspected to inhibit nucleation and/or growth of the Ti_3B_4 phase. (Ti powders obtained via chlorine process (99.9% pure) and MER process (98.5% pure) lead to nonequilibrium final composition, whereas hydride-dehydride powders (99.99% pure) and Plasma Arc Rotating Electrode processed (under Ar) powder (99+% pure) were found to be sufficiently pure not to effect the attainment of equilibrium) (ii) Low-melting grain boundary film-forming impurities, like Co, deteriorate high temperature properties of the produced composites.

7. FUTURE WORK

1. Among the most interesting findings of the present study are the effects of deformation mode (triaxiality) on the final microstructure and porosity. From this study it is clear that the operating variables are triaxiality, nominal pressure, strain rate, total strain (reduction in height) and particle sizes of the starting powders as well as diffusion distances of the reacting species. The experimental program designed to elucidate and quantify the effects of these variables on final microstructure can be based on the comparison of the hot-pressed microstructures, produced at different deformation levels. The level of deformation and the resulting total strain (reduction in height) can be relatively easily varied if the pre-sintered (at temperatures lower than the reaction onset temperature of 800°-900°C) green-bodies of different aspect ratios (with the initial cross-sectional area smaller than that of the die) are to be used in these experiments. In addition to deformation level (reduction in height), the flow and diffusion conditions can be systematically varied by deforming compacts of starting powder mixtures with varying particle size ratios during isothermal step at different temperatures and pressures.

2. Application-oriented tests of the produced composites such as fabrication and testing of complex shapes and cutting inserts has to be performed to prove positively the application potential of the TPP-processed composites.

3. Implementation of TPPP in Ti-Si-C and other transition metal ternary systems and identification of different possible transient plastic phases and corresponding reaction phases are required to demonstrate the viability and versatility of TPPP as general processing approach.

LIST OF REFERENCES

LIST OF REFERENCES

1. C.H. Li and J. Yamanis, "Super-Tough Silicon Nitride with R-curve Behavior", *Ceram. Eng. Sci. Proc.*, **10** [7-8] 632-645 (1989).

2. A.J. Pyzik, and D.R. Beaman, "Processing, Microstructure and Properties of Self-Reinforced Si_3N_4", 14th Conf. on Composites and Advanced Ceramics, 1990.

3. D.F. Carroll, and A.J. Pyzik, "Microstructural/Mechanical Property Relationship in Self-Reinforced Si_3N_4", 14th Conf. on Composites and Advanced Ceramics, 1990.

4. A.J. Pyzik, D.F. Carroll, C.J. Hwang, and A.F. Prunier, "Self-Reinforced Silicon Nitride - A New Microengineered Ceramic", Proc. Fourth Int. Conf. on Ceramic Materials for Engines, Goeteborg, Sweden, 1991.

5. T.D. Claar, W.B. Johnson, C.A. Anderson, and G. H. Schiroky, "Microstructure and Properties of Platelet-Reinforced Ceramics Formed by the Directed Reaction of Zirconium with Boron Carbide", Cer. Eng. Sci. Proc., Vol. 10, No. 7-8, pp. 599-609, 1989.

6. W.B. Johnson, T.D. Claar, and G. H. Schiroky, "Preparation and Processing of Platelet-Reinforced Ceramics by the Directed Reaction of Zirconium with Boron Carbide", Cer. Eng. Sci. Proc., Vol. 10, No. 7-8, pp. 588-598, 1989.

7. W.B. Johnson, A.S. Nagelberg, and E. Breval, "The Kinetics of Formation of Platelet-Reinforced Ceramic Composite Prepared by the Directed Reaction of Zirconium with Boron Carbide", J. Am. Ceram. Soc., 74 [9] 2093-101 (1991).

8. M.W. Barsoum and B. Houng, "Transient Plastic Phase Processing of Titanium-Boron-Carbon Composites", *J. Am. Ceram. Soc.*, **76** [6] 1445-51, (1993).

9. M. W. Barsoum, "Methods of Densifying and Strengthening Ceramic-Ceramic Composites by Transient Plastic Phase Processing", U.S. Patent No. 5 451 365, 1995.

10. M.D. Sacks, N. Bozkurt, and G.W. Scheiffele, "Fabrication of Mullite and Mullite-Matrix Composites by Transient Viscous Sintering of Composite Powders", *J. Am. Ceram. Soc.*, **74** [10] 2428-37 (1991).

11. M.D. Sacks, G.W. Scheiffele, N. Bozkurt, and R. Raghunathan ,"Fabrication of Ceramics and Composites by Viscous and Transient Viscous Sintering of Composite Particles", pp. 437-55 in Ceramic Transactions, Vol. 22, Ceramic Powder Science IV; Ed. G.L. Messing, S.-I. Hirano, and H.H. Hausner, American Ceramic Society, Westerville, OH, 1991.

12. C. H. Henager, Jr., J.L. Brimhall, and J.P. Hirth, "Synthesis of a $MoSi_2$-SiC composite *in situ* using a solid state displacement reaction", *Mater. Sci. and Eng.*, **A155**, 109-114 (1992).

13. C. H. Henager, Jr. and J.L. Brimhall,, "Solid State Displacement Reaction Synthesis of Interpenetrating-Phase Ni-Al/Al_2O_3 Composites", *Scripta Met. et Mater.*, **29**, 1597-1602, 1993.

14. R. Radhakrishnan, C.H. Henager, Jr., J.L. Brimhall, and S.B. Bhaduri, "Synthesis of Ti_3SiC_2/SiC and $TiSi_2$/SiC Composites Using Displacement Reactions in the Ti-Si-C system", *Scripta Met. et Mater.*, in press, 1996.

15. M. Barsoum, A. Zavaliangos, S. Kalidindi, T. El Raghy and D. Brodkin, "Transient Plastic Phase Processing of Ceramic/Ceramic Composites", *JOM*, **47** [11] 52-55 (1995).

16. Tsungchi Lien, M.Sc. Thesis, Department of Material Engineering, Drexel University, 1993.

17. F. de Mestral, F. Thevenot, "Ceramic composites: TiB_2-TiC-SiC. Part I Properties and microstructures in the ternary system", J. Mater. Sci., **26** [20] 5547-60 (1991).

18. H. Holleck, H. Leiste, E. Nold, H. Schulz and A. Skokan, "Multiphase Ceramic Materials and Coatings for Fusion Reactor Applications", J. Nucl. Mater. **155-157A**, 221-224 (1988).

19. E. Nold, H. Holleck, H. Leiste, "High Resolution Auger Electron Spectroscopy of Phase Boundaries in TiC/TiB_2 Materials", *Fresenius' J. Anal. Chem.*, **333** [4-5] 492-497 (1989).

20. H. Holleck, H. Leiste, W. Schneider, "Significance of Phase Boundaries in Wear Resistant TiC/TiB_2 Materials", *Int. J. Refract. Hard Met.*, **6** [3] 149-154 (1987).

21. Yu. G. Tkachenko, S.S. Ordan'yan, V.K. Yulyugin, V.I. Unrod, D.Z. Yurchenko, and A.A. Rogozinskaya, "Preparation and High-Temperature Antifriction Properties of Eutectic Alloys of the Systems $M^{IV}C$-$M^{IV}B_2$", Izvestia Akademii Nauk SSSR, Neorganicheskie Materialy, v.13, No. 8, pp. 1414-1418, 1977.

22. H. Shinno, M. Fujitsuka, T. Tanabe, "Thermal Shock Characteristics of C-B-Ti composite materials", Tanso (Carbons), **152**, pp.91-97, 1992.

23. I.I. Spivak, R.A. Andrievskii, V.V. Klimenko and V. D. Lazarenko, "Creep in the Binary System TiB_2-TiC and ZrB_2-ZrN", Sov. Powder Metall. Met. Ceram., **137**, pp. 617-620, 1974.

24. T.J. Davies and A.A. Ogwu, "Characterization of composite of TiC + TiB_2 bonded with nickel based binder alloy: mechanical and microstructural properties", Powder Metall., **38** [1] 39-44 (1995).

25. C.F. Yen, C.S. Yust and G.W. Clark, "Enhancement of Mechanical Strength in Hot-Pressed TiB_2 Composites by the Addition of Fe and Ni", Report CONF-781093-2, Oak Ridge National Laboratory, Oak Ridge, TN, 1978.

26. Yo. C. Hyun, Y. Miyamoto, Y. Takano, M. Koizumi, O. Yamada, "Fabrication of TiB_2-TiC ceramic composites by high-pressure combustion sintering", Proc. of the 1st MRS International Meeting on Advanced Materials, Tokyo, Japan, May 31-June 3 1988,

Vol. 5 Structural Ceramics/Fracture Mechanics , Publ. Materials Research Soc., Pittsburgh, PA, pp. 119-124, 1989.

27. S.K. Lee, D-H Kim, C. H. Kim, Fabrication of TiB_2/TiC composites by the directional reaction of titanium with boron carbide", *J. Mater. Sci.*, **29** [15], 4125-30 (1994).

28. see for eg. R. Telle and G. Petzow, "Strengthening and Toughening of Boride and Carbide Hard Material Composites", *Mater. Sci. Eng.*, **A105/106**, pp. 97-104, 1988 and references cited therein.

29. see for eg. A. G. Evans, "Perspective on the Development of High-Toughness Ceramics", *J. Am. Ceram. Soc.*, **73** [2] 187-206 (1990) and references cited therein.

30. T.L. Anderson, Fracture Mechanics. Fundamentals and Applications, 2nd edition, pp. 343-361, CRC Press Inc., Boca Raton, Fl, 1995.

31. see for eg. P. F. Becher, "Microstructural Design of Toughened Ceramics", *J. Am. Ceram. Soc.*, **74** [2] 255-69 (1991) and references cited therein.

32. M. Rühle, N. Claussen, and A.H. Heuer, "Transformation and Microcrack Toughening as Complementary Processes in ZrO_2-Toughened Al_2O_3", J. Am. Ceram. Soc., 69 [3], 195-97, 1986.

33. J.C. Amazigo and B.Budiansky, "Interaction of Particulate and Transformation Toughening", J. Mech. Phys. Solids, 36, 581-95, 1988.

34. K.T. Faber and A.G. Evans, "Crack Deflection Processes - I. Theory", Acta Metall., 31 [4] 565-76, 1983.

35. J.W. Hutchinson, "Crack Tip Shielding by Microcracking in Brittle Solids", Acta Metall., 35 [7] 1605-19, 1987.

36. M. Rühle, A.G. Evans, R.M. McMeeking, P.G. Charalambides, and J.W. Hutchinson, "Microcrack Toughening in Alumina/Zirconia", Acta Metall., 35 [11], 2701-10, 1987.

37. D.J. Magley, R.A. Winholtz and K.T. Faber, "Residual Stresses in a Two-Phase Microcracking Ceramic", J. Am. Ceram. Soc., 73 [6], 1641-44, 1990.

38. L.S. Sigl and H.-J. Kleebe, "Microcracking in B_4C-TiB_2 Composites", J. Am. Ceram. Soc., 78 [9], 2374-80, 1995.

39. N. Claussen, J. Steeb and R.F. Pabst, "Effect of Induced Microcracking on the Fracture Toughness of Ceramics", Am. Ceram. Soc. Bull., 56 [6], 559-62, 1977.

40. D. R. Messier, "High Temperature Chemistry of Fibers and Composites", Report No. MTL TR 92-62, U.S. Army Materials Technology Laboratory, Waretown, MS, 1992.

41. K.T. Faber, A.G. Evans and M.D. Drory, in Fracture Mechanics of Ceramics, Vol. 5-6, Ed. R.C. Bradt, A.G. Evans, D.P.H. Hasselman, and F.F. Lange, Plenum, New York, 1982.

42. K.T. Faber and A.G. Evans, "Crack Deflection Processes - II. Experiment", Acta Metall., 31 [4] 577-84, 1983.

43. see for eg. D.R. Clarke, "Interpenetrating Phase Composites", *J. Am. Ceram. Soc.*, **75** [4] 739-59 (1992) and references cited therein.

44. V.A. Ravi, T.D. Claar, J.A. Hornor and W.B. Johnson, "Platelet Reinforced Ceramics for Severe Thermal Shock Applications", pp. 175-183 in "Processing and Fabrication of Advanced Materials for High Temperature Applications", Ed. V.A. Ravi and T.S. Srivatsan, TMS, 1992.

45. C.P. Cameron, J.H. Enloe, L.E. Dolhert, and R.W. Rice, "A Comparison of Reaction vs Conventionally Hot-Pressed Ceramic Composites", Ceram. Eng. Sci. Proc. **11** [9-10] 1190-1202 (1990).

46. R.K. Iler, "Multilayers of Colloidal Particles", J. Colloid Interface Sci., 21, 569-94, 1966.

47. see for eg. M.D. Sacks, H.-W. Lee, and J.A. Pask, "A Review of Powder Preparation Methods of Densification Procedures for Fabricating High-Density Mullite", pp. 167-207 in Ceramic Transactions, Vol. 6, Mullite and Mullite Matrix Composites; Ed. S. Somiya, R.F. Davis, and J.A. Pask, American Ceramic Society, Westerville, OH, 1990 and references cited therein..

48. M.N. Rahaman and D.-Y. Jeng, "Sintering of Mullite and Mullite Matrix Composites", pp. 753-66 in Ceramic Transactions, Vol. 7, Sintering of Advanced Ceramics; Ed. C.A. Handwerker, J.E. Blendell, and W.A. Kaysser, American Ceramic Society, Westerville, OH, 1990.

49. W. Fahrenholtz, J. Ortega, R.E. Loehman, K.G. Ewsuk, and A.P. Tomsia, "Processing Near-Net Shape Metal-Ceramic Composites by Reactive Metal Infiltration", p. 4, Abstracts, ACerS 18th Annual Conference on Composites and Advanced Ceramics, Cocoa Beach Fl, 1994.

50. I. Gotman, E. Stessel and M.J. Koczak, "Processing of In Situ IMCs Employing Self-Propagating Synthesis and Reactive Infiltration Technique", p. 5, Abstracts, ACerS 18th Annual Conference on Composites and Advanced Ceramics, Cocoa Beach Fl, 1994.

51. W.B. Hillig, R.L. Mehan, C.R. Morelock, V.J. DeCarlo, and W. Laskow, "Silicon/Silicon Carbide Composites", Am. Ceram. Soc. Bull., 54, [12], pp. 1054-56, 1975.

52. M.S. Newkirk, H.D. Lesher, D.R. White, C.R. Kennedy, A.W. Urquhart, and T.D. Claar, "Preparation of Lanxide™ Ceramic Matrix Composites: Matrix Formation by the Directed Oxidation Of Molten Metals", Ceram. Eng. Sci. Proc., 8, [7-8], pp. 879-885, 1987.

53. J.R. Strife, J.J. Brennan, and K.M. Prewo, "Status of Continuous Fiber-Reinforced Ceramic Matrix Composites Processing Technology", Ceram. Eng. Sci. Proc., 11, [7-8], pp. 871-919, 1990.

54. P.J. Lamicq, G.A. Bernhart, M.M. Daucier,, and J.G. Mace, "SiC/SiC Composite Ceramics", Am. Ceram. Soc. Bull, 65, [2], pp.336-338, 1986.

55. Y.M. Chiang, J.S. Haggerty, R.P. Meissner, and C.D. Demetry, "Reaction-Based Processing Methods for Ceramic Matrix Composites", Am. Ceram. Soc. Bull, 68, [2], pp.420-428, 1989.

56. D.P. Stinton, T.M. Besmann, and R.A. Lowden, "Advanced Ceramics by Chemical Vapor Deposition Techniques", Am. Ceram. Soc. Bull, 67, [2], pp. 350-355, 1988.

57. W.B. Hillig, M.R. Ramakrishnan, and N. Patibandla, "Kinetics of $MoSi_2$ processing via reactive vapor infiltration", p. 49, Abstracts, ACerS 18th Annual Conference on Composites and Advanced Ceramics, Cocoa Beach Fl, 1994.

58. T.D. Claar, S.M. Mason, K.P. Pochopien, D.W. White, and W.B. Johnson, U.S. patent No. 4 885 130, 1989.

59. M.K. Aghajanian, J.T. Burke, D.R. White, and A.S. Nagelberg, "A New Infiltration Process for the Fabrication of Metal-Matrix Composites, *SAMPE Quart.*, **20** [4] 43-46 (1989).

60. D.C. Halverson, A.J.Pyzik, and I.A. Aksay, "Boron-Carbide-Aluminum and Boron-Carbide-Reactive Metal Cermets", U.S. Patent No. 4 605 440, 1986.

61. A.J. Pyzik and I.A. Aksay, "Microdesigning of B_4C-Al Cermets", in Proceedings of the International Conference on Advances in Processing of Ceramic and Metal Matrix Composites, Ed. H. Mostaghaci, Pergamon Press, Oxford, U.K., 1989.

62. S. Yamada, S. Kimura, E Yasuda, T. Tanabe, and Y. Asami, "A Discussion of the Chemical Mixing Process for in situ Preparation of Silicon Carbide Whiskers in Silicon Nitride Powder", J. Mater. Res., v.3, pp. 538-544, 1988.

63. H. Wang, and G.S. Fishman, "SiC Whisker/Si_3N_4 Composites by a Chemical Mixing Process", Ceram. Eng. Sci. Proc., v. 12, pp. 2135-2141, 1991.

64. S.T. Song, and G.Z. Liu, "A Study on the Preparation and Properties of Self-Reinforced Si_3N_4 Matrix Composites", Proc. Int. Symp. on the Science of Engineering Ceramics, pp. 121-128, 1991.

65. D.R. Messier, and P. Wong, "Duplex Ceramic Structures - Interim Report No.1: Kinetics of Fabrication of Silicon Nitride by Reaction Sintering", U.S. Army Materials Technology Laboratory, AMMRC TR 72-10, March 1972.

66. D.R. Messier, F.L. Riley, R.J. Brook, "The Alpha/Beta Silicon Nitride Phase Transformation", J. Mater Sci., v.13, pp. 1199-1205, 1978.

67. C-M.J. Hwang, A.J. Pyzik, "Self-reinforced silicon nitride ceramic with crystalline grain-boundary phase, and a method of preparing the same", U.S. Patent No. 5 098 449, 1992.

68. T. Ohji, K. Hirao, and S. Kanzaki, "Fracture Resistance Behaviour of Highly Anisotropic Silicon Nitride", *J. Am. Ceram. Soc.*, **78** [11] 3125-28 (1995).

69. M.H. Lewis, "Microstructural Engineering of Ceramics for High-Temperature Structural Application", pp. 713-30 in Fracture Mechanics of Ceramics, Ed. R.C. Bradt, A.G. Evans, D.P.H. Hasselman, and F.F. Lange, Plenum, New York, 1986.

70. F.F. Lange, "Fracture Toughness of Si_3N_4 as a Function of the Initial α-Phase Content", *J. Am. Ceram. Soc.*, **62** [7-8] 428-30 (1979).

71. T. Nishida, Y. Hanaki, T. Nojima, and G. Pezzotti, "Measurement of Rising R-curve Behavior in Toughened Silicon Nitride By Stable Crack Propagation in Bending", *J. Am. Ceram. Soc.*, **78** [11] 3113-16 (1995).

72. "Silicon Nitride Ceramic Spring" Prospectus, NHK Spring Co., Ltd., Japan, 1993.

73. J.J. Cao, W.J. MoberlyChan, L.C. De Jonghe, C. J. Gilbert, and R.O. Ritchie, "In Situ Toughened Silicon Carbide with Al-B-C Additions", **79** [2] 461-69 (1996).

74. R. Rice and W. McDonough, "Intrinsic Volume Changes of Self-Propagating Synthesis", *J. Am. Ceram. Soc.*, **68** [5] C-122-123 (1985).

75. J. W. McCauley, N. D. Corbin, T. Resetar, and P. Wong, "Simultaneous Preparation and Self-Sintering of Materials in the System Ti-B-C", *Ceram. Eng. Sci. Proc.*, **3** [9,10] 538-53, (1982)

76. K.K. Udwadia and J. Puszynski, "Combustion Synthesis and Densification of TiC-TiB_2 and TiC-WC Powders" in *In situ Reactions for Synthesis of Composites, Ceramics and Intermetallics*, edt. E. V. Barrera, F. D. S. Marquis, W. E. Frazier, S. G. Fishman, N. N. Thadhani, and Z. A. Munir, pp. 59-67, Warrendale PA, 1995.

77. J.B. Holt and Z.A. Munir, "Combustion Synthesis of Titanium Carbide: Theory and Experiment", *J. Mater Sci.*, **21**, 251-59 (1986)

78. G.Y. Richardson, R.W. Rice, W.J. McDonough, J.M. Kunetz, and T. Schroeter, "Hot Pressing of Ceramics Using Self-Propagating Synthesis", Ceram. Eng. Sci. Proc., **7** [7-8] 761-70 (1986)

79. R.W. Rice, W.J. McDonough, G.Y. Richardson, J.M. Kunetz, and T. Schroeter, "Hot Rolling of Ceramics Using Self-Propagating High-Temperature Synthesis", Ceram. Eng. Sci. Proc., **7** [7-8] 751-60 (1986)

80. Miyamoto, Y., "Ceramic Processing Approaches Using Combustion Synthesis Under Gas Pressure", *Am. Ceram. Soc. Bull.*, **69** [4] 686 (1990)

81. L.J. Kecsces, T. Kottke, and A. Niiler, "Microstructural Properties of Combustion Synthesized and Dynamically Consolidated Titanium Boride and Titanium Carbide", *J. Am. Ceram. Soc.*, **73** [5] 1274-82 (1990).

82. L. Wang, M.R. Wixom, and L.T. Thompson, "Structural and Mechanical Properties of TiB_2 and TiC Prepared by Self-Propagating High-Temperature Synthesis/Dynamic Compaction", *J. Mater. Sci.*, **29**, 534-543 (1994).

83. J.C. LaSalvia, L.W. Meyer, and M.A. Meyers, "Densification of Reaction Synthesized Titanium Carbide by High-Velocity Forging", *J. Am. Ceram. Soc.*, **75** [3] 592-602 (1992).

84. D.A. Hoke, M.A. Meyers, L.W. Meyer, and G.T. Gray III, "Reaction Synthesis/Dynamic Compaction of Titanium Diboride", Metall Trans., **23A** [1] 77-86 (1992).

85. D.A. Hoke and M.A. Meyers, "Consolidation of Combustion-Synthesized Titanium Diboride-Based Materials", *J. Am. Ceram. Soc.*, **78** [2] 275-84 (1995).

86. R. Telle and G. Petzov, "Reaction Sintering of Boron Carbide (B_4C) with Silicon and Titanium", Horiz. Powder Metall., Proc. Int. Powder Metall. Conf. Exhib., Part II, pp. 1155-58.

87. R. Telle, R.J. Brook, and G. Petzov, "Ion Beam Modification, Reaction Sintering, Precursor Pyrolysis, Clean Room Processing, and Mechanical Testing, Challenges in Processing of Ceramic Hard Materials", *J. Hard Materials*, **2** [1-2], 79-114 (1991).

88. J.S. Haggerty and Y.-M. Chiang, *Ceram. Eng. Sci. Proc.*, **11** [7-8], 757- (1990).

89. H. Wada, "Synthesis of Ti-diboride, Nitride and Carbide", p. 113 in Proc. Am. Ceram. Soc. 93rd Ann. Meeting Exp, 1991, Cincinnati, OH

90. N. Claussen and J.Jahn, *J. Am. Ceram. Soc.*, **63** [3-4] 228-29 (1980).

91. M.R. Anseau, C. Leblud and F. Cambier, *J. Mater. Sci. Lett.*, **2**, 366-70, (1983).

92. E. Di Rupo, M.R. Anseau, R.J. Brook, "Reaction sintering: correlation between reaction and densification", *J. Mater. Sci.*, **14**, 2924-2928, (1979).

93. E. Di Rupo, T.G. Carruthers and R.J. Brook, "Identification of Stages in Reactive Hot-Pressing", *J. Am. Ceram. Soc.*, **61** [9-10] 468-69 (1978).

94. G. Zhang, Z. Jin, and X. Yue, "TiN-TiB_2 Composites Prepared by Reactive Hot Pressing and Effects of Ni Addition", *J. Am. Ceram. Soc.*, **78** [10] 2831-33 (1995).

95. M.W. Barsoum and T. El Raghy "Synthesis and Characterization of Remarkable Ceramic: Ti_3SiC_2", *in press J. Am. Ceram. Soc.*, 1996.

96. F.J.J. van Loo, "Multiphase Diffusion in Binary and Ternary Solid-State Systems", *Prog. Solid St. Chem.*, **20**, 47-99 (1990).

97. L.J. Bowen, T.J. Carruthers and R.J. Brook, "Hot-Pressing of Si_3N_4 with Y_2O_3 and Li_2O as Additives", *J. Am. Ceram. Soc.*, **61** [7-8] 335-39 (1978).

98. R.A. Rapp, A. Ezis and G.J. Yurek, "Displacement Reactions in Solid State", *Metall. Trans.*, **4** [5] 1283-92 (1973).

99. D. Miracle and H. Lipsitt, "Mechanical Properties of Fine-Grained Substoichiometric TiC", *J. Am. Ceram. Soc.*, **66** [8] 592-96 (1983).

100. E. Rudy, "Ternary Phase Equilibria in Transition Metal-Boron-Carbon-Silicon Systems, Part V", Report No. AFML-TR-65-2, Air Force Materials Laboratory, Wright-Patterson Air Force Base, Ohio, 1969.

101. K. E. Spear, P. McDowell, and F. McMahon, "Experimental Evidence for the Existence of the Ti_3B_4 Phase", *J. Am. Ceram. Soc.*, **69** [1] C4-5 (1986).

102. S. Ohmura, Y. Miyamoto, M. Koizumi, "Gas-Pressure Combustion Sintering of TiB_2 -Based Composites", *Ceram. Mater. Compon. Engine, Proc. Int. Symp.*, 3, pp. 247-59, (1989).

103. O. Kubaschewski et al.. "Materials Thermochemistry", 6 ed., 1993, Oxford, Pergamon Press.

104. R. G. Fenish, "Phase Relationships in the Titanium-Boron System", Union Carbide Parma Technical Center Report NRM-138, 1964; pp. 1-37.

105. R. G. Fenish, "A New Intermediate Compound in the Titanium-Boron System, Ti_3B_4" *Trans. Metall. Soc. AIME,* **236,** 804 (1966).

106. S.S. Ordan'yan, V.I. Unrod, and A.I. Avgustinik, "Reactions in the system TiC_x-TiB_2", Sov. Powder Metall. Met. Ceram., No.9(153), 729-731 (1975).

107. E.K. Storms, pp.6-9 in "Refractory Materials: Vol 2, The Refractory Carbides", 1st ed., Academic Press, New York, 1967.

108. C.Cm. Wu, R.W. Rice, C.P. Cameron, L.E. Dolhert, J.H. Enloe, and J.Block, "Diamond Pin-On-Disk Wear of Al_2O_3 Matrix Composites and Nonoxides", Ceram. Eng. Sci. Proc. **12** [7-8] 1485-99 (1991).

109. H. Pastor, "Metallic Borides: Preparation of Solid Bodies-Sintering Methods and Properties of Solid Bodies", in Boron and Refractory Borides, Ed. V.I. Matkovich, Springer-Verlag, New York, N.Y., pp. 475-493, 1977.

110. J.F. Lynch, C.G. Ruderer, and W.H.Duckworth, "Engineering Properties of Ceramics, Borides", American Ceramic Society, 1966.

111. M.K. Ferber, P.F. Becher, and C.B. Finch, "Effect of Microstructure on the Properties of TiB_2 Ceramics", *J. Am. Ceram. Soc.*, **66** [1] C2-C4 (1983).

112. A.G. Evans, "Microfracture from Thermal Expansion Anisotropy: I", *Acta Metall.*, **6** [12] 1845-53 (1978).

113. T. Watanabe and S. Kouno, "Mechanical Properties of TiB_2-CoB-Metal Boride Alloys", *Ceram Bull.*, **61** [9] 970 (1982).

114. J.R. Ramberg and W.S. Williams, "High Temperature Deformation of Titanium Diboride", *J. Mater. Sci.*, **22**, 1815-1826 (1987).

115. H.R Baumgartner and R.A Steiger, "Sintering and Properties of Titanium Diboride Made from Powder Synthesized in a Plasma-Arc Heater", J.Amer. Cer. Soc., **67**, pp. 207-212, 1984.

116. C. Mroz, "Processing TiZrC and $TiZrB_2$", *Am. Ceram. Soc. Bull.*, **73** [4] 78-81 (1994).

117. ABB Cerama AB "High Performance Ceramics and Composites - Materials of the Future for Today's Applications", Prospectus, ABB Cerama AB, Sweden, 1993.

118. Y. Miyamoto, M. Koizumi, and O. Yamada, "High-Pressure Self-Combustion Sintering for Ceramics", *J. Am. Ceram Soc.*, **67** [11] C-224-225 (1984).

119. see for eg. R.A. Culter "Engineering Properties of Borides" pp.787-803 in ASM Engineered Materials Handbook, Vol. 4: Ceramics and Glasses, ASM, Materials Park, OH, 1991 and references cited therein.

120. G. Petzov and R. Telle, p. 131 in "Advances in Ceramics", Proc. Lectures on Advanced Ceramics, Yokohama, 1983, ed. S. Somiya, Terra Scientific Publishers, Tokyo, 1987.

121. C.E. Ransley, "Refractory Carbides and Borides for Aluminum Reduction Cells", *J. Met.*, **14** [2] 129-135 (1962).

122. R.C. Dorward, "Aluminum Penetration and Fracture of Titanium Diboride", *J. Am. Ceram. Soc.*, **65** [1] C6 (1982).

123. C.B. Finch and V.J. Tennery, Crack Formation and Swelling of TiB_2-Ni Ceramics in Liquid Aluminum, *J. Am. Ceram. Soc.*, **65** [7] C100-C101 (1982).

124. H.R. Baumgartner, "Mechanical Properties of Densely Sintered High-Purity Titanium Diborides in Molten Aluminum Environments", *J. Am. Ceram. Soc.*, **67** [7] 490-97 (1984).

125. W.A. Zdaniewski, "Role of Microstructure and Intergranular Phases in Stress Corrosion of TiB_2 Exposed to Liquid Aluminum", *J. Am. Ceram. Soc.*, **68** [11] C-309-C-312 (1985).

126. W.A. Zdaniewski, "Degradation of Hot-Pressed TiB_2-TiC Composite in Liquid Aluminium", *Ceram. Bull.*, **65** [10] 1408-14 (1986).

127. T. Ya. Kosolapova, Ed., "Properties, Production and Applications of Refractory Materials", "Metallurgiya", Moscow, 1986.

128. S. Ranganath, M. Vijayakumar, J. Subrahmany, "Combustion-Assisted Synthesis of Ti-TiB-TiC Composite via the Casting Route", Materials Science and Engineering A-Structural Materials: Properties Microstructure and Processing, Vol. 149, No. 2, pp. 253-257, 1992.

129. W.S. Williams and R.D. Schaal, "Elastic Deformation, Plastic Flow, and Dislocations in Single Crystals of Titanium Carbide", *J. Appl. Phys.*, **33** [3] 955-62 (1962).

130. D.K. Chatterjee, M.F. Mendiratta, and H.A. Lipsitt, "Deformation Behavior of Single Crystals of Titanium Carbide", *J. Mater. Sci.*, **14**, 2151-56 (1979).

131. G. E. Hollox and R.E. Smallman, "Plastic Behavior of Titanium Carbide", *J. Appl. Phys.*, **37** [2] 818-23 (1966).

132. F.R. Chien, S.R. Nutt, and D. Cummings, "Defect Structures in Single Crystal TiC", *Philos. Mag.*, **68** [2] 325-48 (1993).

133. Fen-Ren Chien, R.J. Clifton, and S. R. Nutt, "Stress-Induced Phase Transformation in Single Crystal Titanium Carbide", *J. Am. Ceram. Soc.*, **78** [6] 1537-45 (1995).

134. G. Das, K.S. Mazdiyasni and H.A. Lipsitt, "Mechanical Properties of Polycrystalline TiC", *J. Am. Ceram. Soc.*, **65** [2] 104-10 (1982).

135. A.P. Katz, H.A. Lipsitt, T. Mah, M.G. Mendiratta, "Mechanical Behavior of Polycrystalline TiC", *J. Mater. Sci.*, **18**, 1983-1992 (1983).

136. W.S. Williams, "Dispersion Hardening of Titanium Carbide by Boron Doping", *Trans. Metall. Soc. AIME*, **236** [27] 211-16, 1966.

137. W.S. Williams, "Influence of Temperature, Strain Rate, Surface Condition and Composition on the Plasticity of Transition-Metal Carbide Crystals", *J. Appl. Phys.*, **35** [4], 1329-38 (1964)

138. J.D. Venables, "The Nature of Precipitates in Boron-Doped TiC", *Philos. Mag.*, **16** [143] 873-90, 1967.

139. O.Yamada, Y. Miyamoto, and M. Koizumi, "High-Pressure Self-Combustion Sintering of Titanium Carbide", *J. Am. Ceram. Soc.*, **70** [9] C-206-208 (1987).

140. B.A. Movchan, A.V. Demchishin, and G.F. Badlenko, "Structure-Property Relationships in Microlaminate TiC/TiB_2 Condensates", Thin Solid Films, **97** [3] 215-219 (1982)

141. M. Lahres, "Multiphase TiC/TiB_2-Hard Coatings. Production, Constitution, Properties and Application Behavior", Dissertation, Karlsruhe University (T.H.), Karlsruhe, Germany, 1991.

142. S.S. Ordan'yan, E.K. Stepanenko, I.V. Sokolov, and A.V. Vasil'ev, "Densification Behavior of Two-Phase MeC-MeB_2 Powders during Sintering", Sov. Powder Metall. Met. Ceram., **25** [6] 464-467 (1986).

143. S.M. Kats, S.S. Ordan'yan, and V.I. Unrod, "Compressive Creep of Alloys of the ZrC-ZrB_2 and TiC-TiB_2 systems", Sov. Powder Metall. Met. Ceram., No. 12, 70-75 (1981).

144. C.C Sorrel, H.R. Beratan, R.C. Bradt, and V.S. Stubican, "Directional Solidification of the (Ti,Zr) Carbide-(Ti,Zr) Diboride Eutectics", *J. Am. Ceram. Soc.*, **67** [3] 190-94 (1984)

145. P. Mochel, C. Allison, and W.S. Williams, "Study of TiC Precipitates in TiB_2 by Electron Energy Loss Spectroscopy", J. Am. Ceram. Soc., **64** [4] 185-87 (1981).

146. S.S Ordan'yan, "Specific mechanical properties of sintered composite: models of 'coarse agglomerate' eutectics", pp. 102-109 in Physics of the Strength of Composite Materials [in Russian], Izd. Fiz.-Tekh. Inst., Leningrad , 1980.

147. B.A. Friedlender, S.S. Ordan'yan, V.S. Neshpor, and G.A. Savel'ev, "Thermal conductivity and thermal diffusivity of materials of TiC-TiB_2 system at high temperatures", Teplofiz. Vys. Temp., Vol. 18, No. 5, 1002-1006 (1980).

148. F. de Mestral, F. Thevenot, "Ceramic composites: TiB_2-TiC-SiC. Part II Optimization of the composite 20% TiB_2-55% (mol%) TiC- 25% SiC", J. Mater. Sci., **26** [20] 5561-65 (1991).

149. S.F. Wayne, J.G. Baldoni, and S.T. Buljan, "Abrasion and Erosion of WC-Co with Controlled Microstructures", Tribol. Trans., 33 [4], pp. 611-617, 1990.

150. A.G Evans and D.B. Marshal, "Wear Mechanisms in Ceramics", pp. 439-452, ASM Fundamentals of Friction and Wear of Materials, (1980).

151. C.W. Beeghly and A.F. Shuster, "Application-Specialized Ceramics: A Silicon Nitride for Machining Gray Cast Iron", pp. 91-99 in "Tool Materials for High Speed Machining", Proc. Conf. Advances in Tool Materials for Use in High Speed Machining, February 1987, Scottsdale, AZ, publ. ASM International, 1987.

152. P.K. Mehrotra, "Evaluation of Engineering Ceramics for Wear Applications", Wear of Materials 1987 - Volume One, ed. K.C. Ludema, ASME, New York, 1987.

153. M.F. Ashby and R.A. Verall, "Diffusion-accommodated flow and superplasticity", *Acta Metall.*, **21** [2] 149-163 (1973).

154. Roy W. Rice "Reactant Compact and Product Microstructures for TiC, TiB_2, and TiC/TiB_2 from SPS Processing", Ceram. Eng. Sci. Proc. **11** [9-10] 1203-1225 (1990).

155. B. D. Cullity, "Elements of X-ray Diffraction", 2nd Ed. Addison-Wesley Publishing Co., Reading, 1978.

156. A.G. Evans and A.E. Charles, "Fracture Toughness Determinations by Indentation", *J. Am. Ceram. Soc.*, **59**, [7-8] 371-72 (1976)

157. D. Munz, R.T. Bubsey, and J.L. Shannon Jr., "Fracture Toughness Determination of Al_2O_3 Using Four-Point-Bend Specimen with Straight-Through and Chevron Notches", J. Am. Ceram. Soc., 63 [5-6], pp. 300-305, 1980.

158. G. Himsolt, D. Munz, and T.Fett, "A Modified Chevron Specimen for Ceramic Materials", J. Am. Ceram. Soc., 70 [6], pp. C133-C135, 1987.

159. J. Sung and P.S. Nicholson, "Valid K_{Ic} Determination via In-Test Subcritical Precracking of Chevron-Notched Bend Bars", J. Am. Ceram. Soc., 72 [6], pp 1033-36, 1989.

160. S.D. Conzone, W.R. Blumenthal, and J.R. Varner, "Fracture Toughness of TiB_2 and B_4C Using the Single-Edge Precracked Beam, Indentation Strength, Chevron Notched Beam, and Indentation Strength Methods", J. Am. Ceram. Soc., 78 [8], pp 2187-92, 1995.

161. D.G. Munz, J.L. Shannon Jr., and R.T. Bubsey, "Fracture Toughness Calculation From Maximum Load in Four Point Bend Tests of Chevron Notch Specimens", Int. J. Fract., 16 [3], pp. R137-R141, 1980.

162. J.I. Bluhm, "Slice Synthesis of a Three Dimensional "Work of Fracture" Specimen - for Brittle Materials Testing", Eng. Fract. Mech., 7, pp. 593-604, 1975.

163. L.M. Buchatskij, S.I. Khudyaev, G.V. Shkadinskaya, "Propagation of combustion wave along powder material under pressing conditions", Fizika Goreniya i Vzryva, V. 28, No. 1, pp 58-66, 1992.

164. V.A. Gruzdev, Yu.P. Zarichnyak, Yu.A. Kovalenko, "Effect of pressing process parameters on the thermal conductivity of cold-pressed porous powder composites", Soviet Powder Metallurgy and Metal Ceramics, V. 28, No. 3, pp. 164-168, 1989.

165. G.R. Hadley, "Thermal Conductivity of Packed Metal Powders", Int. J. Heat and Mass Transfer, 29 [6] pp 909-920, 1986.

166. R.W. Rice, G.Y. Richardson, J.M. Kunetz, T. Schroeter, and W.J. McDonough, "Effects of Self-Propagating Synthesis Reactant Compact Character on Ignition, Propagation and Resultant Microstructure", Ceram. Eng. Sci. Proc., **7** [7-8] 737-50 (1986).

167. T. Ya. Kosolapova, Ed., pp. 333-35 in "Properties, Production and Applications of Refractory Materials", "Metallurgiya", Moscow, 1986.

168. "Diffusion in Materials", p 441, Eds. A.L. Laskar, J.L. Bocquet, G. Brebec, and C. Monty, Kluwer Academic Publishers, Netherlands 1990.

169. P. Mogilevsky, E.Y. Gutmanas, I. Gotman and R. Telle, "Reactive Formation of Coatings at Boron Carbide Interface with Ti and Cr Powders", *J. Eur. Ceram. Soc.*, (1995).

170. A.S. Helle, K.E. Easterling and M.F. Ashby, "Hot-Isostatic Pressing Diagrams: New Developments", Acta Metall., 33 [12], pp. 2163-74, 1985

171. see for eg. J.S. Kircaldy and D.J. Young, Diffusion in the Condensed State, The Institute of Metals, London, England, 1987, and references cited therein.

172. W. Shum, "Bridging effects on Toughness", Ph.D. Thesis, Harvard University, Cambridge, MA, 1989.

173. K. Satyamurthy, J.P. Singh, D.P.H. Hasselman, and M.P. Kamat, "Transient Thermal Stresses in Cylinders with Square Cross Section Under Conditions of Convective Heat Transfer", J. Am. Ceram. Soc., 63 [11-12] 694-98 (1980).

174. T. Sato, T. Endo, and M. Shimada, "Postsintering Hot Isostatic Pressing of Ceria-Doped tetragonal Zirconia/Alumina Composites in an Argon-Oxygen Gas Atmosphere", *J. Am. Ceram. Soc.*, **72** [5] 761-64 (1989).

175. D.B. Marshall, M.D. Drory, R.L. Loh and A.G. Evans, "The Thermal Fracture of Alumina", pp. 336-363 in Fracture in Ceramic Materials: Toughening Mechanisms, Machining Damage, Shock; ed. A.G. Evans, Noyes Publications, Park Ridge, NJ, 1984.

176. S.F. Wayne and S.T. Buljan, "The Role of Thermal Shock on Tool Life of Selected Ceramic Cutting Tool Materials", J. Am. Ceram. Soc., 72 [5] pp. 754-60, 1989.

177. A. Tampieri and A. Bellosi, "Oxidation Resistance of Alumina-Titanium Nitride and Alumina-Titanium Carbide Composites", *J. Am. Ceram. Soc.*, **75** [6] 1688-1690 (1992).

TABLES

TABLE I. Toughened Ceramics

Toughening Mechanism	Maximum Toughness, MPa$\sqrt{m}$	Representative Materials	Limitations
Fiber reinforced	~30	CAS*/SiC LAS§/SiC Al_2O_3/SiC SiC/C Al_2O_3/Al_2O_3	Processing Coatings Fibers
Whisker/platelet reinforced	~15	Si_3N_4/SiC Si_3N_4/Si_3N_4 Al_2O_3/SiC	Oxidation t°≤1200°C
Ductile network	~25	Al_2O_3/Al ZrB_2/ZrC/Zr Al_2O_3/Ni B_4C/Al WC/Co	t°≤1000°C Oxidation
Transformation toughened	~20	PSZ¶ (ZrO_2+MgO) TZP† (ZrO_2+Y_2O_3) ZTA$ (Al_2O_3+TZP) HfO_2	t°≤600°C
Microcrack toughened	~7	Al_2O_3/ZrO_2 Si_3N_4/SiC SiC/TiB_2 B_4C/TiB_2	t°≤1000°C Strength

*Calcium aluminum silicate glass-ceramic. §Lithium aluminum silicate glass-ceramic. ¶PSZ-partially stabilized zirconia. †TZP-polycrystalline tetragonal zirconia. $ZTA-zirconia-toughened alumina.

TABLE II. Properties of Monolithic TiC and TiB_2 Ceramics Compared to the Equimolar TiC/TiB_2 Composite [17,18].

Property	TiC	TiB_2	Equimolar TiC/TiB_2 Composite*
Structure	Cubic a=4.33	Hexagonal a=3.03 c=3.23	–
Density, g/cm^3	4.92	4.52	4.7
Microhardness, GPa	upto 34	upto 32	–
Hardness, GPa 25°C 600°C	 28 7	 29 8	 23.5 (25.3) 8.5
K_{IC}, $MPa\sqrt{m}$ (indentation method) 25°C 1000°C	 4.8 (4.4) 4.0	 5.8 (5.0) 4.7	 7.1 (5.2) 6.0
Melting Temperature, °C	3070	3225	2500
Elastic Modulus, GPa	420	475	440
Thermal Expansion Coefficient, $10^{-6}/K$	8.1 (8.4)	7.8 (7.8) α_a=7.2; α_c=9.8	8.0 (7.8)
Thermal Conductivity, $Wm^{-1}K^{-1}$	17-20	60-70	34§
Electrical Resistivity, $10^{-8}\Omega$-m	60 (64.0)	10 (13.1)	(21.1)
Abrasion Resistance km/cm^3 against Al_2O_3 against SiC	 4.2 1.2	 9.6 2.9	 6.7 2.4
Wear Number (for turning of steel) μm/min	>600	70	3

*Data after Holleck et al. [18], in addition, given in brackets are the results reported by De Mestral and Thevenot [17] for the same composition.

§ Estimated from the reported value of electrical conductivity, σ, using Wiedemann-Franz law for metallic conductors: $k=L\sigma T$, where k - thermal conductivity, $L=2.44\times10^{-8}\Omega$-$W/K^2$- constant, T - absolute temperature.

TABLE III. Properties of Selected Cutting Tool Ceramics Compared to Titanium Borides-Titanium Carbide Composites.

Material	Flexural Strength (MPa)	Fracture toughness*, K_{IC} (MPa$\sqrt{m}$)	Hardness (GPa)	Elastic Modulus (GPa)	Thermal Expansion Coefficient ($K^{-1}x10^6$)	Thermal Conductivity ($Wm^{-1}K^{-1}$)	Wear Factor†	Abrasion Wear ASTM G65 Procedure A, mm^3/test	Source
Al_2O_3-TiC	910[3pt]	4.5	20	420	8.5	13.0	1.22	4.8	[151,152]
Sialon (Si_3N_4)	760-830[3pt]	6.5	14.6-15.6	300	3.1	9.7-17.2	1.21-1.34	9.8	"-"
Cemented Carbides (WC-Co)	2080[3pt]	8.5	17.6	610	5.1	72.7	1.03	2.2-14.3	"-"
Equimolar TiC-TiB_2 Composite	950[3pt]	5.2-7.1	23.5-25.3	440	7.8-8.0	~34§	1.78-1.87	-	"-"
Refined Platelet Composite ($TiC_{0.65}$-TiB_2-Ti_3B_4)	800[4pt]	5.3	20	450	6.5	~26§	1.26	11.1	this work

† $K_{1c}^{0.5}E^{-0.8}H^{1.43}$ after Evans and Marshal [150].

§ Estimated from the measured electrical conductivity, $\sigma=3.6x10^6(\Omega m)^{-1}$, using Wiedemann-Franz law for metallic conductors: $k=L\sigma T$, where k - thermal conductivity, $L=2.44x10^{-8}\Omega$-W/K^2- constant, T - absolute temperature.

TABLE IV. Mechanical Properties of TiC, TiB_2, and TiC-TiB_2 Composites Fabricated by Various Processing Techniques.

Composition	Process	Temperature (°C)	Pressure (MPa)	Density (% Th.)	Grain Size (μm)	Flexural Strength (MPa)	Hardness /load, kg/ (GPa)	K_{1c} (MPa$\sqrt{m}$)	Ref.
TiB_2	sintering	2100	-	99.3	2.8	363 (1000°C)	-	5.0^{DTP}	[124]
TiB_2	hot-pressing	1900	21	99	(5.3)*	579	18.2 (0.5)	7.3^{IF}	[116]
TiB_2	HIP	1900	200	99.6	-	700	25 (0.5)	5.2^{CVNB}	[117]
TiB_2-1wt%CoB	hot-pressing	1700	20	98.5	7	700	20 (20)	-	[113]
TiB_2-5 wt% W_2B_5-1wt% CoB	hot-pressing	1700	20	99.8	3	1000	22 (20)	-	[113]
TiB_2	hot-pressing	1800-1950	40	>98	(4)*	890	17.5 (1)	5^{IF}	[17]
TiB_2	SHS/DC	-	-	98	-	-	33 (0.1) 23 (0.4)	-	[81]
TiB_2	SHS/DC	-	-	99.3	17-18	-	33.5 (0.1) 12 (10)	-	[82]
TiB_2	SHS/HIP	-	3000	95			20 (0.2)	-	[118]
$TiC_{0.8}$	SHS/DC	-	-	98	-	-	20 (0.1) 16 (0.4)		[81]
TiC	SHS/DC	-	-	96.8	35-43	-	30 (0.1) 15 (10)	-	[82]
TiC	SHS/DC	-	-	96	44	-	22.6 (0.3)	-	[83]
TiC	hot-pressing	1900	21	99	(2.3)*	412	17.3 (0.5)	4.2^{IF}	[116]
TiC	hot-pressing	1600	70	99.5	8	540^{4pt}	19.7 (1)	-	[134]
TiC	hot-pressing	1700	60	98	12	480^{4pt}	-	-	[135]
TiC	hot-pressing	1800-1950	40	>98	(3)	550	26.7 (1)	4.4^{IF}	[17]
TiC	SHS/HIP	-	3000	96.5	-	-	31 (0.1)	-	[139]
1:1 TiC/TiB_2	sintering	1700 (6hr)	-	99	(1.5)*	-	23.5 (2)	7.1^{IF}	[18]
1:1 TiC/TiB_2	sintering	2000	-	99	3	954	21.5 (0.2)	-	[21]
1:1 TiC/TiB_2 +2.5wt%(Ni+X)	sintering	1550	-	>90	-	1100	18.3 (30)	7.1^{IF}	[24]
TiC/TiB_2-(5-10)wt% Ni	directional reaction of Ti with B_4C	1600-1800	-	>99	-	450-700	-	-	[27]
2:1 TiC/TiB_2	hot-pressing	1800-1950	40	>98	(3,4)*	1080	24.8 (1)	5.2^{IF}	[17]
2.5:1 TiC/TiB_2	reactive hot-pressing	1600	40	>95	(6,10)*		22 (10)	-	this work
1:1$TiC_{0.5}$/TiB_2	reactive hot-pressing	1600	60	99	2	800^{4pt}	24 (10)	4.1^{CVNB}	this work
$TiC_{0.65}$/TiB_2/Ti_3B_4	reactive hot-pressing	1600	70	99	(8)*	800^{4pt}	20 (10)	5.3^{CVNB}	this work

* Given in brackets are starting powders particle sizes, μm.
DTP-Double Torsion Plate; IF-Indentation Fracture; CVNB-Chevron-Notched Beam.

Table V. Characteristics and sources of starting powders.

Powder	Shape	Particle size median±S.D. (μm)	Purity / Known impurities (% wt.)	Supplier
Titanium dehydride, Ti (4N)	angular	43±21	99.99%*	Alta Group, Fombell, PA
Titanium hydride, Ti (H4N)	angular	33±21	99.99%* (4 at% H)	Alta Group, Fombell, PA
Titanium, Ti (98.5)	spherical	5±2	98.5% (0.8% O, 0.3% Fe)	MER Corp., Tucson, AZ
Boron Carbide, B_4C	angular	6±2	99+%	ESK, Germany
Substoichiometric Titanium Carbide, $TiC_{0.5}$	angular	13±4	(~1% WC)	Custom-produced (SHS), Exotherm Corporation, Camden, NJ
Titanium Diboride, TiB_2	angular	10±5	99.5%*	Johnson Matthey Company, Ward Hill, MA

* Metal Basis

Table VI. Summary of X-ray diffraction results of the studied compositions. Runs 1-7 are listed in terms of increasing TiC_x content.

The number of samples for each composition are shown in brackets.

Run #	Starting Composition	As hot pressed composition	Composition after vacuum annealing for 16 hr at 1600°C	Composition after vacuum annealing for 32 hr at 1600°C
Equilibrium compositions:				
1.	4:1 Ti/B_4C (5)	● TiB_2; ● Ti_3B_4; ● $TiC_{0.64}$	● TiB_2; ● Ti_3B_4; ● $TiC_{0.64}$	● TiB_2; ● Ti_3B_4; ● $TiC_{0.64}$
2.	1:0.5:1 Ti/C/TiB_2 (2)	● TiB_2; ● Ti_3B_4; ● $TiC_{0.64}$	● TiB_2; ● Ti_3B_4; ● $TiC_{0.64}$	● TiB_2; ● Ti_3B_4; ● $TiC_{0.64}$
3.	4.67:1 Ti/B_4C (2)	● TiB_2; ● Ti_3B_4; ● TiB; ● $TiC_{0.64}$	◑ TiB_2; ● Ti_3B_4; ● TiB; ● $TiC_{0.64}$	● Ti_3B_4; ● TiB; ● $TiC_{0.64}$
4§	5:1 Ti/B_4C (2)	◑ TiB_2; ● Ti_3B_4; ● TiB; ● $TiC_{0.64}$	● Ti_3B_4; ● TiB; ● $TiC_{0.64}$	----
5§	5.25:1 Ti/B_4C (1)	◑ TiB_2; ● Ti_3B_4; ● TiB; ● $TiC_{0.64}$	● Ti_3B_4; ● TiB; ● $TiC_{0.64}$	----
6§	6:3:1 Ti/C/TiB_2 (1)	◑ TiB; ● $TiC_{0.61}$	● TiB; ● $TiC_{0.6}$	----
7§	7:3.5:1 Ti/C/TiB_2 (1)	◑ TiB; ● $TiC_{0.63}$	◑ TiB; ● $TiC_{0.6}$	----
Non-equilibrium compositions:				
8.	4:1 Ti† /B_4C	● TiB_2; ● $TiC_{0.5}$	● TiB_2; ● $TiC_{0.5}$	----
9.	1:1 $TiC_{0.5}/TiB_2$	● TiB_2; ● Ti_3B_4; ● $TiC_{0.6}$	● TiB_2; ● Ti_3B_4; ● $TiC_{0.6}$	● TiB_2; ● Ti_3B_4; ● $TiC_{0.6}$
10	3:1 $TiC_{0.5}/TiB_2$	● TiB_2; ◑ Ti_3B_4; ◑ TiB; ● $TiC_{0.56}$	◑ TiB_2; ● Ti_3B_4; ○ TiB; ● $TiC_{0.57}$	○ TiB_2; ● Ti_3B_4; ○ TiB; ● $TiC_{0.57}$
11	5:1 $TiC_{0.5}/TiB_2$	○ TiB_2*; ○ Ti_3B_4; ● TiB; ● $TiC_{0.57}$	◑ Ti_3B_4; ◑ TiB; ● $TiC_{0.57}$	● Ti_3B_4; ○ TiB; ● $TiC_{0.57}$

The relative scale of intensity of X-ray peaks: ● very strong; ◉ strong; ◉ medium; ◑ weak; ○ very weak.

§ Compositions 4-7 were cold-pressed at 400 MPa and pressureless-sintered in vacuum at 1600°C for 4 hours.

† Low purity (98.5 %) Ti powder.

* Contrary to X-ray results, according to microstructural observations the volume fraction of TiB_2 was actually higher than the other borides.

TABLE VII. Summary of Composites Produced in This Study for Property Evaluation.

Composite	Starting Composition (mole ratio)	Final Composition (vol% of phases)	Starting Powders Particle Size, μm (area-based* mean±S.D.)	Final Grain Sizes, μm	
				TiC_x	TiB_2
Platelet	4:1 Ti/B_4C	$Ti_3B_4/TiB_2/TiC_{0.65}$ (33%:30%:37%)	Ti-36±17 B_4C-5±3	6	≤1
Equilibrium Equiaxed	1:0.5:1 $Ti/C/TiB_2$	$Ti_3B_4/TiB_2/TiC_{0.65}$ (36%:30%:34%)	Ti-17±9 TiB_2-6±4	–	4-25
Platelet-Refined	4:1 Ti(hydride)/B_4C	$Ti_3B_4/TiB_2/TiC_{0.65}$	Ti-7±4 to 9±6 B_4C-5±3	–	≤1
Nonequilibrium Equiaxed-7 μm grain	1:1 $TiC_{0.5}/TiB_2$	$TiC_{0.5}/TiB_2$ (44%:56%)	$TiC_{0.5}$-7±3 TiB_2-6±4	7	7
Nonequilibrium Equiaxed-4 μm grain	1:1 $TiC_{0.5}$/TiB	$TiC_{0.5}/TiB_2$ (44%:56%)	3.5±4 (WC-milled 12hrs)	4	4
Nonequilibrium Equiaxed-2 μm grain	1:1 $TiC_{0.5}/TiB_2$	$TiC_{0.5}/TiB_2$ (44%:56%)	2.6±3 (WC-milled 24hrs)	2	2
TiC0.57	5:1 $TiC_{0.5}/TiB_2$	$TiC_{0.57}$ + 20 vol% of borides (TiB_2, Ti_3B_4, TiB)	$TiC_{0.5}$-7±3 TiB_2-6±4	–	–

TABLE VIII. Summary of the room temperature mechanical properties for the composites tested in this study. Numbers in brackets indicate the number of samples used for each measurement.

Composite	Elastic Modulus GPa	Vickers Hardness* GPa	Flexural Strength* MPa	Fracture Toughness* MPa$\sqrt{m}$	Critical Flaw Size§ μm
Platelet (36 μm Ti)	450	19 ± 3	630 ± 50 (5)	5.8 ± 0.6 (3)	27.0
Equilibrium Equiaxed	450	21 ± 2	515 ± 10 (3)	4.4 ± 0.4 (3)	23.2
Platelet-Refined (9 μm Ti)	450	20 ± 2	800 ± 30 (5)	5.3 ± 0.5 (4)	14.0
Nonequilibrium Equiaxed-7 μm grain	460	23 ± 3	430 ± 20 (5)	_	28.9
Nonequilibrium Equiaxed-4 μm grain	460	23 ± 3	700 ± 10 (5)	4.1 ± 0.5 (4)	10.9
Nonequilibrium Equiaxed-2 μm grain	460	24 ± 2	790 ± 15 (3)	_	8.6
TiC0.57	350	16±2	525 ± 10 (3)	_	_

* A 10 kg load was used in these measurements.

§ Calculated using the Griffith relationship $a_c=(K_{IC}/\sigma)^2/\pi$, assuming a semicircular surface crack or half-length of a circular volume crack.

TABLE IX. Comparison of the Calculated and Measured Thermal Shock Resistance Characteristics for the Composites Studied in This Work and Comparable Materials.

Composite (specimen size)	Flexural Strength, MPa	Calculated Thermal Shock Parameter*, °C $R=\sigma_{fl}(1-\nu)/E\alpha$	Measured Critical Temperature Change, ΔT_c	Calculated Ratio of $\Delta T_c/R$, $(\sigma_t/\sigma_{fl})*F(k/rh)$	Source
equiaxed-4 μm grain (1.5x2x25mm^3)	700	174	330-380	1.9-2.2 (≈2.05)	this work
equiaxed-2 μm grain (1.5x2x25mm^3)	790	196	430-480		"-"
equiaxed-2 μm grain-heat-treated (1.5x2x25mm^3)	870	215	**440**-calculated		"-"
platelet-refined (Ti-11μm) (1.5x2x25mm^3)	830	210	330	1.6	"-"
20% TiB_2-55%TiC-25%SiC, molar% (3x4x18mm^3)	1200	286	300	1.05	[148]
ZrO_2-20wt%Al_2O_3 (2x4x15mm^3)	~700	~230	280	~1.2	[174]

*The measured values of elastic modulus (E) for the produced composites are given in Table VIII, Poisson's ratio (ν) and thermal expansion coefficient (α) are taken to be 0.2 and $7x10^{-6}K^{-1}$, respectively.

TABLE X. Wear Resistance of Optimized Platelet Composite Compared to Selected Engineering Ceramics (Data Obtained by ASTM G65 A Dry Sand Abrasion Wear Test).

Material	Volume Loss, mm^3	Source of Data
Platelet composite (TiC-TiB_2-Ti_3B_4)	11.1	This work
Al_2O_3	41.7	Ref. [152]
Al_2O_3-TiC	4.8	"-"
Sialon	9.8	"-"
SiC	7.3	"-"
Cemented Carbides	2.2-14.3	"-"

FIGURES

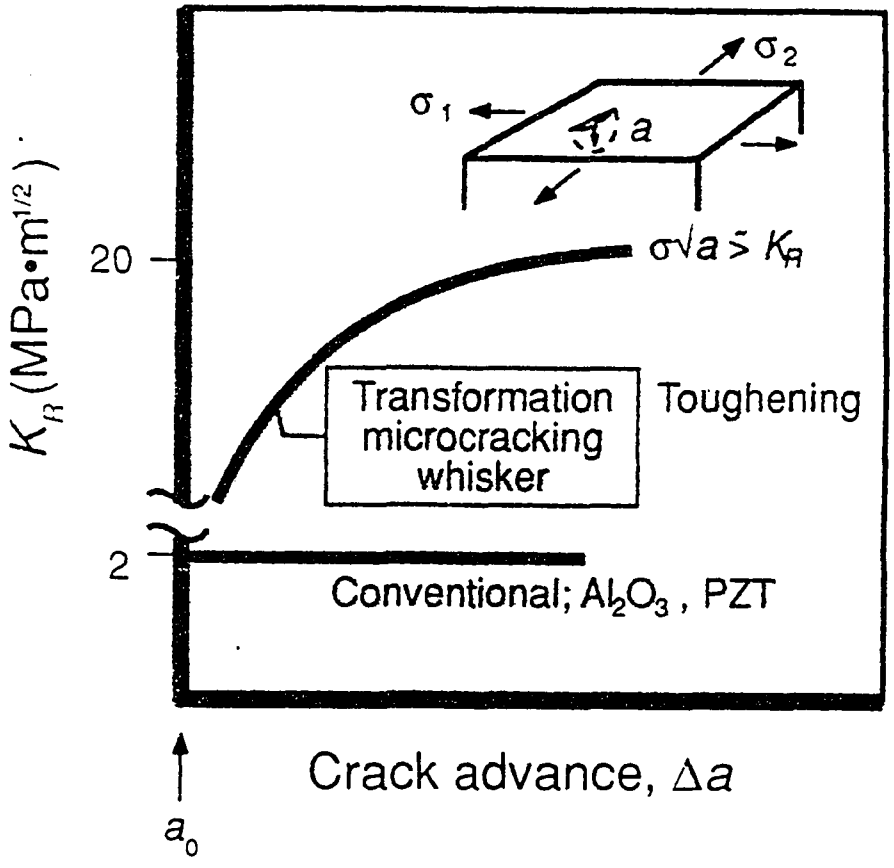

Figure 1 Resistance-curve behavior characteristic of tough ceramics [29]: K_R is the fracture resistance and Δa is the crack extension.

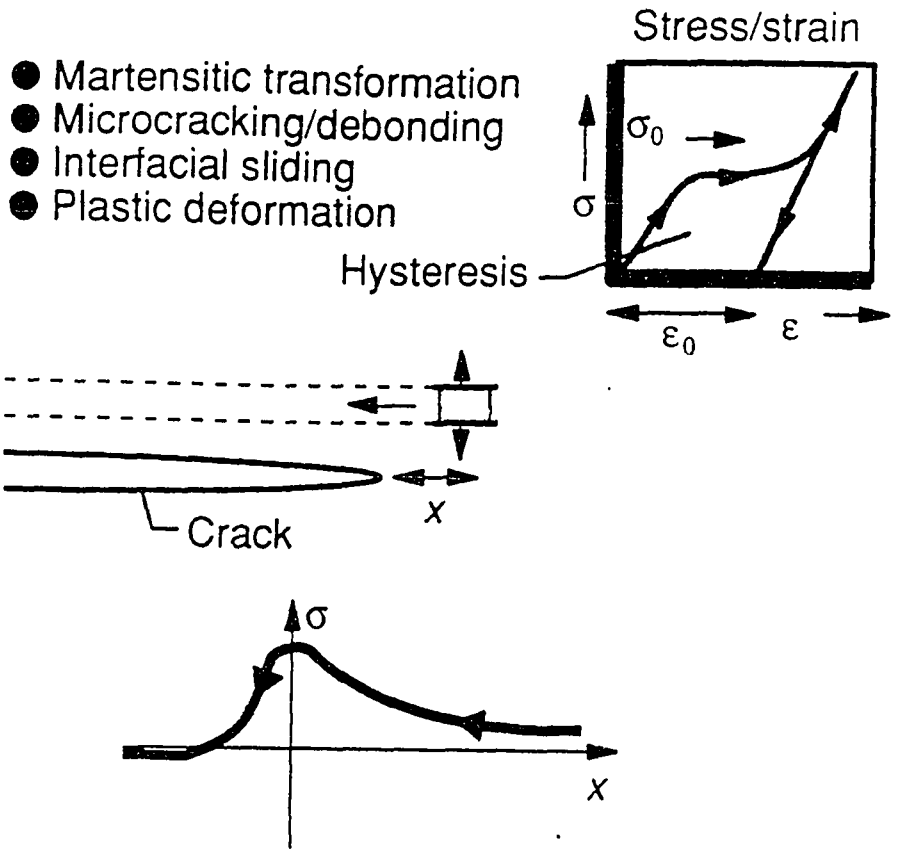

Figure 2 Schematic diagram illustrating non-linear elemental response and the resulting stress-strain hysteresis associated with major toughening mechanisms in ceramics [29].

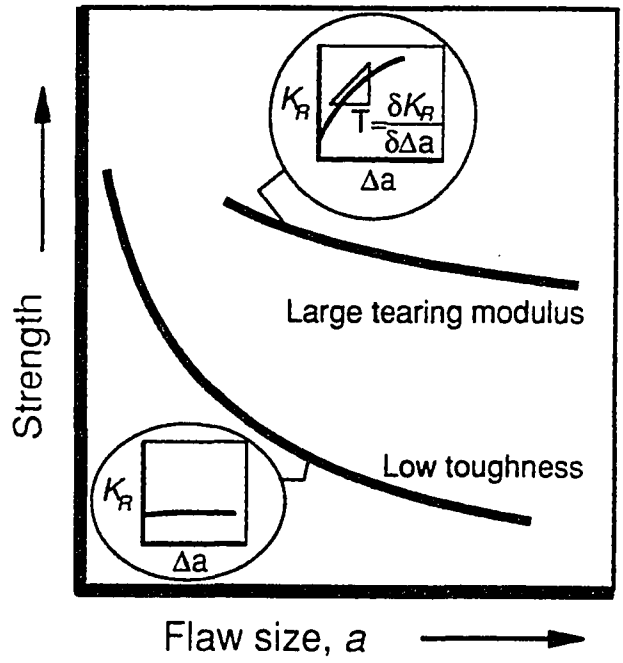

Figure 3 Effects of damage (crack extension) on the strength of low-toughness and idealized high-toughness high-strength ceramics [29]. The tearing modulus (T) is the slope of the resistance curve. Flaw-tolerant ceramics is associated with large tearing modulus but rarely with high strength.

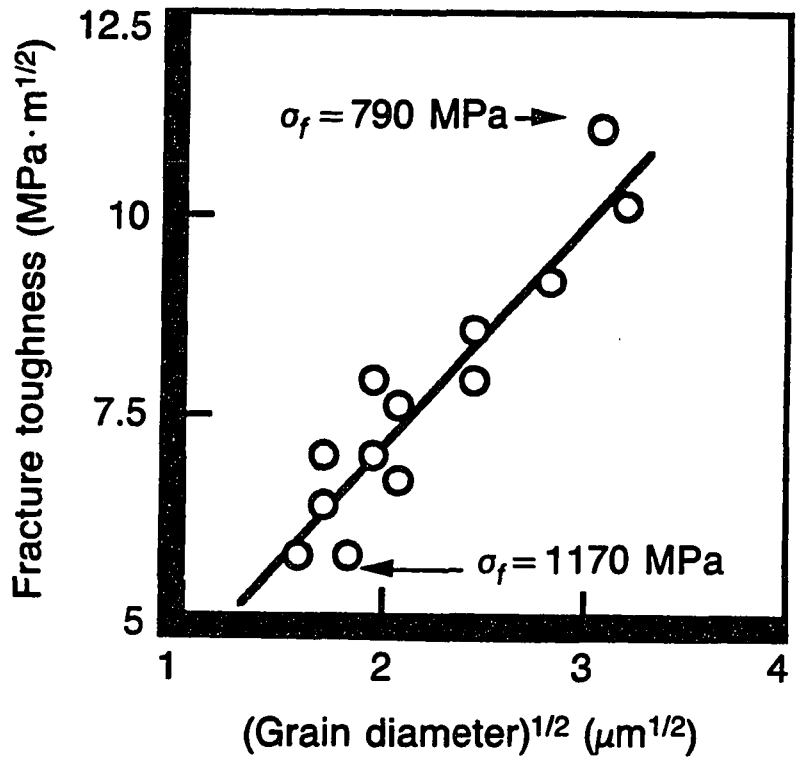

Figure 4 Increase in fracture toughness and simultaneous decrease in strength of self-reinforced silicon nitride with increase in diameter of the elongated grains [31]. Toughening is associated with crack bridging and pullout of the elongated matrix grains, however, the presence of these large grains and glassy grain boundary phase deteriorate the attendant strength

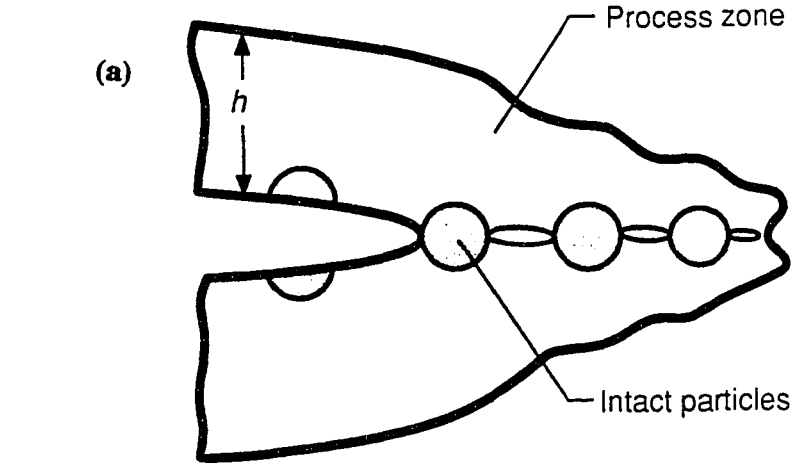

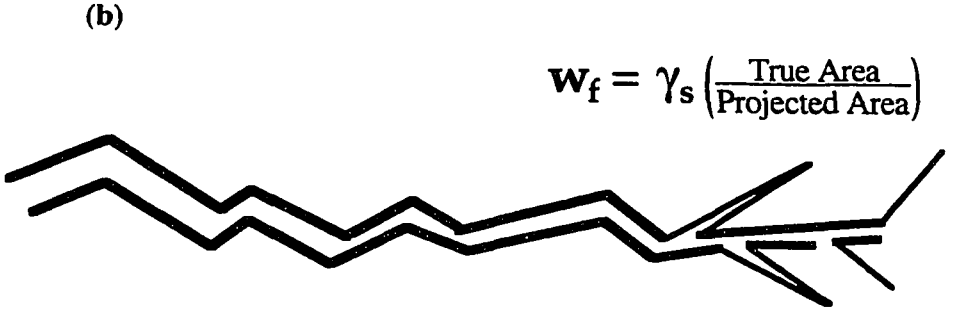

Figure 5 Schematic diagram illustrating three principal toughening mechanisms: (a) process-zone and bridging-zone mechanisms [29]; (b) crack deflection and crack branching [30].

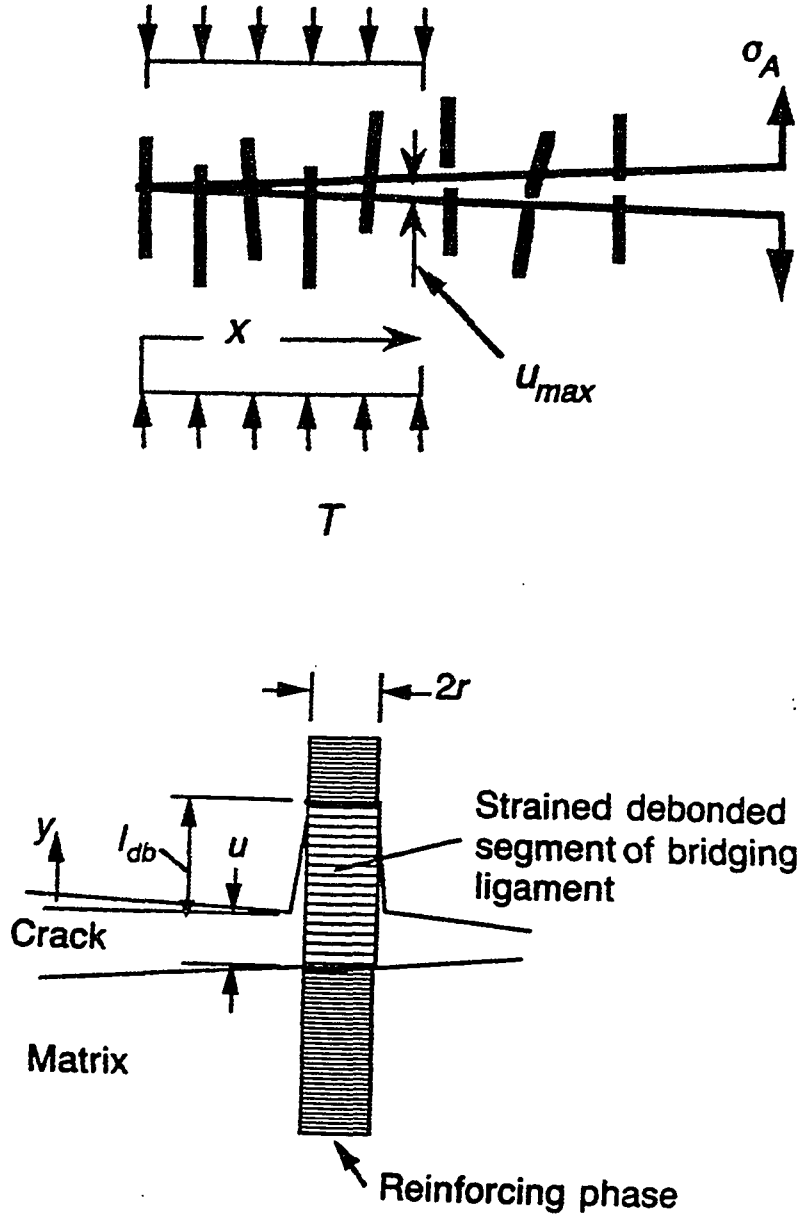

Figure 6 Schematic of crack bridging by discontinuous reinforcing phases [31]: (a) Intact ligaments of discontinuous reinforcing phase impose a crack closure stress in the wake of the crack tip and enhance the fracture resistance of the brittle matrix; (b) Crack-opening displacement characterizing bridging zone is related to the tensile displacement in elastic bridging ligaments in the absence of interfacial friction. At the end of the bridging zone, the maximum crack opening is equivalent to the displacement in the ligament corresponding to its fracture stress.

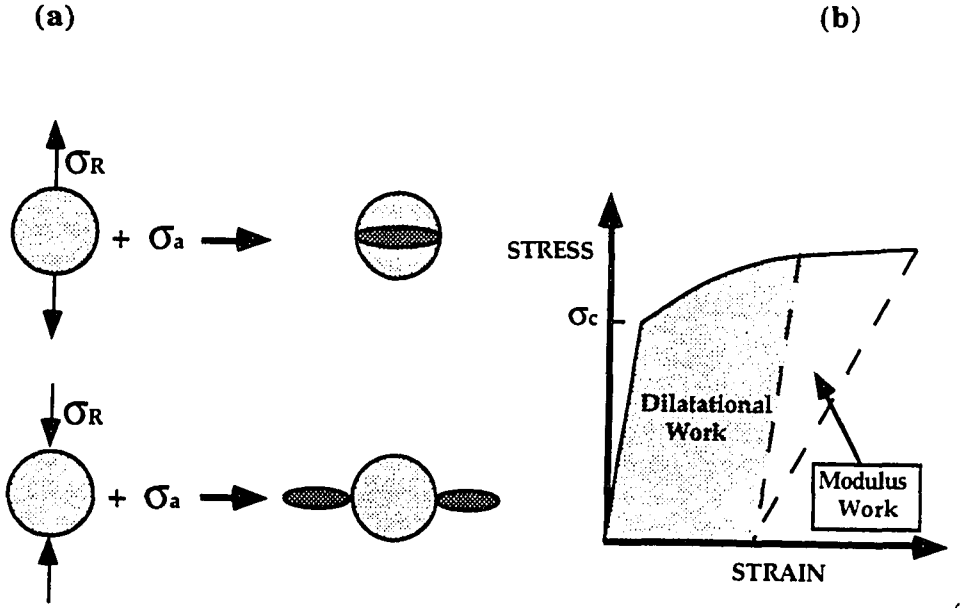

Figure 7 Schematic of microcrack toughening [29]: (a) formation of the residual stress-induced microcracks in or near second phase particles results in release of strain energy (modulus work) and residual microcrack opening (dilatational work); (b) the resulting stress-strain response.

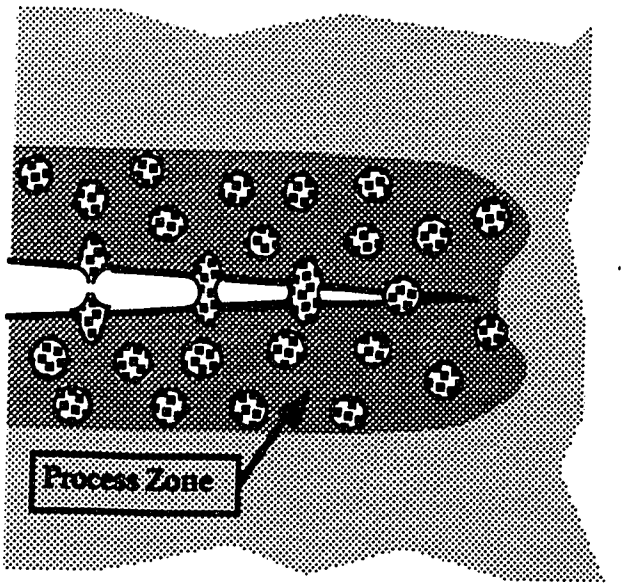

Figure 8 Schematic of ductile phase toughening [30]. Ductile second-phase particles increase the attendant toughness by plastic dissipation in the process zone, as well as by crack bridging.

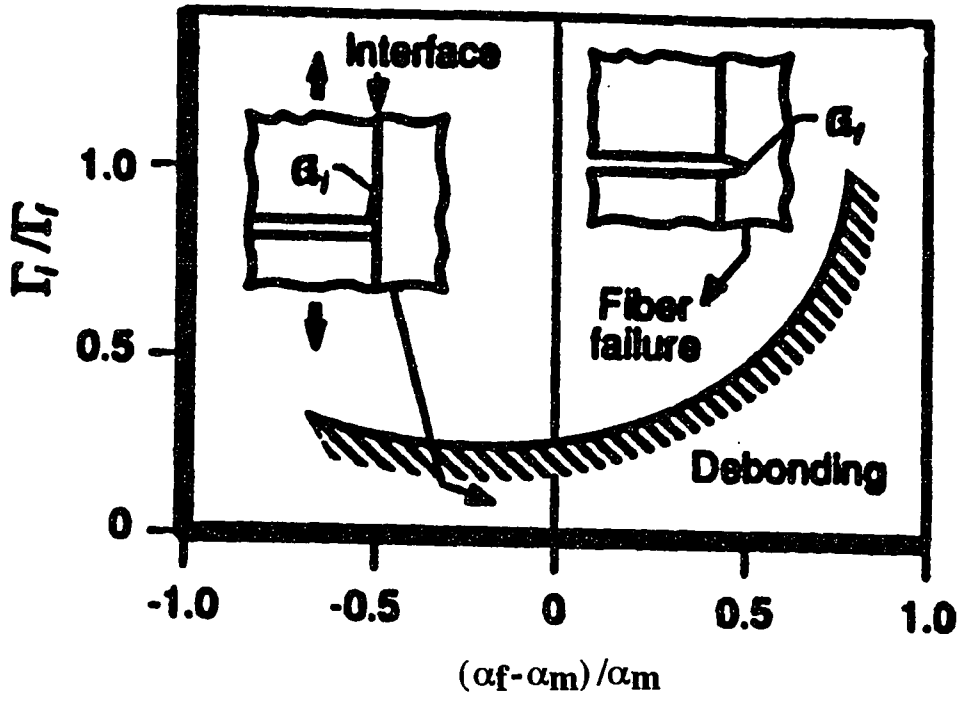

Figure 9 Fracture energy and thermal expansion mismatch requirements for crack-front debonding [29]. Γ_i/Γ_f -ratio of fracture energy of the bridging ligament to that of the reinforcement-matrix interface, $(\alpha_f-\alpha_m)/\alpha_m$ -relative thermal expansion mismatch between matrix and reinforcing phase.

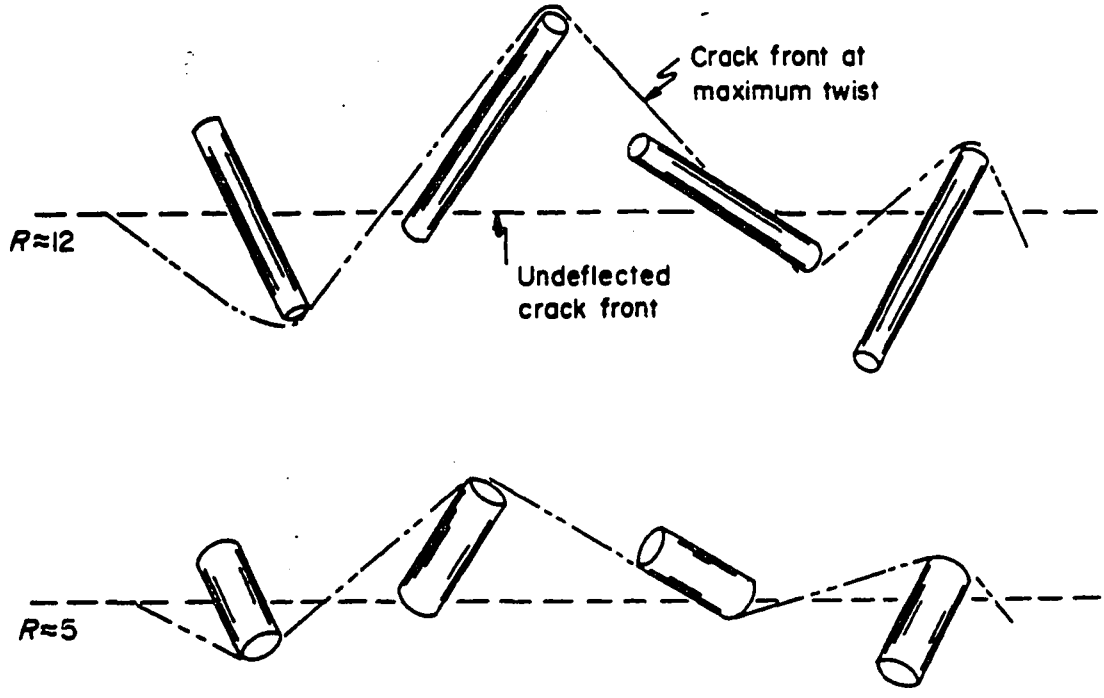

Figure 10 Schematic of twist of a crack around rod-like reinforcements of two aspect ratios (R) at constant volume fraction [34].

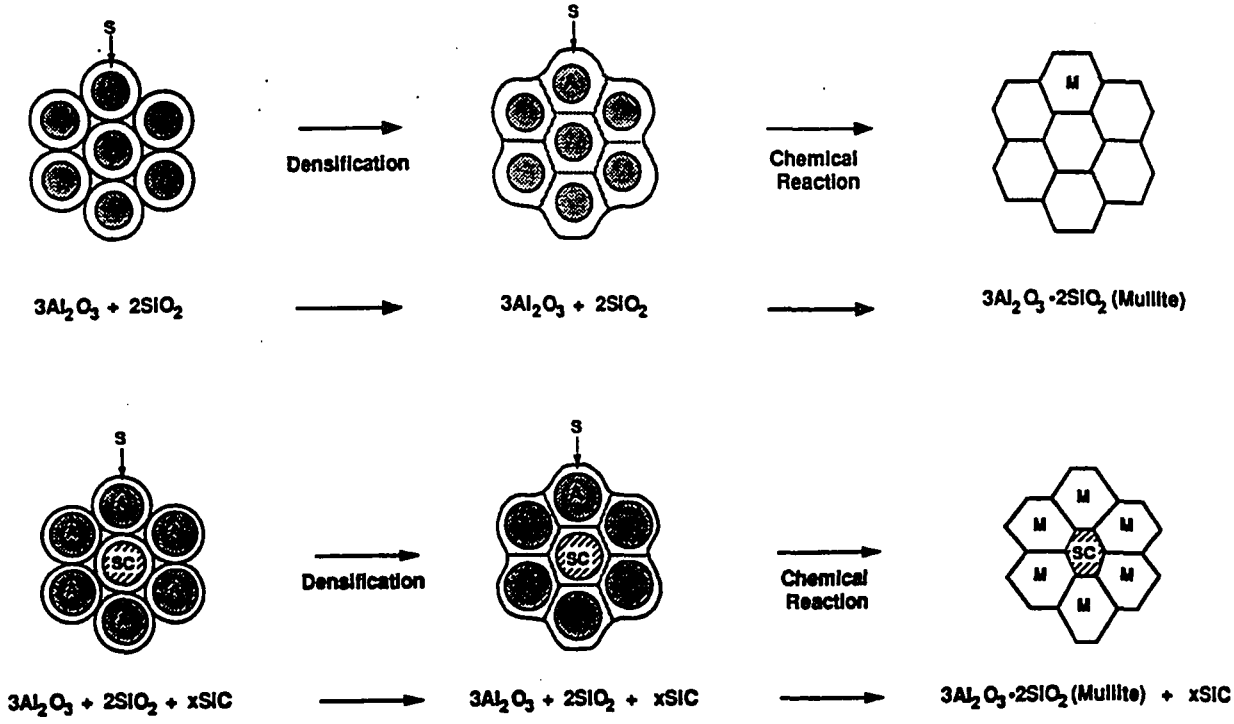

Figure 11 Schematic of Transient Viscous Sintering Process [10] for the formation of (top) single-phase mullite and (bottom) mullite/silicon carbide composite.

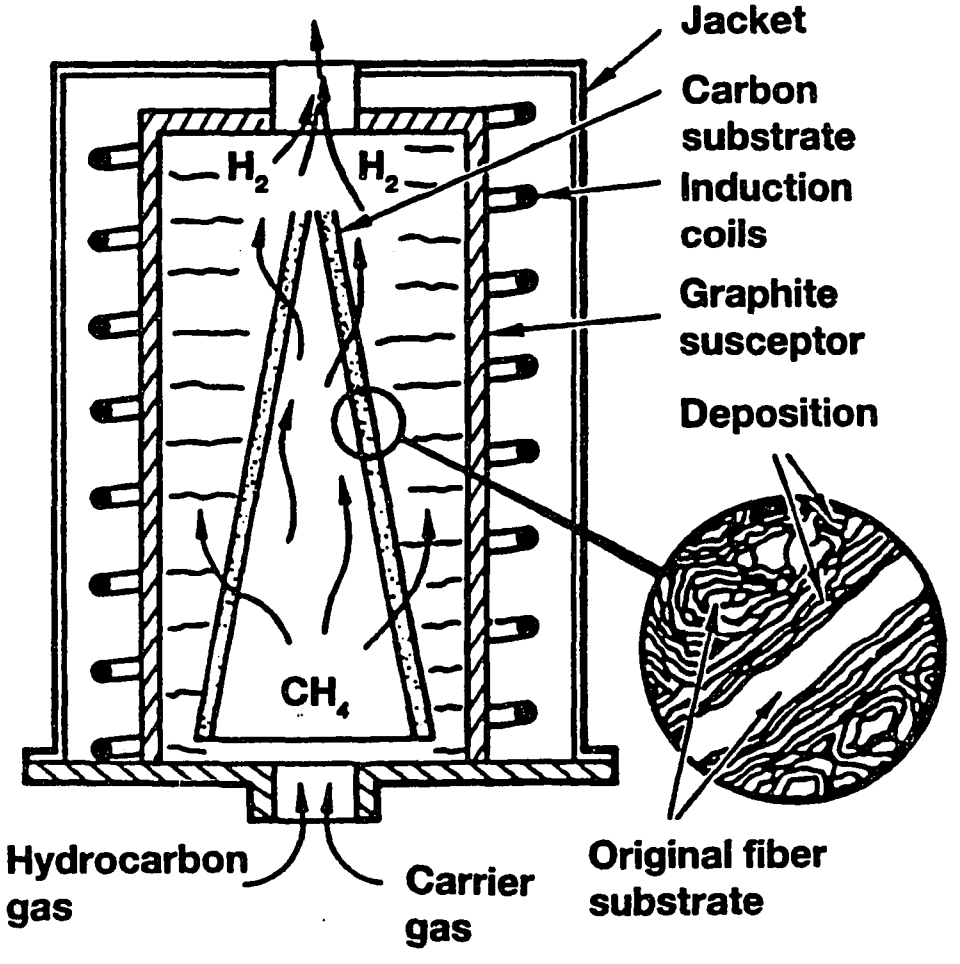

Figure 12 Schematic of isothermal CVI process for fabrication of carbon/carbon composites [53].

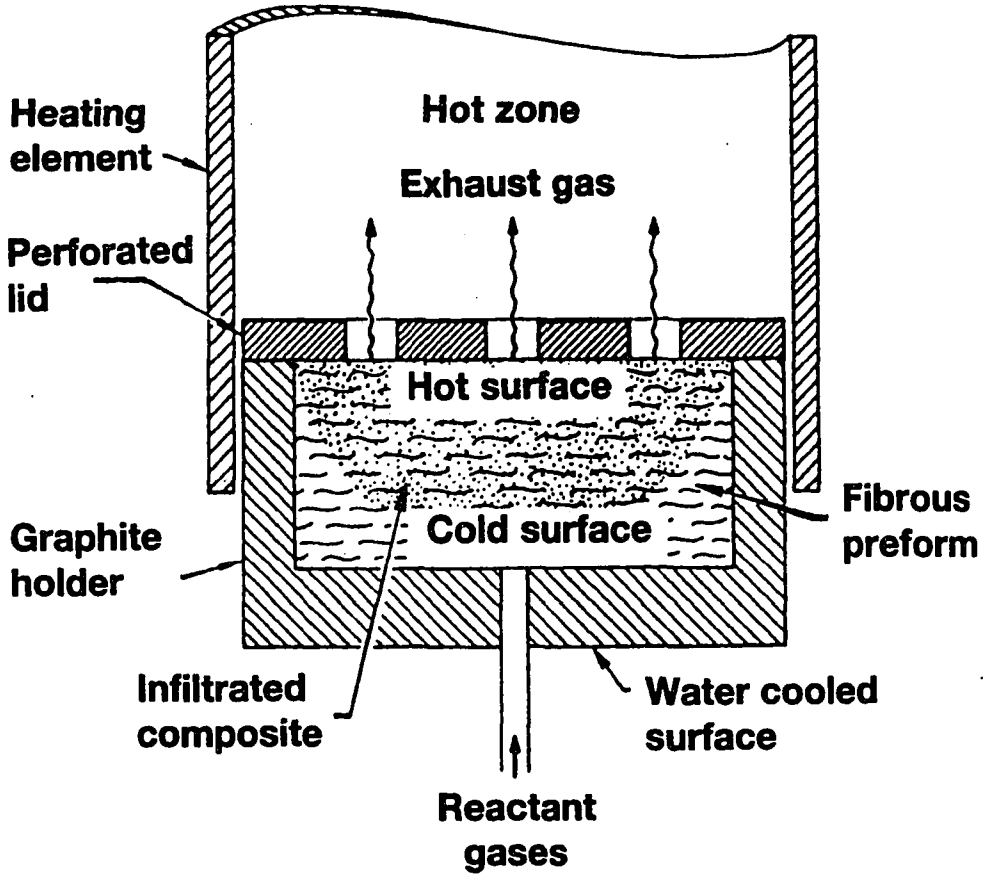

Figure 13 Schematic of forced CVI process (thermal/pressure gradient CVI) [56].

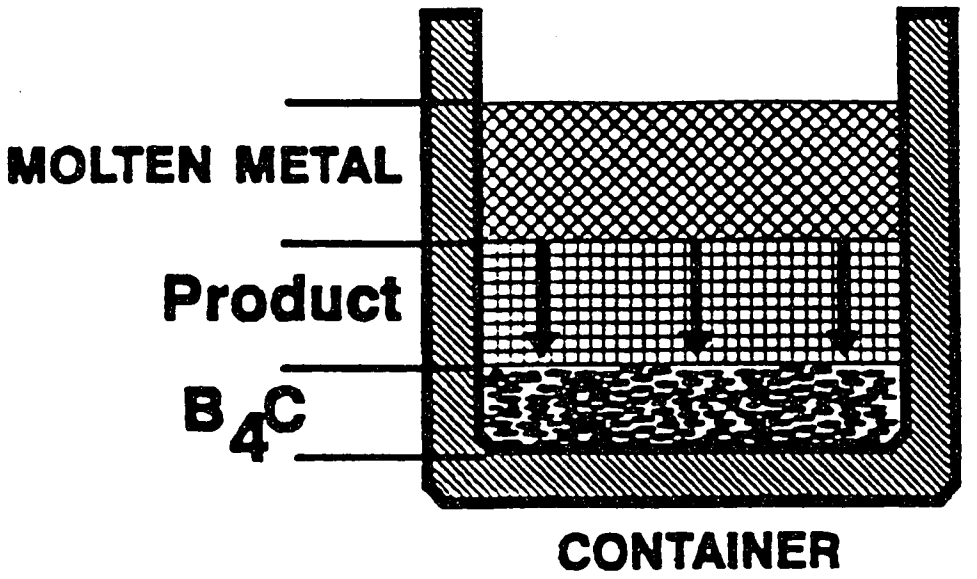

Figure 14 Schematic diagram of the DIMOX™ (direct metal oxidation) process for the fabrication of platelet-reinforced ZrB_2/ZrC/Zr composites [6].

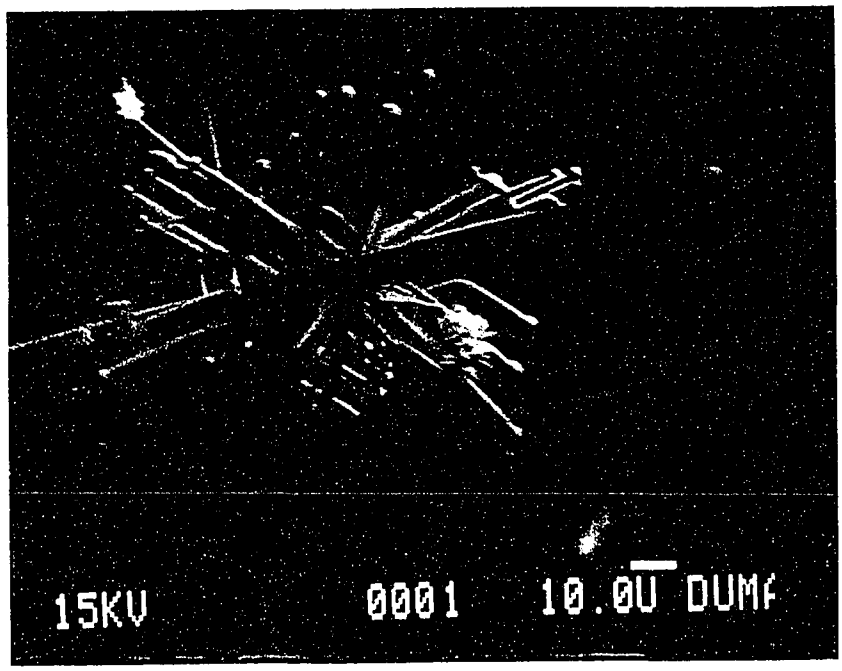

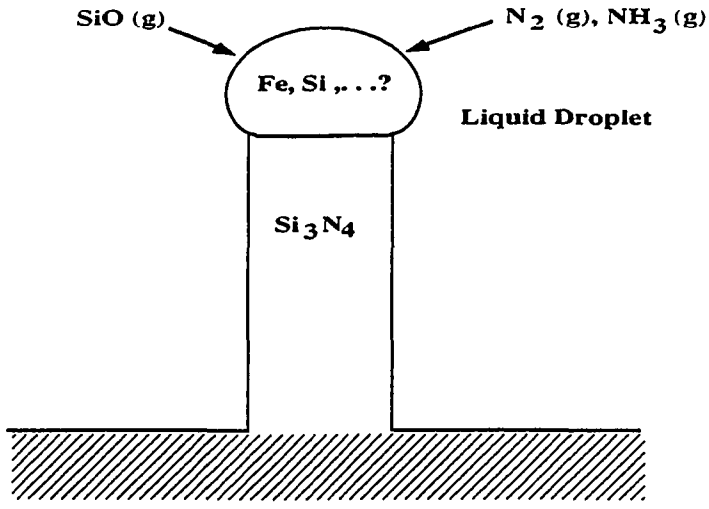

Figure 15 Illustration of potential approach for fabrication of duplex Si_3N_4 matrix-Si_3N_4 whisker microstructures:

(a) SEM micrograph of α-silicon nitride whiskers (grown by VLS mechanism on a graphite substrate placed in the flow of SiO-enriched nitrogen) similar to those formed during reaction bonding of silicon powder compacts;
(b) schematic of the VLS mechanism for growth of Si_3N_4 whiskers.

■MAIN FEATURES

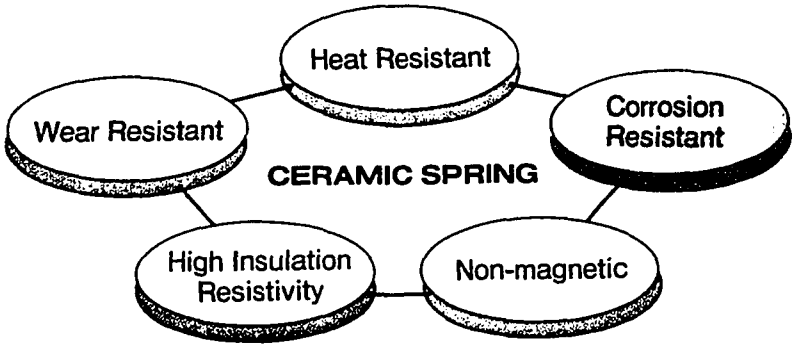

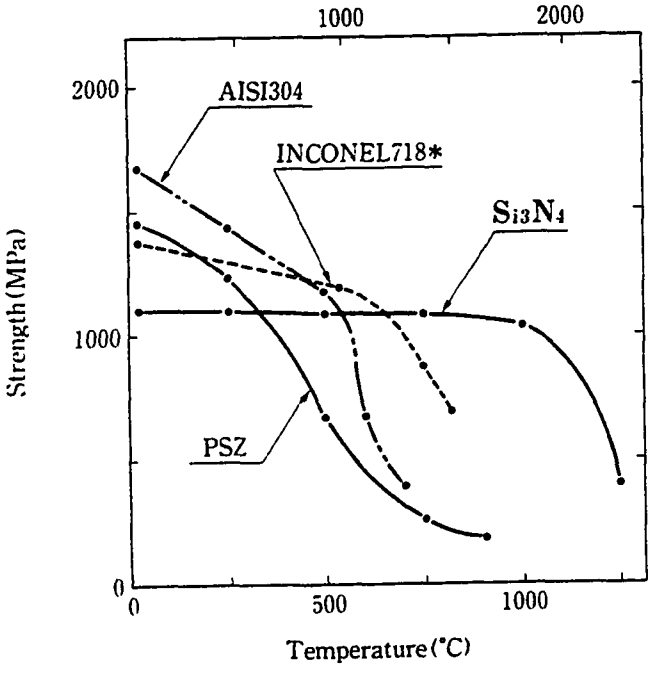

High temperature strength of various spring metarials

Ceramics: Bending strength
Metals: Tensile strength

Figure 16 Advantages of self-reinforced silicon nitride for applications as ceramic springs [73].

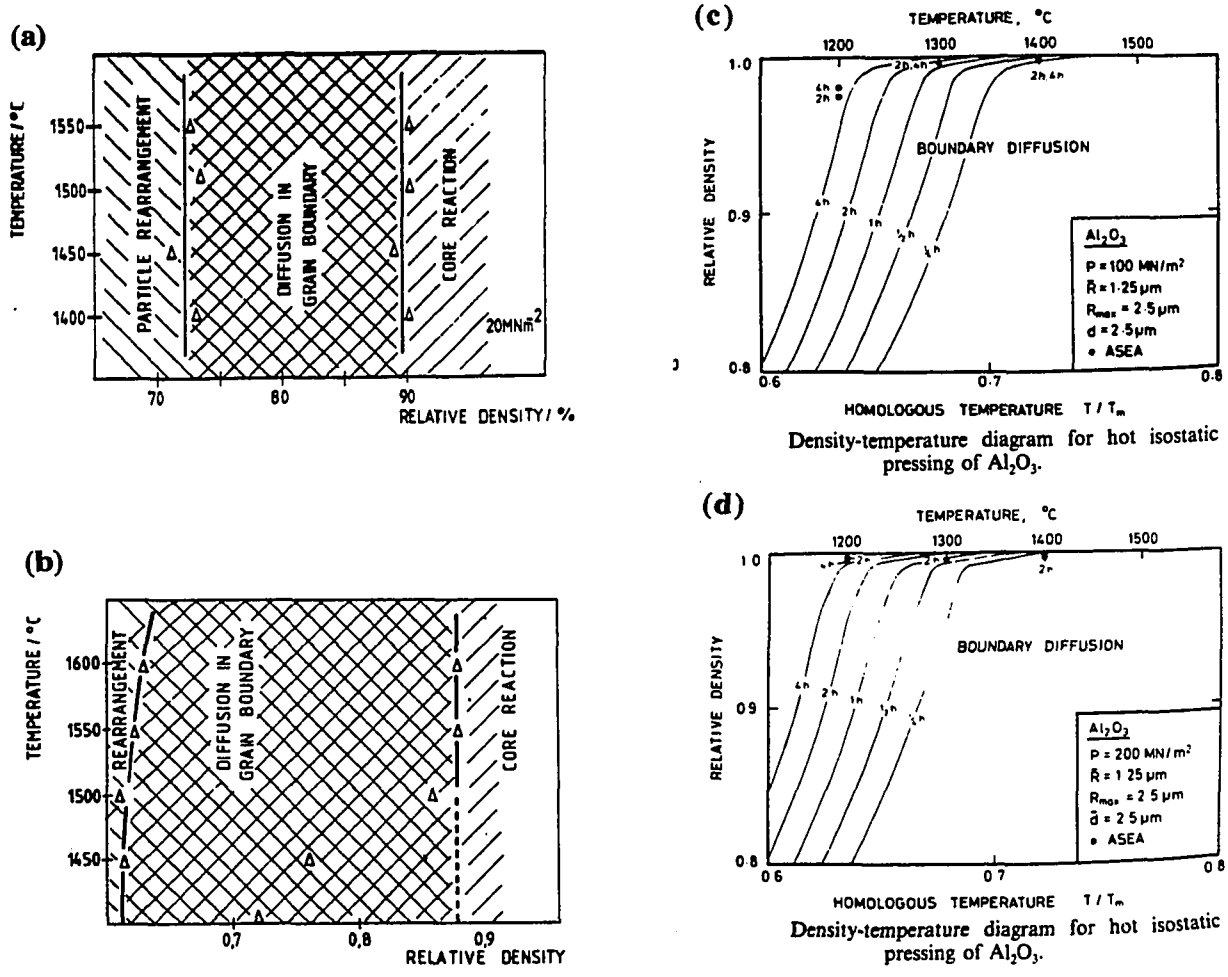

Density-temperature diagram for hot isostatic pressing of Al_2O_3.

Density-temperature diagram for hot isostatic pressing of Al_2O_3.

Figure 17 Densification maps used for comparison of dominant densification mechanisms during: (a) reactive hot-pressing of alumina zircon mixtures at 20 MPa [92]; (b) reactive sintering of the same [92]; (c,d) HIP consolidation of alumina at 100 MPa and 200 MPa, respectively [170].

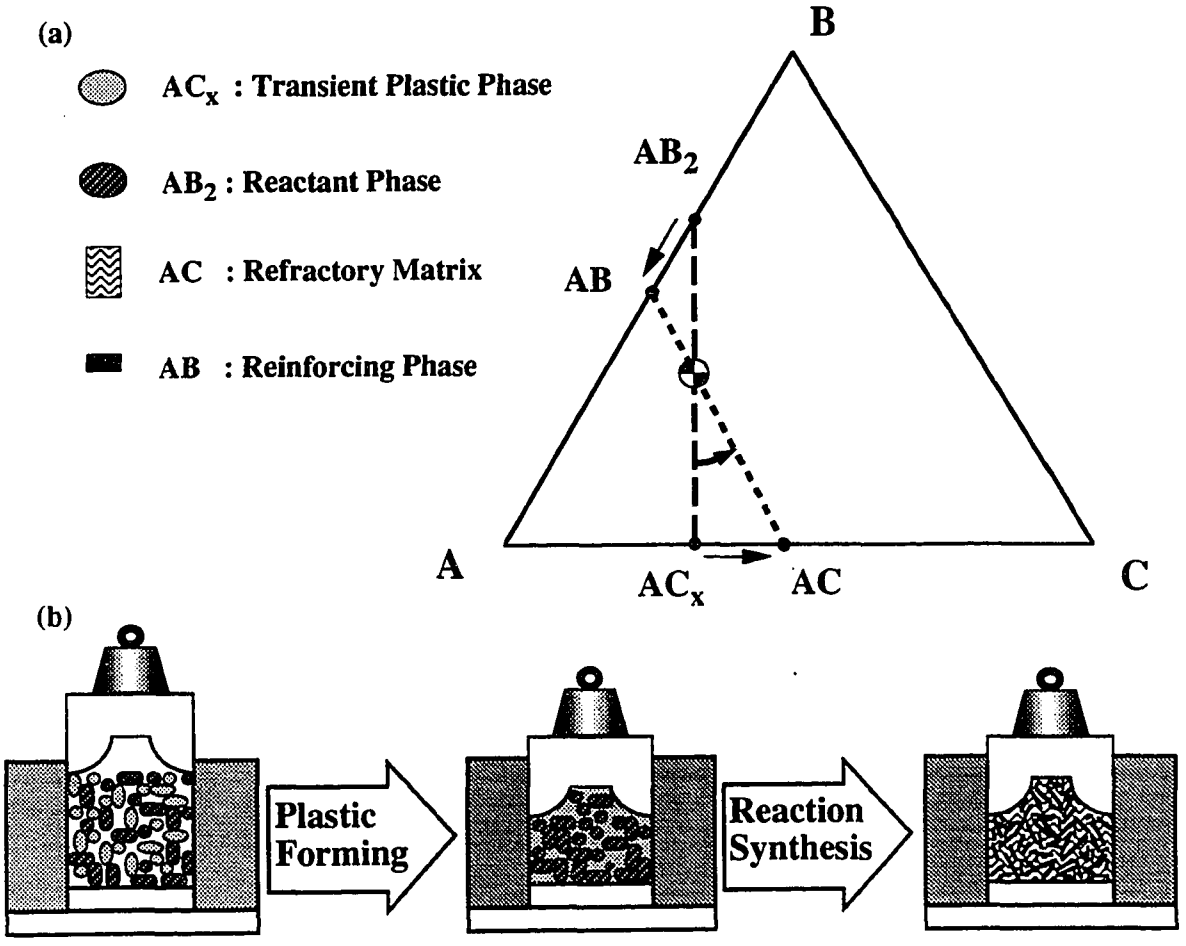

Figure 18 (a) Starting and final phases and the corresponding compositional changes during Transient Plastic Phase Processing (TPPP) in the hypothetical A-B-C ternary system; (b) Schematic of steps involved in TPPP.

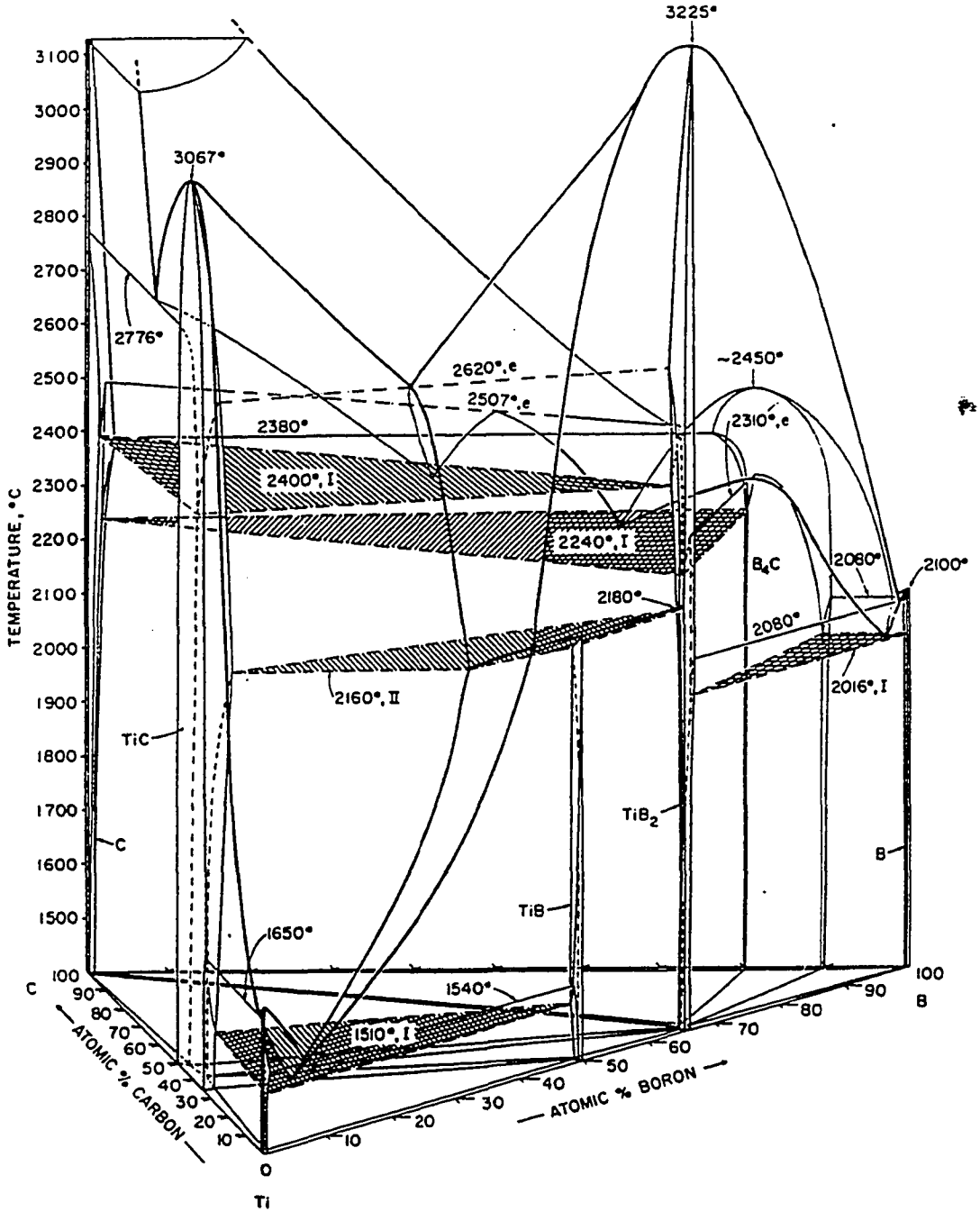

Figure 19 Isometric view of the Ti-B-C phase diagram after Rudy [100].

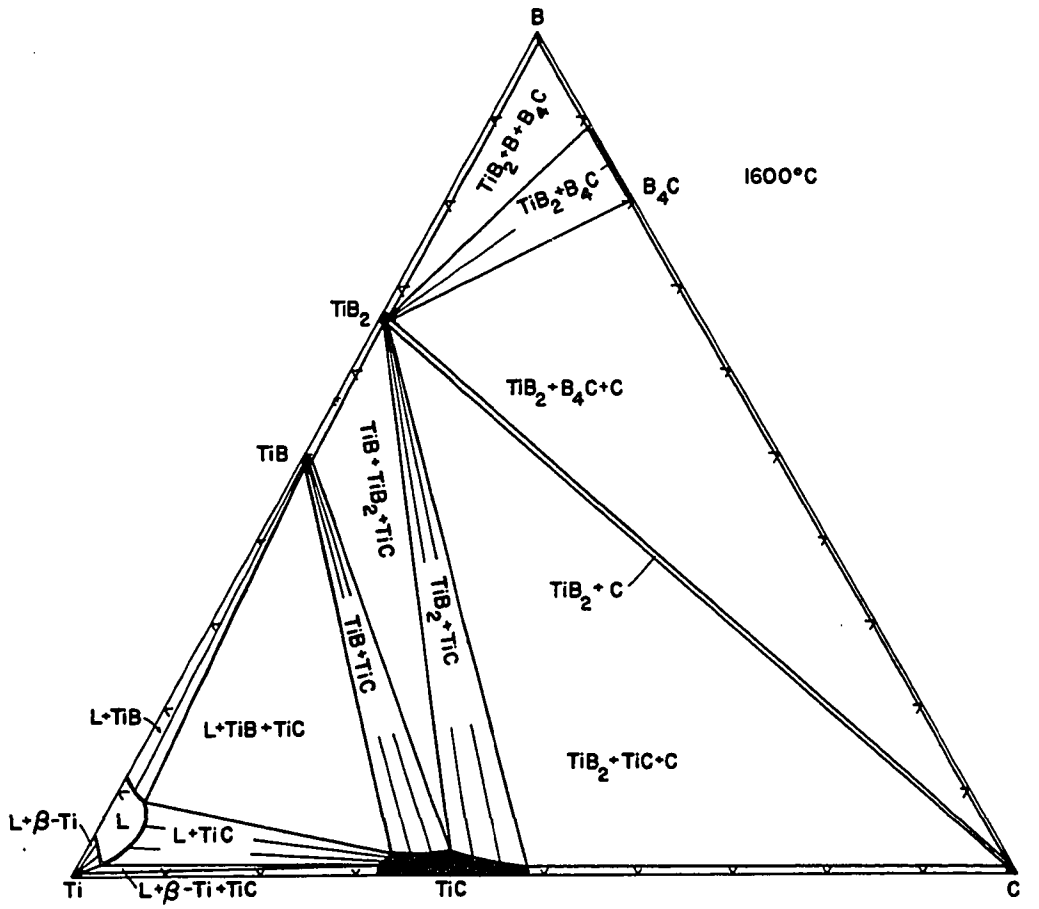

Figure 20 1600°C isothermal section of the Ti-B-C phase diagram after Rudy [100].

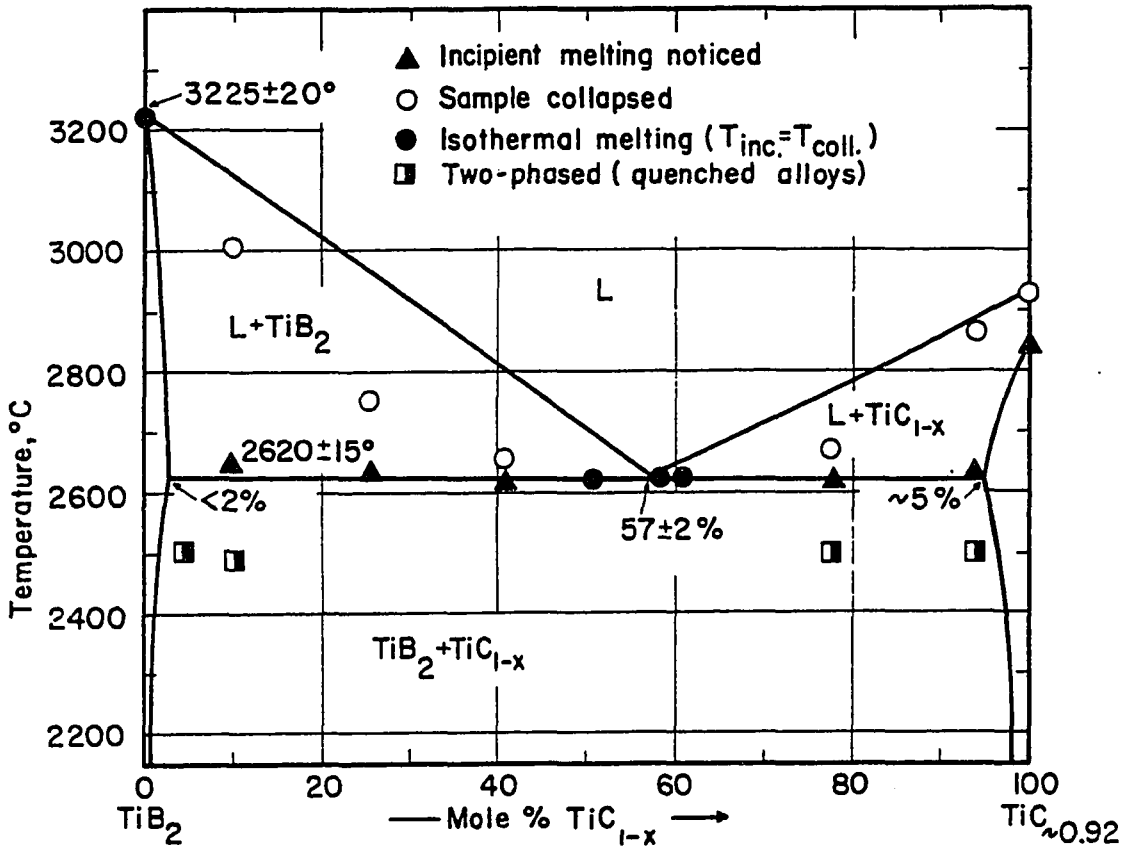

Figure 21 TiB_2-$TiC_{0.92}$ pseudobinary phase diagram after Rudy [100].

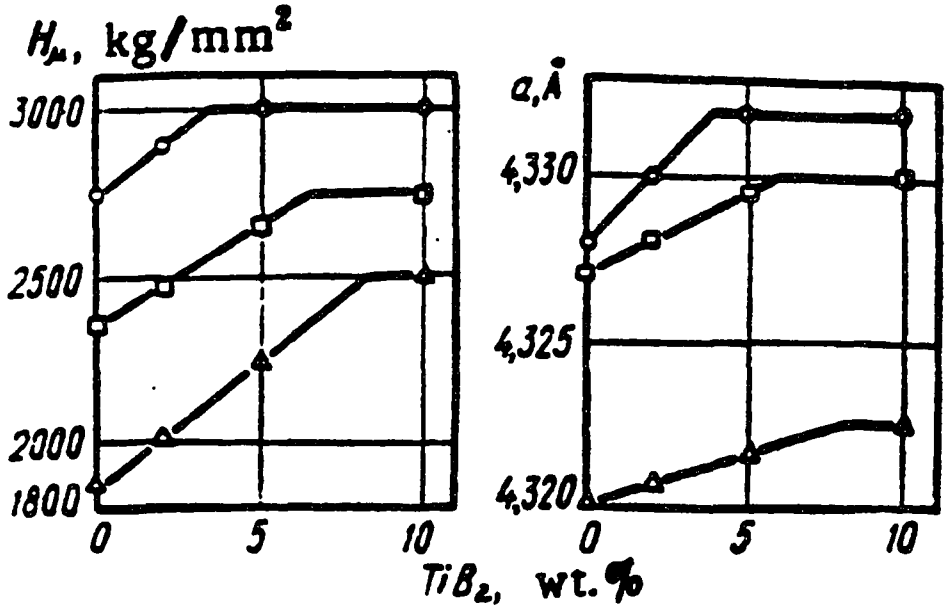

Figure 22 Effects of dissolution of TiB_2 in TiC_x alloys [106] on their (a) microhardness, H_μ, and (b) lattice constant: (O) $TiC_{0.95}$; (□) $TiC_{0.8}$; (Δ) $TiC_{0.68}$.

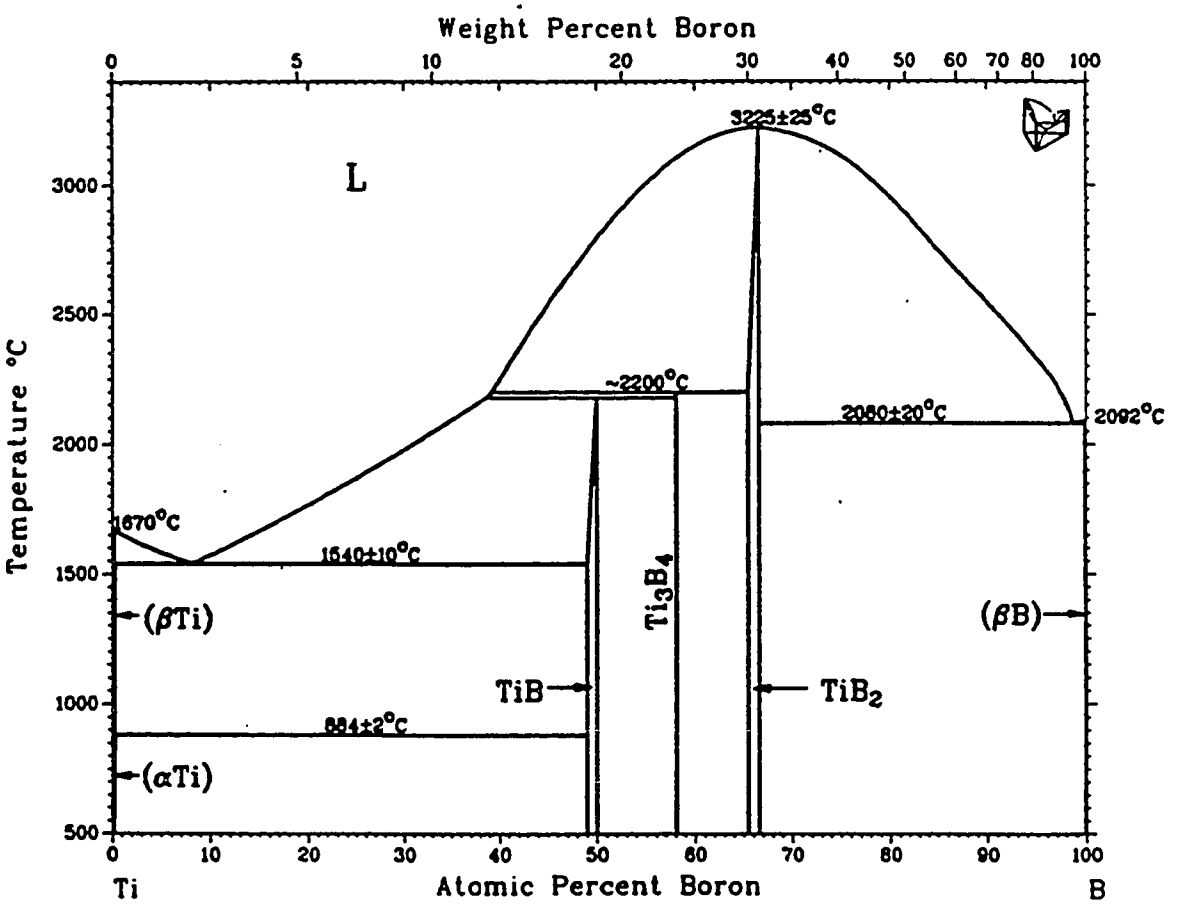

Figure 23 Ti-B binary phase diagram [101].

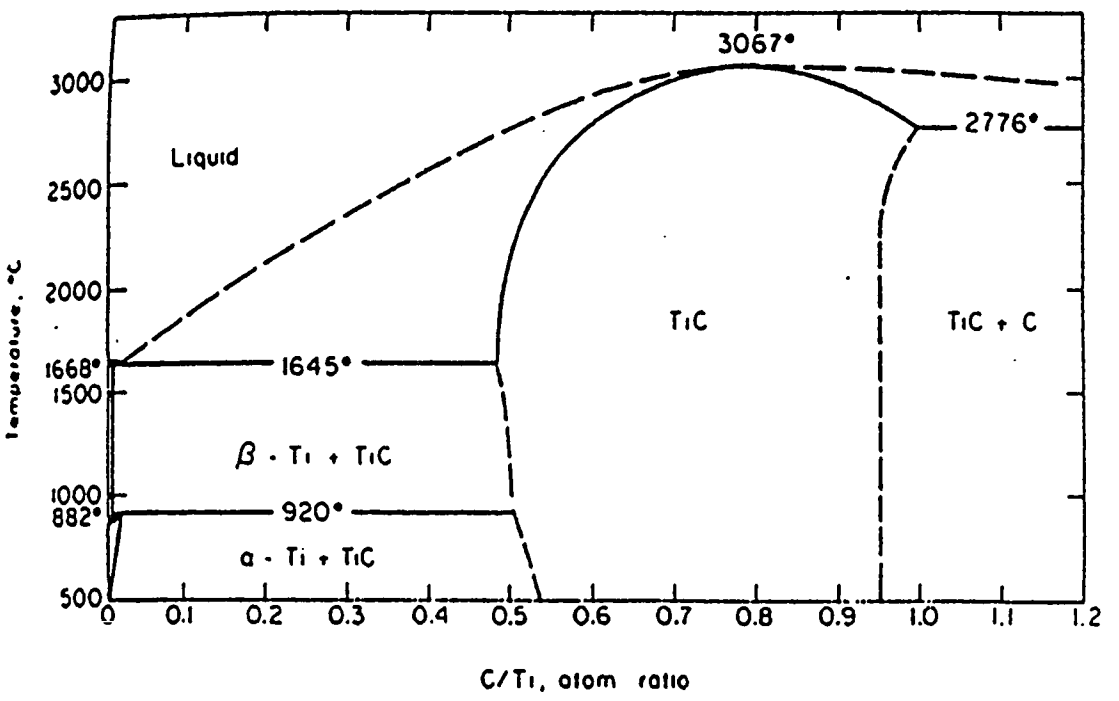

Figure 24 Ti-C binary phase diagram [100].

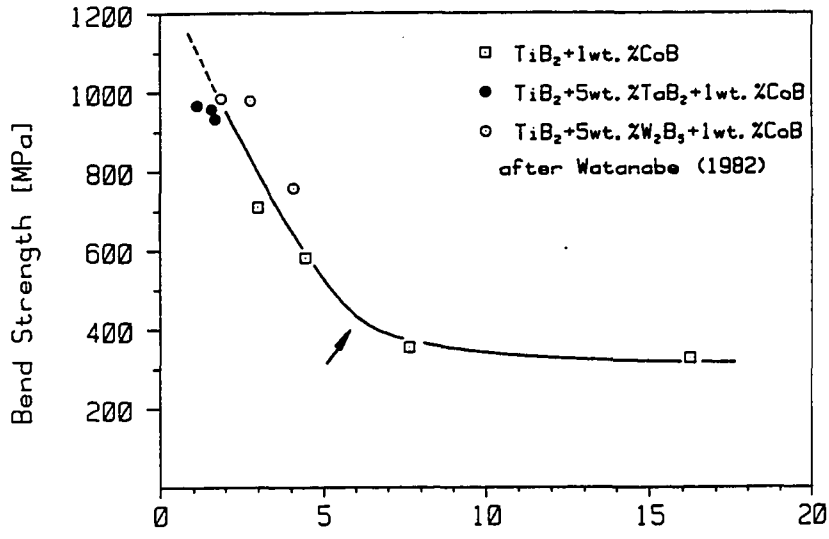

Figure 25 Dependence of the flexural strength on the average grain size of TiB_2 [28]. The arrow indicates the critical grain size, above which spontaneous cracking is considered to occur.

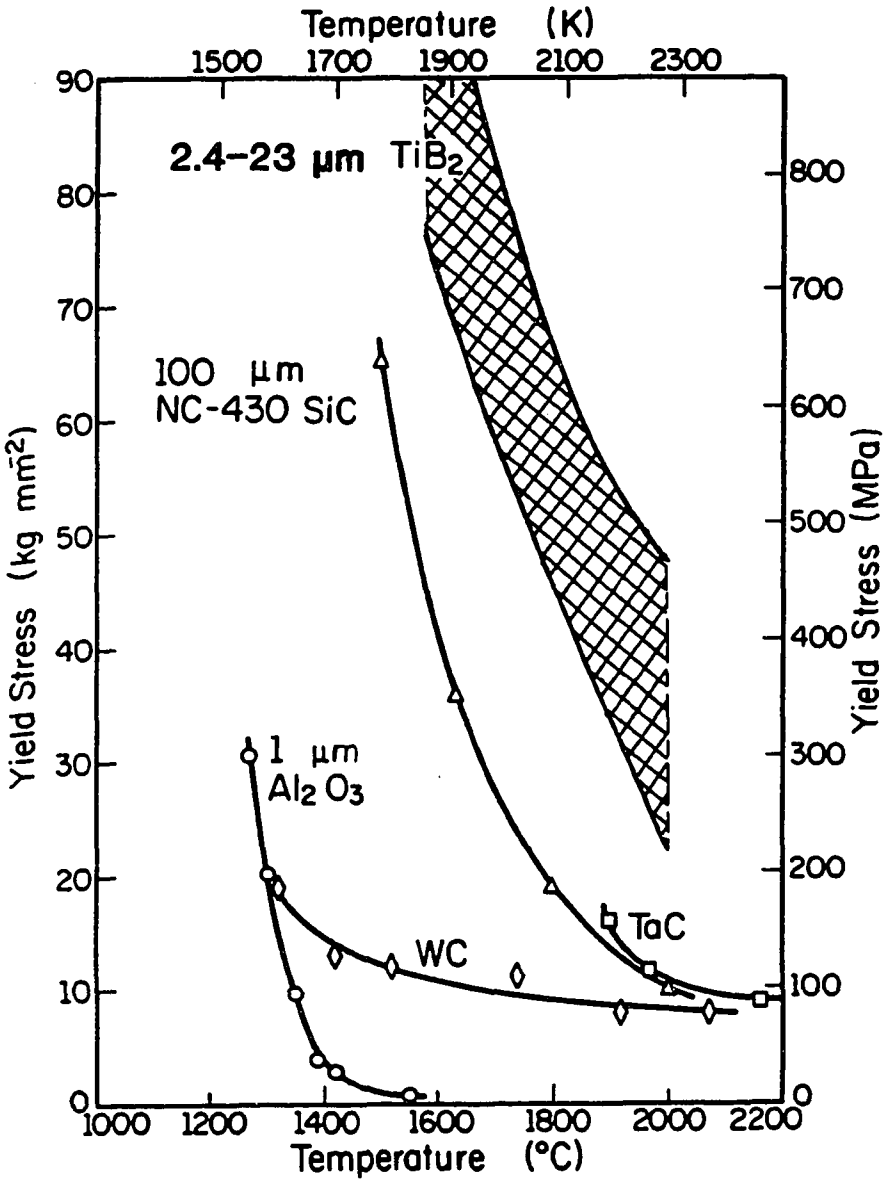

Figure 26 High temperature yield stress of TiB_2 compared to several structural ceramics (Data after ref. [114]).

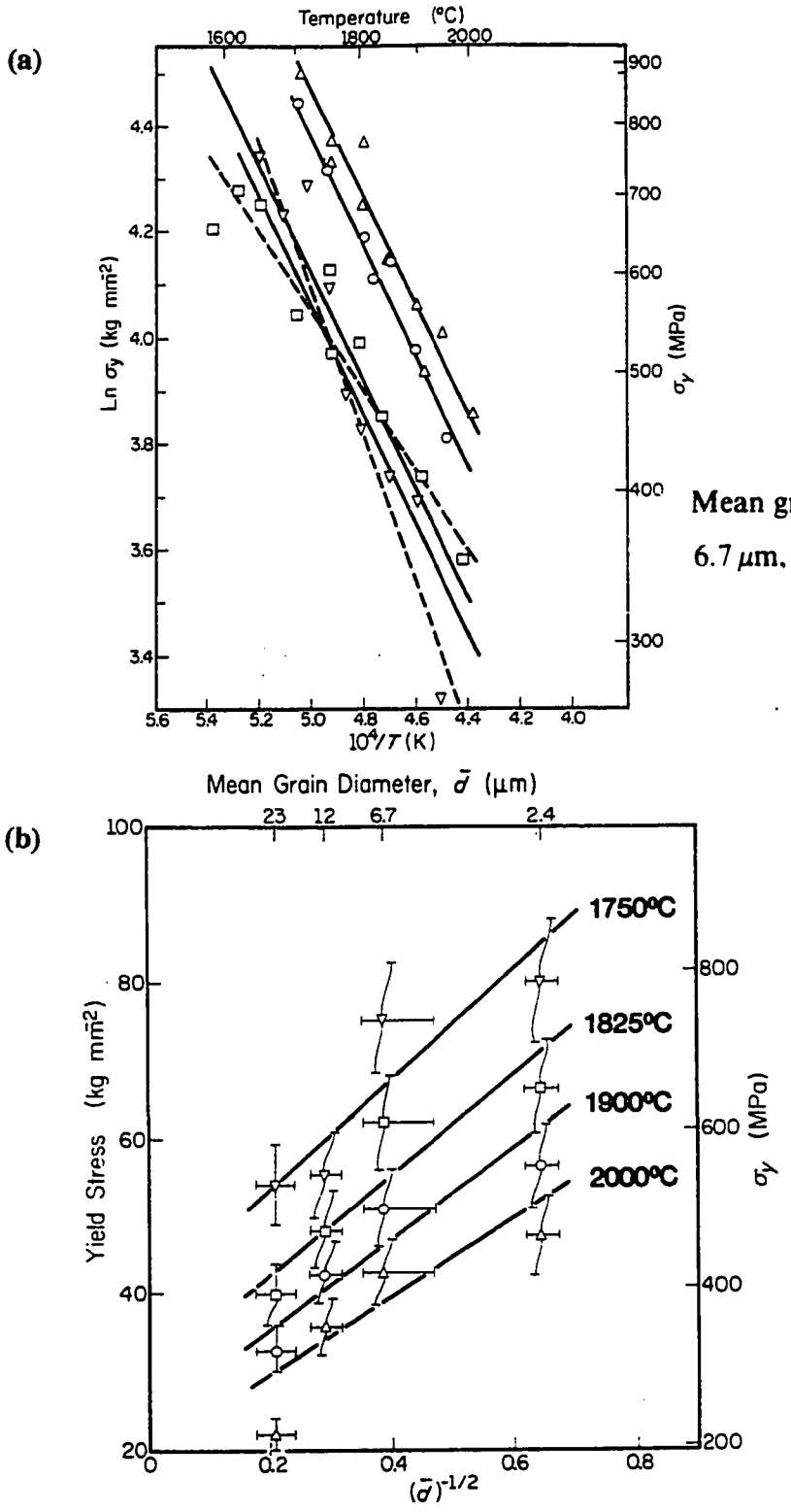

Figure 27 Dependence of the compression yield stress (σ_y) of TiB_2 on (a) reciprocal of absolute temperature (Arrhenius plots) for TiB_2 of different grain sizes; (b) reciprocal square root of mean grain size (Hall-Petch plots) at temperatures indicated (Data after ref. [114]).

(a)

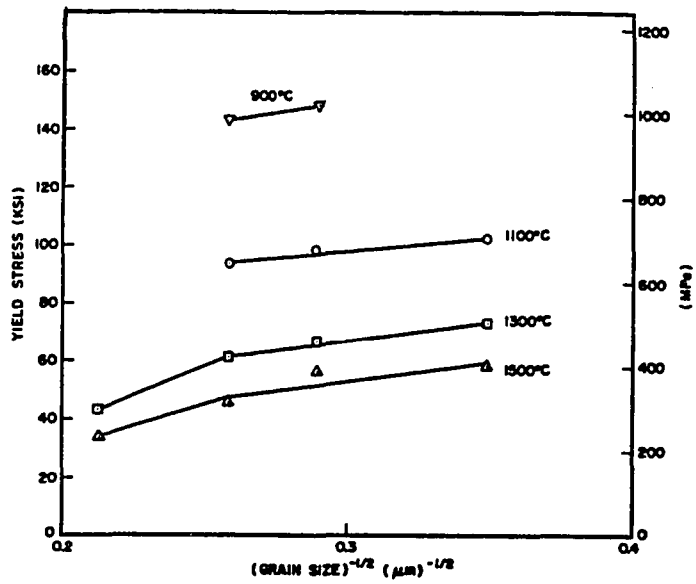

(b)

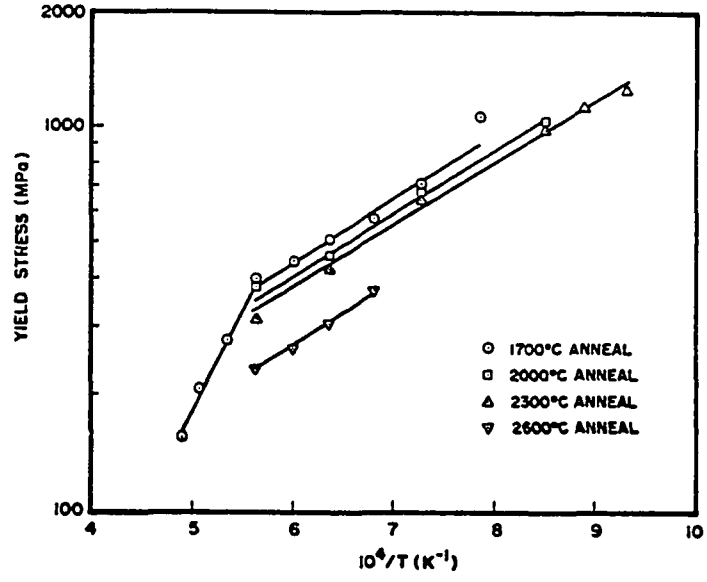

Figure 28 Dependence of the compression yield stress of TiC on (a) reciprocal square root of mean grain size (Hall-Petch plots) at various temperatures; (b) reciprocal of absolute temperature (Arrhenius plots) for TiC of different grain sizes produced by annealing (4 h, vacuum) at temperatures indicated, the corresponding grain sizes are 8μm (1700°C), 12μm (2000°C), 15μm (2300°C), 22μm (2600°C) (Data after ref. [134]).

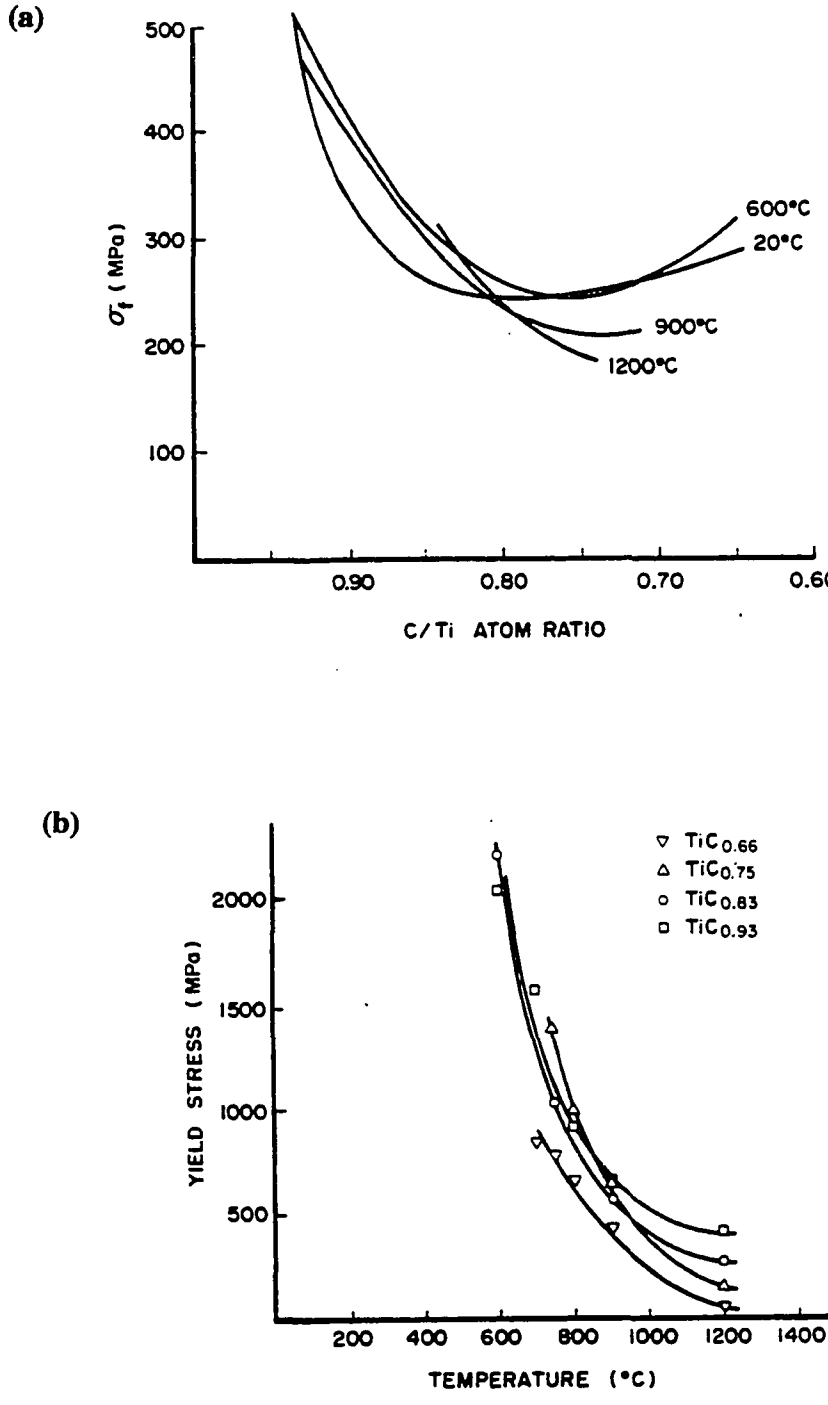

Figure 29 (a) Variation of four-point flexural strength of substoichiometric TiC_x with C/Ti atom ratio for temperatures indicated; (b) Yield stress of TiC_x as a function of temperature for C/Ti atom ratios indicated. Data after ref. [99].

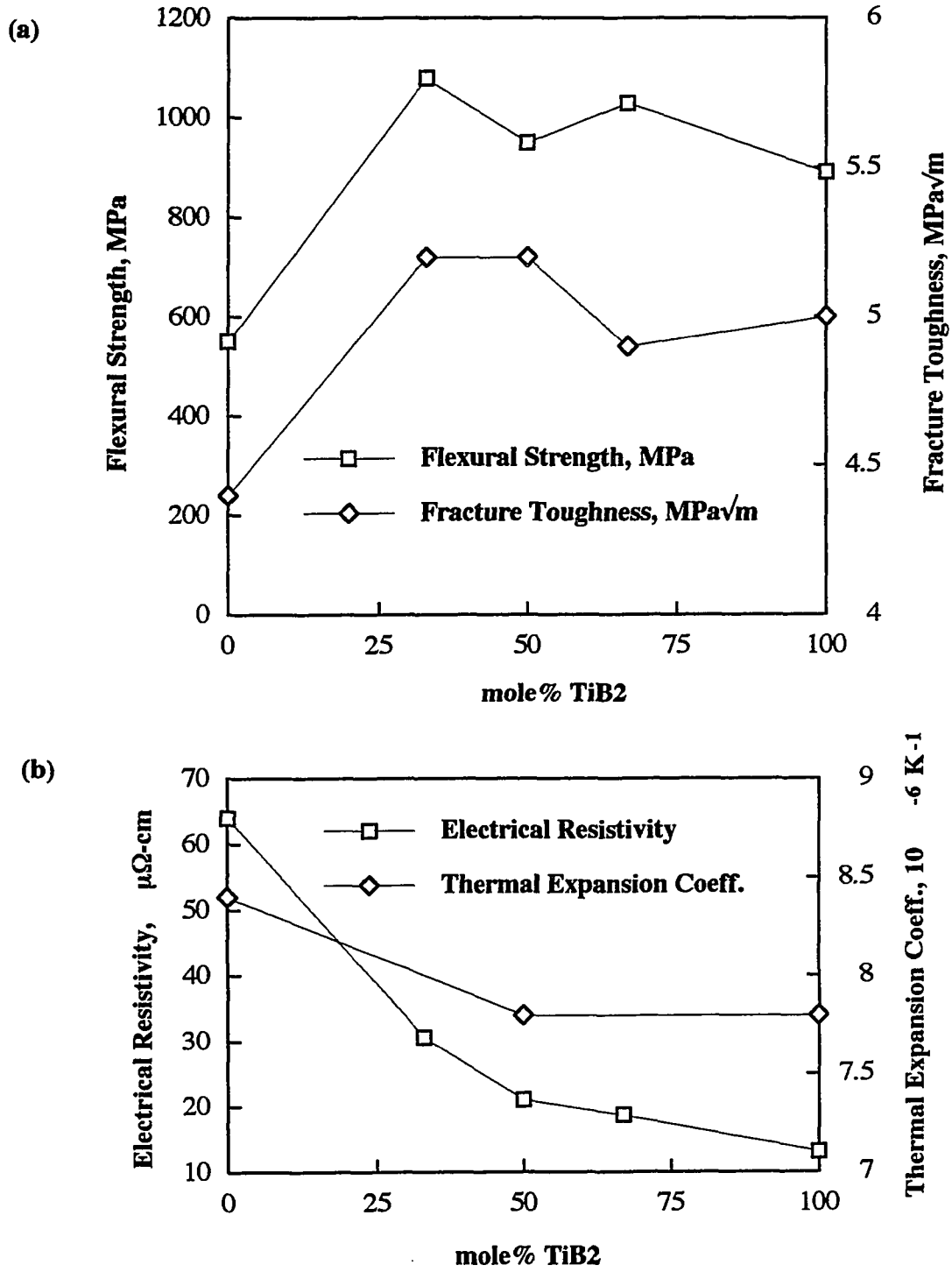

Figure 30 Variation of properties of TiC-TiB_2 composites with mole% of TiB_2 (after De Mestral and Thevenot [17]): (a) three-point flexural strength and indentation fracture toughness; (b) electrical resistivity and coefficient of thermal expansion.

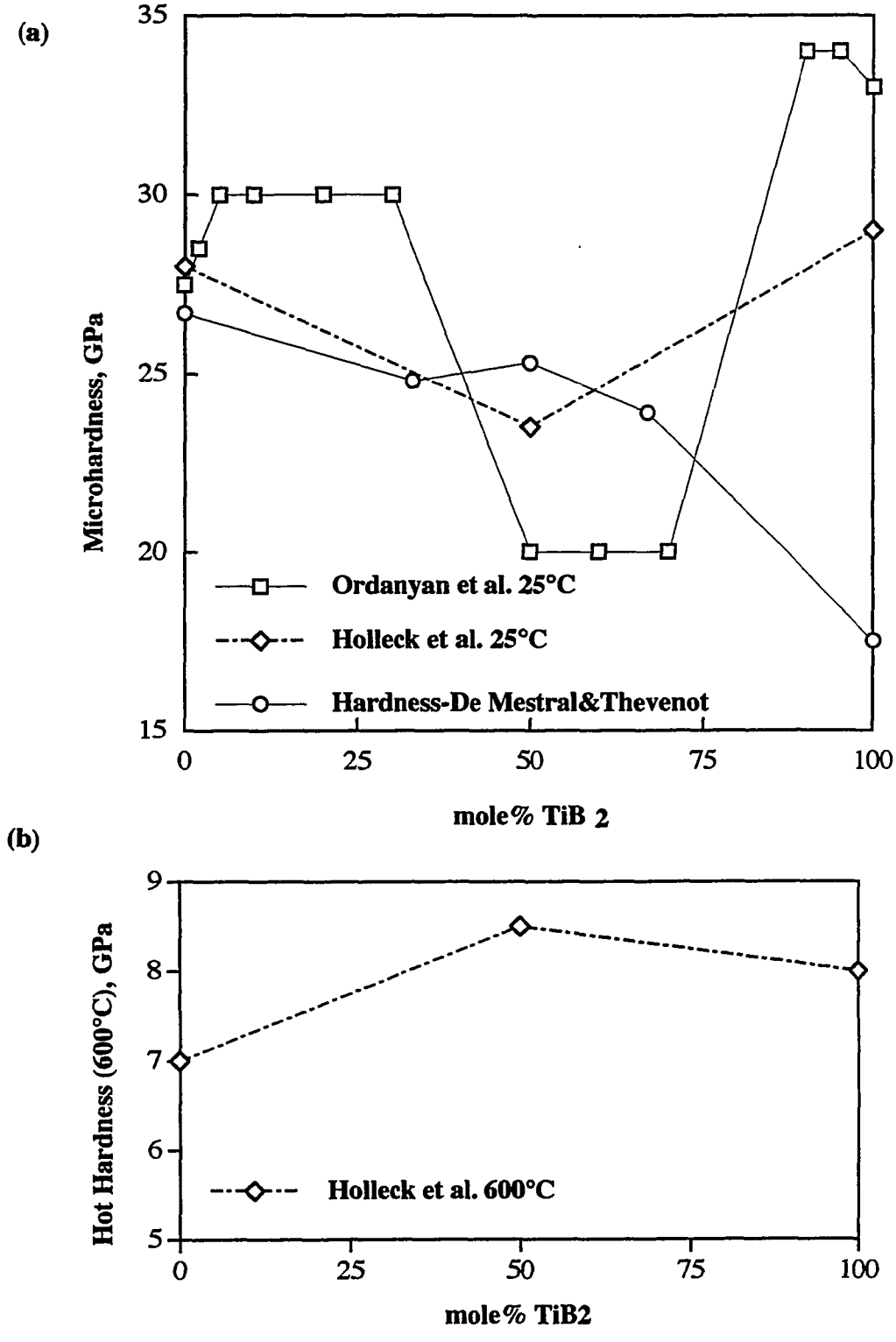

Figure 3/ Summary of the hardness of TiC-TiB_2 ceramics as a function of composition for (a) room temperature [17, 18, 106]; and (b) 600°C [18]. The presented data reveals both intrinsic compositional trends (Ordanyan et al. [106], Holleck et al. [18]) and compositional trends affected by processing-related factors (De Mestral and Thevenot [17]), most probably residual porosity.

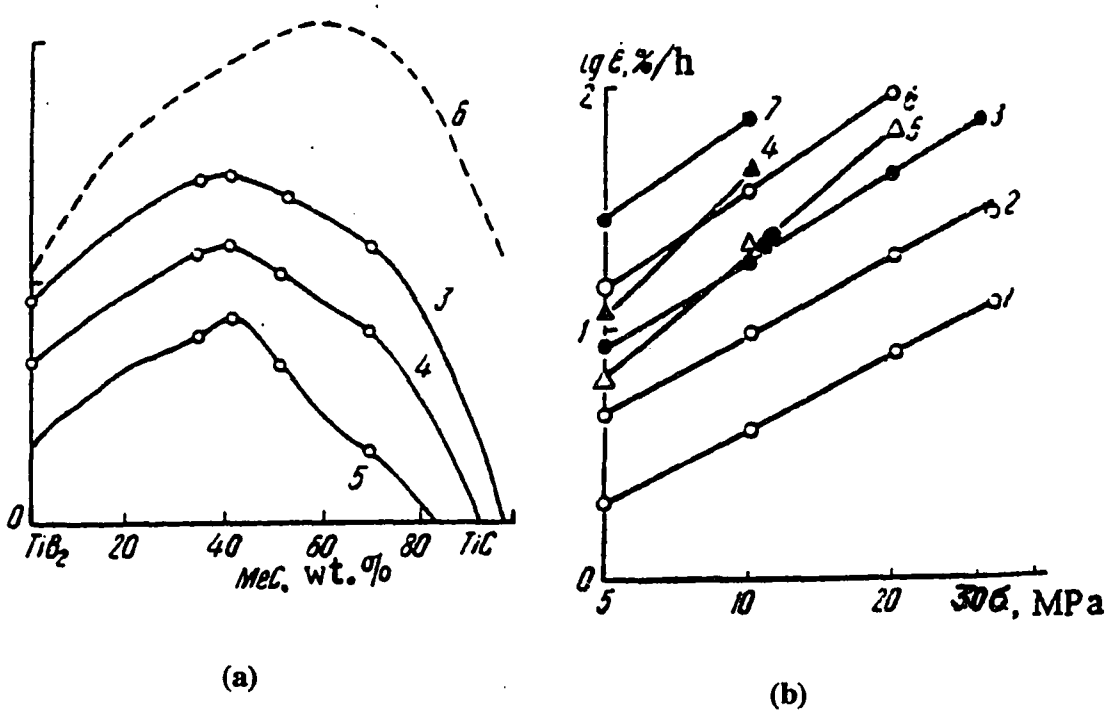

(a) (b)

Figure 32 High-temperature bending creep behavior in TiC-TiB_2 system reported by Kats et al. [143]:

(a) Variation of steady-state creep rates with composition for σ_c=5 MPa and temperatures of 2300°C (3), 2200°C (4), 2100°C (5), compared with the results of Spivak et al. [23] at 2300°C (6);

(b) Effect of stress on creep rates for the following compositions and temperatures: (3) TiC-65%TiB_2 at 2150°C, (4) the same at 2300°C, (5) TiC-57%TiB_2 at 2100°C, (6) the same at 2280°C, (7) TiC-49%TiB_2 at 2315°C, compared with (1) ZrC-55% ZrB_2 at 1900°C and (2) ZrC-80% ZrB_2 at 2000°C.

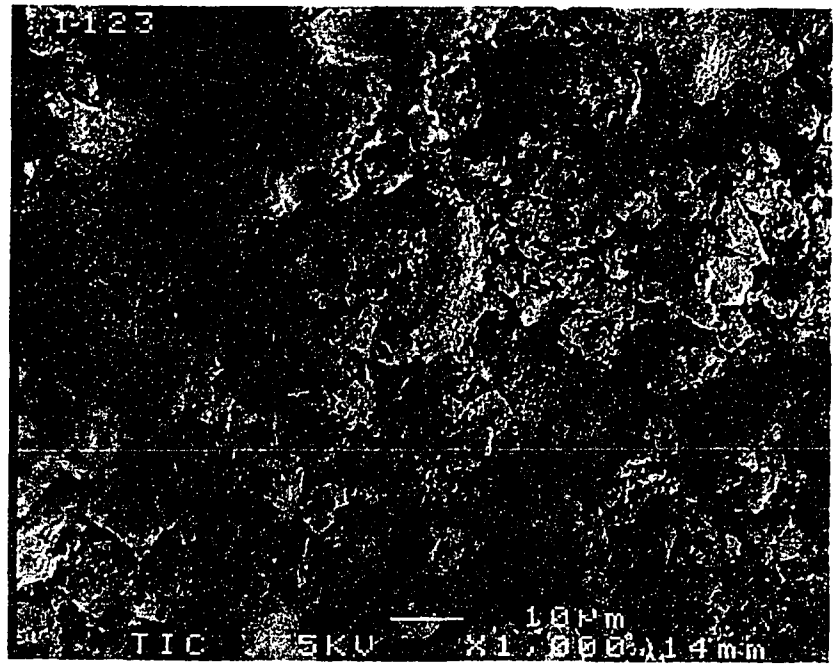

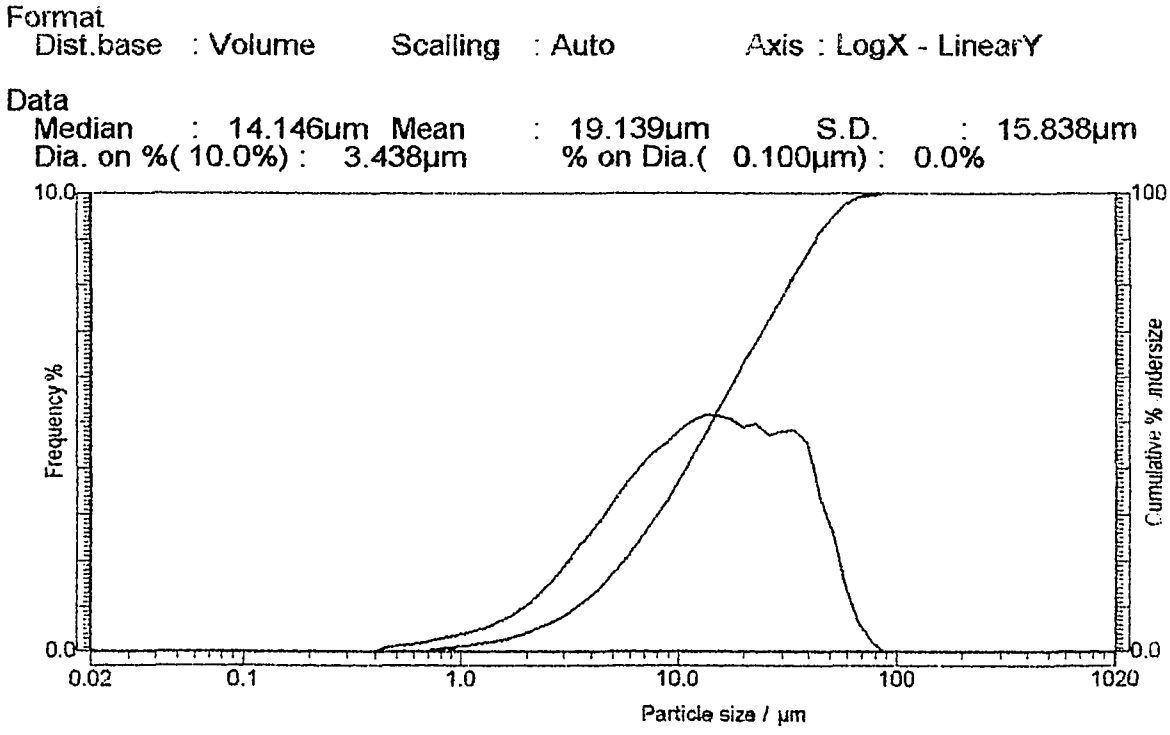

Figure 33 $TiC_{0.5}$ powder: (a) SEM micrograph; (b) particle size distribution.

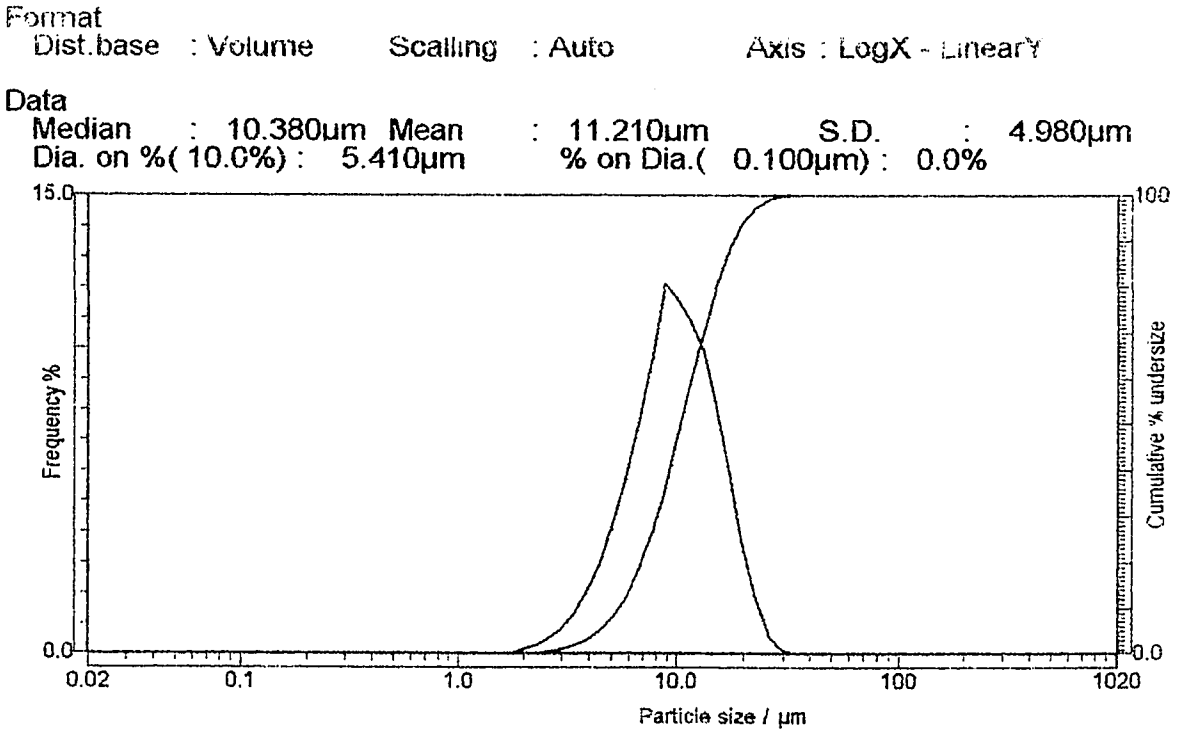

Figure 34 TiB_2 powder: (a) SEM micrograph; (b) particle size distribution.

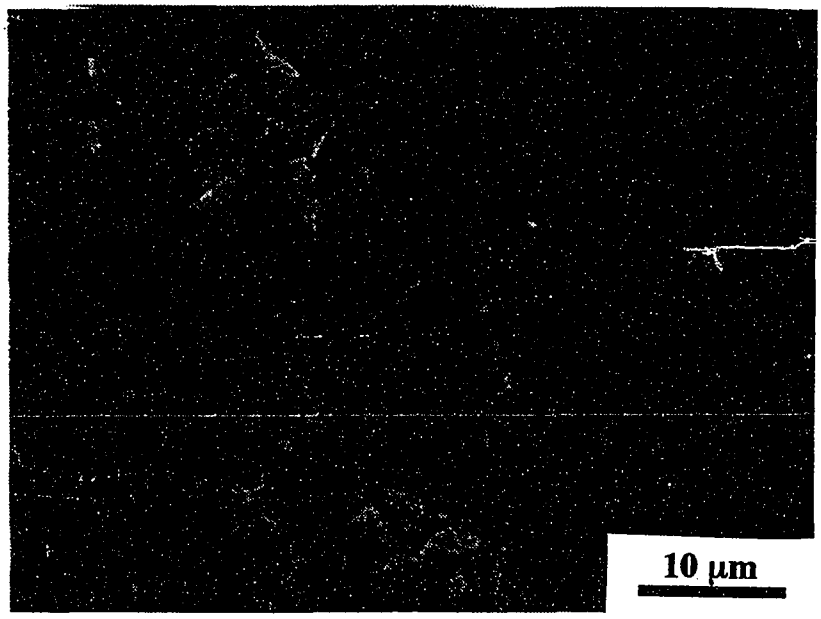

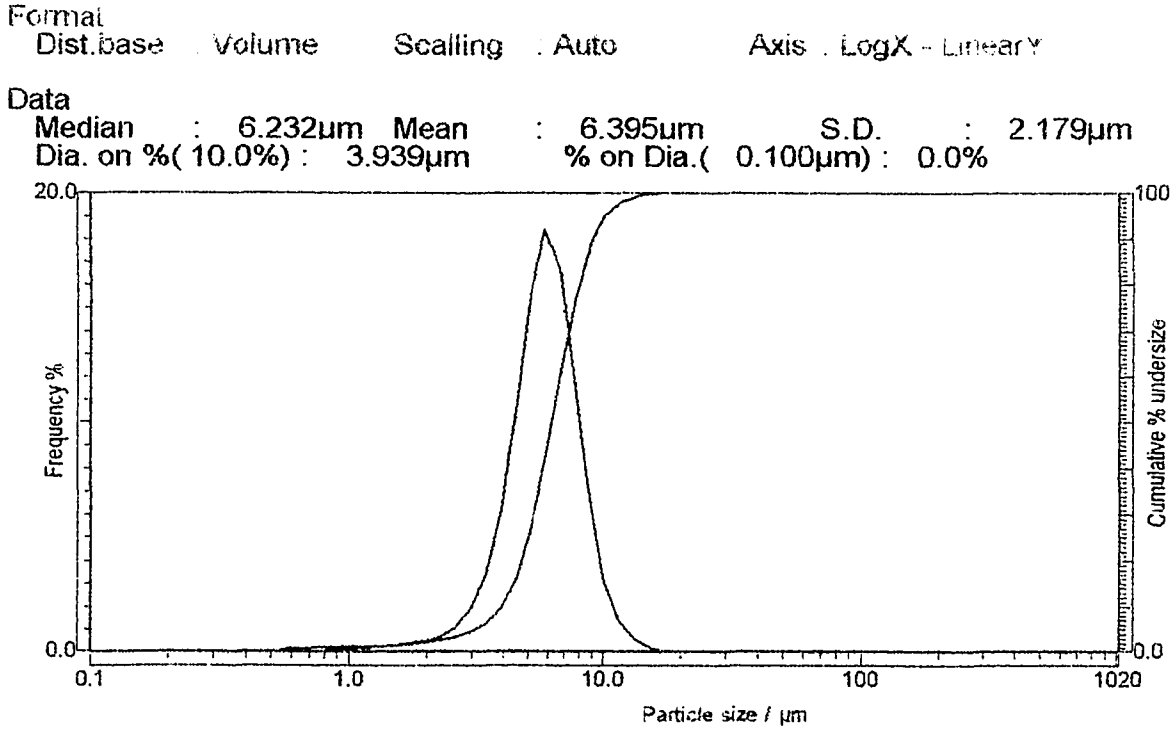

Figure 35 B_4C powder: (a) SEM micrograph; (b) particle size distribution.

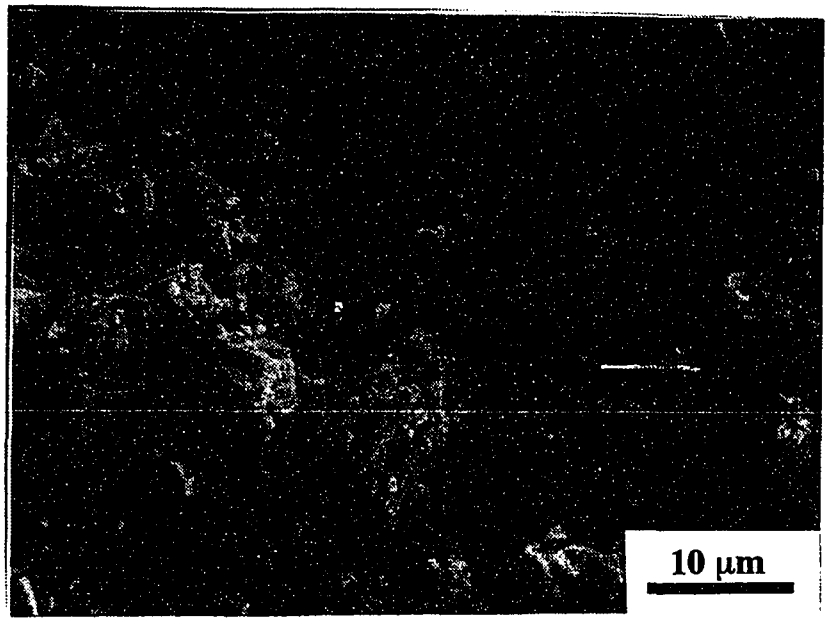

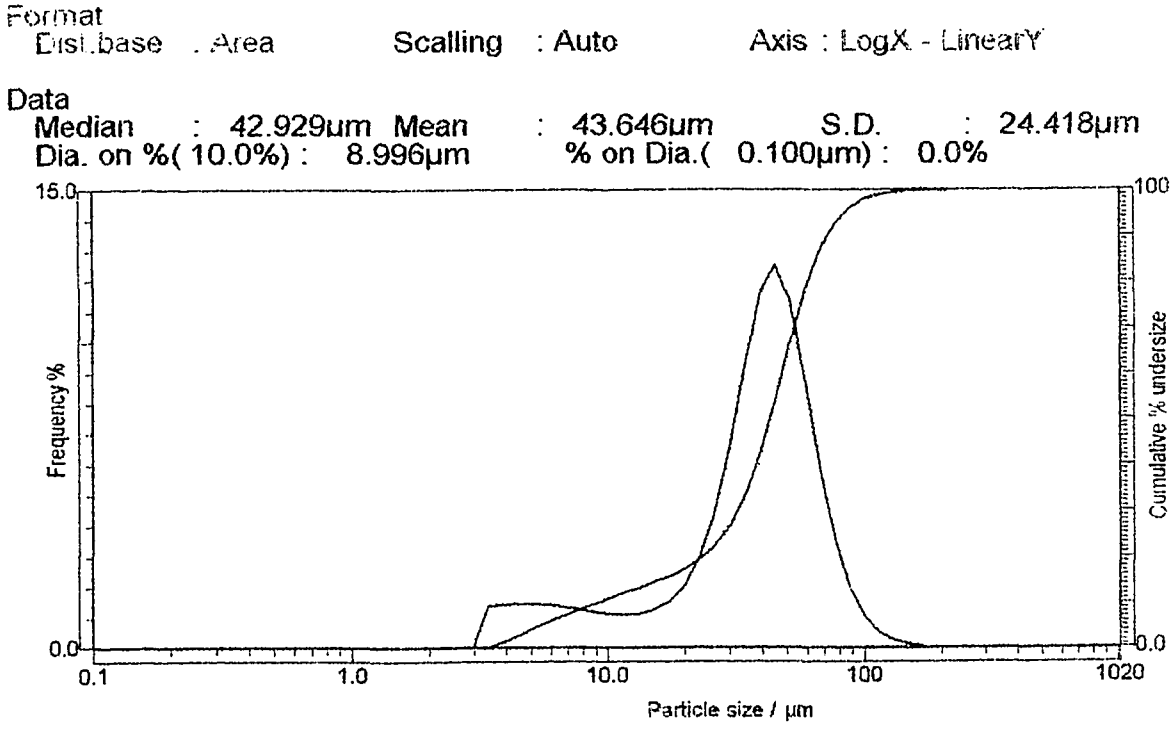

Figure 36 Ti-dehydride (4N) powder: (a) SEM micrograph; (b) particle size distribution of as-received (-325 mesh) powder

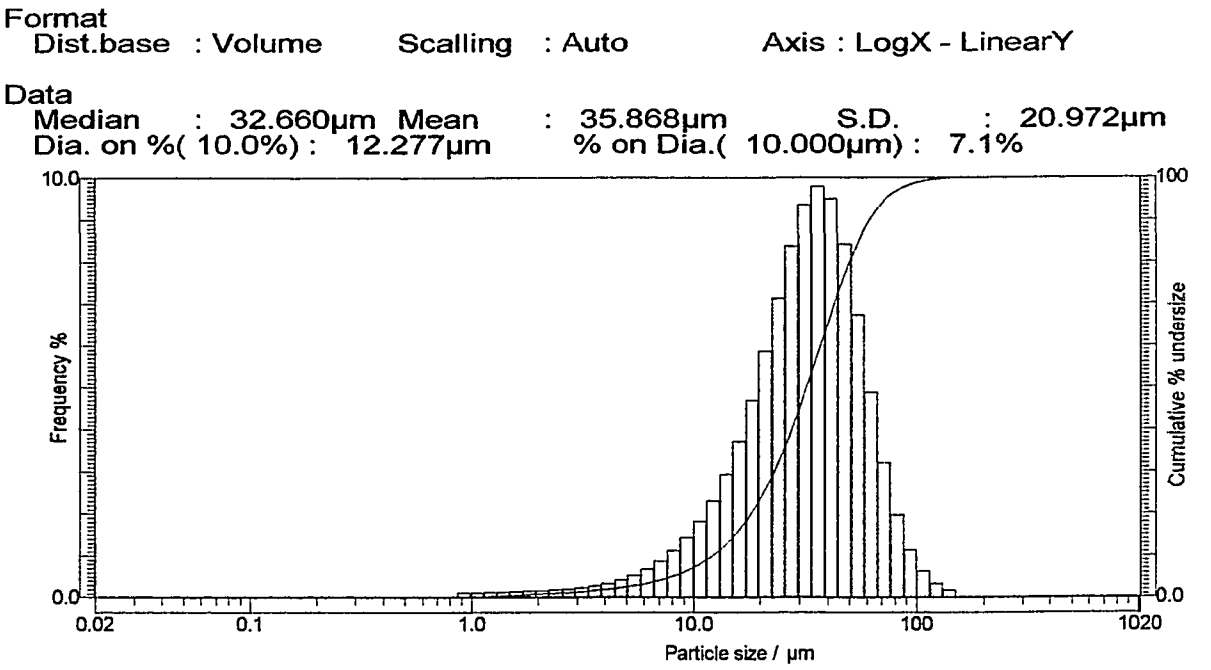

Figure 37 As-received Ti-hydride (4N) powder: (a) SEM micrograph; (b) particle size distribution.

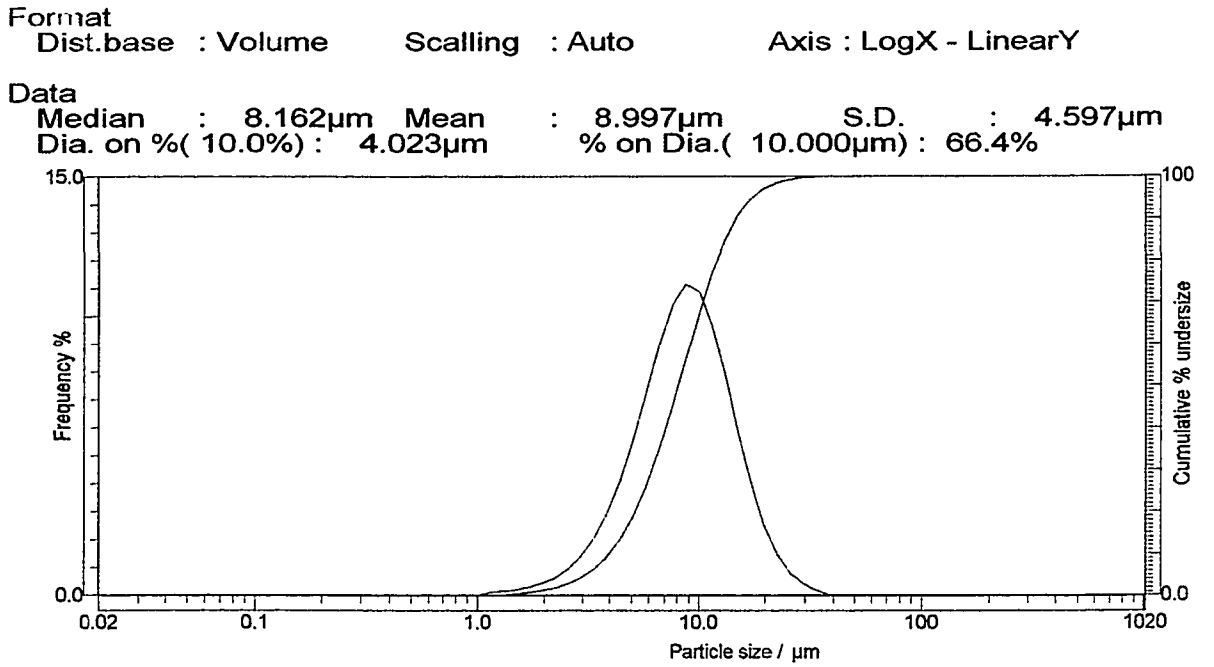

Figure 38 Jet-milled Ti-hydride powder (~8 μm): (a) SEM micrograph; (b) particle size distribution.

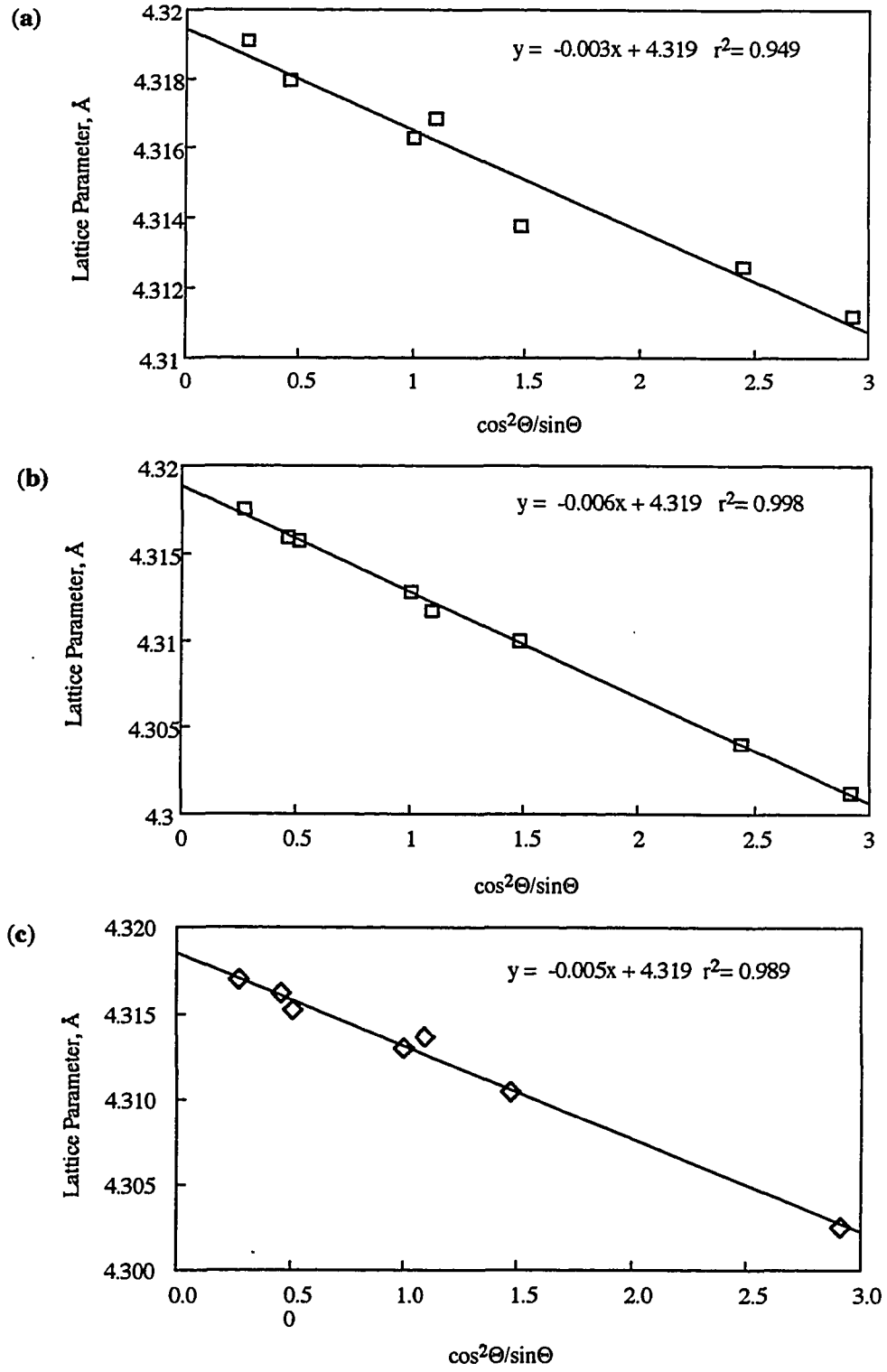

Figure 39 Typical results of the least-squares fitting lattice parameters of TiC_x (determined from individual X-ray peaks) as a function of the $\cos^2\Theta/\sin\Theta$ for (a) run 2 with composition in Ti_3B_4-TiB_2-$TiC_{0.65}$ compatibility triangle (see Table VI); (b) run 3 with composition in TiB-Ti_3B_4-$TiC_{0.65}$ compatibility triangle and located in close proximity to Ti_3B_4-$TiC_{0.65}$ line; and (c) run 5 with composition in TiB-Ti_3B_4-$TiC_{0.65}$ compatibility triangle. The accurate lattice parameters are obtained by extrapolation of the shown linear functions onto $2\Theta=180°$.

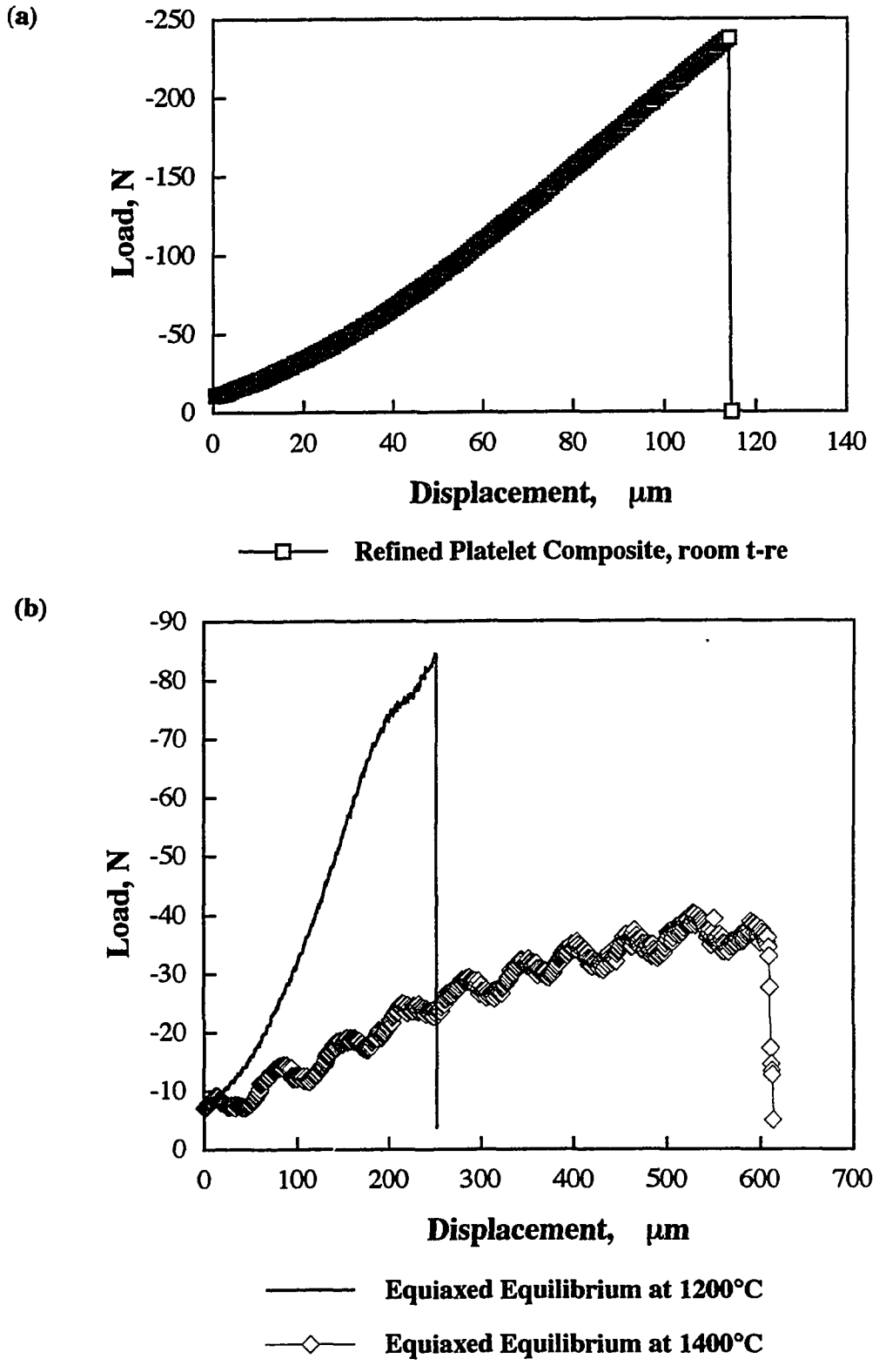

Figure 40 Typical load-displacement curves obtained in four-point bending tests: (a) at room temperature; (b) at high temperatures.

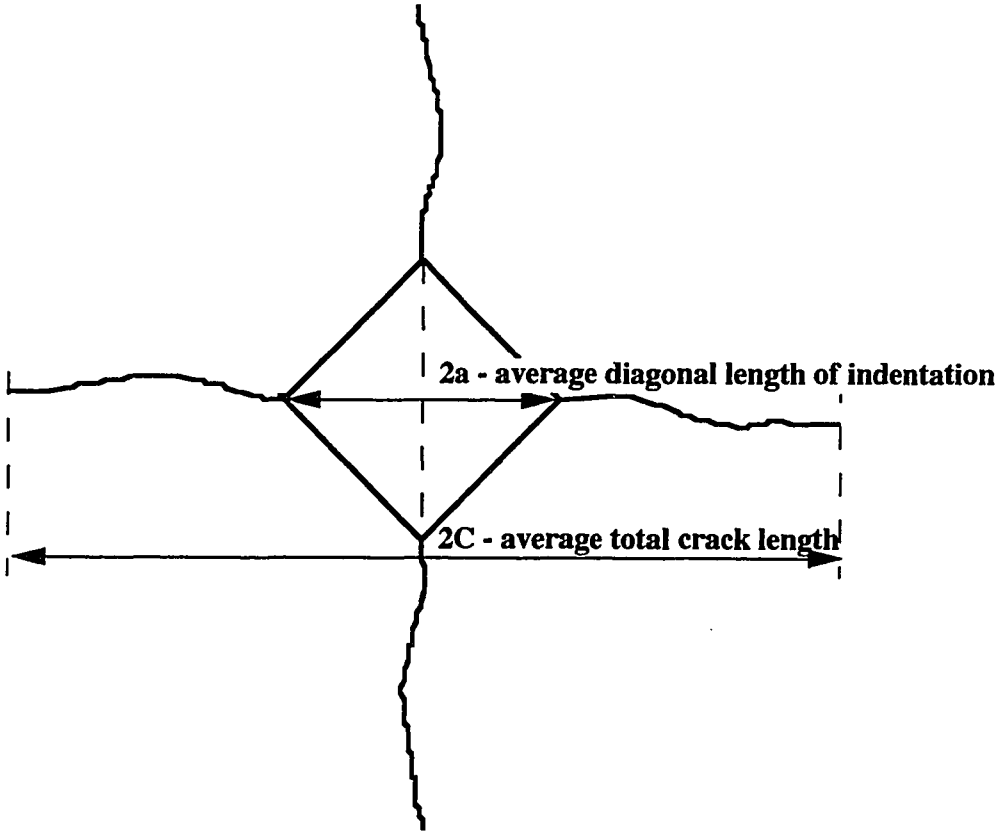

Figure 41 Indentation fracture method for measuring fracture toughness: (a) Schematic diagram of median cracks, emanating from Vickers indentation in brittle material, illustrating the parameters used in calculation of fracture toughness; (b) SEM micrograph of typical indentation observed in this study (platelet composite)

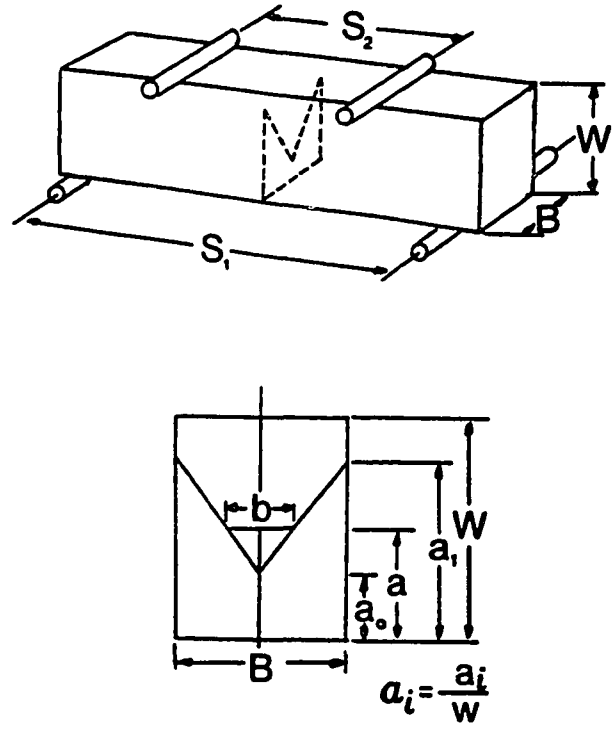

Figure 42 Schematic of the loading configuration and specimen geometry used in the chevron-notched beam fracture toughness test.

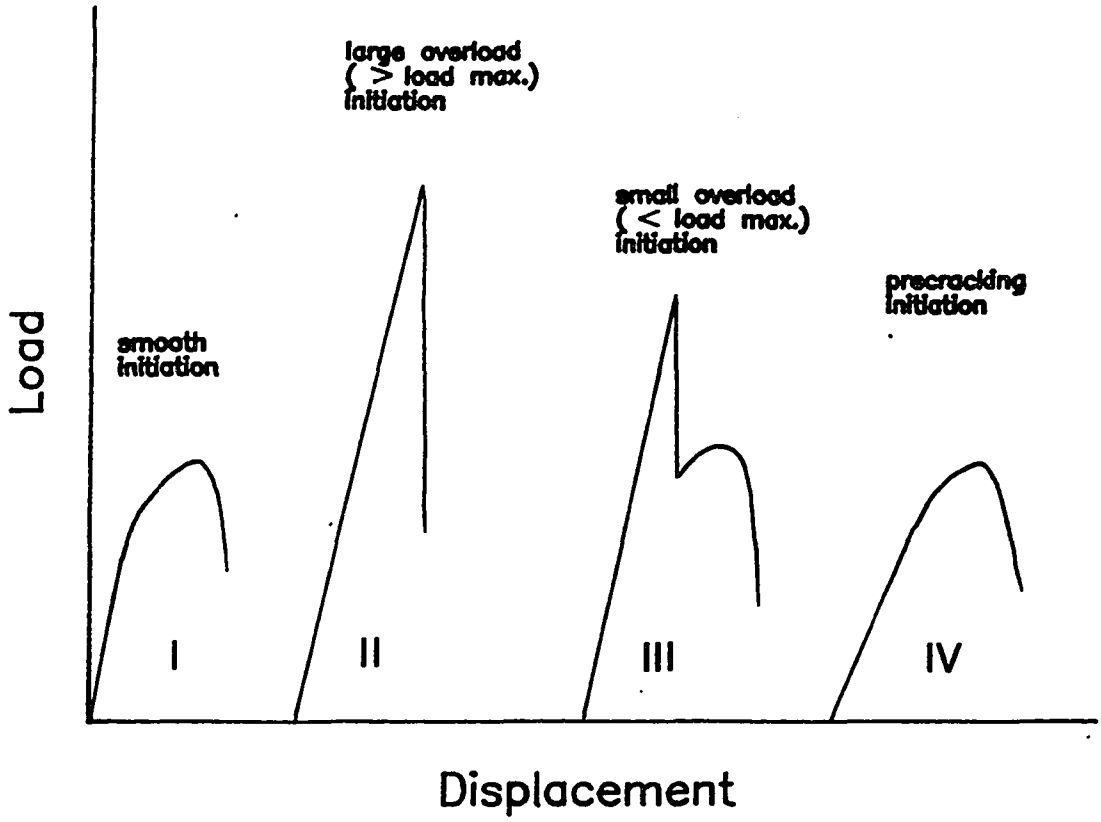

Figure 43 Various types of load-displacement curves resulting from different crack initiation conditions in a chevron-notched beam fracture toughness test [159].

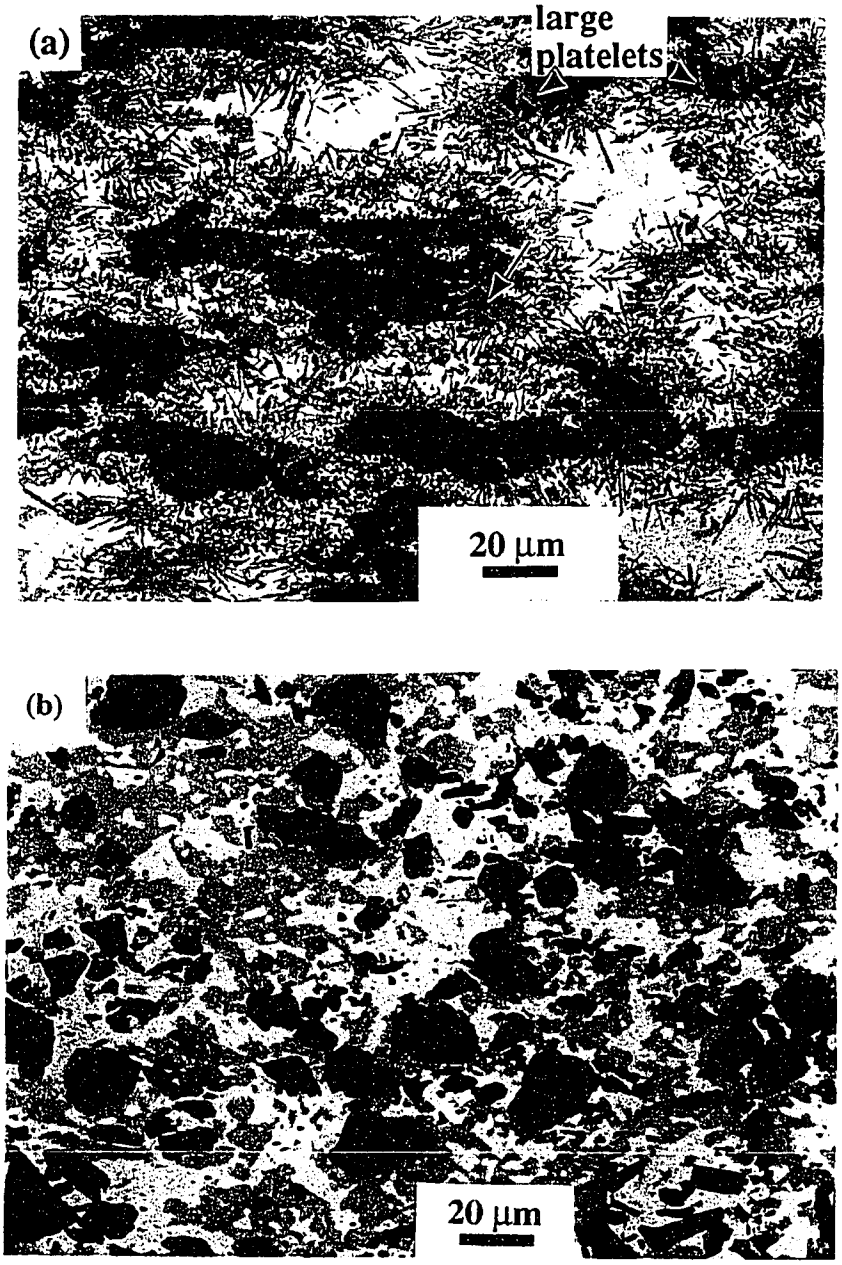

Figure 44 Backscattered SEM micrographs of the composites fabricated by TPPP. Phases: white - TiC_x; black - TiB_2, gray - Ti_3B_4. (a) Starting composition of 4:1 Ti/B_4C with an average Ti particle size of 43 μm. (b) Starting composition of 1:0.5:1 $Ti/C/TiB_2$ with an average Ti particle size of 20 μm.

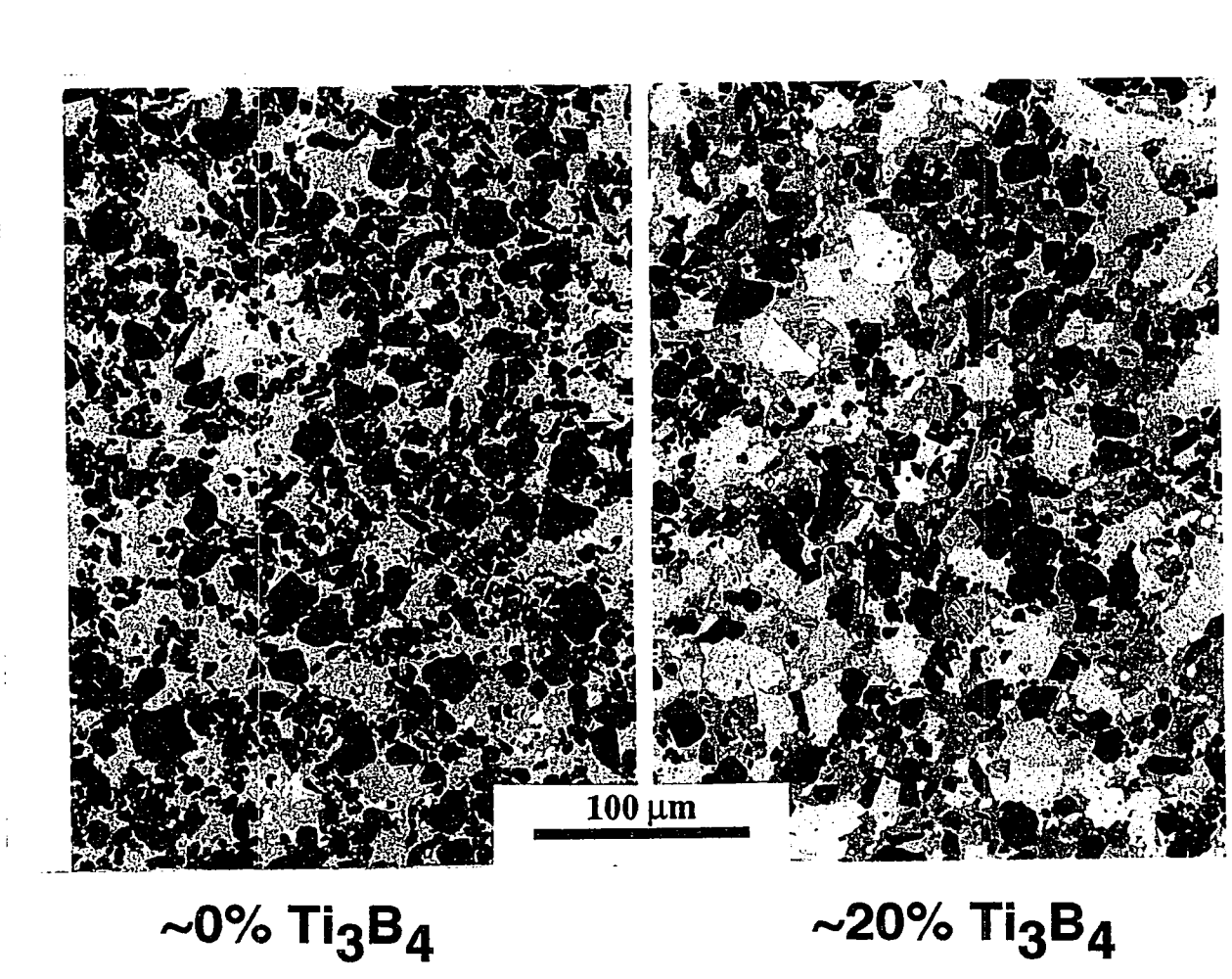

Figure 44 Backscattered SEM micrographs of the composites fabricated by TPPP. (c) Starting composition of 1:1 $TiC_{0.5}/TiB_2$ (nonequilibrium) devoid of Ti_3B_4 in the final microstructure. (d) Same as (c) with ~20 vol% of Ti_3B_4.

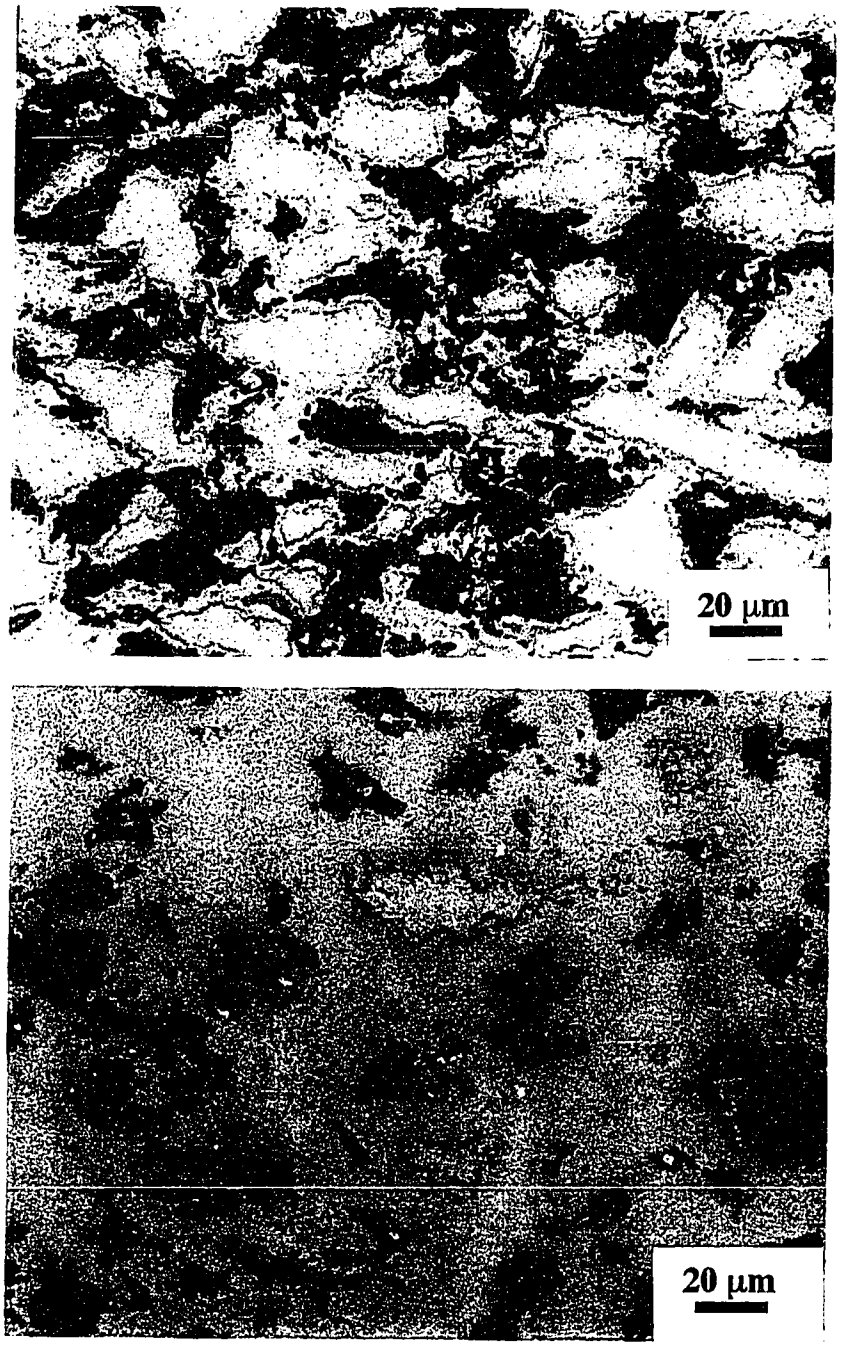

Figure 45 Evolution of microstructure in the processing of 4:1 Ti/B_4C starting composition:
(a) Optical micrograph of the 1000°C interrupted run specimen: the reaction layer is clearly visible at the periphery of the Ti particles.
(b) Optical micrograph of the 1200°C interrupted run specimen: the reaction has consumed all but the largest Ti particles.

(c)

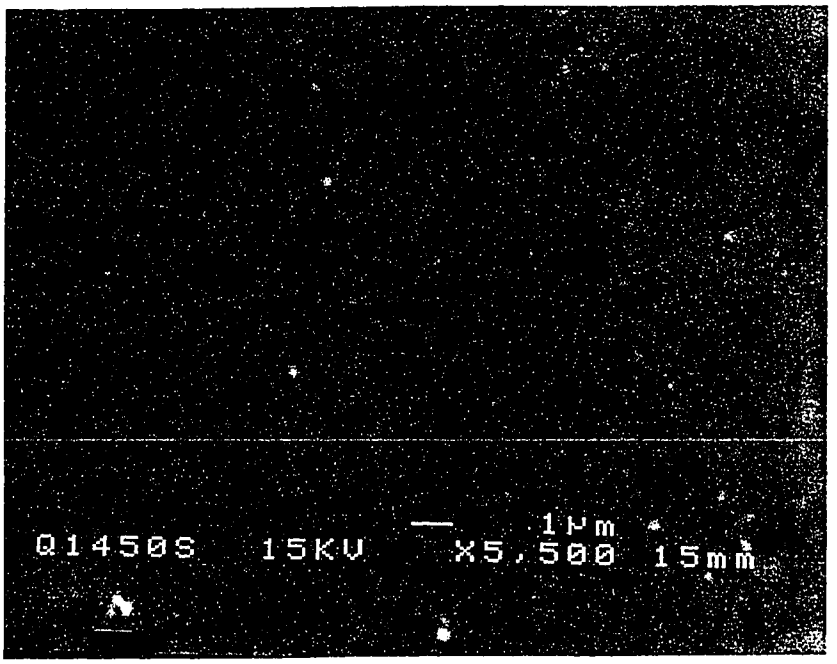

(d)

Figure 45 Evolution of microstructure in the processing of 4:1 Ti/B_4C starting composition:
(c) Backscattered micrograph of the specimen quenched from 1450°C: shown is the development of platelet-like phase (TiB and/or Ti_3B_4).
(d) Backscattered micrograph of the 1600°C interrupted run specimen.

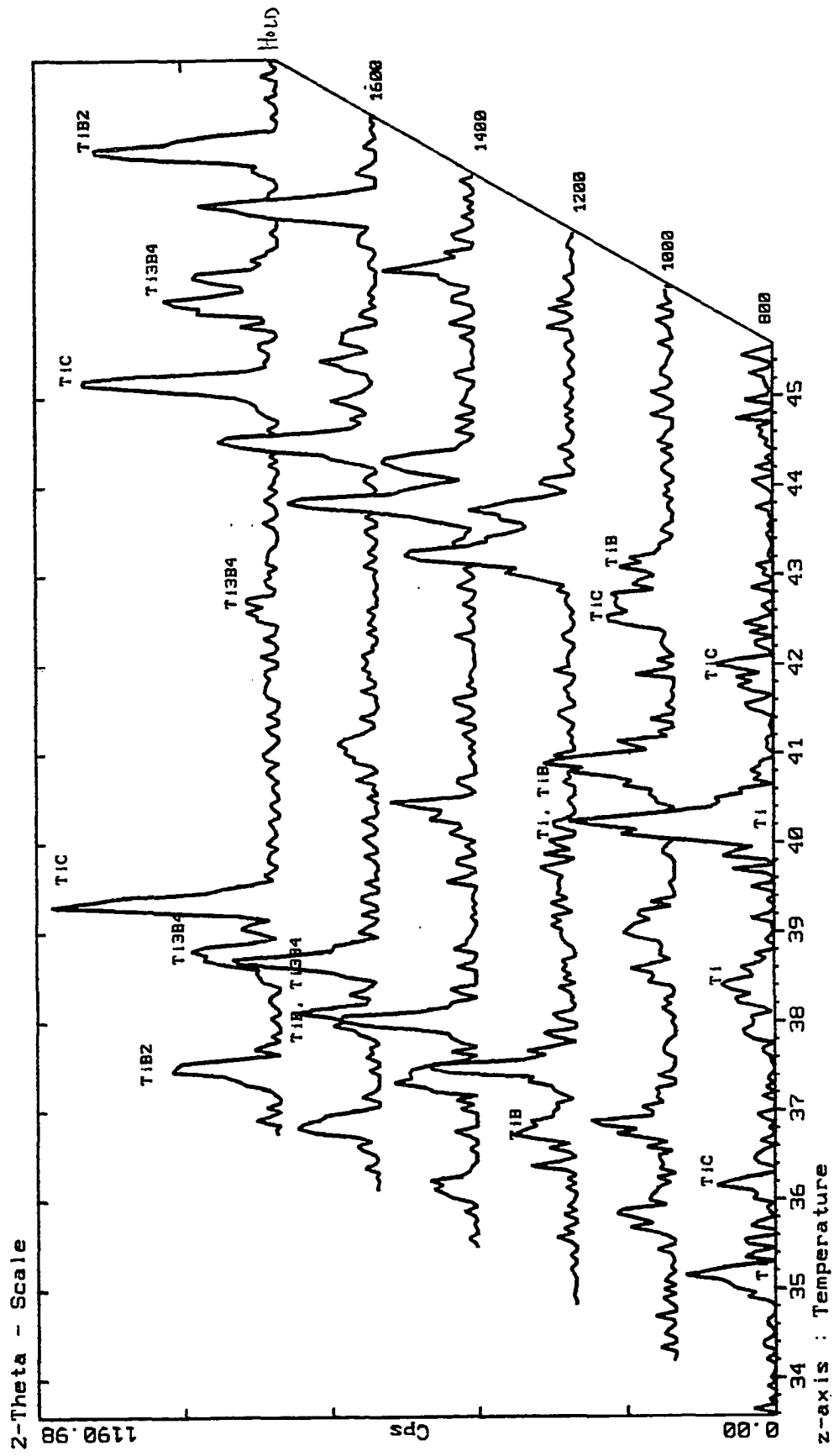

Figure 46 Summary of X-ray diffraction results from the interrupted hot-pressed runs and quenching experiments.

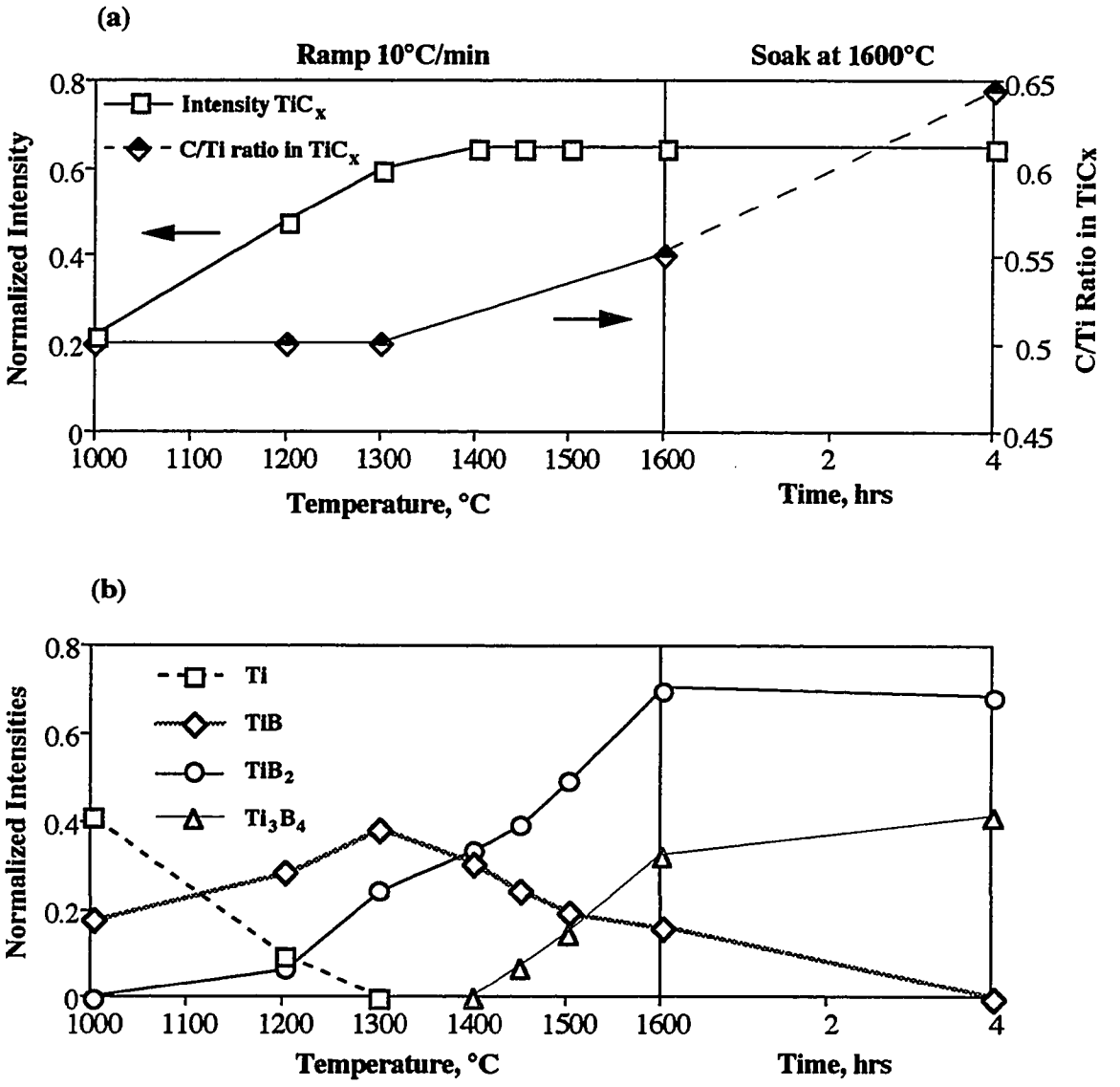

Figure 47. Evolution of phases during TPPP of 4:1 Ti/B_4C composition: (a) TiC_x (200) peak intensity and stoichiometry; (b) Other phases. All peak intensities are normalized by the intensities of (116) peak from the α-Al_2O_3 internal standard.

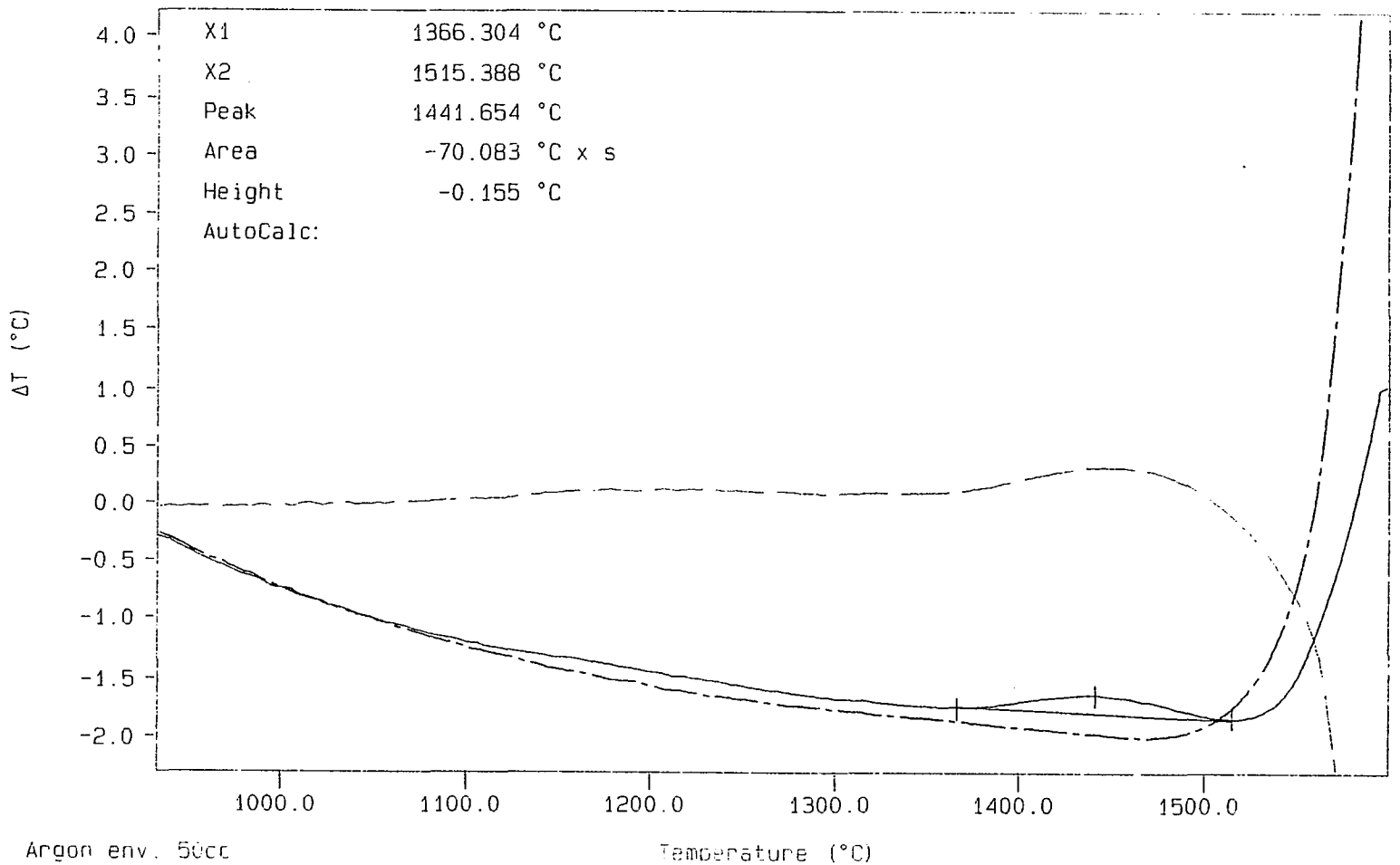

Figure 48 The DTA curve from the 1:1 $TiC_{0.5}/TiB_2$ powder mixture heated at 10°C/min to 1550°C under flow of argon. The observed weak exothermic peak centered around 1450°C is attributed to the sluggish reaction between the $TiC_{0.5}$ and TiB_2 components yielding the Ti_3B_4 phase.

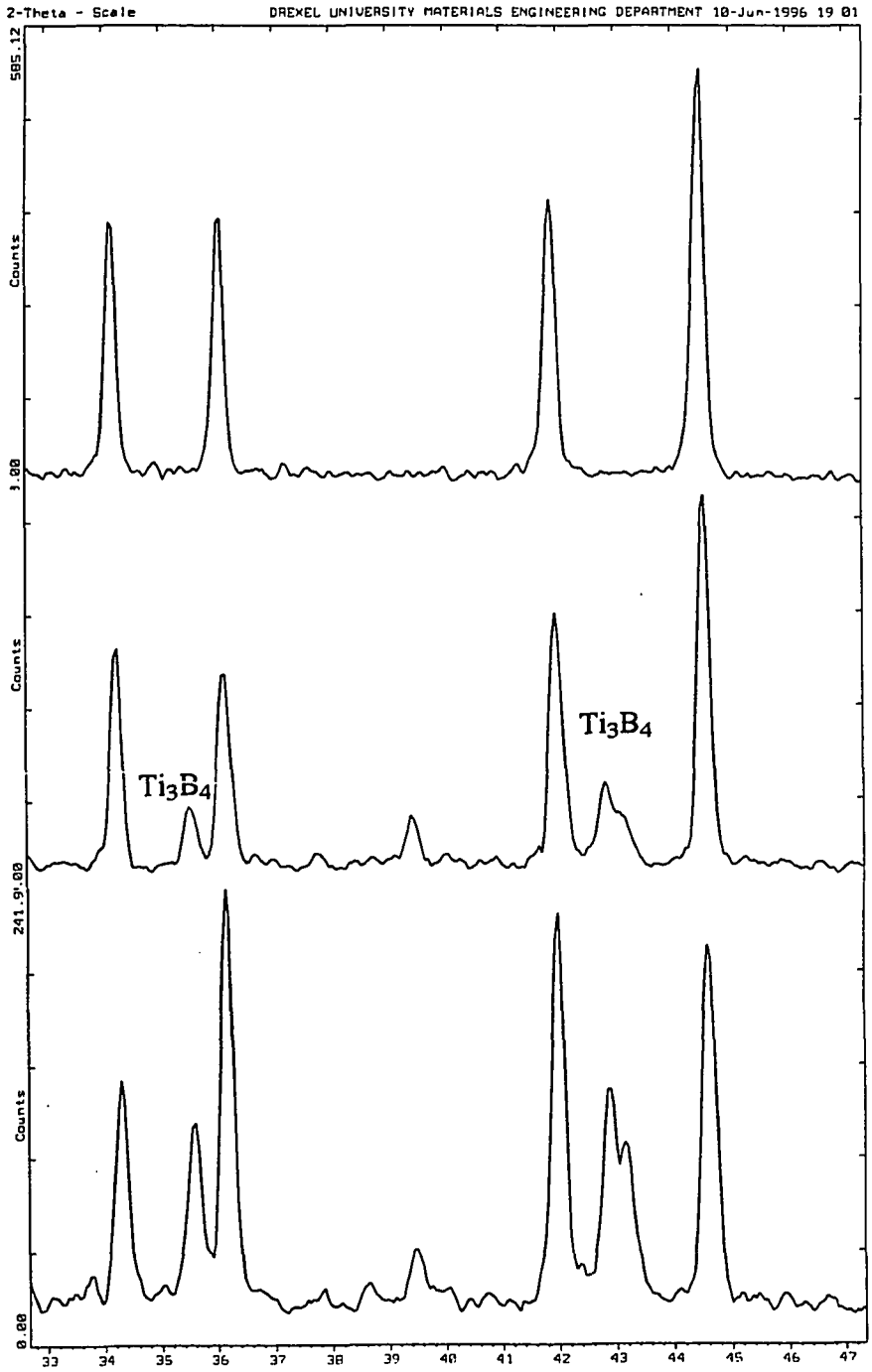

Figure 49 X-ray diffraction patterns of 1:1 $TiC_{0.5}/TiB_2$ starting composition for (a) material obtained in a hot press run interrupted at 1400°C; (b) powder mixture heated to 1550°C and held at that temperature for 10 min in DTA; and (c) composite shown in Figure 44(d).

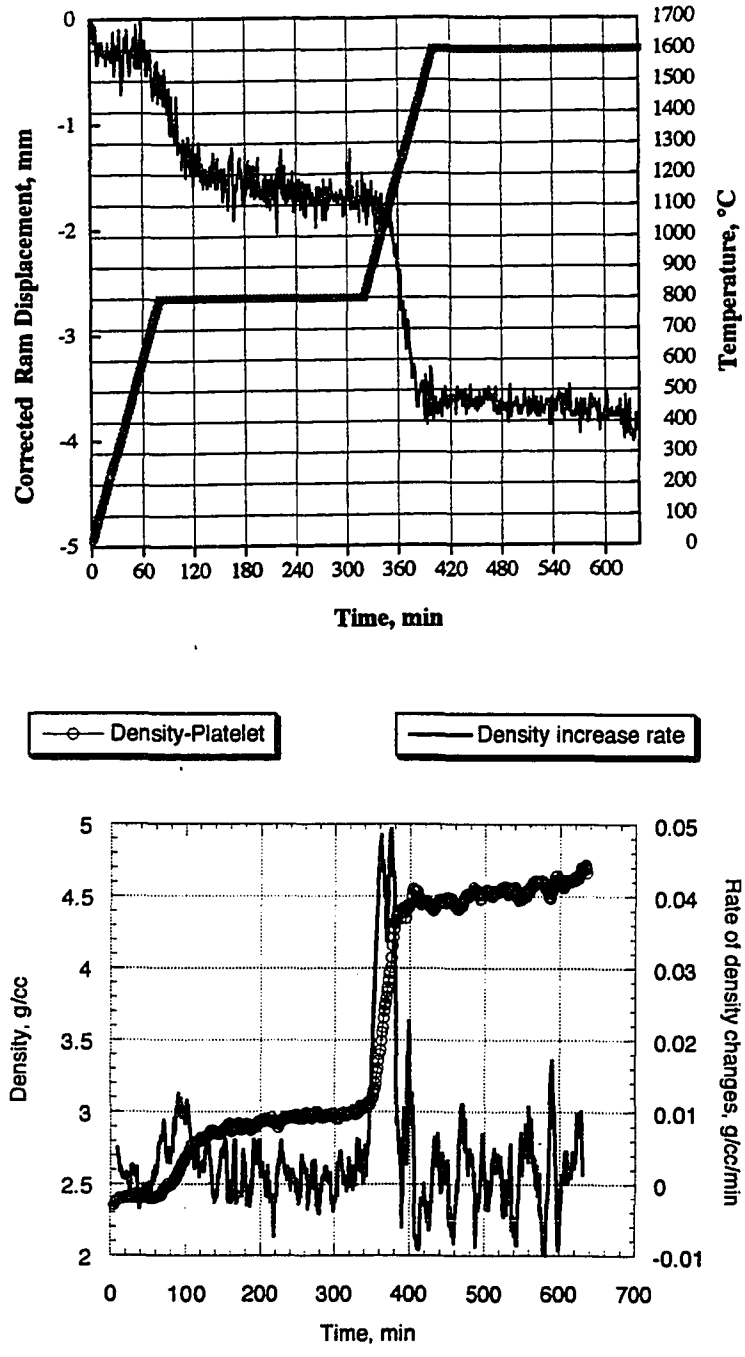

Figure 50 Densification of the platelet composite (4:1 Ti/B_4C starting composition):
(a) Ram displacement and temperature during typical hot-pressing run;
(b) Density and densification rate vs time for the same run.

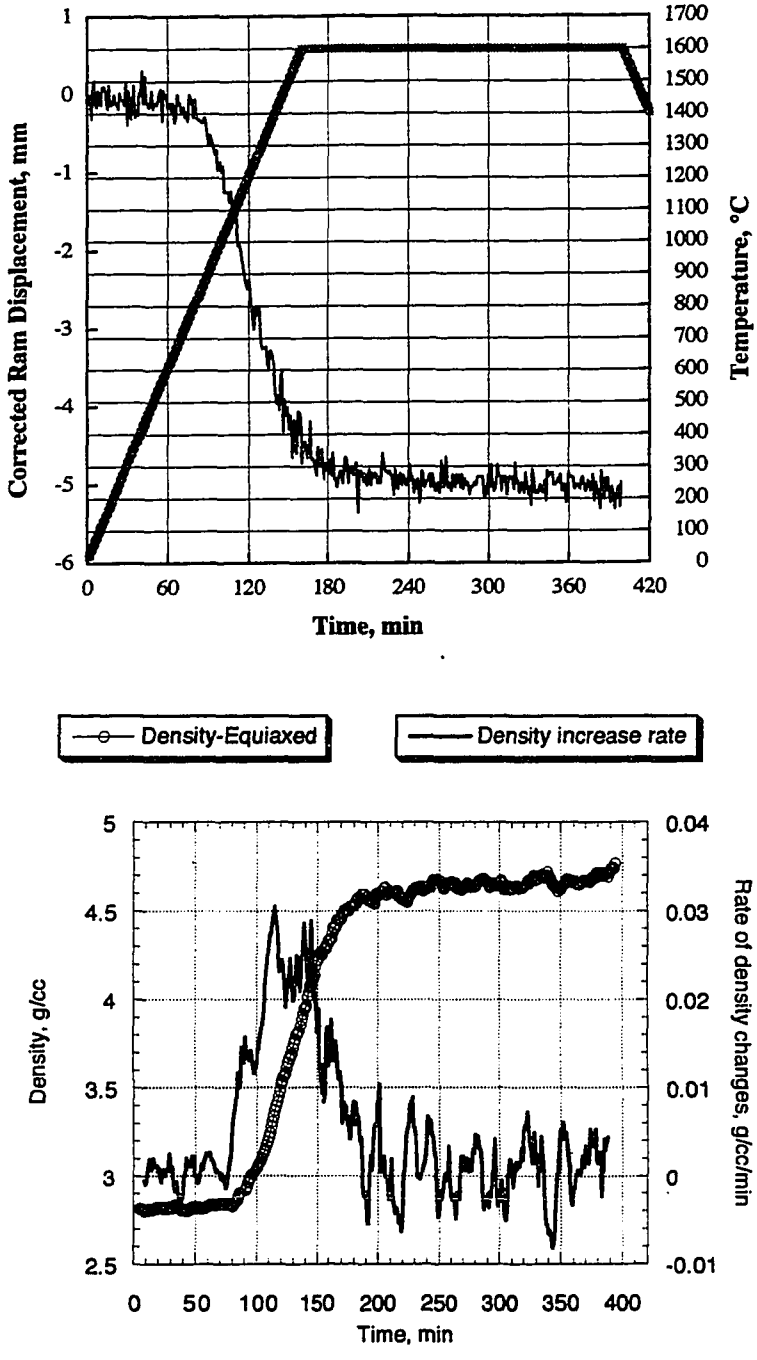

Figure 51 Densification of the equiaxed composite (1:1 $TiC_{0.5}/TiB_2$ starting composition):
(a) Ram displacement and temperature during typical hot-pressing run;
(b) Density and densification rate vs time for the same run.

(a)

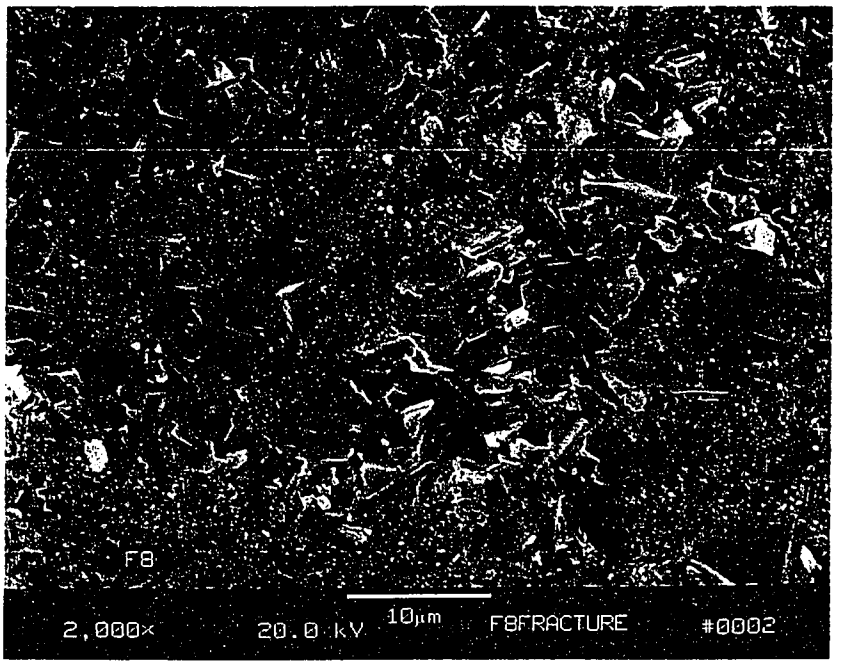

Figure 52 Fracture and crack morphology in the platelet composites: (a) SEM micrograph of the fracture surface for the composite tested in 4-point bending at room temperature.

(b)

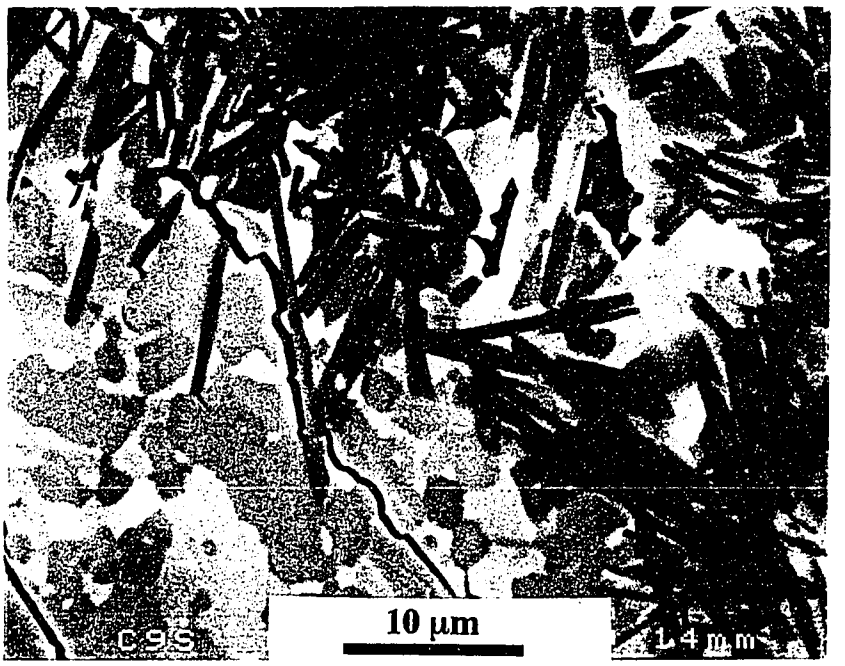

(c)

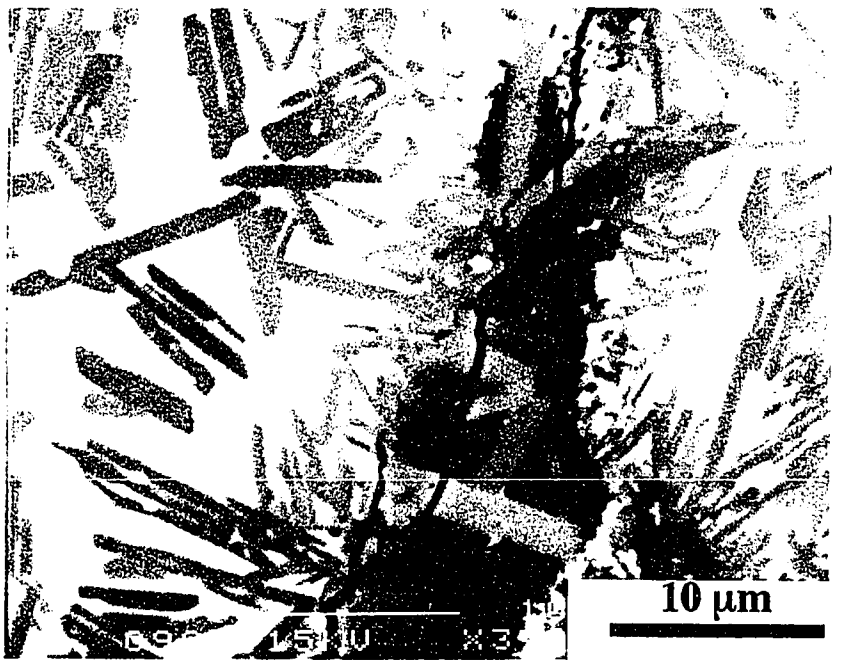

Figure 52 Fracture and crack morphology in the platelet composites: (b) SEM micrograph of the indentation crack propagating through $TiC_{0.65}$ regions with small Ti_3B_4 platelets; (c) SEM micrograph of the indentation crack propagating through TiB_2 regions with large Ti_3B_4 platelets.

(a)

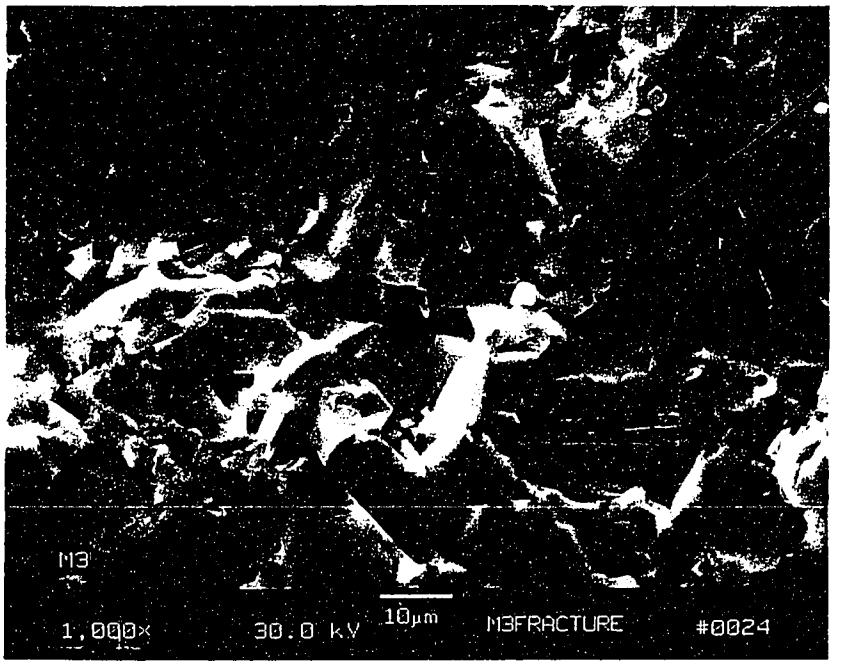

(b)

Figure 53 Fracture and crack morphology in the equilibrium equiaxed composites:
(a) SEM micrograph of the fracture surface for the composite tested in 4-point bending at room temperature;
(b) SEM micrograph of the crack emanating from Vickers indentation.

(a)

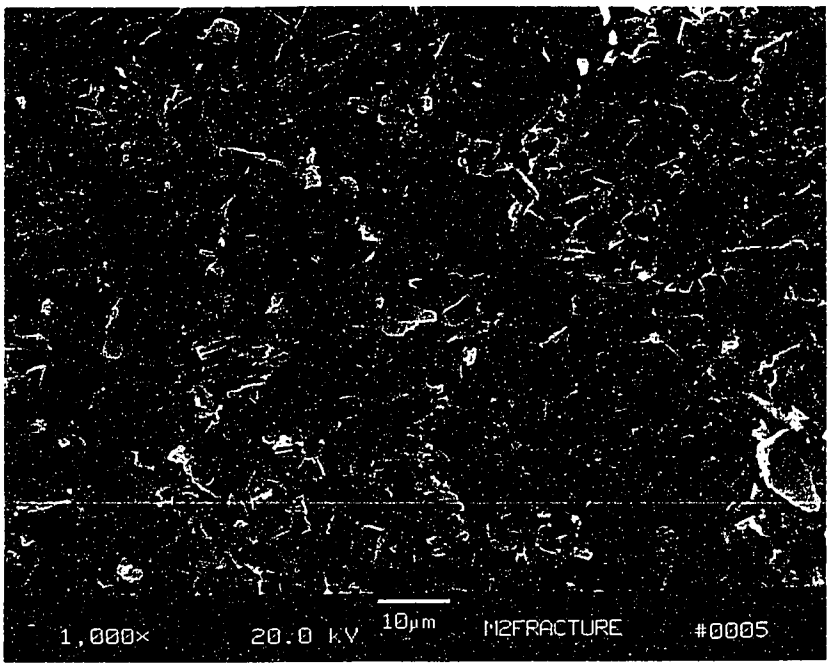

(b)

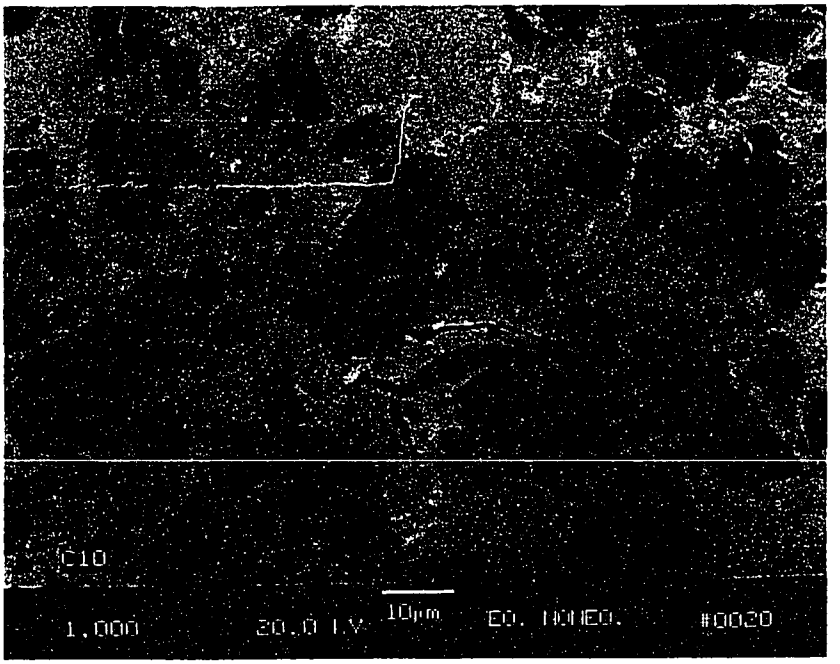

Figure 54 Fracture and crack morphology in the non-equilibrium equiaxed composites:
(a) SEM micrograph of the fracture surface for the composite tested in 4-point bending at room temperature;
(b) SEM micrograph of the crack emanating from Vickers indentation.

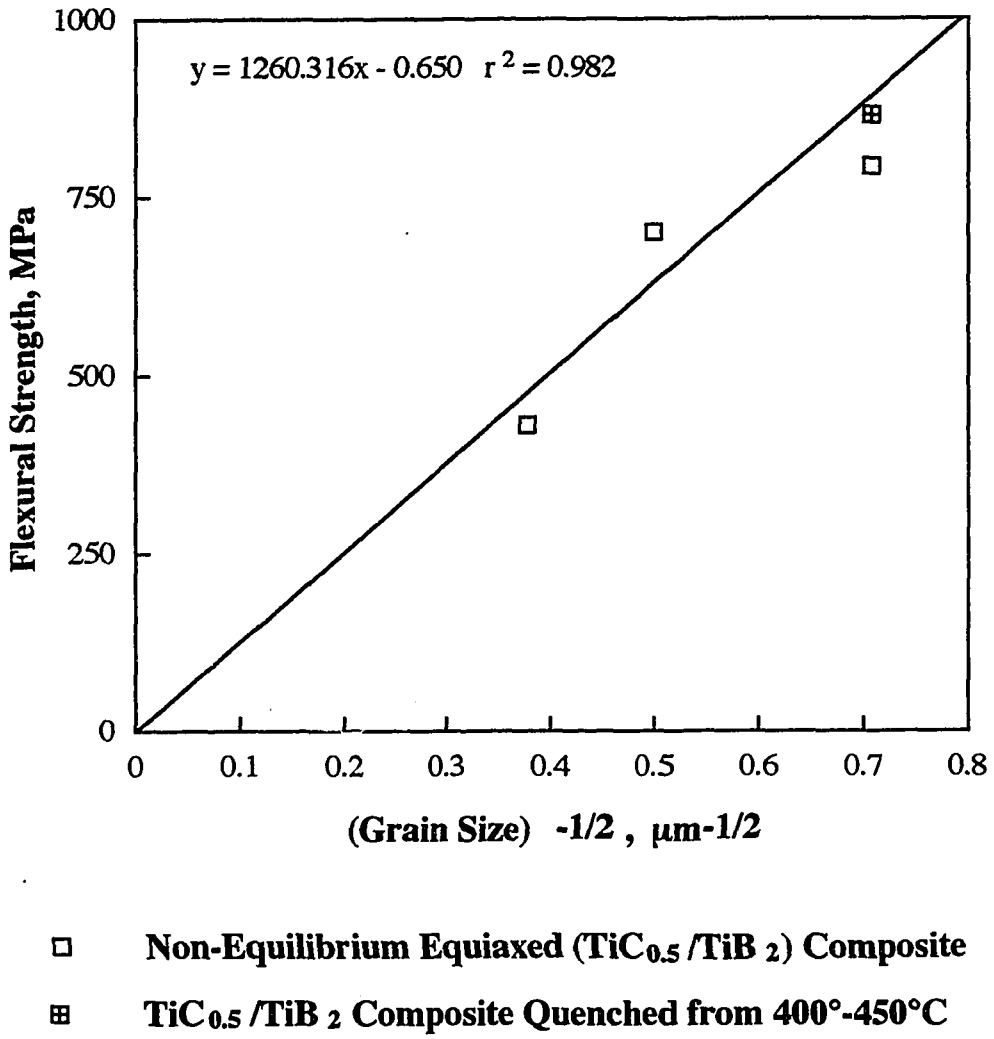

Figure 55 Variation of the flexural strength of the non-equilibrium equiaxed composites with the reciprocal of the square root of the average grain size in the composite.

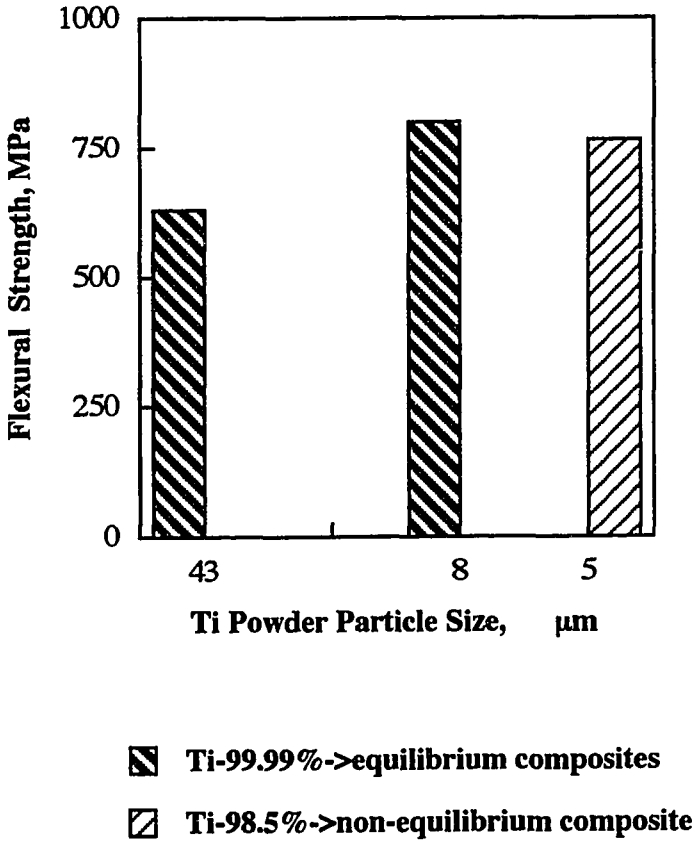

Figure 56 Comparison of the flexural strength of the platelet composites (4:1 Ti/B_4C starting composition) fabricated using Ti powder of different particle sizes.

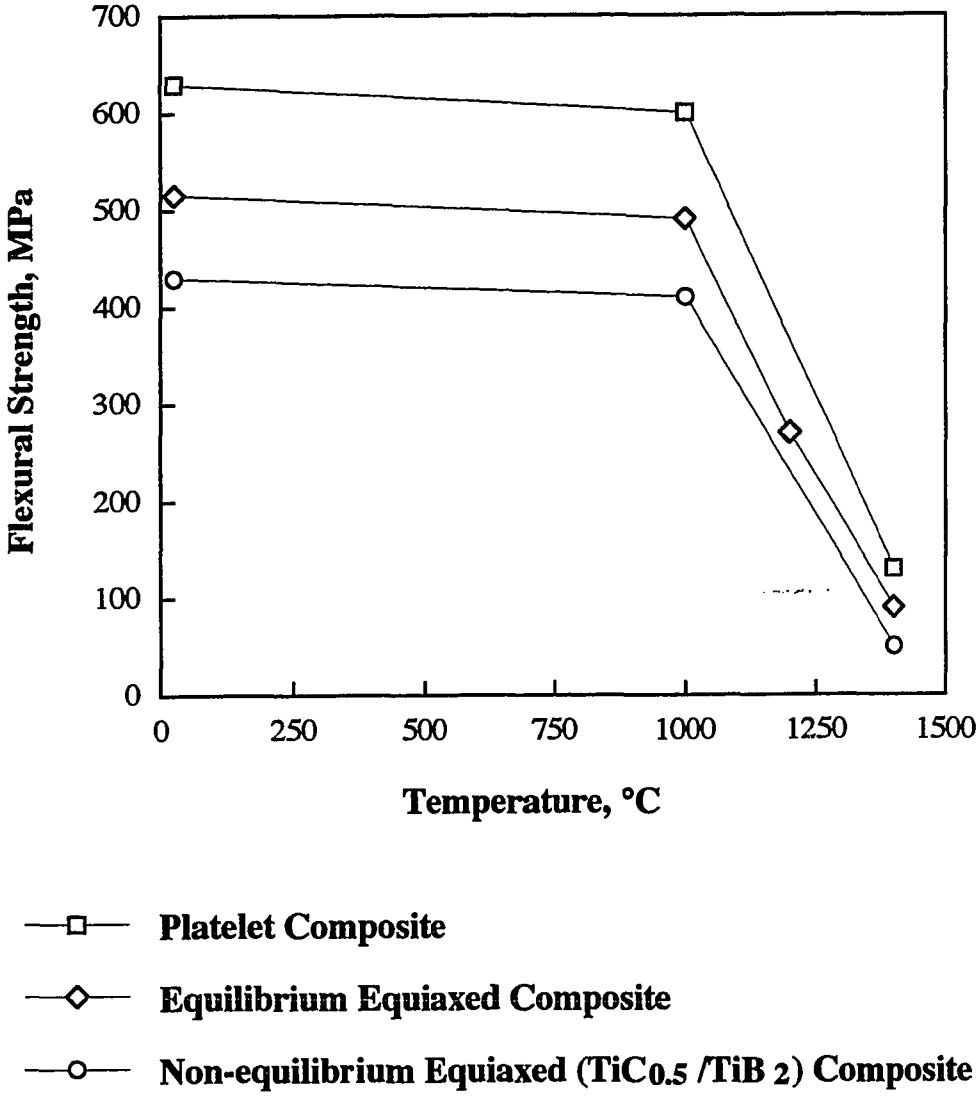

Figure 57 Variation of the flexural strength with temperature for the equilibrium platelet composite, the equilibrium equiaxed composite, and the non-equilibrium equiaxed composite.

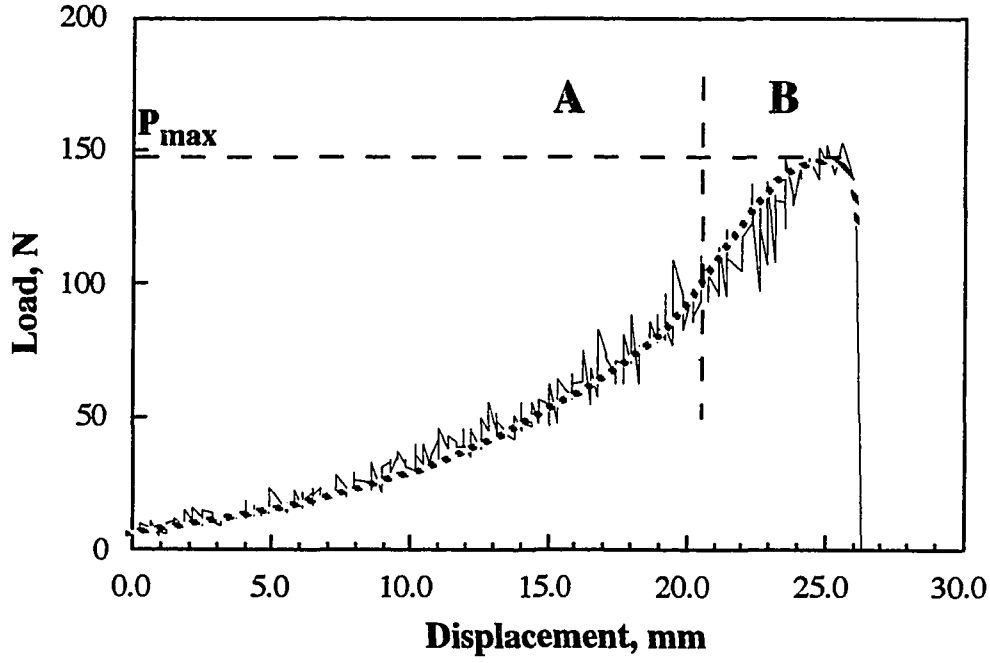

A: increasing slope due to compliance of the machine

B: decreasing slope due to stable crack growth

Figure 58 Typical load-displacement curve obtained in a valid chevron-notched beam test carried out at room temperature.

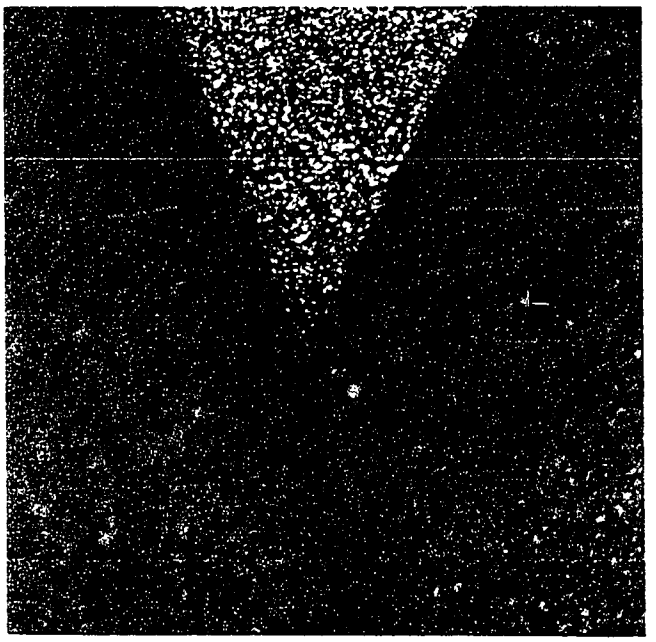

Figure 59 Photomicrograph of the fracture surface showing the color contrast between the stable crack growth region and the fast fracture region in the chevron-notched beam tested at 500°C and displacement rate of 0.002 mm/min.

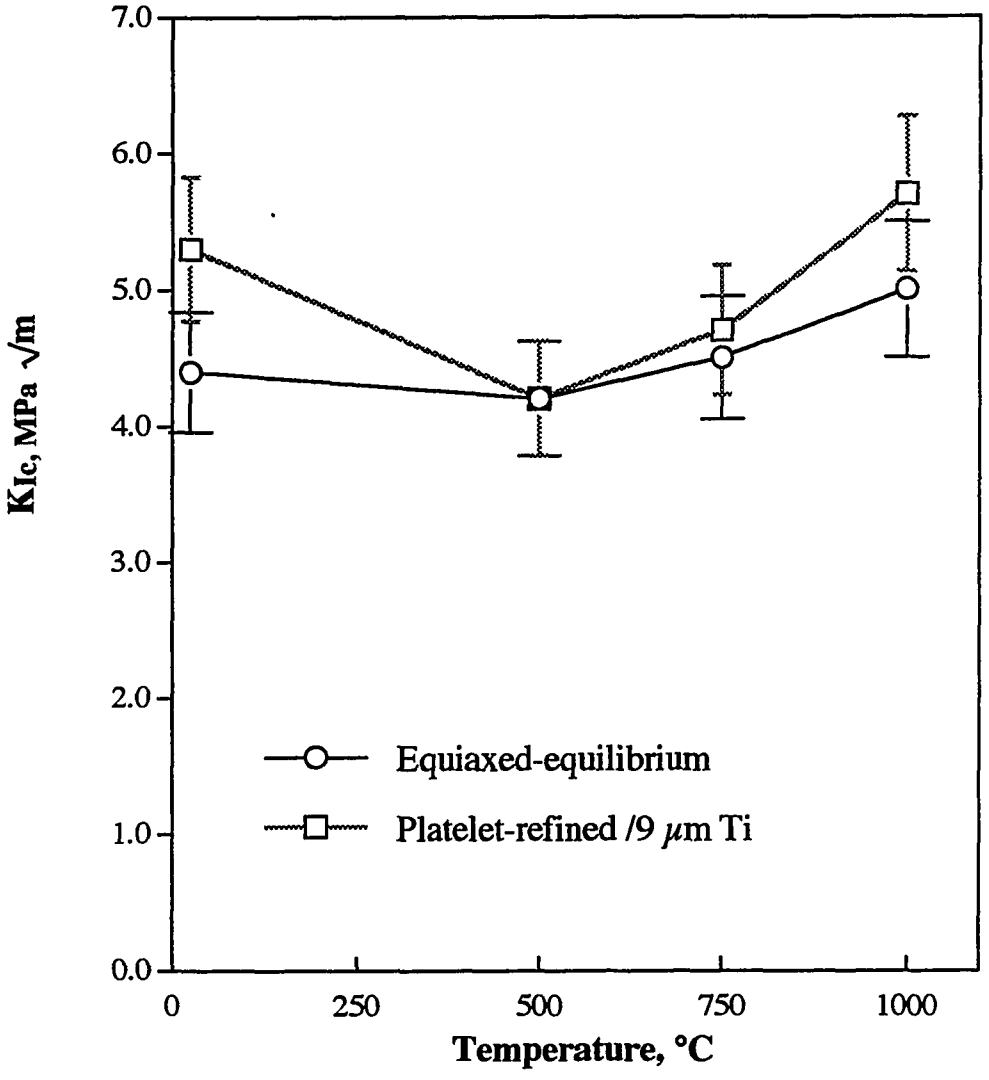

Figure 60 Variation of the fracture toughness with temperature for the refined equilibrium platelet composite and the equilibrium equiaxed composite.

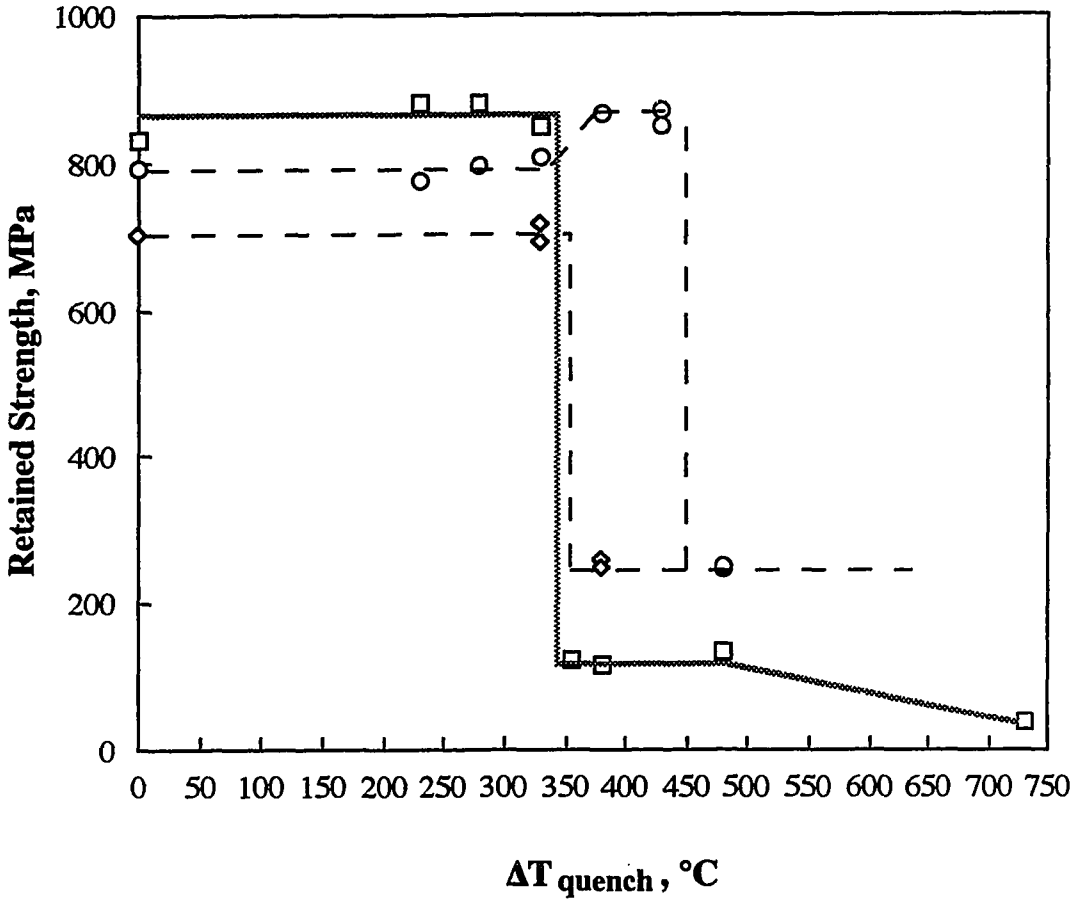

Figure 61 Retained strengths of the refined platelet composite and the refined non-equilibrium composites quenched in water as a function of temperature drop.

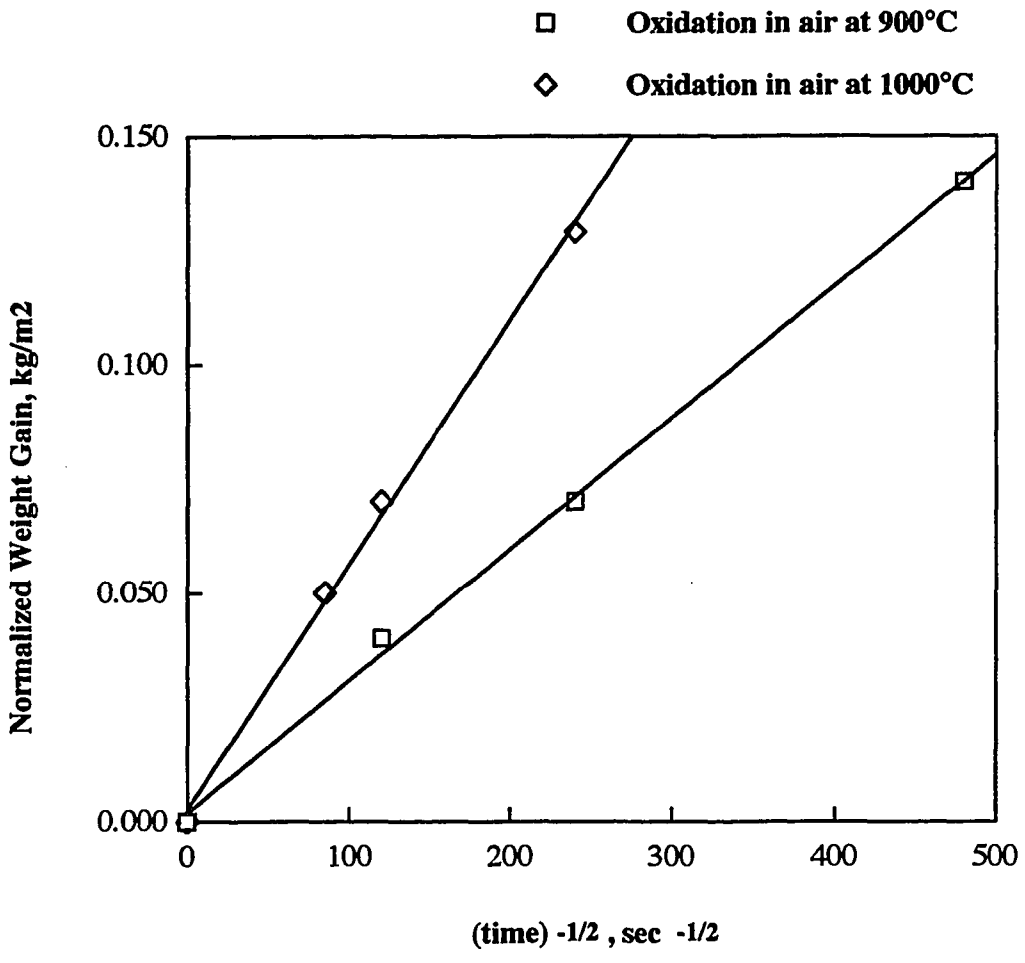

Figure 62 Weight gain (normalized by surface area) during oxidation in air for the refined platelet composite at 900°-1000°C.

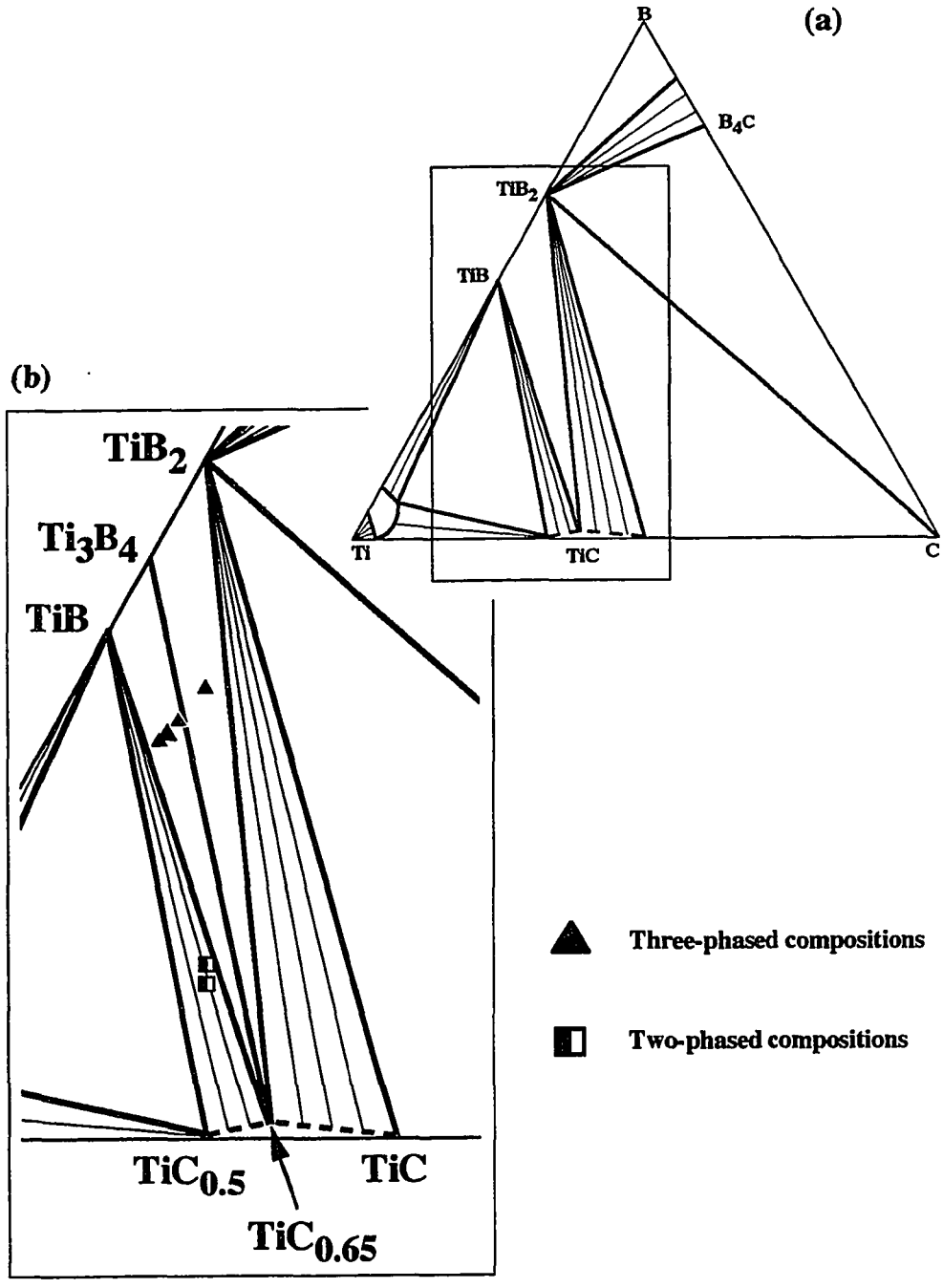

Figure 63 Isothermal section of the Ti-B-C phase diagram at 1600 °C. (a) as reported by Rudy [100] (here shown schematically, see Figure 20 for the original version); (b) based on this work.

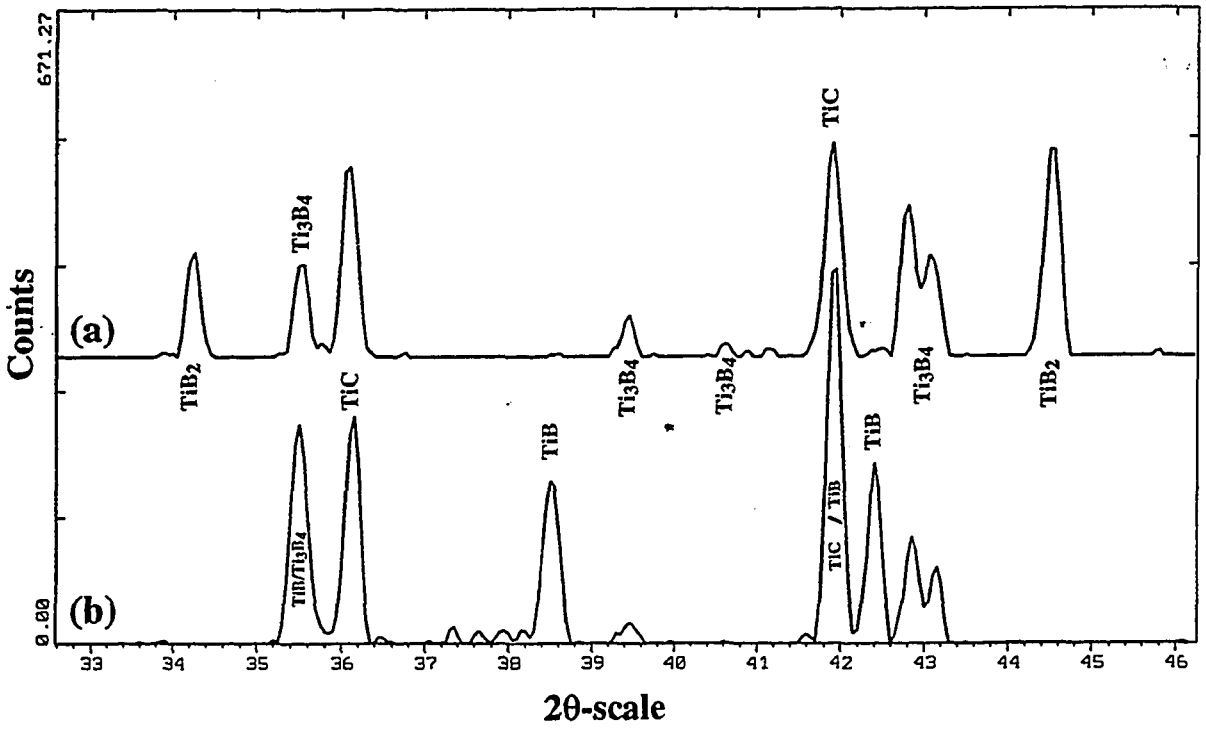

Figure 64 X-ray diffraction pattern of (a) specimen produced in run 1, in which the starting composition belongs to the TiB_2-Ti_3B_4-$TiC_{0.65}$ compatibility triangle, and (b) specimen, in which the starting composition belongs to the TiB-Ti_3B_4-$TiC_{0.65}$ compatibility triangle, produced in run 5 and consequently annealed for 32 h in vacuum.

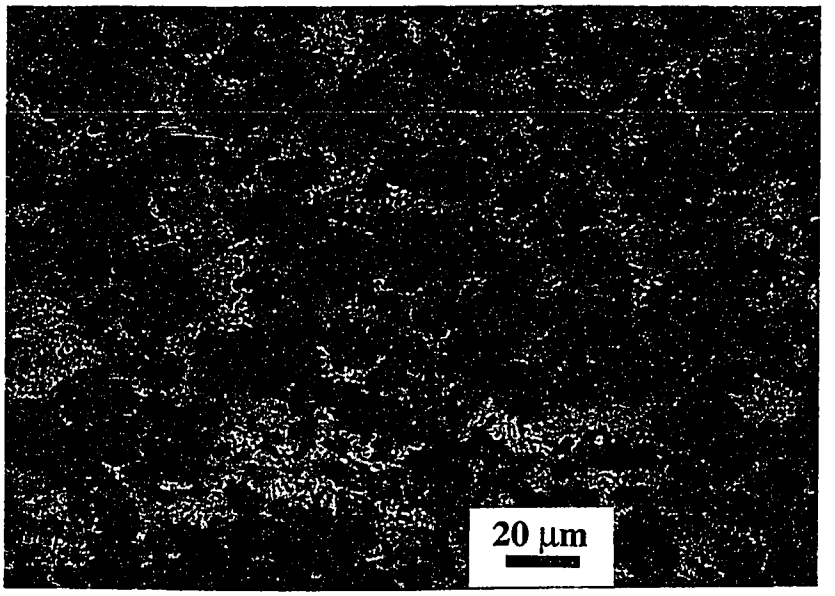

Figure 65 Backscattered SEM micrograph of the sample produced from the 1:0.5:1 $Ti/C/TiB_2$ starting composition (run 2) and consequently annealed for 32 h in vacuum. Phases: white - $TiC_{0.65}$, black - TiB_2, gray - Ti_3B_4.

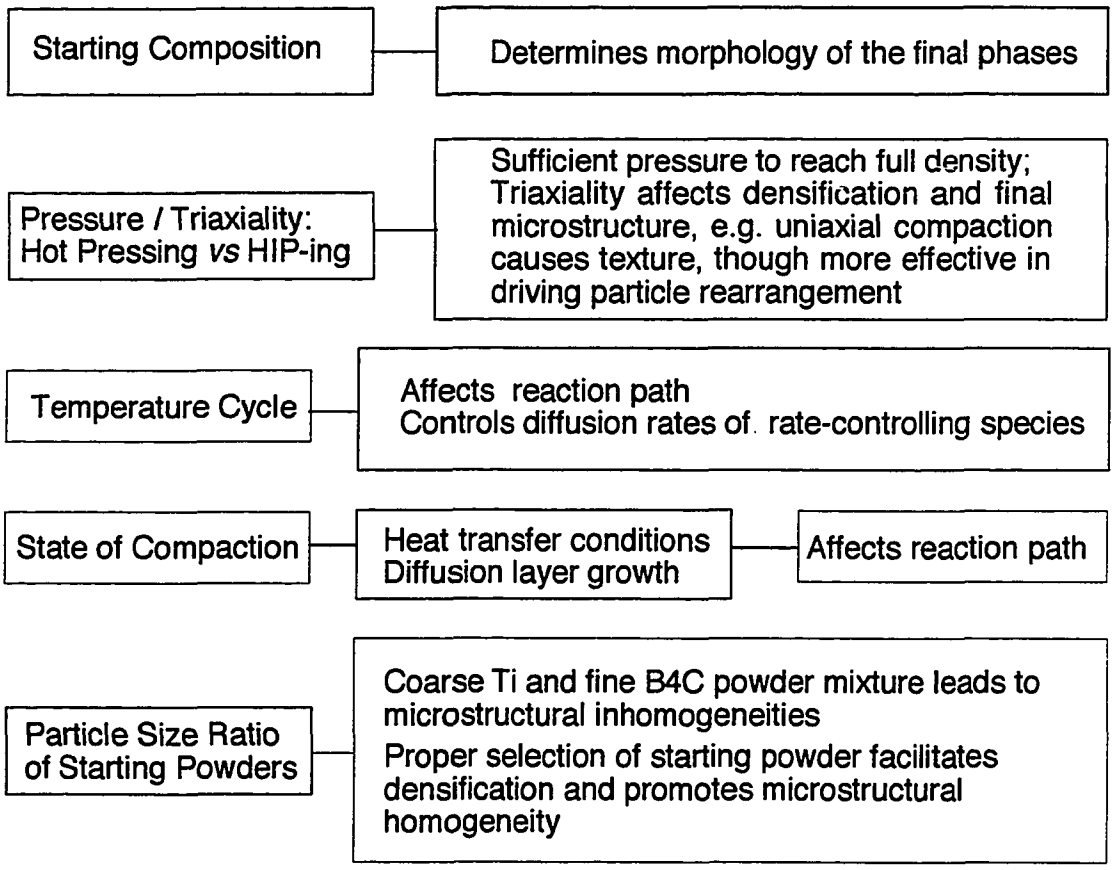

Figure 66 Dominant processing parameters in TPP-processing of TiC_x-TiB_2-(Ti_3B_4) composites.

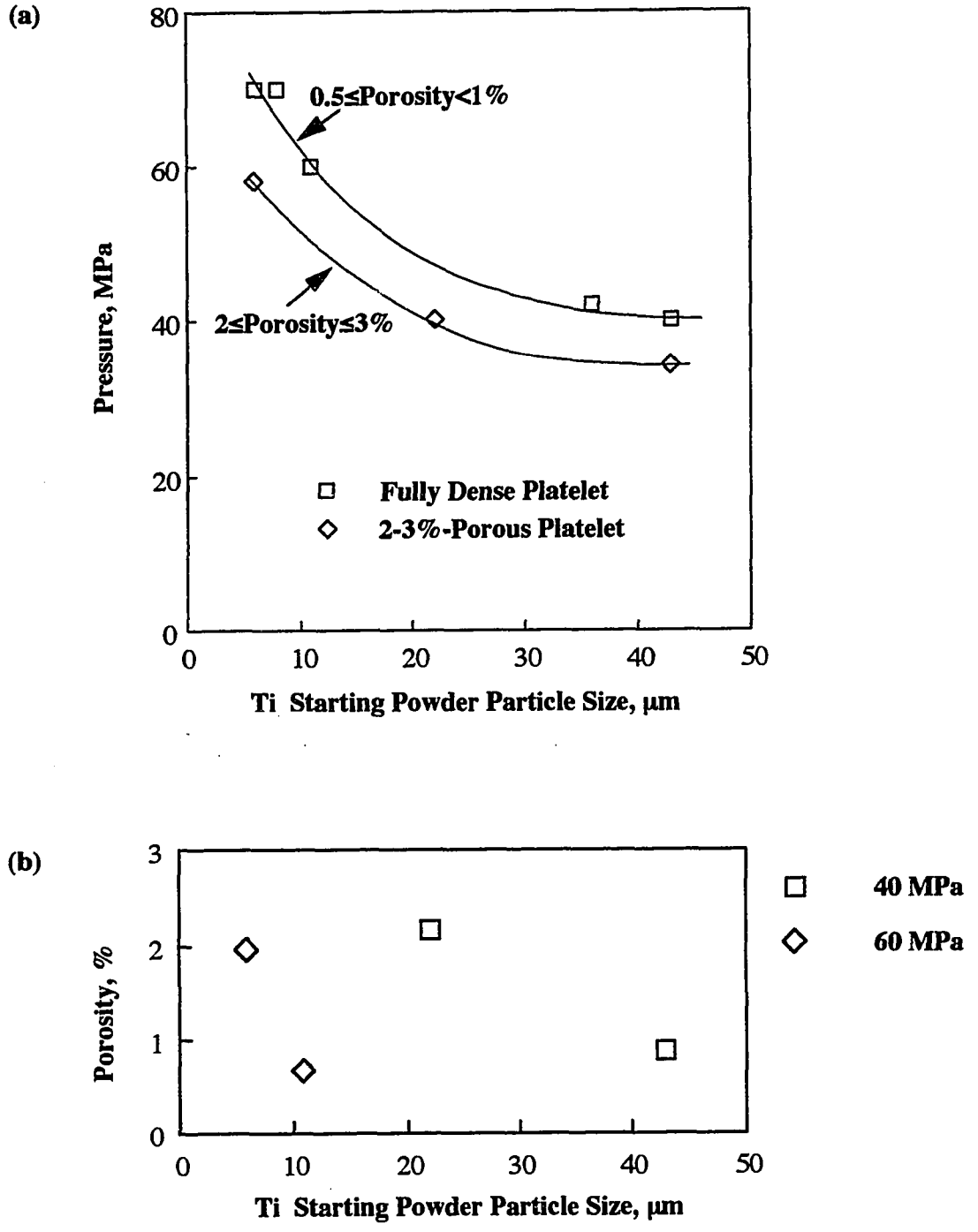

Figure 67 Hot-pressing diagrams for the platelet composition: (a) The applied pressure required to achieve the certain level of porosity as a function of the starting Ti powder particle size; (b) The final porosity in the produced composites as a function of the starting Ti powder particle size for the applied pressures indicated.

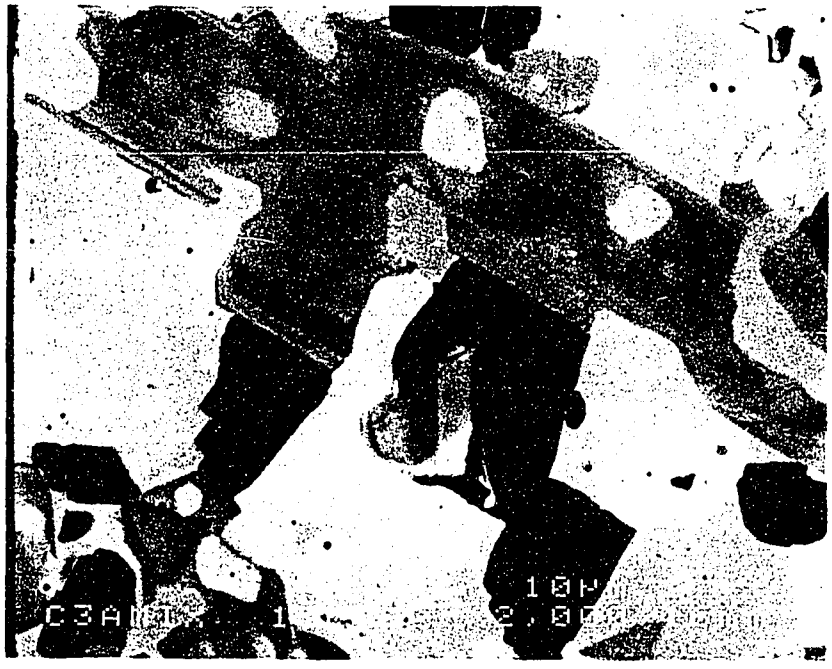

Figure 68 High-magnification backscattered micrograph of the non-equilibrium equiaxed composite with ~20 vol% of Ti_3B_4 phase showing the Ti_3B_4 phase surrounding multiple small TiC_x particles seemingly excluded from the reaction.

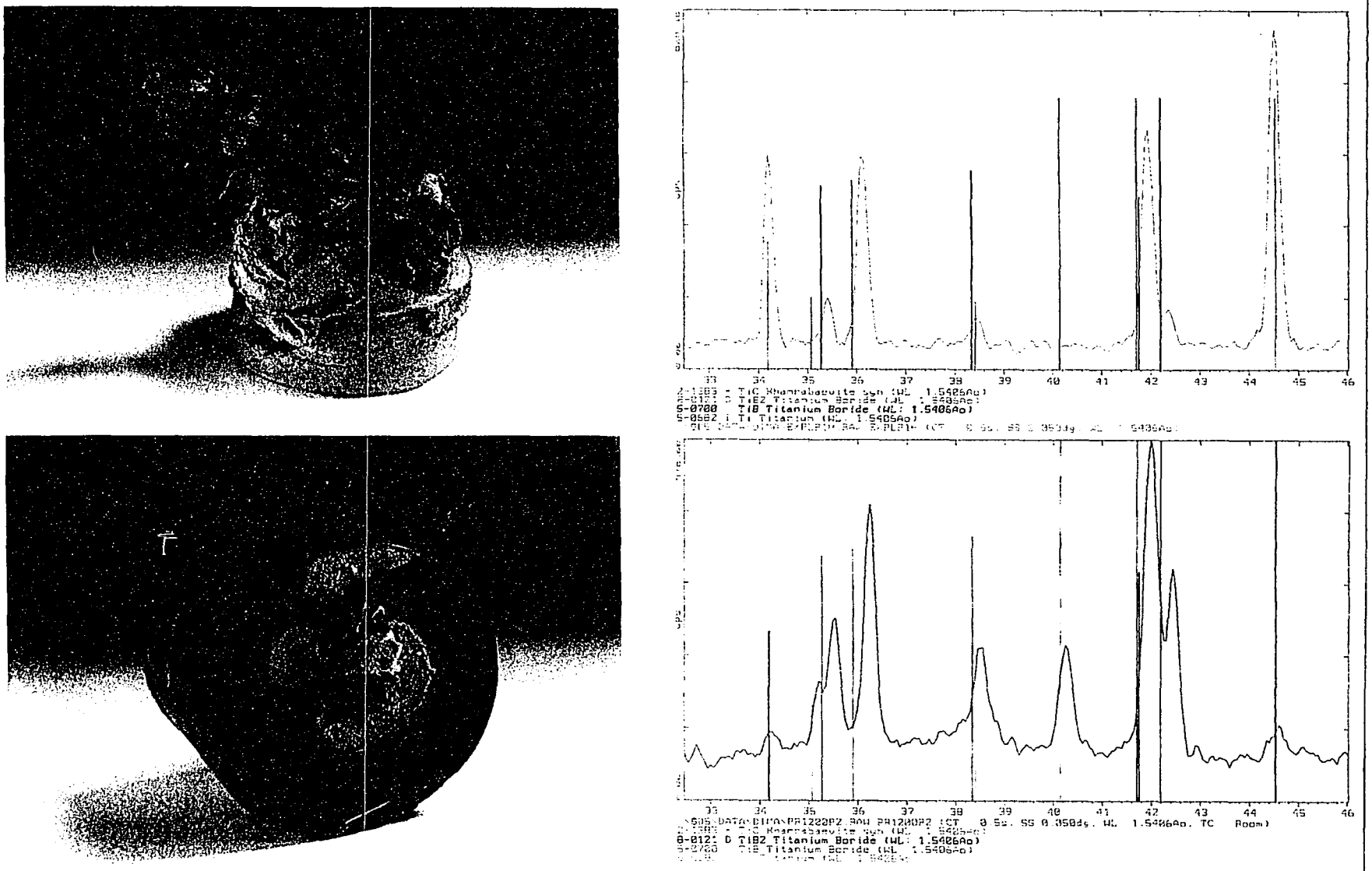

Figure 69 Dependence of the reaction path on the green density (state of compaction) of the 4:1 Ti/B_4C samples reacted by heating in vacuum (10^{-4} torr, 10°C/min) to 1200°C: (a) loose powder mixture; (b) pre-compacted specimen of 74% green density.

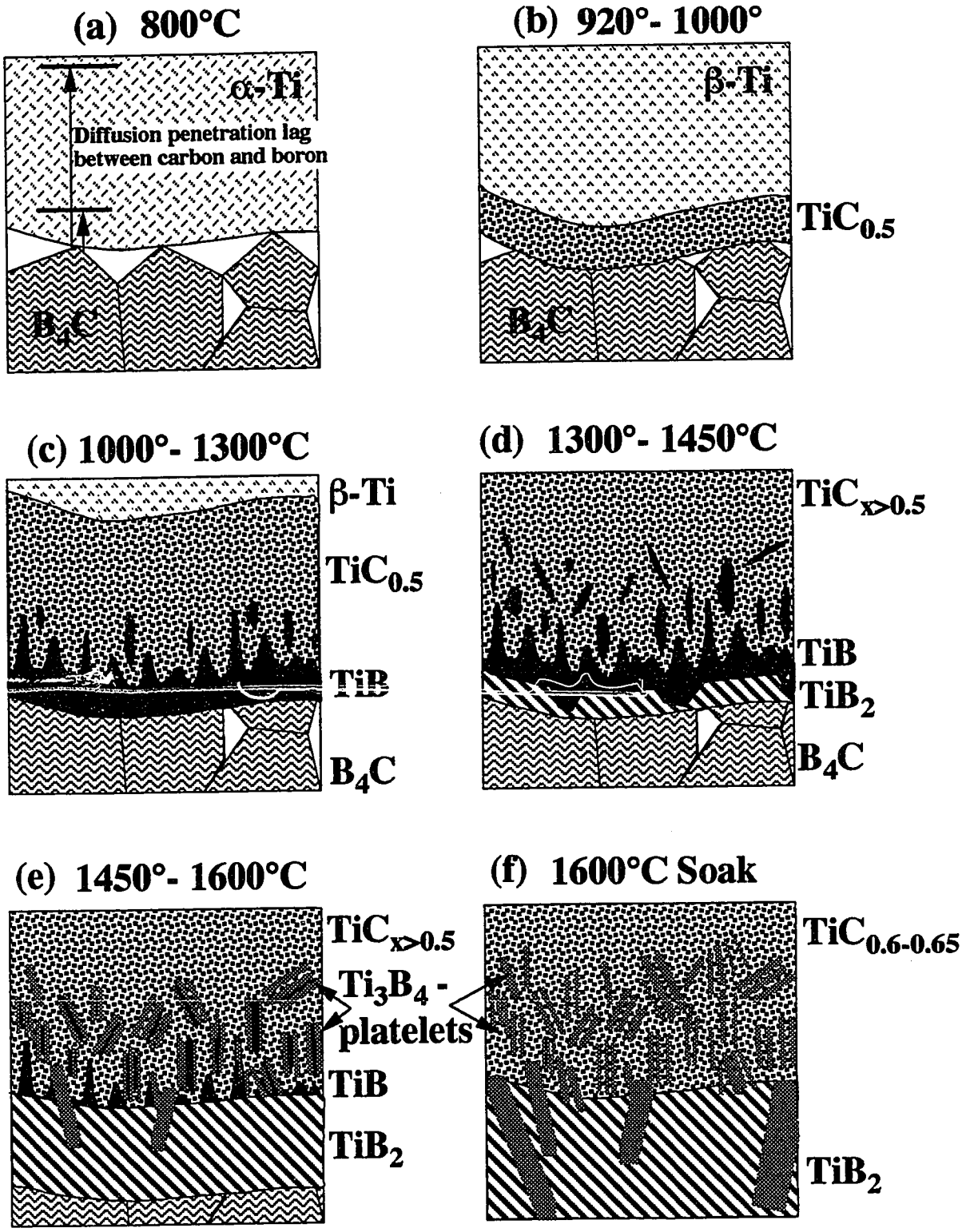

Figure 70 Schematic of microstructural evolution in the "platelet" composites.

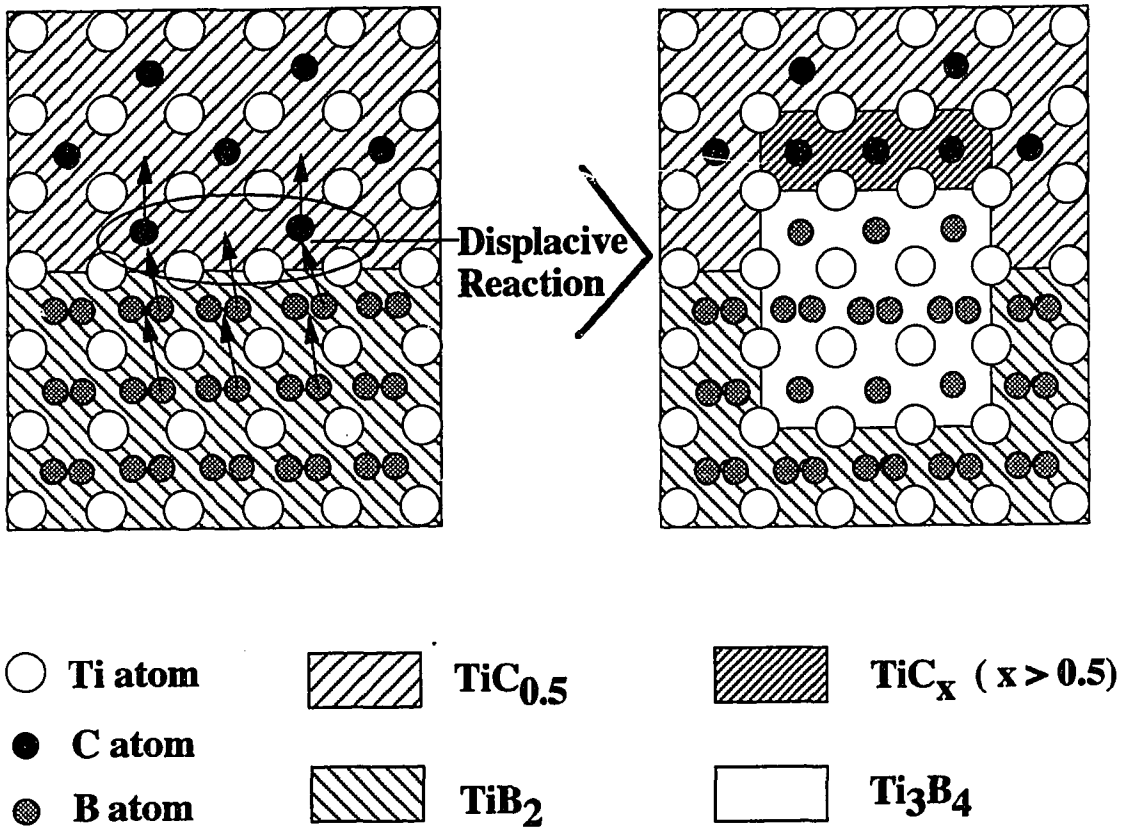

Figure 71 Proposed mechanism of the Ti_3B_4 phase formation in the equiaxed composites by displacement of C with B rather than mobility of Ti.

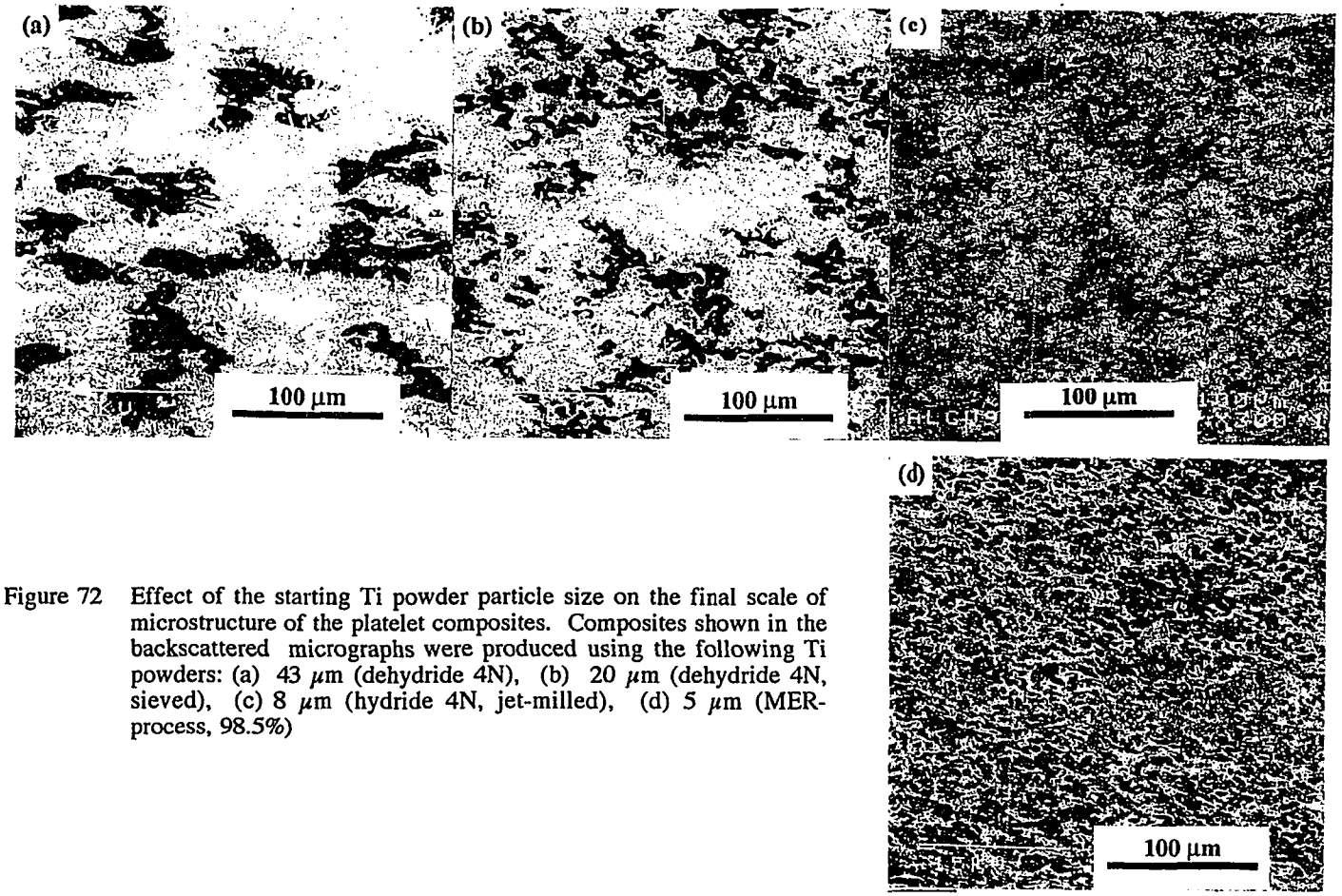

Figure 72 Effect of the starting Ti powder particle size on the final scale of microstructure of the platelet composites. Composites shown in the backscattered micrographs were produced using the following Ti powders: (a) 43 μm (dehydride 4N), (b) 20 μm (dehydride 4N, sieved), (c) 8 μm (hydride 4N, jet-milled), (d) 5 μm (MER-process, 98.5%)

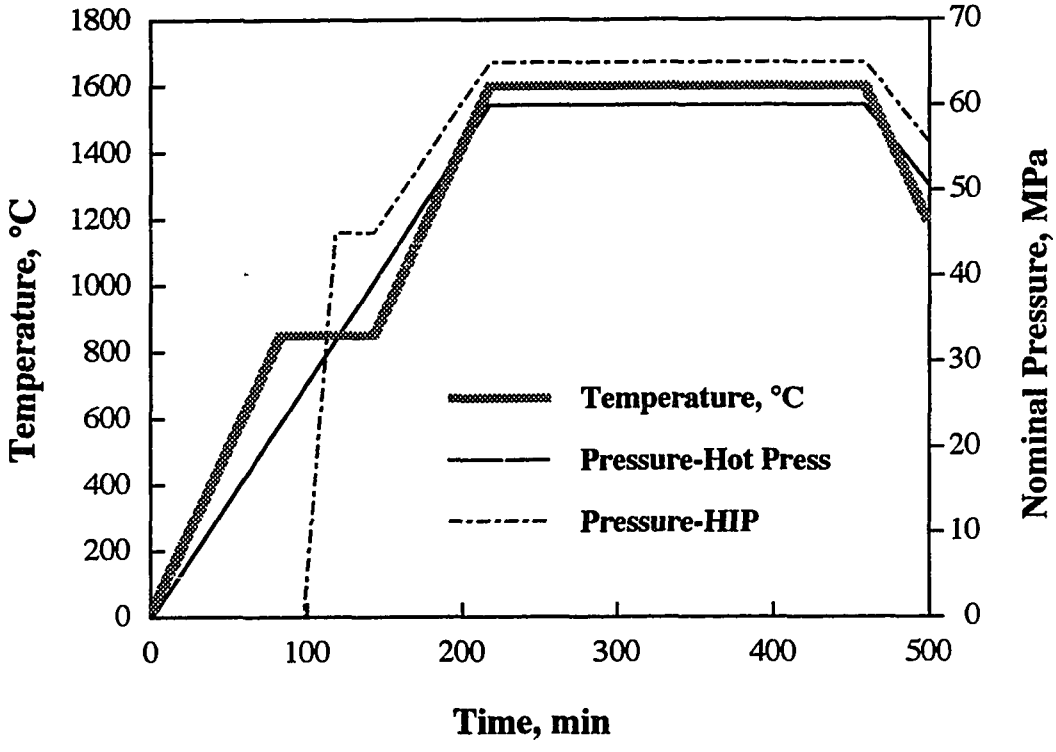

Figure 73 Temperature and pressure schedules for the HIP and hot press runs which yielded platelet composites shown in Figures 74 (a) and 74 (b,c), respectively.

(a)

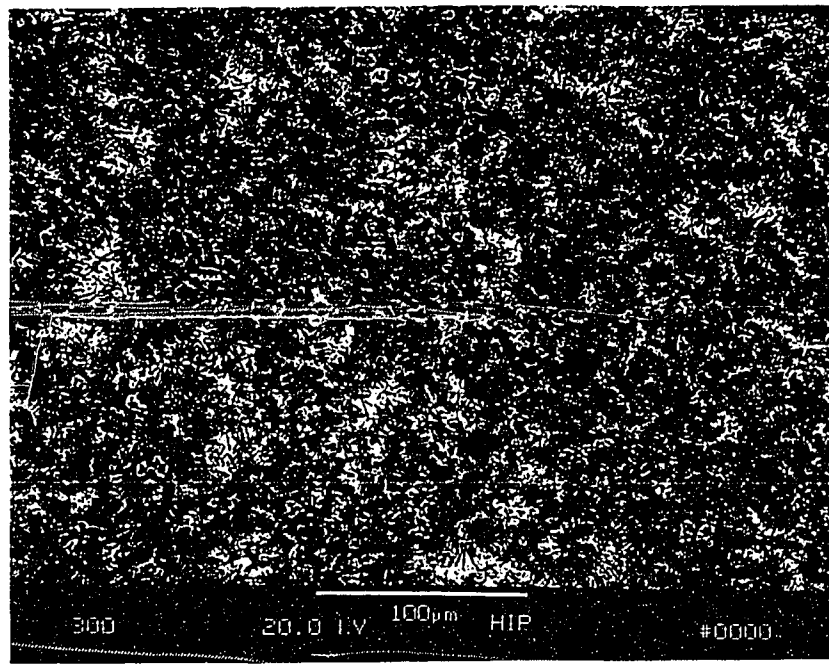

(b)

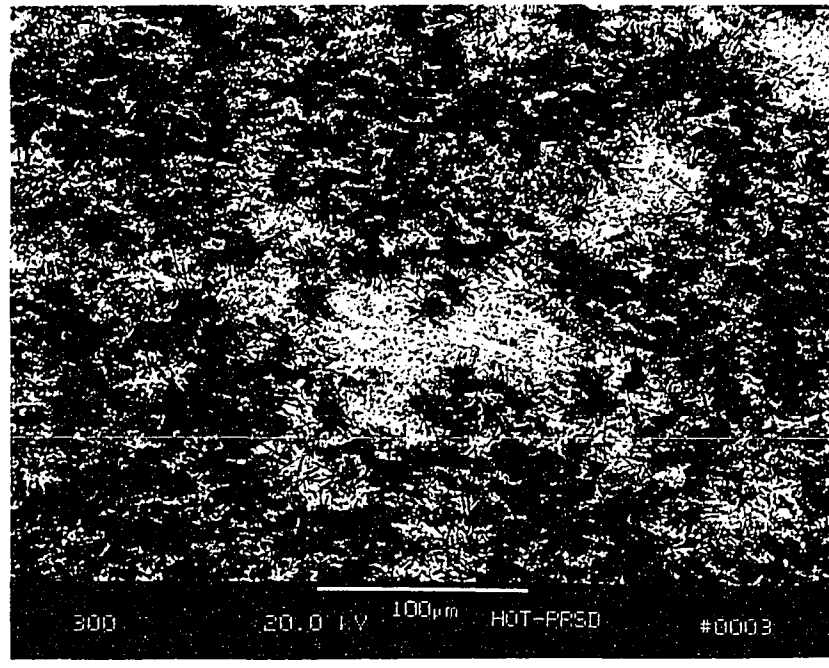

Figure 74 Microstructures of the platelet composites produced by (a) HIP-ing - backscattered micrograph; (b) Hot-pressing - backscattered micrograph of a transverse section;

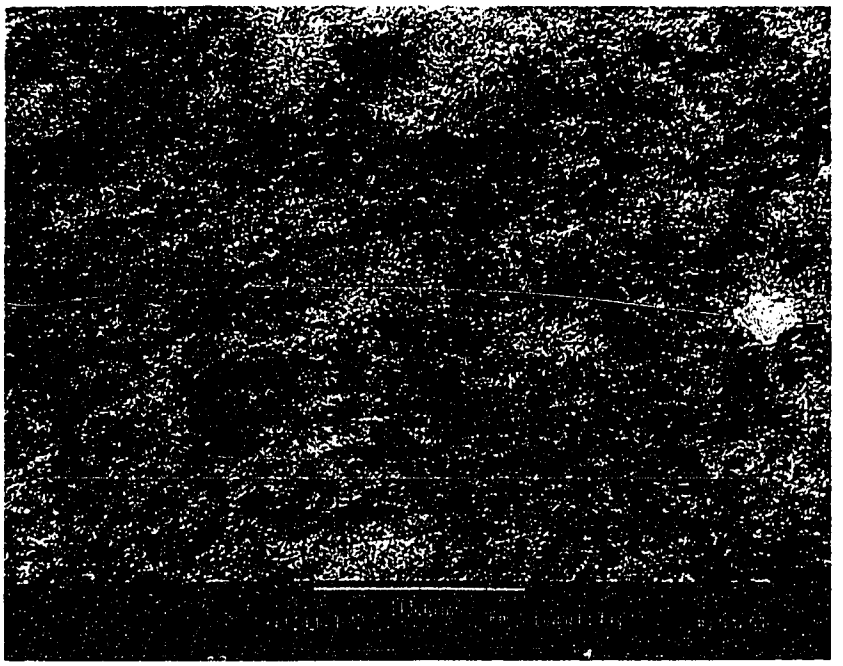

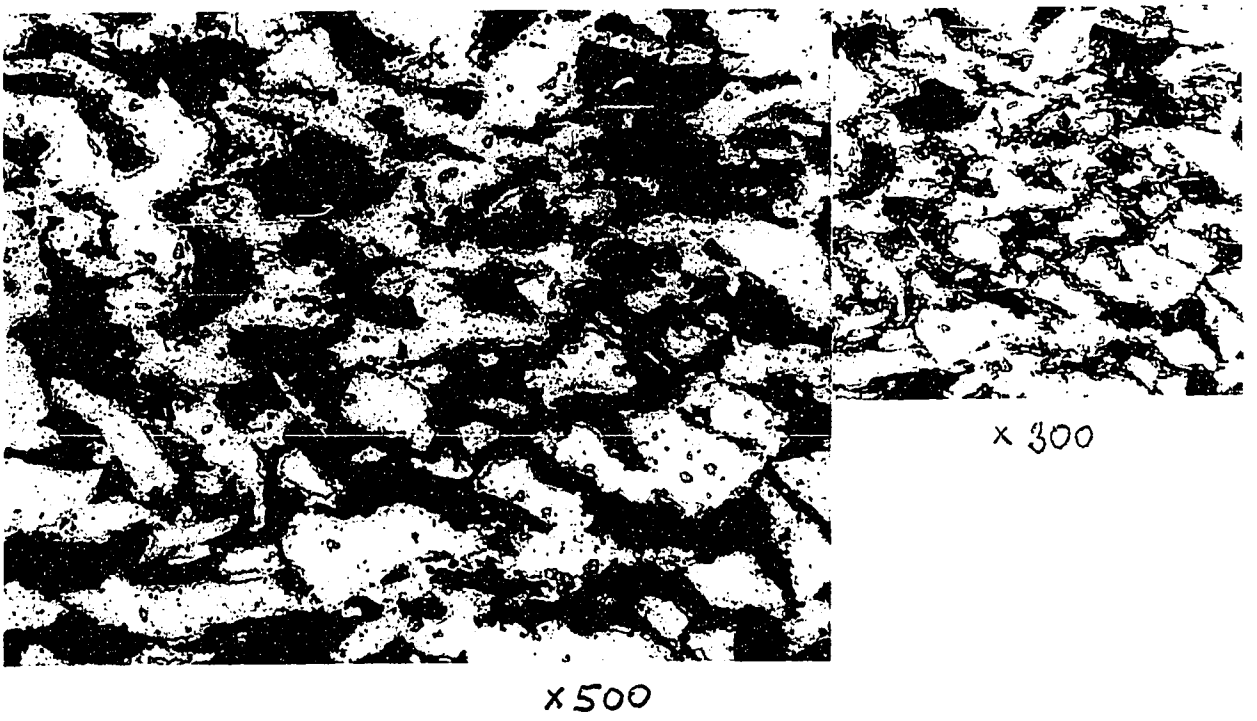

Figure 74 Microstructures of the platelet composites produced by (c) Hot-pressing - backscattered micrograph of a longitudinal section; (d) optical micrograph of the sample from the hot-pressed run interrupted at 800°C (mag. x500).

Figure 75 Backscattered micrograph of the nearly laminate-type microstructure, comprised of alternating layers of TiB_2-Ti_3B_4 (black and gray) and $TiC_{0.65}$ (white) that was produced by occasional forging when the reaction product flew into the narrow gap between the die cavity and the pushing rod.

(a)

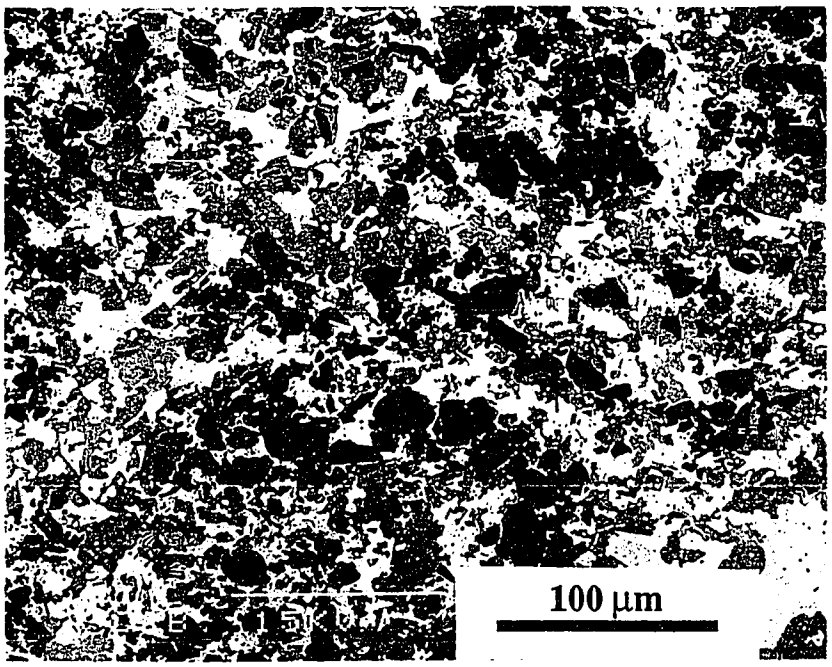

(b)

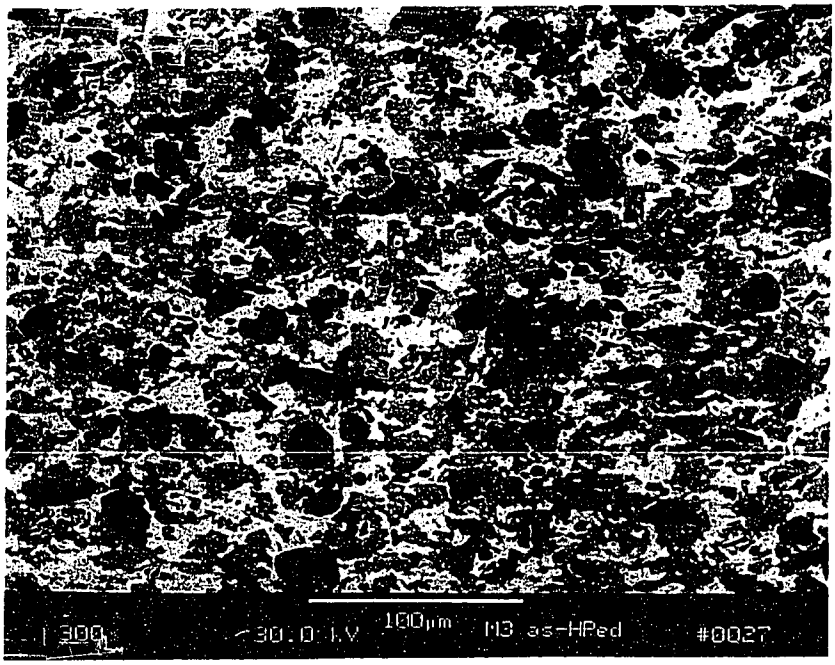

Figure 76 Effect of the starting Ti powder particle size on the morphological texture formation in the equilibrium equiaxed composites. Composites shown in the backscattered micrographs were produced using the following Ti powders: (a) 43 μm (dehydride 4N), (b) 20 μm (dehydride 4N, sieved).

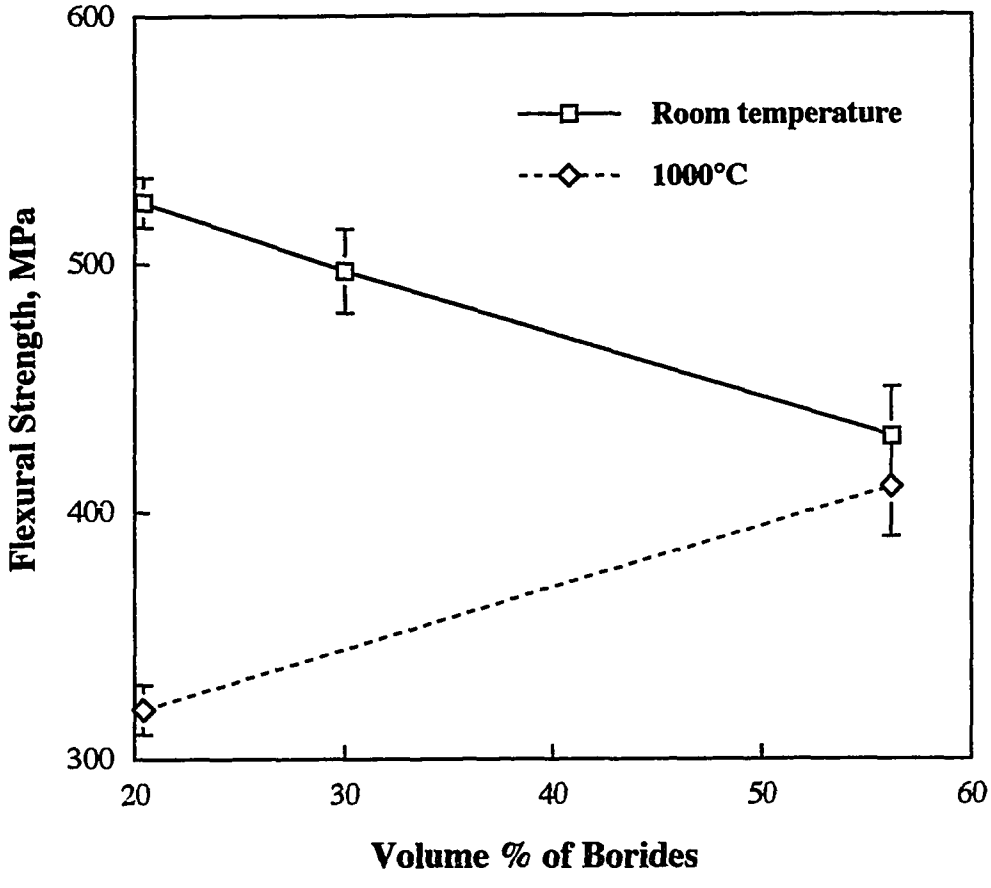

Figure 77 Variation of the room and high temperature flexural strengths of the coarse-grained non-equilibrium equiaxed ($TiC_{0.5}/TiB_2$) composites, fabricated with different carbide/boride mole ratios, with the volume fraction of TiB_2.

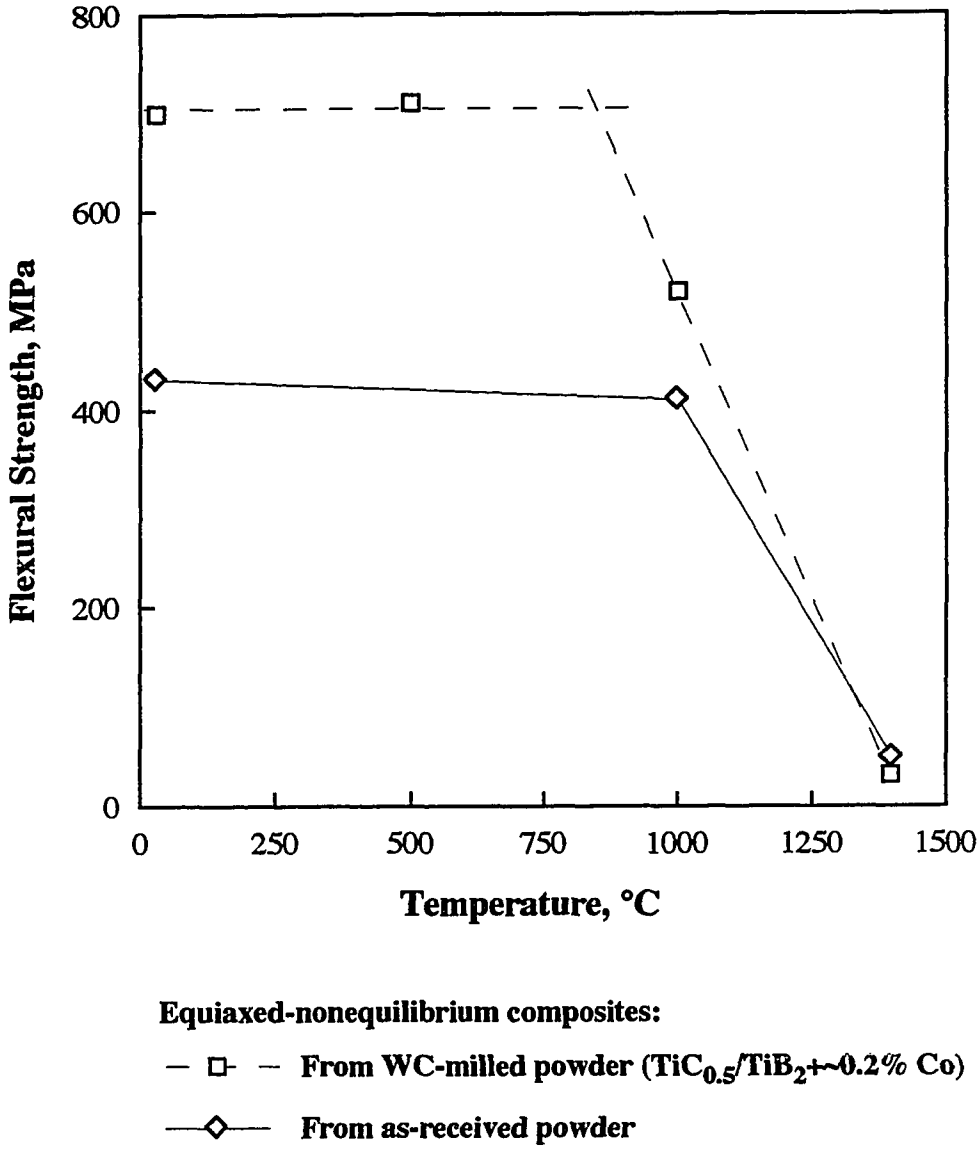

Figure 78 Variation of the flexural strength with temperature for the two non-equilibrium equiaxed composites with the different impurity levels. Impurities (~0.2 wt.% Co) were introduced in the refined non-equilibrium equiaxed composite during ball-milling by WC-Co grinding media.

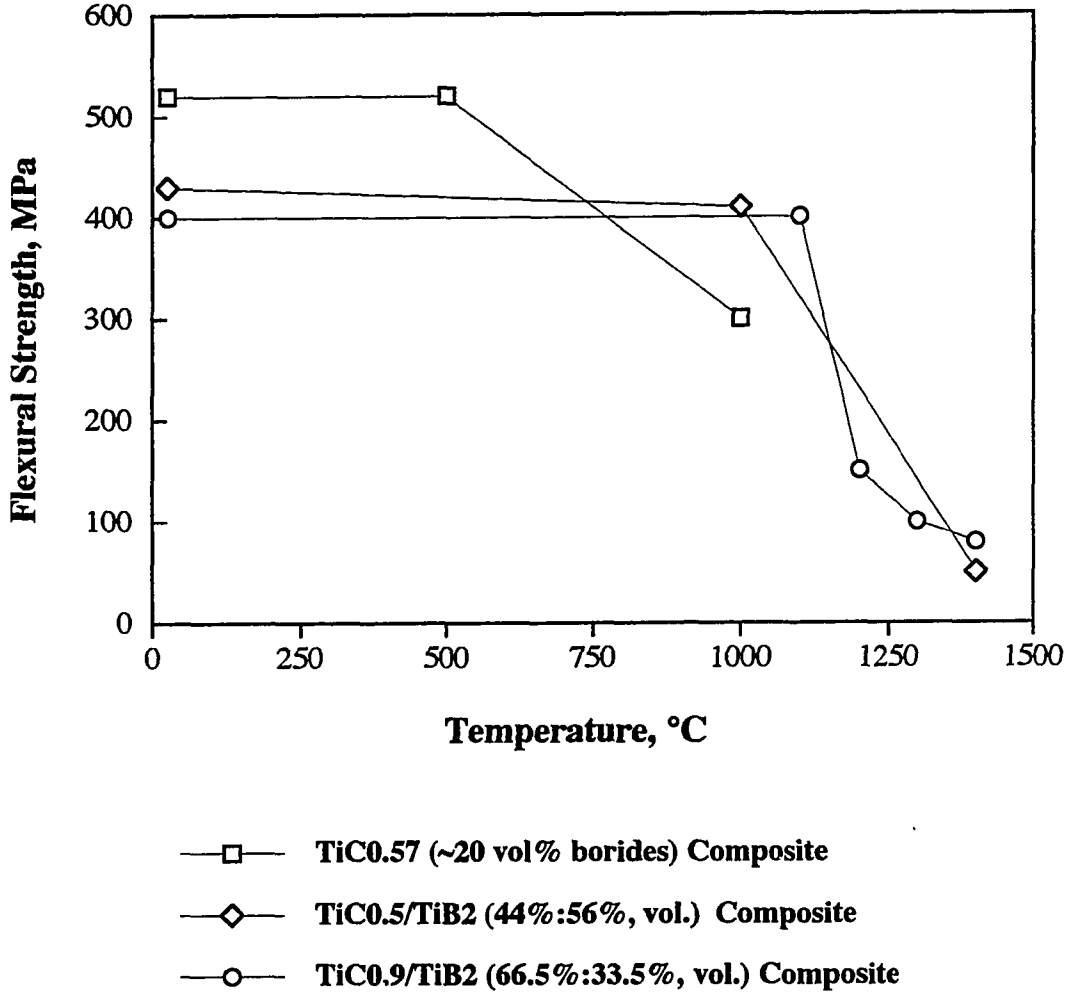

Figure 79 Variation of the flexural strength with temperature for the TiC_x/TiB_2 composites with the different stoichiometries of TiC_x and different volume fraction of borides as indicated.

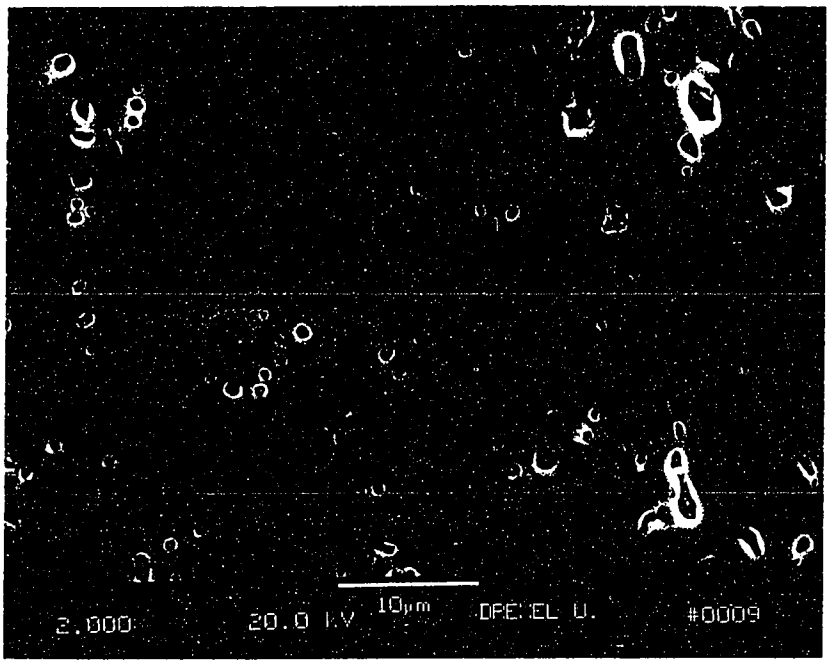

Figure 80 Backscattered micrograph of the $TiC_{0.9}$-33.5 vol% TiB_2 composite.

APPENDICES

APPENDIX I

Linearized Calibration Curve for C/Ti Ratio vs Lattice Parameter for TiC_x, x=0.5-0.7

The following figure shows results of a linear fit of the data available in the literature on relation between stoichiometry (x) of TiC_x and its lattice parameter for x=0.5-0.7. Summarized in this figure is the data reported by Rudy [100], Miracle and Lipsitt [99], Ordan'yan et al. [106], and Storms [107].

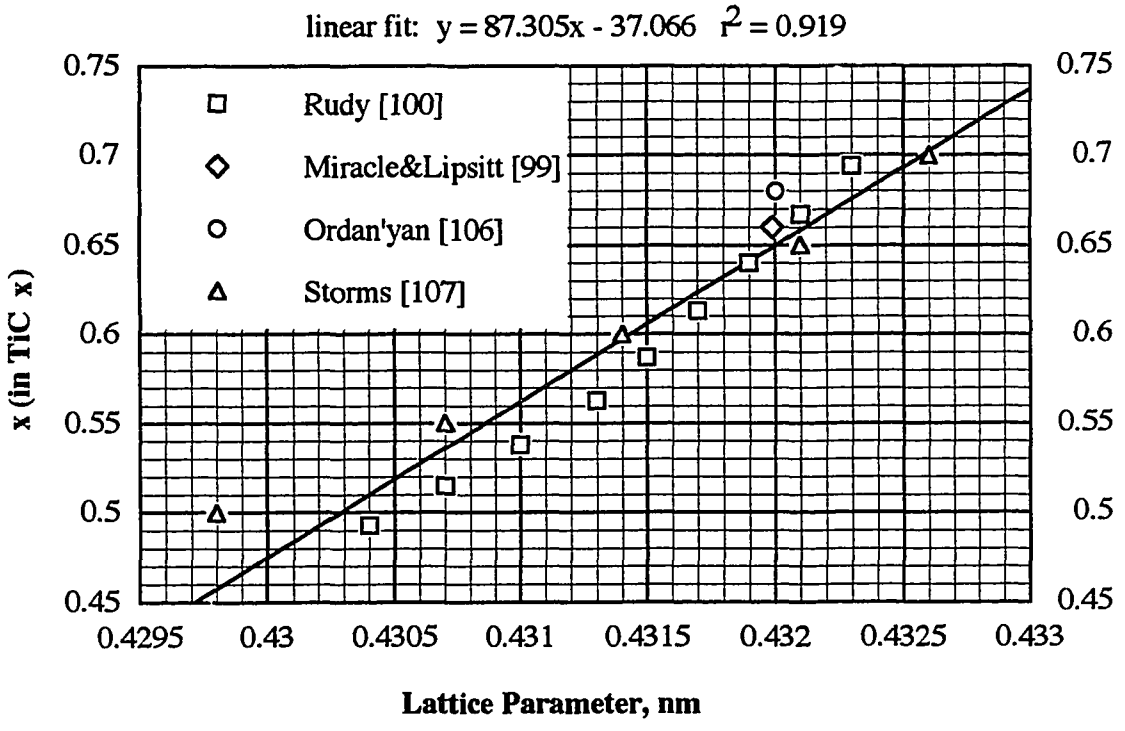

APPENDIX II

Calculation of critical crack length for chevron notched beam tested in 4-point bending configuration

As discussed in Section 3.7.5.2, the compliance function $Y^*(\alpha)$ is a dimensionless geometric function of the relative crack length (α) and characterizes the stress intensity factor per unit load (K_I/P). For chevron-notched specimen this function passes through a minimum Y^*_{min} when $\alpha=\alpha_m$ i.e. $Y^*_{min}=\min (Y^*(\alpha))=Y^*(\alpha_m)$; at this relative crack length, α_m, the applied load reaches a maximum value, P_{max}.

The compliance function for chevron notched beam employed in this study for fracture toughness measurements was derived by Munz et. al. [157] based on the straight-through crack assumption (STCA). In this approach it is assumed that, for a specimen with a chevron notch, the derivative of the compliance with respect to α , is the same as for a specimen with a straight-through crack. Munz et. al. showed that the compliance function (Y^*) for a chevron-notched beam subjected to pure bending is related to the compliance function (Y) of a beam with a straight-through crack as

$$Y^*=Y[(\alpha_1-\alpha_0)/(\alpha-\alpha_0)]^{1/2} \qquad (22)$$

where α_o and α_1 are dimensionless parameters illustrated in Figure 42. The compliance for a specimen with a straight-through crack (Y) is given by Munz et al. as

$$Y=\frac{S_1-S_2}{W}\frac{3\Gamma_M\sqrt{\alpha}}{2(1-\alpha)^{3/2}} \qquad (23)$$

where S_1 is outer and S_2 is inner span of four-point bending fixture, W is the thickness of the specimen (see Figure 2), and Γ_M is the function of the relative crack length, α, and was given [157] as

$$\Gamma_M = 1.9887 - 1.326\alpha - \frac{(3.49 - 0.68\alpha + 1.35\alpha^2)\alpha(1-\alpha)}{(1+\alpha)^2} \qquad (24)$$

For the specimen employed in this study $\alpha_o = a_o/W = 0.2$, $\alpha_1 = a_1/W = 1.0$, $S_1 = 20$ mm and $S_2 = 10$ mm. The computation of the corresponding $Y^*(\alpha)$ based on Eq.22-24 were carried out in Maple. The program and the resulting plot of Y^* as a function of the relative crack length ($x=\alpha$) are shown below. The critical crack length, a_m, for the chosen geometry was computed to be $\approx 0.4W$. The amount of crack extension ($a_m - a_o$) at Y^*_{min} is 102 μm.

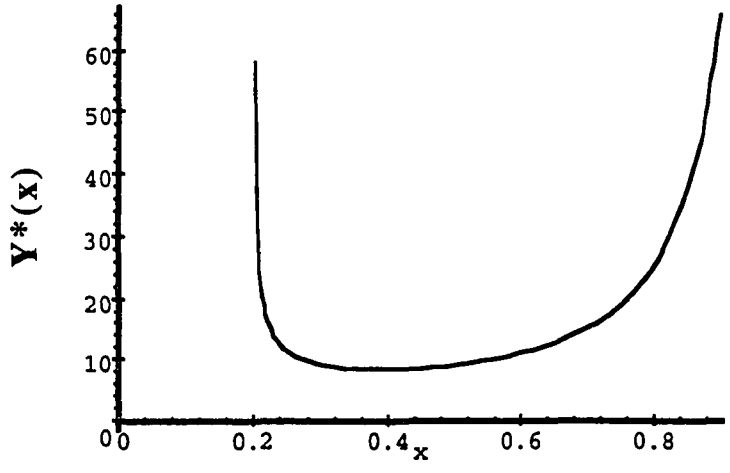


```
> plot(2.952*x^0.5/(1.0-x)^1.5*(1.9887-1.326*x-(3.49-
.68*x+1.35*x^2.0)*x*(1.0-x)/(1.0+x)^2.0), x=0..1.0);
```

```
> plot(0.8944/(x-0.2)^.5*2.952*x^0.5/(1.0-x)^1.5*(1.9887-1.326*x-(3.49-
.68*x+1.35*x^2.0)*x*(1.0-x)/(1.0+x)^2.0), x=0..0.9);
```

```
> fsolve(diff(0.8944/(x-0.2)^.5*2.952*x^0.5/(1.0-x)^1.5*(1.9887-1.326*x-
(3.49-.68*x+1.35*x^2.0)*x*(1.0-x)/(1.0+x)^2.0), x) = 0.0, x, x=0..0.9);

                              .3894588280
```

VITA

VITA

DMITRI G. BRODKIN

DOB: June 28, 1964
CITIZENSHIP: Russia

EDUCATION: **Ph.D.** in Materials Engineering, 1996
Drexel University, Philadelphia, PA
MS in Physical Chemistry, 1987
Moscow Institute of Steel and Alloys, Moscow, Russia

PROFESSIONAL EXPERIENCE

Academic:

9/1992-present Drexel University, Department of Materials Engineering, Philadelphia, PA
Research Specialist Innovative process development and characterization of advanced ceramic materials. Material systems: Si_3N_4, TiC-TiB_2, machinable nano-laminate ceramics: Ti_3SiC_2, Ti_3GeC_2, Ti_2AlC, Ti_2AlN.
Research Assistant Project: "Processing-Structure-Properties Relations in Ultra-Refractory Composites Fabricated by Transient Plastic Phase Processing" funded by the Structural and Mechanical Systems Division of the NSF.
Teaching Assistant "Fundamentals of Materials".

Industrial:

1990-1991 Russian-Austrian Joint Venture "GEOSOFT", Moscow, Russia
R&D Engineer Developed electrochemical techniques and devices for research and commercial applications:
- sensors for field and deep-water environmental measurements;
- impressed current automotive anticorrosion devices.

1987-1990 State Research Institute for Nonferrous Metals "GINTSVETMET" Moscow, Russia
Research Engineer, Electrochemical Division Developed novel technologies for electrolysis:
- production of nickel and cobalt powders;
- sponge-nickel electrodeposition;
- reduction of acid aerosol formation by fluoro-organic surfacants.

PATENTS

(1.) M.Barsoum, T. El-Raghy, D. Brodkin, A. Zavaliangos, and S. Kalidindi, "Synthesis of 3-1-2 Phases and Composites Thereof", non-provisional patent application filed 3/6/96.

(2.) M.Barsoum, T. El-Raghy, and D. Brodkin, "Synthesis of H-phase products", in preparation for non-provisional patent application, provisional patent application filed 1/16/96.

PUBLICATIONS

(5 papers in conference proceedings are not included)

(1.) L.G. Rasgovornova, L.A. Andreev, E.A. Kalashnikova and D.G. Brodkin, "Influence of Carbide Phase on The Solubility and Diffusion of Hydrogen in Low-Alloy Steel", *Metal Science and Heat Treatment of Metals*, **31** [2] 6-9 (1989).

(2.) M. Barsoum, A. Zavaliangos, S. Kalidindi, T. El Raghy and D. Brodkin, "Transient Plastic Phase Processing of Ceramic/Ceramic Composites", *JOM* , **47** [11] 52-55 (1995).

(3.) D. Brodkin and M. Barsoum, "Isothermal Section of Ti-B-C Phase Diagram at 1600°C", *J. Am. Ceram. Soc.*, **79** [3] 785-87 (1996).

(4.) D. Brodkin, S. Kalidindi, M. Barsoum, and A. Zavaliangos, "Microstructural Evolution During Transient Plastic Phase Processing of Titanium Carbide - Titanium Boride Composites", *in press J. Am. Ceram. Soc.*, 1996.

(5.) D. Brodkin, S. Kalidindi, M. Barsoum, and A. Zavaliangos, "Room and High Temperature Properties of Titanium Carbide-Titanium Boride Composites Fabricated by Transient Plastic Phase Processing", *in review J. Am. Ceram. Soc.*, 1996.

(6.) M. Barsoum, D. Brodkin and T. El-Raghy, "Machinable Layered Ceramics for High Temperature Applications", *in review Scripta Metallurgica.*